NASA SP-243

INTRODUCTION TO EXPERIMENTAL TECHNIQUES OF HIGH-ENERGY ASTROPHYSICS

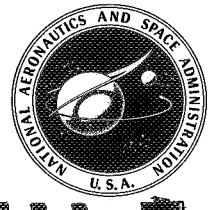

NATIONAL AERONAUTICS AND SPACE ADMINISTRATION

NASA SP-243

INTRODUCTION TO EXPERIMENTAL TECHNIQUES OF HIGH-ENERGY ASTROPHYSICS

EDITED BY
H. ÖGELMAN AND J. R. WAYLAND

PREPARED BY
NASA GODDARD SPACE FLIGHT CENTER

Scientific and Technical Information Division
OFFICE OF TECHNOLOGY UTILIZATION 1970
NATIONAL AERONAUTICS AND SPACE ADMINISTRATION
Washington, D.C.

For sale by the Clearinghouse for Federal Scientific and Technical Information, Springfield, Virginia 22151
CFSTI price $3.00
Library of Congress Catalog Card Number 78-608300

FOREWORD

As a continuation of the 1968 summer course in high-energy-astrophysics*, the department of Physics and Astronomy of the University of Maryland and High-Energy Astrophysics Branch of Goddard Space Flight Center jointly presented a course entitled "Introduction to Experimental Techniques of High-Energy Astrophysics" during the summer of 1969. Throughout the lectures, notes were distributed to the students to serve as basic text material for the course; this publication is an edited compilation of these notes. The students attending the course were first or second year graduate students, establishing the level of the notes.

The intention of the course was primarily to expose the students to the experimental techniques of high-energy astrophysics, seasoned with theoretical motivations and existing experimental data.

Some topics involving general discussion, such as interaction of gamma rays with matter, are covered in more than one place so as to make each chapter an independent reading unit.

The editors thank the Editorial Branch of Goddard Space Flight Center for its assistance in the preparation of this book.

H. Ögelman†
Goddard Space Flight Center

J. R. Wayland
University of Maryland

*Ögelman, H., and Wayland, J. R., "Lectures in High-Energy Astrophysics," NASA Special Publication 199, 1969.

†National Academy of Sciences, Postdoctoral Resident Research Associate. Present address: Faculty of Science, Middle East Technical University, Ankara, Turkey.

CONTENTS

I. THE MEASUREMENTS OF NON-RELATIVISTIC CHARGED PARTICLES OF EXTRA-TERRESTRIAL ORIGIN

G. Gloeckler*
University of Maryland
College Park, Maryland

INTRODUCTION

The study of cosmic rays or energetic particles of extra-terrestrial origin is important because of the information that they carry about the structure of the universe. For example, the energy spectra and chemical and isotopic composition provide clues not only about the nature of cosmic-ray sources but also about propagation in interstellar and interplanetary space. One studies the nature of solar-magnetic-field interactions with cosmic rays by observing the variations of the abundances and energy spectra with time. In this respect measurements not only near the earth but at different heliocentric locations are important. Low-energy ($\lesssim$200 MeV) cosmic rays are influenced most by the various physical phenomena in the universe; hence it is easy to comprehend the importance of measuring extra-terrestrial charged particles in this energy range.

Only in the last five years or so has it been possible to attempt many of these measurements. The strong magnetic field and atmosphere of the earth are effective in screening out low-energy charged particles; we could obtain meaningful results only by going outside this environment. Experiments had to be designed for flights on high-altitude balloons, rockets, satellites, and space probes. This, and the nature of the cosmic radiation, placed severe constraints on the types of instruments that could be used.

Before discussing the specific experimental techniques employed, we will briefly summarize our present knowledge of low-energy cosmic rays of solar and of galactic origin. Then we shall examine the problem

*Department of Physics and Astronomy.

of charged-particle interaction with matter. Following this, we shall discuss the principles of operation of several charged particle detectors. Finally, we shall describe several low energy cosmic ray instruments that are being used to measure the energy spectra and chemical and isotopic abundances of charged particles as a function of time.

SUMMARY OF LOW-ENERGY COSMIC-RAY MEASUREMENTS

Table 1 lists the relative abundances of galactic cosmic rays. The energy range for these measurements is about 50-200 MeV/nucleon, and the time period covered is from 1965 to 1967. Basically, elements fall into several distinct abundance groups, with hydrogen and helium being most abundant.

Table 1. Relative Abundance Groups of Chemical Elements

Element	Relative Abundance at 50-200 MeV/nucleon
	(Oxygen = 100)
H^1	20,000
He^4	4,500
He^3, H^2	~400
C, O	100
Li, B, N, Ne, Mg, Si	20-30
Be, Na, Al, S, P-K, Ca-Cr, Mn-Ni	5-10
F, P	1-3

The differential energy spectra for protons and helium nuclei are shown in Figure 1. Note that the differential intensity of protons, the most abundant element in the cosmic rays, has an average value of only 1 $(m^2\text{-sec-ster-MeV})^{-1}$ in the energy range ~50-200 MeV. The flux of some of the rare elements such as fluorine is reduced by a factor of 10,000. Such low intensities make the precise determination of the energy spectra of the less abundant elements very difficult.

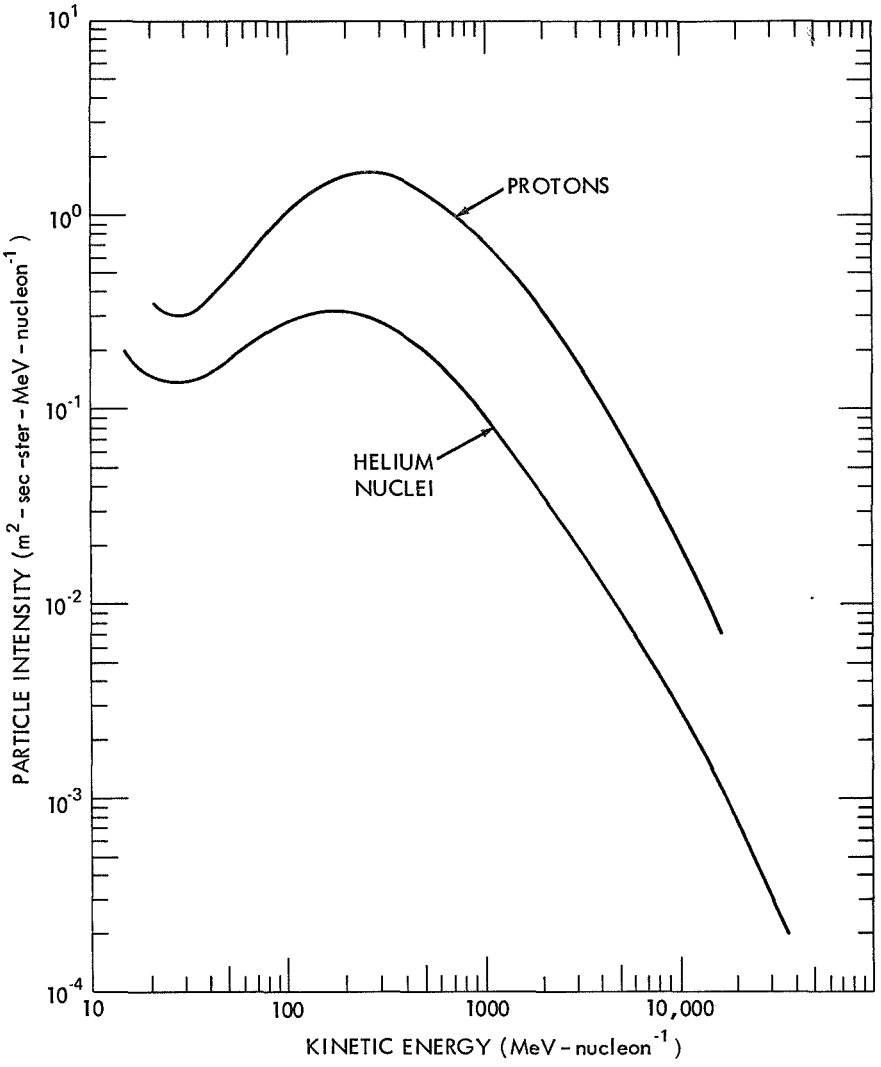

Figure 1–Differential energy spectra of galactic protons and helium nuclei measured near earth in 1965.

Below ~1000 MeV/nucleon, the energy spectra of protons and helium nuclei are different. However, the energy spectra of elements heavier than helium seem to have the same shape as the helium spectrum, at least within experimental error.

The intensity and energy spectra of galactic cosmic rays observed near earth exhibit a long-term cyclic time variation with a period of approximately eleven years. The spectra shown in Figure 1 have been measured near minimum solar activity when the cosmic-ray intensity reaches its maximum value.

Solar "cosmic rays" or energetic particles of solar origin may be grouped into three categories. First, energetic particles are observed following solar flares. The shapes of the energy spectra, relative abundances of protons to helium, and absolute intensities of flare particles are highly variable from one event to the next. However, the relative abundances of nuclei with $Z > 2$ relative to helium remains reasonably constant and tends to reflect the composition of the sun. Table 2 lists the abundances of several chemical elements found in solar cosmic rays relative to oxygen and compares these with the solar composition.

Table 2. Abundance of Different Chemical Elements, Relative to Oxygen, in Solar Cosmic Rays and at the Sun

Element	Solar Cosmic Rays	Solar Composition
He	10,700	?
Li		$\ll 0.1$
B	<2	$\ll 0.1$
C	59	60
N	19	10
O	100	100
F	<3	$\ll 0.1$
Ne	13	?
Na		0.2
Mg	4	2.7
A		0.2
Si	3	3.5

The intensity variation with time for protons associated with a solar flare is illustrated in Figure 2. It can be seen that for solar flare particles the intensity may change by a factor of 10^4 - 10^6 in a few hours and that the intensity typically exhibits many small-scale variations of shorter duration.

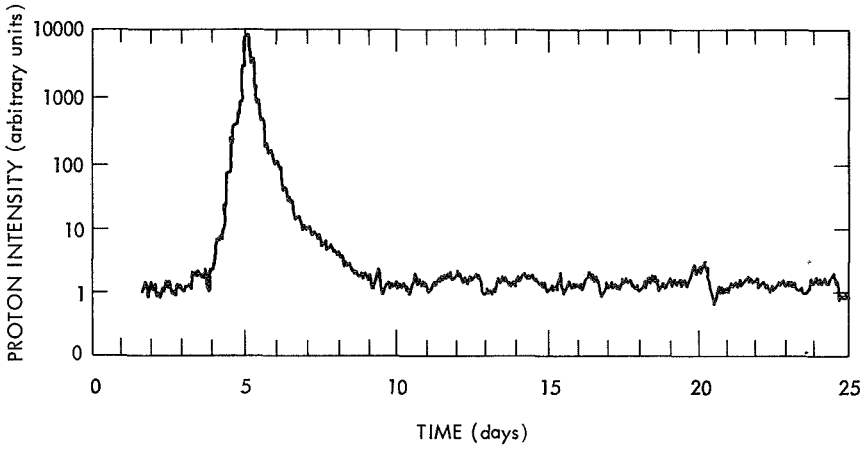

Figure 2–Time variation of the proton intensity for a typical solar-flare event.

The second class of solar particles is associated with persistent active regions on the sun. The intensity-time profiles of particles associated with these regions exhibit a 27-day recurrence corresponding to the period of rotation of the sun. Figure 3 illustrates a typical 27-day recurrent event. The intensity increase is 10 to 100 above background, persists for several days, and reappears about 27 days later.

Finally, it is believed that the sun emits low-energy ($\lesssim$20 MeV) particles more or less continuously. The energy spectra of this steady solar component have a positive slope and contribute to the increase in intensity below $\sim$20 MeV/nucleon, as apparent in Figure 1.

The energy spectra of solar energetic particles have a positive slope; that is, the intensity increases with decreasing energy down to the lowest observable energies around 1 MeV.

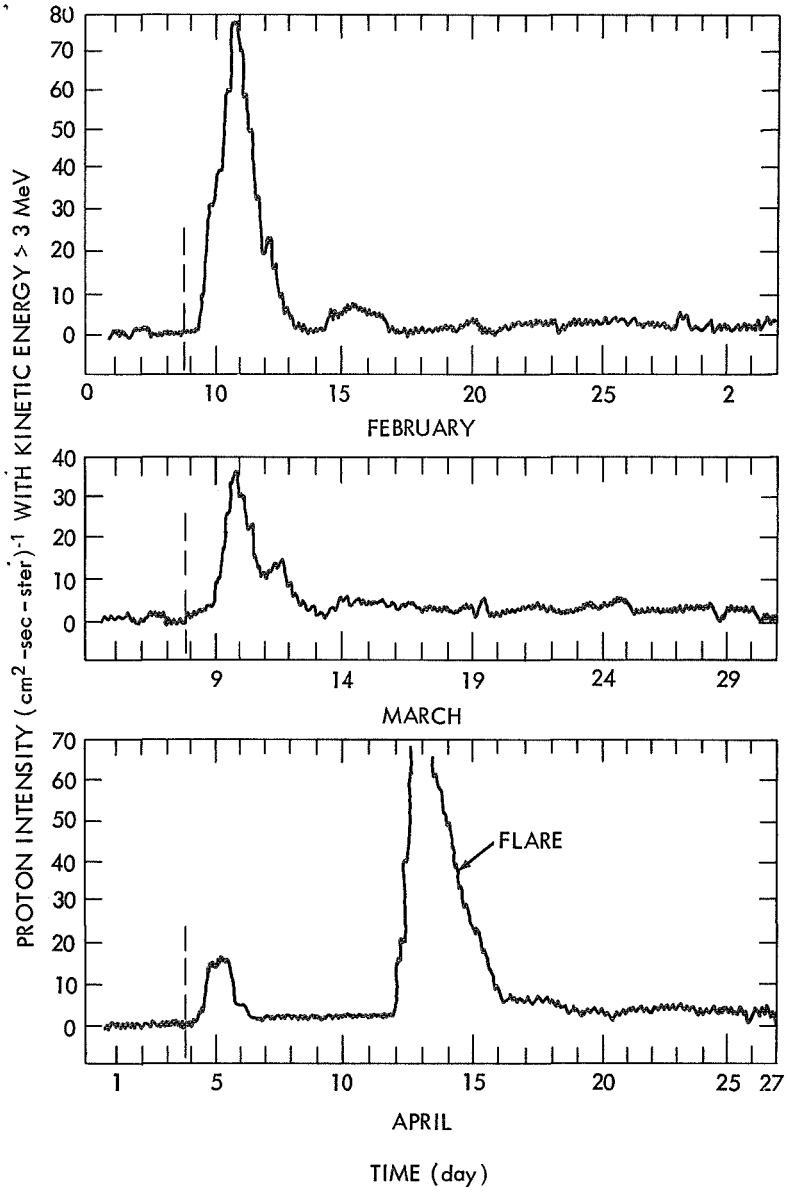

Figure 3–Time-intensity profiles for a 27-day recurrent event. The dashed line is a 27-day fiducial marker.

In view of the properties of cosmic rays discussed above, an instrument designed for cosmic-ray studies must be able to respond to very small fluxes, yet cover intensity increases of $\sim 10^6$ without saturating, and be capable of a fine time resolution.

INTERACTION OF CHARGED PARTICLES WITH MATTER

The principal mode of energy loss of a charged particle (with mass $M \gg$ electron mass m) in matter is by the electromagnetic interactions that raise the electrons of the material to excited energy states. This could lead either to an ionized state for the electron or to an excited bound state, depending on the amount of energy transferred to the electron by the penetrating particle. In either case the increment of energy given to the electron comes from the kinetic energy of the incident particle. This process of losing energy is called energy loss by ionization or simple ionization loss.

It is a fairly straight-forward operation to derive a simplified expression for the ionization loss of heavy particles in matter. Consider an electron of mass m at a perpendicular distance b (impact parameter) from the path of an incident particle with charge Ze, mass M, and velocity V (see Figure 4). We assume that the electron is free and

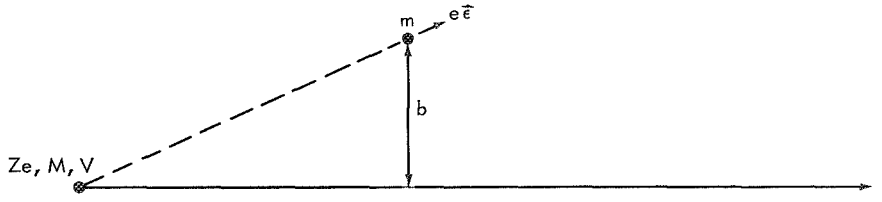

Figure 4—Force $e\vec{\mathcal{E}}$ on the electron at rest due to a charged heavy particle of mass M and velocity V.

initially at rest, that the velocity V is greater than the velocity acquired by the electron in the interaction, and that the electron moves only slightly during the collision. First, we find the momentum acquired by the electron. From this we compute the incremental energy lost by the incident particle in the collision with a single electron. Then we obtain the total energy lost in ionization, by summing over all electrons contained in a unit volume of the material.

As the heavy particle passes, the electrostatic force at the position of the electron, $e\vec{\epsilon}$, changes direction. Under our assumptions that the electron remains stationary, it follows that the total impulse in the direction parallel to the path of the particles averages out to zero. To estimate the impulse perpendicular to the path, $I_\perp$, we note that

$$I_\perp = \int F_\perp \, dt$$

$$\sim \frac{Ze^2}{b^2} \cdot \frac{b}{V}$$

$$= \frac{Ze^2}{bV} .$$

Let us compute this impulse more exactly using Gauss's theorem:

$$\int_{surface} \vec{\epsilon} \cdot \vec{dS} = 4\pi Ze .$$

For the surface take an infinitely long cylinder of radius b with the axis along the path of the particle. Now,

$$I_\perp = e \int_{-\infty}^{\infty} \epsilon_\perp \, dt$$

$$= e \int_{-\infty}^{\infty} \epsilon_\perp \frac{dx}{V}$$

$$= \frac{e}{V} \int_{-\infty}^{\infty} \epsilon_\perp \, dx .$$

But from Gauss's theorem,

$$\int_{-\infty}^{\infty} \epsilon_{\perp} \, 2\pi \, b \, dx \;=\; 4\pi \, Ze$$

or

$$\int_{-\infty}^{\infty} \epsilon_{\perp} dx \;=\; \frac{2Ze}{b} \, .$$

So

$$I_{\perp} \;=\; \frac{e}{V} \frac{2Ze}{b} \;=\; P \, ,$$

the momentum acquired by the electron. The energy is

$$\frac{P^2}{2m} \;=\; \frac{2Z^2 \, e^4}{mV^2 \, b^2} \tag{1}$$

for a single collision. Next we compute the number of collisions per unit path length that have impact parameters in the range from b to b + db. This number is the density times the volume of a cylindrical shell of radius b, thickness db, and unit length. Let N be the number of electrons per unit volume. Then

$$dE(b) \;=\; \frac{2Z^2 \, e^4}{mV^2 \, b^2} \, 2\pi \, b \, N \, db$$

and the total energy lost per unit path length, dx, is

$$-\frac{dE}{dx} \;=\; \int_{b_{min}}^{b_{max}} dE(b) \, dE \;=\; \frac{4\pi \, Z^2 \, e^4 \, N}{mV^2} \, \ln \frac{b_{max}}{b_{min}} \, . \tag{2}$$

We can express N in terms of the mass density of the material, ρ, its charge number, z, mass number, A, and Avogadro's number N_0. Then

$$N = N_0 \rho \frac{z}{A} .$$

Furthermore, we define $C = \pi N_0 r_e^2 (z/A)$, which corresponds to the total "area" covered by electrons contained in one gram of material with each electron considered as a sphere with radius $r_e = e^2/mc^2$. Then Equation 2 becomes

$$-\frac{dE}{dx} = \frac{4Z^2 mc^2}{\beta^2} C\rho \ln \frac{b_{max}}{b_{min}} , \tag{3}$$

where $\beta^2 = V^2/c^2$, and c is the velocity of light. Since $mc^2 = 0.511$ MeV and $c = 0.15 z/A\ g^{-1}\ cm^{-2}$, the energy lost due to ionization expressed in MeV/cm is

$$-\frac{dE}{dx} = 0.307 \frac{Z^2}{\beta^2} \left(\frac{z}{A} \rho\right) \ln \frac{b_{max}}{b_{min}} , \tag{4}$$

or, expressed as energy lost in MeV per g/cm^2 units,

$$-\frac{dE}{d\xi} = -\frac{1}{\rho}\frac{dE}{dx} = 0.307 \frac{Z^2}{\beta^2} \left(\frac{z}{A}\right) \ln \frac{b_{max}}{b_{min}} . \tag{5}$$

Let us next estimate values for b_{max} and b_{min}. The time interval, τ, during which the electron experiences the electric field of the incident particle, is of the order $\tau \approx b/V$. If $1/\tau \ll \nu$, the frequency of vibration of the electron, then the electron absorbs practically no energy. The proof of this statement is left as an exercise for the reader. To make the argument relativistically correct, we note that the field "sharpens up," and ϵ approaches $\epsilon/\sqrt{1-\beta^2}$ as V approaches c. Hence, $\tau \to (b/V)\sqrt{1-\beta^2}$. To transfer energy to the electron we must have $1/\nu \gtrsim \tau$ or $b \lesssim V/\nu\sqrt{1-\beta^2}$. Thus the maximum value of b, b_{max}, may be

taken to be

$$b_{max} = \frac{V}{\nu\sqrt{1-\beta^2}} \cdot \tag{6}$$

To find b_{min}, we note that classically the maximum velocity acquired by the electron is 2V. Hence the maximum energy transferred is $E_{max} = 2mV^2$. From Equation 1, the energy transferred per collision is $2Z^2 e^4/mV^2 b^2$ and must not exceed $2mV^2$. Thus, $b \gtrsim Ze^2/mV^2$ and

$$\left(b_{min}\right)_{cl.} = \frac{Ze^2}{mV^2} \cdot \tag{7}$$

This classical treatment is valid only if the Coulomb field of the incident particle varies little over the dimension $\lambda\!\!\!^{-}$, where $\lambda\!\!\!^{-}$ is the de Broglie wavelength of the electron as seen by the incident particle. Thus, $b > \lambda\!\!\!^{-} = \hbar/p = \hbar\sqrt{1-\beta^2}/mV$, and the quantum-mechanical limit for b is

$$\left(b_{min}\right)_{Q.M.} = \frac{\hbar\sqrt{1-\beta^2}}{mV} \cdot \tag{8}$$

It can be shown that for values V where $b_{max} > b_{min}$, $\left(b_{min}\right)_{Q.M.} > \left(b_{min}\right)_{cl.}$ (where Q.M. refers to quantum mechanical value, and cl. refers to classical value) and hence Equation 8 must be used. Substituting Equations 6 and 8 in 3, we have

$$-\frac{dE}{d\xi} = \frac{4Z^2 mc^2}{\beta^2} C \ln \frac{mc^2 \beta^2}{\hbar\nu\left(1-\beta^2\right)} \cdot \tag{9}$$

A more precise calculation—see, for example, Reference 1 (page 24)—gives

$$-\frac{dE}{d\xi} = \frac{4Z^2 mc^2}{\beta^2} C \left(\ln \frac{2mc^2 \beta^2}{\bar{I}\left(1-\beta^2\right)} - \beta^2\right) , \tag{10}$$

where $\bar{I} = \hbar\nu \sim (13.5\ z)$ eV, is the average ionization potential of electrons in the absorber.

The energy-loss-by-ionization formula for electrons differs from that for heavy particles (Equation 10), because (a) the incident electron will be considerably deflected in a collision, and (b) for collisions involving identical particles exchange phenomena must be taken into account. Møller (Reference 2) obtains the following expression for the ionization energy loss of electrons:

$$-\left.\frac{dE}{d\xi}\right|_{el} = \frac{2C\,mc^2}{\beta^2}\left[\ln\frac{mc^2\,\beta^2\,T_e}{2\bar{I}^2\left(1-\beta^2\right)} - \ln 2\left(2\sqrt{1-\beta^2} - 1 + \beta^2\right) + 1 - \beta^2\right] \quad (11)$$

Here the kinetic energy of the electron is given by

$$T_e = mc^2\left(\frac{1}{\sqrt{1-\beta^2}} - 1\right) .$$

Returning to Equation 10 we examine the dependence of $-dE/d\xi$ for, say, protons on the proton kinetic energy T. For $\beta \ll c$,

$$T = \frac{1}{2}MV^2 ,$$

$$-\frac{dE}{d\xi} = 0.153\,\frac{z}{A}\left(\frac{Mc^2}{T}\right)\ln\left(4\,\frac{mc^2\,T}{Mc^2\,\bar{I}}\right)$$

$$= 0.153\,\frac{z}{A}\left(\frac{Mc^2}{T}\right)\left(\ln\frac{4mc^2}{\bar{I}} + \ln\frac{T}{Mc^2}\right)$$

$$= 0.153\,\frac{z}{A}\left(\frac{Mc^2}{T}\right)\left(11.9 - \ln z + \ln\frac{T}{Mc^2}\right) . \quad (12)$$

The dominant energy dependence is contained in the first term. Note that the dependence on the material is given primarily by the ln z term, since $z/A \sim 1/2$ for most elements. Thus, for the same energy, the loss per g-cm^{-2} will be <u>less</u> in a heavy (high z) material than in a light material. As an example, take protons with $T/Mc^2 \sim 0.1$ (~100 MeV protons) passing through 1 g-cm^{-2} of silicon ($z \sim 14$). From Equation 12, $dE/d\xi$ is derived as 5.3 MeV-gm^{-1} cm^{-2}. On the other hand, 100-MeV protons will lose ~4.8 MeV in 1 g-cm^{-2} of copper.

In the relativistic limit, where $T \sim E \gg Mc^2$ and $\beta \sim 1$, Equation 10 reduces to

$$-\frac{dE}{d\xi} \sim 0.307 \frac{z}{A}\left[10.1 + 2 \ln\left(\frac{T}{Mc^2}\right) - \ln z\right] . \qquad (13)$$

For 10^4-MeV protons passing through 1 g-cm^{-2} of silicon the energy lost is ~1.5 MeV. Using Equations 12 and 13, we show in Figure 5 the behavior of $dE/d\xi$ as a function of T/Mc^2. Note the minimum in the curve at $T/Mc^2 \sim 1$-5. Also, at very low energies, Equation 10 breaks down because the particles have velocities comparable with those of orbital electrons and because the efficiency of energy exchange is much lower. The minimum value of $dE/d\xi$ is about 1-2 MeV per g/cm^2.

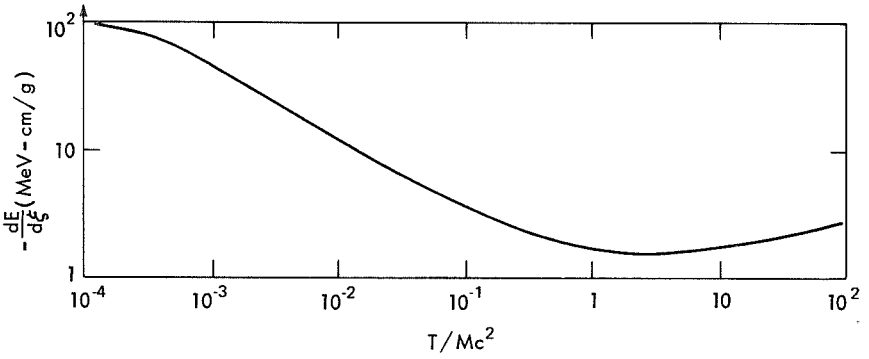

Figure 5–Energy loss by ionization as a function of the kinetic energy of the incident particle.

The important feature of Equation 10 is that the energy lost by ionization for particles other than protons can be obtained in a simple fashion, once the proton energy loss is known. The relation is,

$$\left(\frac{dE}{d\xi}\right)_{\substack{Z\neq 1 \\ T=AT_p}} = Z^2 \left(\frac{dE}{d\xi}\right)_{\substack{p \\ T=T_p}} . \tag{14}$$

Thus, a 100-MeV α particle (A = 4, z = 2) will lose 4 times the energy that a 25-MeV proton will lose in passing through the same amount of absorber.

Using the energy-loss equation it is possible to compute how far a particle with kinetic energy T_0 will travel in an absorber before losing all its energy. This distance, or <u>range</u>, is given by

$$R = -\int_{T_0}^{0} \frac{1}{\frac{dE}{dx}}\, dE \qquad (cm) ,$$

or

$$R = -\int_{T_0}^{0} \frac{1}{\frac{dE}{d\xi}}\, dE \qquad \left(g/cm^2\right) . \tag{15}$$

In general, Equation 15 is integrated numerically, using Equation 10. To obtain a very rough approximation of R for protons, we use Equation 12 and neglect $\ln\left(T/Mc^2\right)$ as compared with the constants. Then

$$R = \int_0^{T_0} \frac{T\, dT}{0.153\,(z/A)\,Mc^2\,(11.9 - \ln z)} = \alpha\, T_0^2 \ (g/cm^2) , \tag{16}$$

where $\alpha = 1.4 \times 10^{-3}$ g(MeV-cm)$^{-2}$ for Si(z = 14). Thus, the range of 100 MeV protons in Si is about 12 g-cm^2.

More precise integration using Equation 10 for $dE/d\xi$ shows that $R \propto T^{\alpha}$ where α is slightly energy-dependent and has a value between 1 and 2. Figure 6 shows a typical range-energy curve.

To generalize range-energy relations to particles heavier than protons, we use $dE/d\xi$ from Equation 14.

$$R_{Z\neq 1}\left(T = AT_p\right) = \frac{1}{Z^2}\int_0^{AT_p} \frac{dT}{\left(\frac{dE}{d\xi}\right)_{T_p}}$$

$$= \frac{A}{Z^2}\int_0^{T_p} \frac{dT_p}{\left(\frac{dE}{d\xi}\right)_{T_p}}$$

$$= \frac{A}{Z^2} R_p\left(T_p\right) . \qquad (17)$$

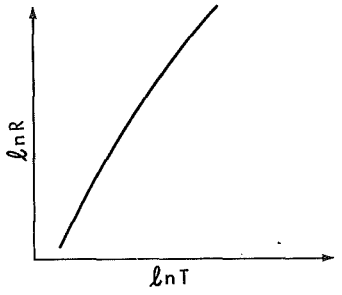

Figure 6–Typical range-energy curve.

Thus, the range of a 400-MeV α-particle is the same as that of a 100-MeV proton in the same material.

More precise computations of energy loss by ionization are given in Rossi (Reference 1), and tabulation of $dE/d\xi$ and R vs T are available. (See, for example, Berger and Selzer (Reference 3); Barkas and Berger (Reference 4); Skyrme (Reference 5).

PRINCIPLES OF OPERATION OF CHARGED-PARTICLE DETECTORS

General Discussion

Methods of detecting charged particles are generally based on the process of ionization or excitation of atoms in the detection medium through which the charged particle is allowed to pass. The techniques by which the ions, electrons, or excited atoms are subsequently detected vary widely. Many different types of detectors exist which employ gas, liquid, or solid detection materials with and without applied electric fields.

In gaseous and solid counters, electrons and ions (holes) liberated by ionization can be collected at the boundary electrodes under an applied electric field. In the scintillation counter, light emitted by excited atoms is detected by photosensitive devices such as photomultiplier tubes or photo-diodes. In a nuclear emulsion, ionization is the principal cause of activation by which grains of silver halide are rendered developable. In solid-state track detectors, ionization produced by incident particles weakens the molecular bonds of the material which is then etched preferentially, making particle tracks visible. We shall discuss in any detail only those detection methods that have been used in cosmic-ray experiments—even here we must be somewhat selective because of lack of space. We shall not discuss the electronic equipment that generally must be used with these detectors.

Gas-Filled Counters

Gas-filled counters are the oldest radiation detectors. They are generally classified under three heads: ionization chambers, proportional counters, and the Geiger-Müller (G-M) tubes. Each of these detectors is basically a gas-filled chamber with a central electrode well insulated from the chamber walls, as shown in Figure 7.

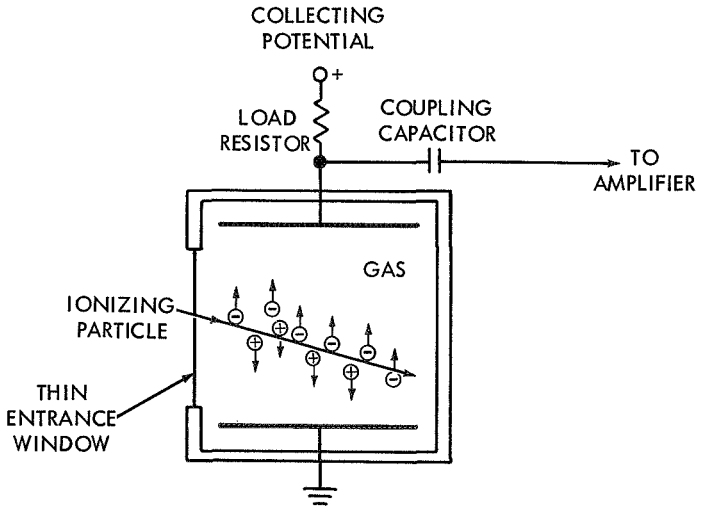

Figure 7–Schematic diagram of a gaseous ionization chamber.

A charged particle passing through such a device will ionize the gas along its path. The applied potential difference between the electrodes tends to sweep the positive and negative charges toward the respective electrodes, causing a charge Q to appear on the capacitor. The resulting voltage pulse is then amplified and recorded.

The amount of charge collected, and hence the amplitude of the voltage pulse, will depend on the applied voltage, V, as is illustrated in Figure 8. The curve of pulse height vs applied voltage may be divided into four main regions. In region I, the electric field is so weak that recombination of charges takes place long before they can drift apart to be collected. Clearly, no output results from such a device. In region II, the loss of ions due to recombination is small so that the charge collected is $Q = Ne$, where N is the number of ion pairs produced

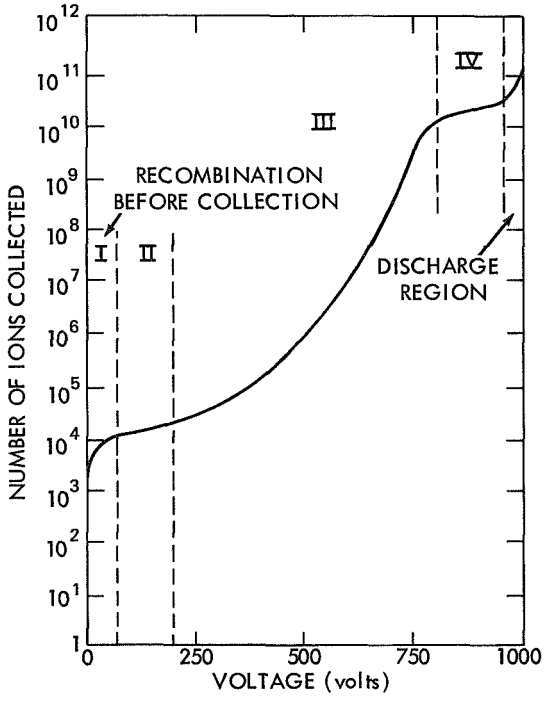

Figure 8–Pulse height as a function of applied voltage, illustrating the regions of operation of a gas chamber. Regions II, III, and IV correspond respectively to the ionization chamber, the proportional counter, and the Geiger-Müller mode of operation.

by the incident particle. This region is called the ionization chamber region. In region III, the charge collected is increased by a factor M through gas multiplication. The electrons released in the primary ionization will acquire enough energy from the electric field to produce additional ionization and thus add to the total charge. At the onset of region III, the multiplication factor M is independent of the initial ionization. Thus the output pulses will be proportional to the amount of primary ionization. This proportionality breaks down towards the end of region III, where the pulses tend to be nearly independent of the initial ionization. The two portions of region III are called the proportional counter region and region of limited proportionality. In region IV, the charge collected is completely independent of the initial ionization; its value depends on the characteristics of the chamber and associated electronics. This region is known as the Geiger-Müller or G-M region. The examination of the detailed operation of these detectors is left as a problem.

Scintillation Detectors

In the scintillation detector, the light emitted by atoms excited directly or indirectly by the passage of a charged particle is converted to an electrical signal. The scintillation material may be a solid, a liquid, or even a gas; the device converting light into an electrical signal is generally a photomultiplier tube, although in some applications photo-diodes are used. Solid scintillators have the obvious advantage over gas counters of having a detecting medium with a high electron density. Hence, energetic particles may be stopped in a relatively small volume of the detector. In addition, these counters have a faster response and can operate at much higher counting rates than gas counters. Their main disadvantages are due to problems of light collection and conversion to electrical signals, which require high voltage supplies, phototubes etc. The use of photo-diodes tends to reduce some of these problems.

A typical scintillation counter assembly is shown in Figure 9.

The initial step leading to the formation of an output pulse is the interaction of a charged particle with the atoms of the scintillator, causing the particle to give up part or all of its energy. Only a small fraction, η, of the lost energy, ΔE, is converted into light, which is characterized by some spectral distribution with E_{ph}, the average energy of the emitted photons. The number of photons, N_0, produced is

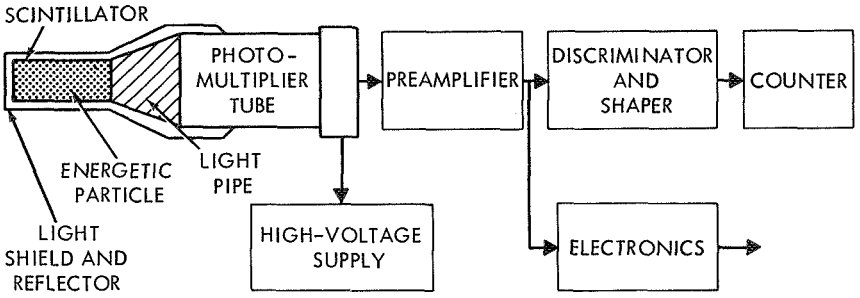

Figure 9–Schematic diagram of a scintillation detector with typical electronic circuitry.

$N_0 \sim \eta \Delta E / E_{ph}$. The number of photons that reach the photocathode of the tube is less than N_0 because of losses in reflections from the walls and in passage through the crystal and optical coupling, or light pipe. Thus, $N = \omega N_0$, where ω is the optical efficiency. If a photomultiplier tube is used, the ejection of an electron from the photocathode by a photon occurs with a probability θ, the photoelectrons reach the first dynode with an efficiency $\mu < 1$ and, by secondary emission, the number of electrons is increased K times. Combining all these processes leads to a charge Q produced at the photomultiplier tube output given by

$$Q = \Delta E \frac{\eta \omega \theta \mu}{E_{ph}} Ke ,$$

where e is the charge of an electron. Clearly the constant of proportionality between Q and ΔE depends critically on the type of scintillator, light-coupling, photomultiplier tube, etc., that are used; in general, it is almost impossible to calculate this constant. For some of the more efficient inorganic scintillator assemblies it takes about 300 eV to produce one photoelectron.

Two types of scintillators are used: organic and inorganic. The organic scintillator material consists of aromatic hydrocarbons whose molecules contain benzene-ring structures along with various non-aromatic substitutions. Examples of organic scintillator are anthracene and stilbene crystals. Inorganic scintillators are crystals of

inorganic salts, primarily alkali halides containing small amounts of impurities as activators for light emission. The desirable properties of a good scintillator are high conversion efficiency η, high transparency to its fluorescent radiation, short decay times for fluorescent radiation, and a spectral distribution consistent with the responses of available photosensitive devices.

The mechanism for converting ionization energy to scintillation energy is different for the two types of scintillators. In the organic crystal the luminescence process is best discussed in terms of a potential-energy graph for the molecule. A typical diagram is shown in Figure 10. The two curves respectively represent potential energy vs interatomic distance for two cases: (1) when all electrons of the molecule are in the ground state, and (2) when one electron is in the excited state. For each of these potential-energy curves, the allowed vibrational levels are indicated by horizontal lines. The passage of a charged particle through the crystal may transfer an electron of the molecule into an excited state, as is represented by line AB. According to the Frank-Condon principle, the time required for this transfer is so short that the interatomic distance remains essentially unchanged. Therefore the electron at B may be in a highly excited state. The extra energy is lost as heat from lattice vibration of the crystal, and the electron may drop to the ground state while emitting fluorescent radiation (line CD). The time scale for this process is of the order of 10^{-8} sec. In the final transition from D to A again, the extra energy is dissipated as heat.

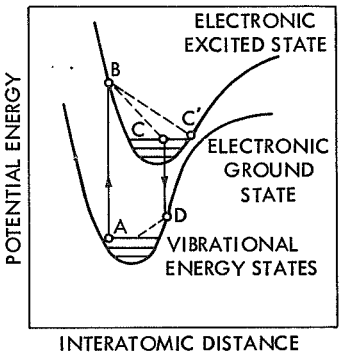

Figure 10–Potential-energy diagram for an organic scintillator.

There are several ways in which fluorescent radiation may be prevented. If the level B is sufficiently high, the molecule may simply dissociate. If the electron happens to find itself at point C', where the ground and excited states are close, direct transfer of energy may take place between these two levels.

It is apparent from this diagram that the crystal will be transparent to its own radiation, since it takes more energy to go from A to

B than is recovered by fluorescent emission (D to C). Hence only the most energetic photons will be absorbed in the crystal.

In inorganic crystals we can best describe the scintillation process by considering the band structure of the crystal. A pure alkali-halide crystal is represented in the band theory by a filled valence band and an empty conduction band, the two being separated by a forbidden energy gap, as is shown in Figure 11. A charged particle passing through

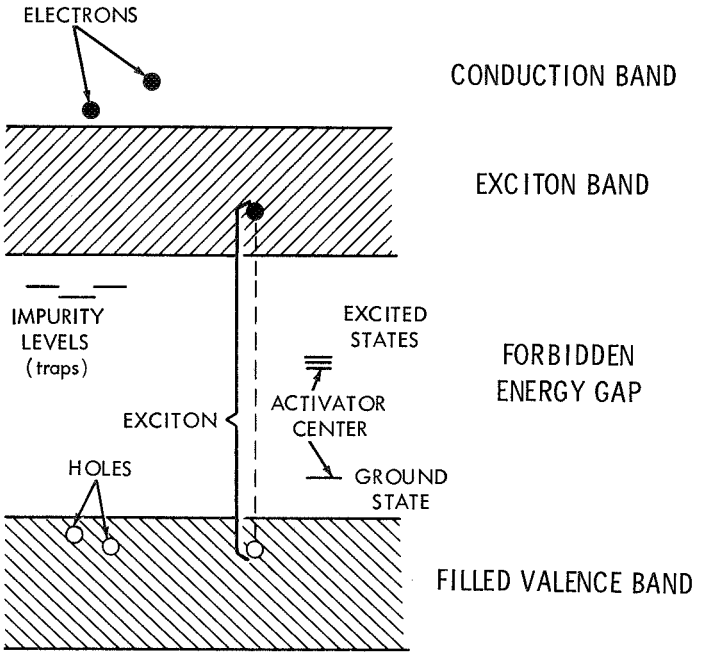

Figure 11–Band picture of alkali-halide crystals with activator centers and impurity levels.

the crystal can move an electron from the valence band into the conduction band. This process of ionization will create electrons in the conduction band, and holes or electron vacancies in the valence band. In many crystals the electrons and holes can move about independently. However, in many inorganic scintillators the electron-hole pair remains strongly coupled and moves about as a hydrogen-like "atom." These strongly coupled electron-hole pairs are called excitons (see

Figure 11). Excitons form a band of their own whose lower boundary corresponds to the ground state of the exciton, while the upper boundary coincides with the lowest energy of the conduction band. The excitons wander until they encounter a crystal imperfection (impurity atom, lattice defect, etc.). These imperfections create energy levels in the forbidden gap, as shown schematically in the diagram, and the probability for capturing excitons at the sites of the imperfections is large. Capture of excitons at an impurity-atom or activator site results in an excited state for that atom, which may then decay by emission of a photon or by a non-radioactive transition.

Because of the important role of exciton capture at activator sites, a controlled amount (typically 0.1 percent) of the proper impurity atoms is added to inorganic scintillators. Some inorganic crystals along with their activators are sodium iodide (NaI) and cesium iodide (CsI) with thallium (Tℓ), lithium iodide (LiI) with europium (Eu), and zinc sulfide (ZuS) with silver (Ag) as an activator.

The inorganic crystals are also transparent to their scintillation, because the fluorescent radiation has in general insufficient energy to excite electrons in the crystal. In inorganic crystals the conversion of nuclear-particle energy into light energy is more efficient than in organic crystals and may reach values of 20 to 30 percent. The decay time of fluorescence, on the other hand, is much longer, being of the order of 10^{-6} sec.

The conversion efficiency from particle energy to light energy varies with the type of particle, its energy, and the type of scintillator used. This is clearly a disadvantage of scintillation detectors, if one wishes to measure the energy lost by the particle in the detector. A measure of the degree to which a particular scintillator is affected by the type of particle it detects is given by the α-to-β ratio. This is the ratio of the conversion efficiency of a 5.3-MeV α particle and that of a high-energy ($\gtrsim$2 MeV) electron. For organic crystals, the α/β ratio is typically $\sim$10 percent while in inorganic crystals it approaches 100 percent.

A more fundamental way to show the dependence of conversion efficiency on particle type is to display the light output per unit energy lost, dL/dE, as a function of the stopping power dE/dx of the particle. Figure 12 shows experimental results for various heavy particles passing through a thickness Δx of NaI (Tℓ).

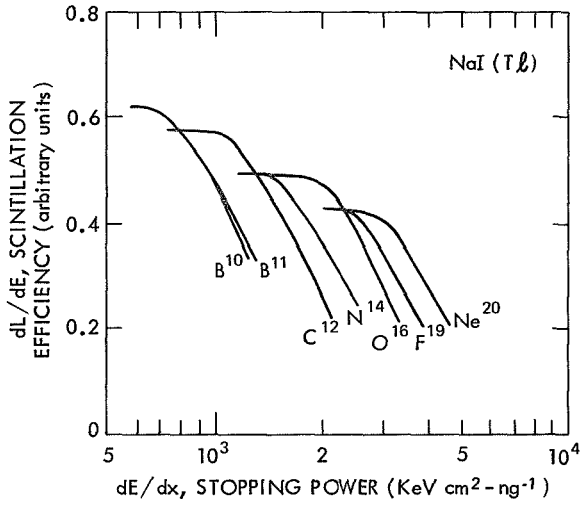

Figure 12–Experimental scintillation efficiency vs dE/dx for heavy ions in NaI (Tℓ).

For organic scintillators the reduction of the conversion efficiency for heavy particles is attributed to the relatively large fraction of non-radioactive transitions. These transitions occur from states excited by low-energy electrons (δ-rays) produced in the passage of high-energy particles. In the inorganic scintillator, the reduction in conversion efficiency is probably due to a saturation of the activator sites along the track of a heavily ionizing particle. More complete information is to be found in the references at the end of this paper.

Solid-State Detectors

Solid-state detectors are basically solid-state ionization counters. An electric field is set up within a semiconductor crystal by a voltage applied across opposite faces of the crystal. Radiation penetrating the crystal produces secondary electrons; these, in turn, produce further ionization in the crystal until no electron has enough energy left to ionize the atoms further. The electric field inside the crystal sweeps out the liberated charges, their number being proportional to the energy lost by the primary radiation.

There are several advantages which solid-state detectors have over gas-filled counters. First, because of the higher density of the

detection material, these counters are far more effective in stopping particles, and hence absorbing their energy, than are gaseous counters. Secondly, solid-state detectors can be made thin and essentially windowless. This is an important advantage in their application as dE/dx counters. Finally, because it takes on the average less energy for the production of an ion pair, the measurement of the incident particle energy in these detectors is more precise than in gaseous or scintillation counters.

Semiconductor material must have certain special properties before it can be used in the fabrication of detectors. The resistivity of the material must be high enough to support the required electric field without creating an excessive leakage current. The charge carriers must have a high mobility in the crystal in order to be collected in a reasonably short time. The trapping rate for the carriers must be low, in order to maintain a high efficiency for charge collection and to reduce space-charge buildup within the crystal. The average energy required to produce an ion pair must be low, in order to give better energy resolution. Finally, the crystal must be uniform and its properties stable over prolonged time periods.

Properties of Semiconductors

Silicon and germanium semiconductors have properties that make them useful in the fabrication of radiation detectors. For room-temperature operation only silicon can be used—therefore we shall primarily discuss detectors produced from this material. To understand how a semiconductor detector works, it is necessary to discuss first some basic properties of the material. In the band theory of solids, a semiconductor is represented by a completely filled valence band and an empty conduction band separated by a forbidden energy gap. This is similar to the description of the inorganic scintillator, except that the energy gap in semiconductors is smaller than in scintillation crystals. At absolute-zero temperature the semiconductor has infinite resistivity since the conduction band is empty. As the temperature is increased, a number of electrons jump the energy gap. The vacancies in the conduction band behave very much as positively charged carriers whose mass and mobility depend on the properties of the crystal. We refer to these positive carriers as holes. In a perfectly pure or intrinsic semiconductor the number n of electrons per cm^3 in the conduction band is equal to the number p of holes in the

valence band and is given by

$$n = p = A \cdot \exp\left(-\frac{E_g}{2kT}\right), \tag{18}$$

where E_g is the energy gap in eV, k is the Boltzmann constant, and T is the absolute temperature. The value of A is $\sim 10^{19}$. At room temperature, kT = 0.026 eV, $E_g \sim 1$ eV in silicon, and $n \sim 2 \times 10^{10}$ cm^{-3}. (Compare this with $\sim 10^{22}$ for a metal.) It can be shown that the theoretical resistivity of silicon at room temperature is around 10^5 ohm-cm. This resistivity is not enough to support the required electric fields without admitting large currents through the crystal.

There is another way in which electron-hole pairs may be produced in a semiconductor. A charged particle passing through the crystal loses energy by ionization, and in the collision process lifts electrons from the valence band or deeper-lying electronic bands to the conduction band or higher-lying unoccupied bands. The highly excited states quickly ($\sim 10^{-12}$ sec) decay until the electrons are near the bottom of the conduction band and the holes are near the top of the valence band. Decay of these highly excited states produces additional electron-hole pairs. This process is shown schematically in Figure 13. On the average, for every 3.6 eV a charged particle loses in the crystal, one electron-hole pair is produced. Assuming that the resistivity of the material is high enough (for example, T is low enough) to support an applied electric field E, the electrons and holes will drift toward the respective electrodes with drift velocities, $v_n = \mu_n E$ and $v_p = \mu_p E$, respectively. For silicon the electron and hole mobilities μ_n and μ_p are $\sim$1500 and 500 cm^2/volt-sec, respectively. Under ideal conditions the total charge collected will be Ne, where N is the number of electron-hole pairs released. There are, however, several processes that tend to remove a fraction of the carriers and reduce the total charge collected. One way to lose carriers is by recombination of electron-hole pairs; another way is for carriers to be trapped long enough to prevent their collection at the electrodes.

Incomplete charge collection in a detector is undesirable for several reasons. First, pulse size may become a function of applied voltage. Second, detector energy resolution is degraded. Third, if charge carriers are not quickly removed, internal electric fields are set up opposing the applied field. This further reduces charge-collection efficiency.

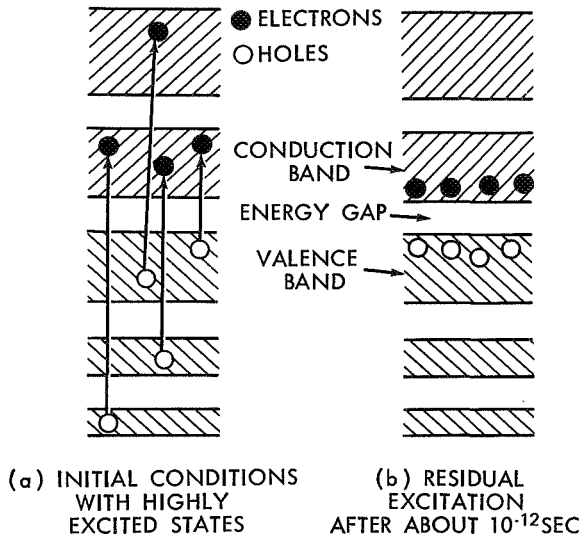

Figure 13–Production of electrons and holes in a semiconductor due to passage of an energetic charged particle.

It is impossible at this time to grow pure or intrinsic silicon; there are always small amounts of impurity atoms that produce energy levels in the forbidden gap and contribute additional charge carriers (see Figure 14). Impurity atoms can supply either additional electrons (donor impurities) or additional holes (acceptor impurities); both types of impurity may be present in the same crystal at the same time. Donors have energy levels in the forbidden zone near the conduction band; acceptors near the valence band. Because the energy gap between impurity levels and the conduction (valence) band is small, the number of free carriers is large (see Equation 18). These extra carriers add significantly to the conductivity of the material.

Semiconductor material is classified as either n type or p type depending on whether it contains more donor or more acceptor impurities. If the number of donors, N_D, is equal to the number of acceptors, N_A, the crystal behaves like an intrinsic semiconductor. This property is used to increase the resistivity of a crystal by doping or compensating it with the appropriate impurity to make $N_A \cong N_D$. Unfortunately, compensation also increases the number of traps. This, as we saw

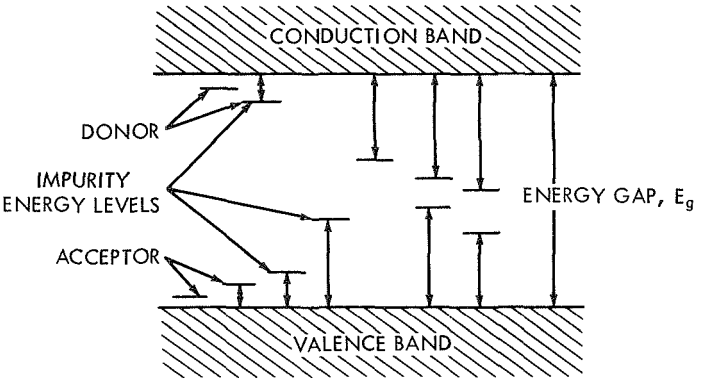

Figure 14–Impurity energy levels in a semiconductor.
Arrows show possible transitions.

earlier, is undesirable since the presence of traps tends to reduce collection efficiency and carrier lifetime and enhance the buildup of space charge.

Detectors made from compensated semiconductor material have only had limited success. Although compensation combined with cooling can increase resistivity to acceptable levels, the penalty is a drastic reduction in carrier lifetime.

The most successful semiconductor detectors are those employing a p-n junction under reverse bias. In this manner a charge-deficient region, called the depletion region, is produced in the vicinity of the junction interface. Three types of detector will be discussed: diffused-junction, surface-barrier and lithium-drifted detectors.

P-N Junction

When p-type and n-type semiconductors are brought into electrical contact, the electrons from the n material diffuse into the p material while the holes diffuse the other way, until a new equilibrium condition is established. The energy-band diagram and charge distribution across a p-n junction are shown in Figures 15a and 16. The depletion region x_0 contains no free carriers. We can increase the extent of the depletion region by applying a reverse bias across the junction. The energy-band diagram is appropriately modified as shown in Figure 15b. The

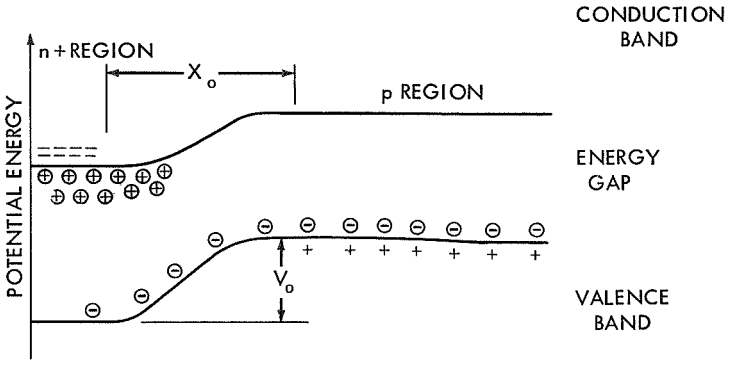

(a) NO APPLIED BIAS

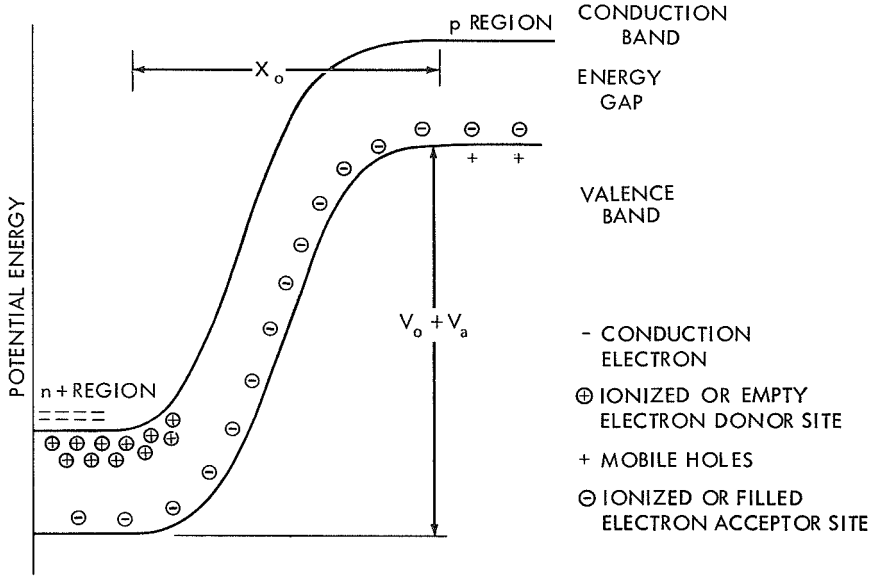

(b) REVERSE BIAS ACROSS JUNCTION

Figure 15–Diffused n^+-p junction band structure, illustrating the formation of the depletion region.

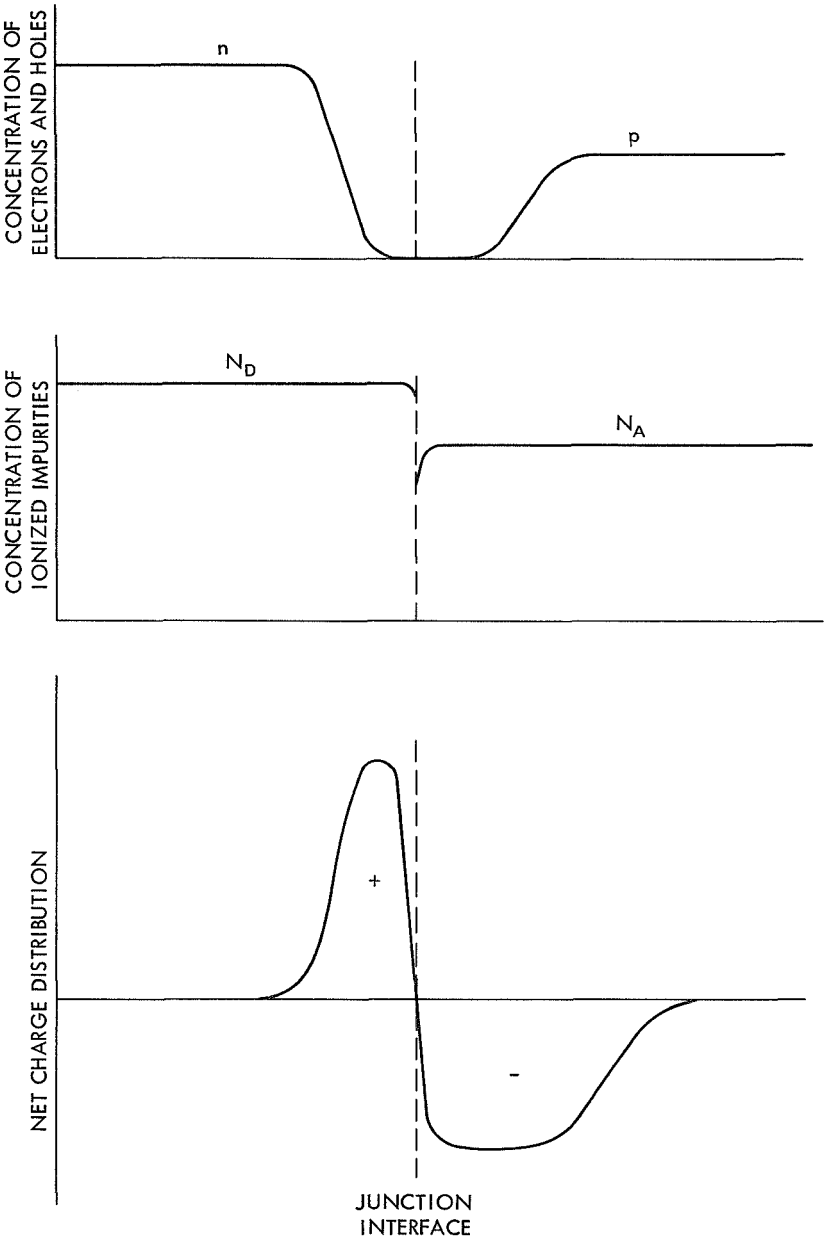

Figure 16–Charge distribution in a p-n junction with no applied voltage.

electric field produced by the applied voltage V_a pulls out additional free carriers from the depletion region until a new equilibrium is established. The resulting charge distribution for a p-n junction under reverse bias is shown in Figure 17.

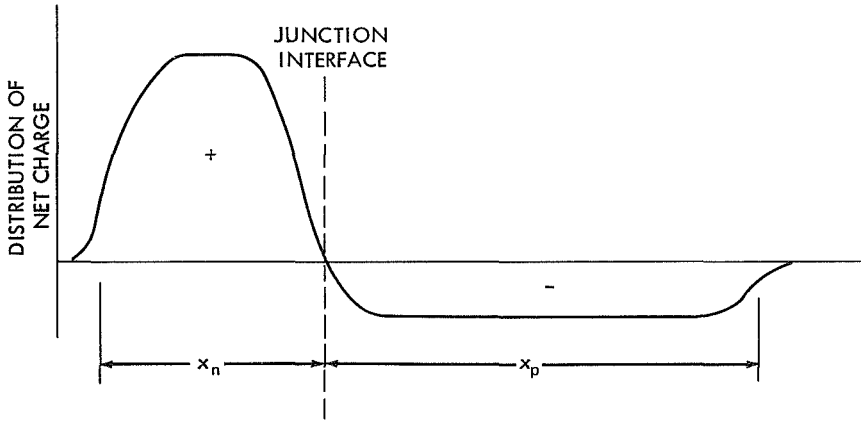

Figure 17–Charge distribution in a p-n junction with reverse bias.

The extent of the depletion region can be estimated from the solution of the one-dimensional Poisson's equation. Consider the n side of the junction:

$$\frac{\partial^2 V}{\partial x^2} = \frac{4\pi e}{\epsilon}\left(N_D - n + p\right) , \tag{19}$$

where ϵ is the dielectric constant and e the electron charge. In the depletion region the concentration of holes, p, and electrons, n, is small compared with the density of ionized donors, N_D. Assuming N_D to be constant in the depletion region, we integrate Equation 19 twice to obtain the voltage

$$V(x) = \frac{2\pi e}{\epsilon} N_D \left(x^2 - 2x\, x_n\right) + V_D . \tag{20}$$

At $x = x_n$, the limit of the depletion region on the n side, $V(x_n) - V_0 = V_n$, the potential difference across the n side of the junction. Solving Equation 20 for x_n, we find

$$x_n^2 = \frac{V_n \epsilon}{2\pi e N_D} . \tag{21}$$

A similar analysis for the p side of the junction gives

$$x_p^2 = \frac{V_p \epsilon}{2\pi e N_A} . \tag{22}$$

Since charge neutrality requires that $x_n N_D = x_p N_A$, and for a detector junction either $N_D \gg N_A$ or $N_A \gg N_D$, the depletion depth x_0 is given to a good approximation by

$$x_0^2 = \frac{V \epsilon}{2\pi N_D e} ,$$

or

$$x_0^2 = \frac{V \epsilon}{2\pi N_A e} , \tag{23}$$

where $V = V_n + V_p$ is the applied voltage.

Furthermore, since $\rho_n = (N_D e \mu_n)^{-1}$ for n type material, or $\rho_p = (N_A e \mu_p)^{-1}$ for p material, Equation 23 may be written:

$$x_0 = \sqrt{\epsilon \mu_n \rho V / 2\pi} \qquad \text{(n type)} ,$$

$$x_0 = \sqrt{\epsilon \mu_p \rho V / 2\pi} \qquad \text{(p type)} . \tag{24}$$

Using a value of 12 for ϵ in silicon and $\mu_n = 1500$, $\mu_p = 500$ cm^2/volt-sec, we find

$$x_0 = 5.3 \times 10^{-5} (\rho V)^{1/2} \text{ cm} \qquad \text{n type} ,$$

$$x_0 = 3.2 \times 10^{-5} (\rho V)^{1/2} \text{ cm} \qquad \text{p type} . \tag{25}$$

The capacitance per unit area, C/A, for a depletion region of depth x_0, is given by

$$\frac{C}{A} \propto \frac{1}{x_0} . \tag{26}$$

Diffused-Junction and Surface-Barrier Detectors

The p-n junction in the diffused-junction detector is formed by diffusing a donor impurity, such as phosphorus, to a shallow depth into one face of a high-purity p-type silicon slice. This face becomes heavily doped n^+-type material with a high donor concentration N_D. Similarly, a p^+-n junction can be constructed.

To make a surface-barrier detector junction, high-resistivity n-type material is used. One face of the crystal is chemically etched and then exposed to air (oxygen). Surface states are formed by spontaneous oxidation; these states induce a high density of holes to form a very thin p^+ layer. Electrical contacts are made by the evaporation of gold onto both surfaces. Figure 18 is a schematic representation of the two types of junction detectors.

Lithium-Drifted Detectors

In junction detectors there is an upper limit to the depletion depth. This is because, as the applied voltage is increased to obtain larger depletion, a limiting voltage is reached at which the diode breaks down. For typical detectors this voltage is around 100-500 volts, although with much care reverse bias of up to 5,000 volts has been achieved. Using the highest resistivity material, the maximum depletion depth obtained is at most a few millimeters.

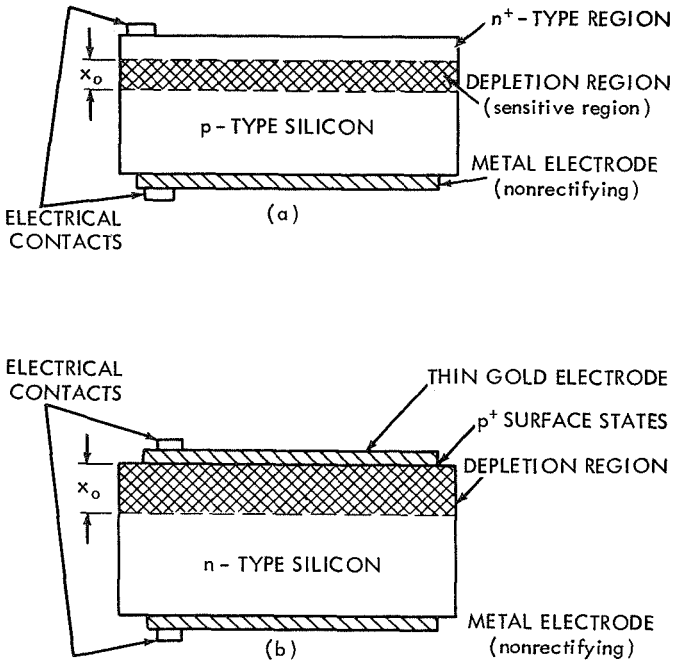

Figure 18–Schematic representations of (a) diffused n^+-p junction detector and (b) surface-barrier detector. Energetic charged particles generally enter close to the depletion region.

A different method is used to obtain larger depletion depths at moderate voltages. The process, called lithium compensation, consists of introducing lithium ions into p-type silicon. Lithium is a donor interstitial impurity; at temperatures between 100° and 400°C the drift motion of Li ions under an applied electric field dominates the random temperature-dependent diffusion. Lithium is applied by evaporation to one face of a heated (300-500°C) slice of silicon and is allowed to diffuse into the crystal to a depth of ~0.1 mm, forming a highly doped n^+ region as indicated in Figure 19a. The junction is then reverse-biased while the crystal is held at a constant elevated temperature. Lithium ions will drift and redistribute themselves so that the Li^+ concentration is exactly equal to the acceptor concentration of the p material, as shown in Figure 19b. The donor (Li) and acceptor (usually boron) impurities completely compensate each other, and an effective intrinsic region is produced between the p and n^+ material. Intrinsic or

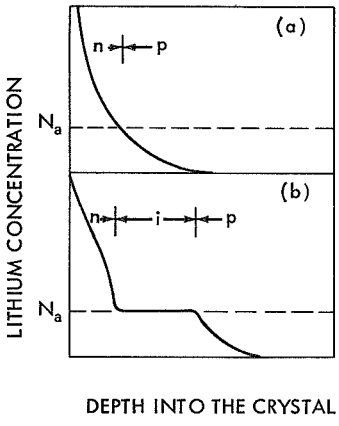

Figure 19–Lithium ion-drift process, (a) after diffusion, (b) after drifting.

depletion depths of up to 1 cm have been achieved in this fashion. The drifting is stopped to leave a small layer of p material. The resulting device is called an n-intrinsic-p (NIP) detector. Clearly, the advantages of the NIP detector are its large depletion depth and small capacitance, both independent of the applied bias voltage. Therefore, these detectors can be operated at moderate voltages (20-50 V) and are more stable against breakdown. The major disadvantage is the presence of windows or insensitive regions on both sides of the device.

The p window may be removed by the following procedure. Lithium drifting is continued until all the p material is compensated for (or the remaining p layer removed by lapping). That face is chemically etched to form a thin surface-barrier p^+ layer. In this way we obtain windowless lithium-drifted detectors.

TECHNIQUES AND INSTRUMENTATION FOR MEASUREMENTS OF NON-RELATIVISTIC PARTICLES IN SPACE

The basic experimental information required in the study of cosmic rays is the energy spectrum of each chemical element and isotope. Additional valuable data consist of the dependence on time, space, and direction of arrival of these particles. Many techniques have been used to obtain this information. Unfortunately we have space to describe only a few of these.

Nuclear Emulsions and Dielectric Track Detectors

Nuclear emulsions and plastic track detectors (also called solid-state track detectors or dielectric track detectors) provide a very powerful tool for determining the identity and energy of a particle stopped in the detecting medium.

A nuclear emulsion (in contrast to an optical emulsion) consists of a high concentration of small silver-halide crystals in a thick gelatin

film. An energetic particle passing through the emulsion activates the silver-halide grains along its path by ionization and excitation of atoms in the grain such that the whole grain can be converted to silver by development of the emulsion. The plastic track detector is simply any electrically non-conductive solid. When a massive charged particle passes through such a solid, it produces along its path a narrow trail of radiation-damaged material. The mechanism for producing radiation-damaged material depends on the type of detection material used. In crystalline solids the atoms are ionized along the path of the energetic particle and repel one another, leaving their original position in the lattice. This creates a cylindrical region of disorder and distortion, easily attacked by an etching reagent. In an organic polymer the energetic charged particle ionizes and excites molecules, breaking the chains. The chain ends form new species that are highly reactive chemically. In either case, the damaged material is etched preferentially, and tracks become visible with the aid of an optical microscope.

Both techniques have several important advantages over other methods of particle detection. The detector is simple and rugged. The sensitive volume can be made large (by the stacking of emulsions or dielectric sheets), and a great amount of information may be stored. Since the particle track can actually be seen, a precise determination of the direction of arrival of the particle is possible. Emulsions and dielectric material can be chosen that are sensitive only to particles whose charge exceeds certain limits, thereby eliminating much of the undesirable background.

Unfortunately these detectors possess no intrinsic time resolution; they must be recovered to yield their data, and the analysis of the data is time-consuming. Furthermore, calibration of the detector material is generally required.

Techniques have been developed for making quantitative measurements of tracks in these detectors, from which the mass, charge, and energy of the incident particle can be derived.

Methods of Particle Identification in Emulsions

For cosmic-ray experiments, emulsions with large sensitive volumes are required because of the extremely low intensities which must be measured and because particles must be stopped in the emulsion to give the most precise identification. Large volumes are obtained from

sheets of emulsion about one millimeter thick, stacked to the desired depth. Various measurements may be made on the particle tracks; all these, however, can be eventually related to the energy lost by ionization per unit path length, dE/dx, and to the total residual energy, E, of the particle.

The grain density, dN/dx, the number of gaps between "blobs" of grains per unit track length, or the density of blobs are all related to dE/dx or Z^2/β^2 of a particle. The thickness of a track, the thinning out of a heavy track at the end of the range, and the density of delta rays, (electrons from ionized atoms), n_δ, along a track can be used to determine the charge, Z, of the incident particle. Small-angle scattering and the residual range along the track provide information about particle energy.

The relationship between grain density and rate of energy loss is shown in Figure 20. The grain-density curve has a lower and upper threshold corresponding respectively to the cases when no grains are developed and when all grains are developed. The thresholds determine the sensitivity of an emulsion. For example, in Figure 20 curve A corresponds to the more sensitive emulsion—one which will detect minimum ionizing particles.

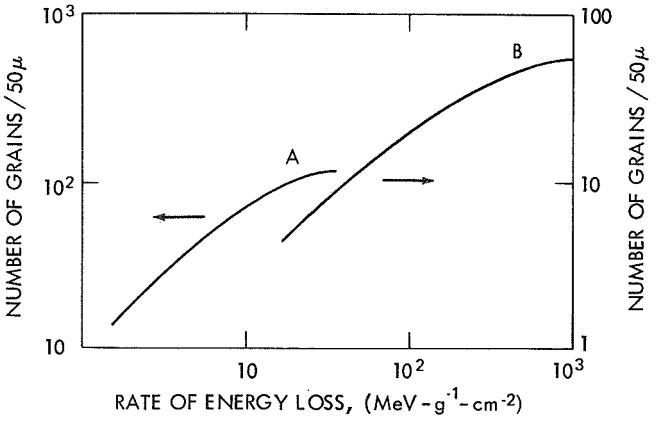

Figure 20–Grain density vs rate of energy loss in emulsions of different sensitivity.

Figure 21 shows delta-ray density as a function of particle range for different values of incident-particle charge. A simultaneous measurement of particle residual range and delta-ray density will determine the charge of the incoming particle.

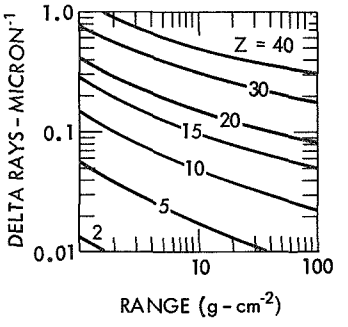

Figure 21–Computed curves for the density of delta rays as a function of residual range and charge of the incident particle.

The amount of small-angle scattering is related to the kinetic energy, T, of a non-relativistic particle. Rossi (Reference 1, p. 140) shows that $|\theta T|_{av} = C\sqrt{d}$, where C is a constant of the particular emulsion and d is the length of the segment used in determining the average scattering angle θ_{av}.

A simultaneous determination of dE/dx and E by any of the methods described above is, in principle, sufficient to determine the mass, charge, and energy of the particle. Because of random or statistical effects that influence the formation of the track, the errors in the determination of dE/dx and E are significant. In fact, only by employing a combination of the methods described has it been possible to determine, on a statistical basis, the isotopic composition of He.

Methods of Particle Identification in Dielectric Track Detectors

Solid-state track detector techniques are relatively new and therefore have not been as well developed as emulsion detectors. Nevertheless, their use for cosmic-ray studies has already provided important information about the composition of elements heavier than iron. By selecting certain solids we can prevent the registration of tracks for all particles with ionization losses, dE/dx, below a critical value characteristic of the material. Since dE/dx increases as the square of the particle charge, this property gives the track detector a certain charge threshold which is extremely useful when the composition of rare heavy elements is studied among the more abundant lighter elements and background events.

Figure 22 illustrates the principle of particle identifications used for dielectric detectors. Consider the situation where ions of Be^{10} and

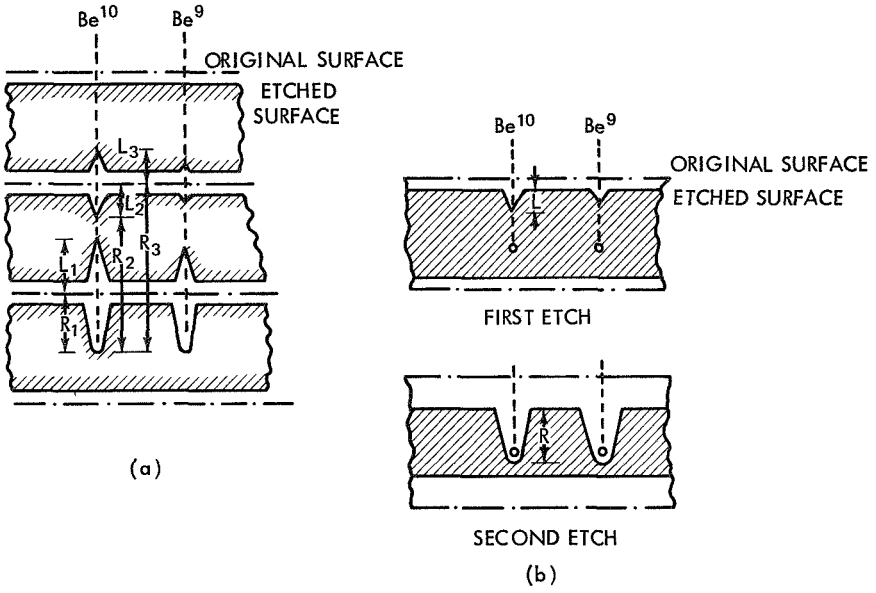

Figure 22–Principle of particle identification in dielectric detectors. (a) particles have penetrated several sheets, and long development time can be used to give measurements of track lengths L_i and residual and residual ranges R_i. (b) particles have stopped in the first sheet, which must be etched for a short time to give track length L, followed by a longer etch to give range R.

Be^9 penetrate several sheets of plastic material to the same depth; that is, they have the same range. Experimentally it has been found that the rate of etching along a particle track in a plastic depends only on the ionization rate dE/dx, which is a function of Z^2/β^2. Thus the rate of etching of the cone-shaped tracks L_i is faster for Be^{10} than for Be^9, and the corresponding tracks are larger for Be^{10} than for Be^9—as shown in Figure 22a. The cone-shaped tracks L_i and the residual ranges R_i can be measured directly. The true lengths are calculated using corrections to the observed lengths for the portion of the surface that was lost in the etching process. For each measured track length L_i, there corresponds a measured residual range, R_i, defined as the distance from the segment L_i to the end of the track. A plot of the track lengths L_i against the residual ranges R_i is shown in Figure 23 for tracks resulting from B^{10}, B^{11}, and N^{14} ions stopped in cellulose nitrate sheets of $\sim 250\,\mu$ thickness. Isotopes of boron are resolved by this method, and the energy is obtained from the total range of the particle. Once

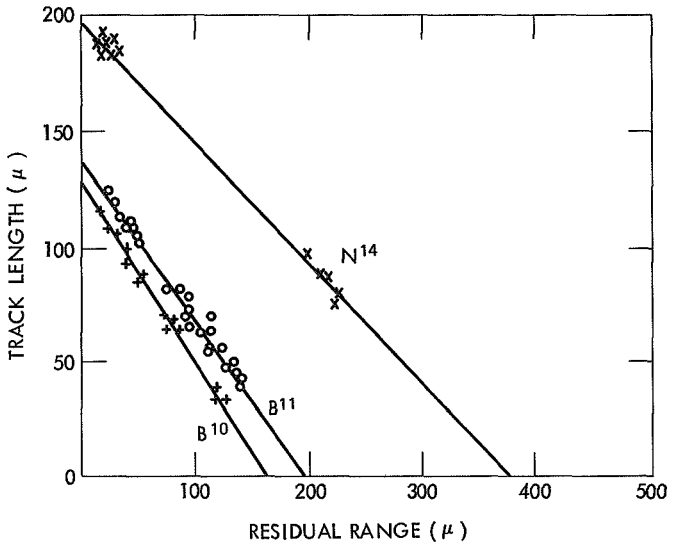

Figure 23–Measurements of track lengths and residual range of B^{10}, B^{11}, and N^{14} ions. The two-dimensional plot of track lengths vs residual range demonstrates isotope resolution of the dielectric track detector.

problems of non-uniformity of large-area material are overcome, it seems feasible to obtain the isotopic composition of cosmic rays Li, Be, and B of ~3-100 MeV-nucleon^{-1} by exposing cellulose-nitrate stacks of 3-cm thickness on balloons, rockets, or recoverable satellites.

Counter Telescopes

A counter telescope is basically an assembly of two or more of the charged-particle detectors here described. Analyzing simultaneously the outputs of these detectors by means of the associated electronics, we can learn the identity of the particle, its energy, and the rate at which particles pass through the telescope detectors.

Counter telescopes have several important advantages over nuclear emulsions and plastic track detectors. They can record each event as a function of time with a typical resolution of about 10^{-6} sec. The instrument need not be recovered; data can be telemetered and recorded at ground stations. It is possible to design instruments that exclude

from analysis all but certain preselected types of events and the mode of operation of the instrument may be changed during operation. Furthermore, the output data from such instruments is well suited for computer analysis. In general, counter-telescope instruments offer a flexibility in the mode of operation and recording of data which is not possible with nuclear emulsions or dielectric track detectors.

The major disadvantage of counter-telescope instruments is their complexity and, consequently, higher probability of failure during prolonged operation. Furthermore, it is more difficult to obtain large enough detector areas required to make statistically significant measurements of the very low cosmic-ray fluxes.

We shall discuss only three basic types of detector systems: (a) dE/dx vs range, (b) dE/dx vs energy, and (c) electrostatic deflection vs energy. With these instruments the energy range from ~100-KeV to ~200-MeV-nucleon^{-1} can be covered and the charge (in some instances even the mass composition) of the cosmic rays determined.

Geometrical Factor

The counting rate of a particular telescope depends on the effective dimensions and efficiencies of the various detectors in the assembly, on their relative positions, and, of course, on the intensity of the radiation. For an ideal telescope—whose efficiency for detecting particles of a given type in a given energy interval is 100 percent, and zero for all other particles and energies—we can express the observed counting rate C as a product of the absolute isotropic intensity I of the incoming particles and the geometrical factor G, which depends only on the geometry of the detector arrangement and has dimensions of area times solid-angle, for example, cm^2-steradian.

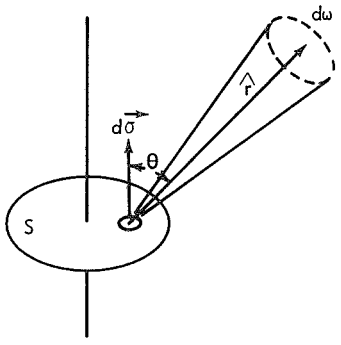

Figure 24—Relationship between $d\vec{\sigma}$, $\hat{r}$, θ, and $d\omega$ for a single plane detector.

Consider the arrangement consisting of a single plane detector (see Figure 24). The observed counting rate is given by

$$C = I \int_{\Omega} \int_{S} (\hat{r} \cdot d\vec{\sigma})\, d\omega \qquad (28)$$

where $\hat{r} \cdot d\vec{\sigma}$ is the effective element of area looking into polar angle θ, $d\omega = d(\cos\theta)\, d\phi$ is the element of solid angle, Ω is the domain of $d\omega$ (full hemisphere in this case), and S is the domain of $d\vec{\sigma}$ (surface area of the detector). Evaluating Equation 28 for the case of a plane detector for which $\hat{r} \cdot d\vec{\sigma} = d\sigma \cos\theta$, we find:

$$C = I\int_{\Omega}\int_{S} \cos\theta\, d\sigma\, d\omega = I\, 2\pi A \int_{0}^{\pi/2} \cos\theta\, d(\cos\theta) = I\pi A \,. \qquad (29)$$

So the geometrical factor of a single detector of area A (with particles incident from one hemisphere) is given by

$$G = \pi A \,. \qquad (30)$$

From this result it follows that the geometrical factor of any single detector that can be approximated by a plane detector (with particles incident from only one hemisphere) is π times the total area.

The coincidence-counting rate of a two-detector telescope (see Figure 25) is again given by

$$C = I\int_{\Omega}\int_{S_2} \left(\hat{r} \cdot d\vec{\sigma}_2\right) d\omega \,. \qquad (31)$$

Here, $d\omega = \left(\hat{r} \cdot d\vec{\sigma}_1\right)/r^2$, and the domain Ω is limited by the top detector. The geometrical factor is now given by

$$G = \int_{S_1}\int_{S_2} \frac{\left(\hat{r} \cdot d\hat{\sigma}_1\right)\left(\hat{r} \cdot d\vec{\sigma}_2\right)}{r^2}$$

$$= \int_{S_1} dA_1 \int_{S_2} dA_2\, \frac{\cos^2\phi}{r^2} \,, \qquad (32)$$

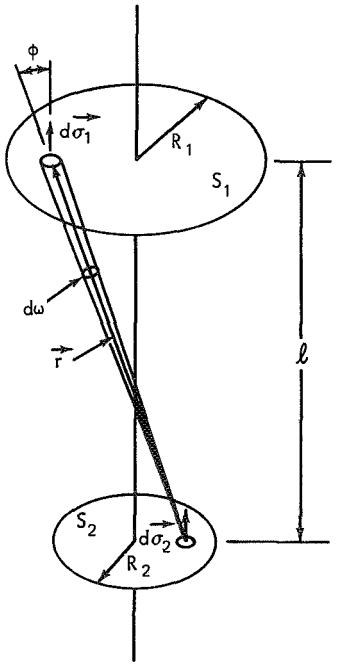

Figure 25–Relationship between $\vec{r}$, $d\vec{\sigma}_1$, $d\vec{\sigma}_2$, $d\omega$, and ϕ for a two-detector ideal telescope.

where ϕ is the angle between $d\vec{\sigma}_1$ and $\vec{r}$. It can be shown, after integrating Equation 32, that

$$G = \frac{\pi^2}{2}\left[R_1^2 + R_2^2 + \ell^2 - \sqrt{\left(R_1^2 + R_2^2 + \ell^2\right)^2 - 4R_1^2 R_2^2}\right] , \qquad (33)$$

where R_1 and R_2 are the radii of the two detectors and ℓ is their separation.

For a telescope composed of n detectors ($n > 2$), the geometrical factor is again given by

$$G = \int_{\Omega}\int_{S_n} \left(\hat{r} \cdot d\vec{\sigma}_n\right) d\omega , \qquad (34)$$

and the domain of Ω is limited by the requirement that the incident particle trajectories must intersect <u>all</u> n detectors.

dE/dx-vs-Range Telescope

One of the simplest types of counter telescope consists of two plane detectors with an absorber between them. By measuring the amount of energy lost in the first detector and recording whether or not the second detector has been "triggered,"* we can determine the energy and charge of incident particles in a certain energy range. Consider the simple detector assembly shown in Figure 26.

The front detector (dE/dx) is a plane detector of thickness Δx. Its output is pulse-height-analyzed (PHA); that is, the amplitude of the output pulse is measured. The back (range) detector is also flat and its output is connected to a threshold discriminator. Depending on the energy of the incident particle, the following three cases can arise: (1) the particle completely stops in the dE/dx detector and its total energy is measured; (2) the particle penetrates the first detector but stops in the absorber, and (3) the particle penetrates the first detector

*A detector is triggered if the amount of energy deposited in the sensitive volume of the detector exceeds a predetermined threshold.

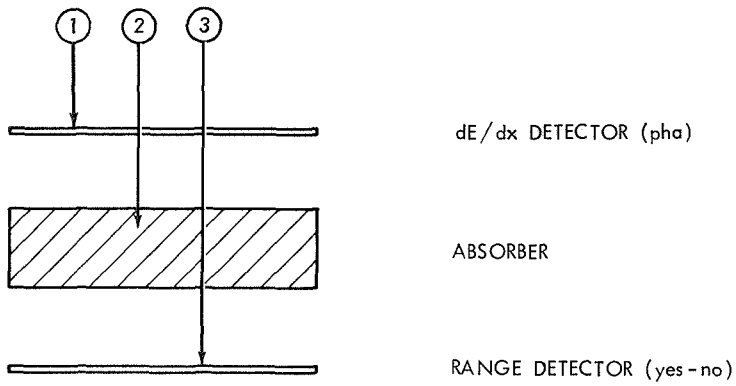

Figure 26–Simple dE/dx-vs-range detector assembly.

and the absorber and triggers the back detector. In the last two cases the energy loss $(dE/dx)\Delta x$ is measured in the front detector. The expected amplitude of the output pulse of the front detector as a function of energy per nucleon of the incident particles is shown in Figure 27.

The shape of the curves in Figure 27 may be verified from Equations 12, 14, and 17.

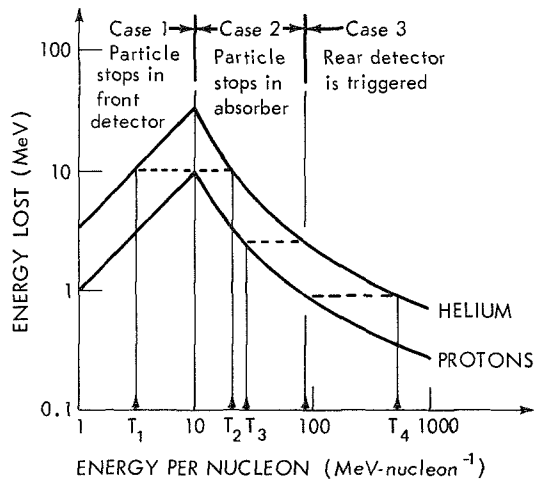

Figure 27–Amplitude of output pulse of dE/dx detector as a function of incident particle energy.

If the output of the dE/dx detector is pulse-height analyzed, a unique separation of protons from α-particles can be achieved only in the energy range T_1 to T_2, as is shown in Figure 27. However, a definite energy assignment is impossible in this energy range because for each value of the dE/dx pulse height there are two values of the incident energy. Charge identification is possible in the energy range T_3 to T_4 where one must use the information of whether or not the back detector has been triggered.

In Figure 28 we illustrate a hypothetical pulse-height distribution of the signals from the dE/dx detector with the back detector not triggered. We assume, for this illustration, that the energy spectra of the

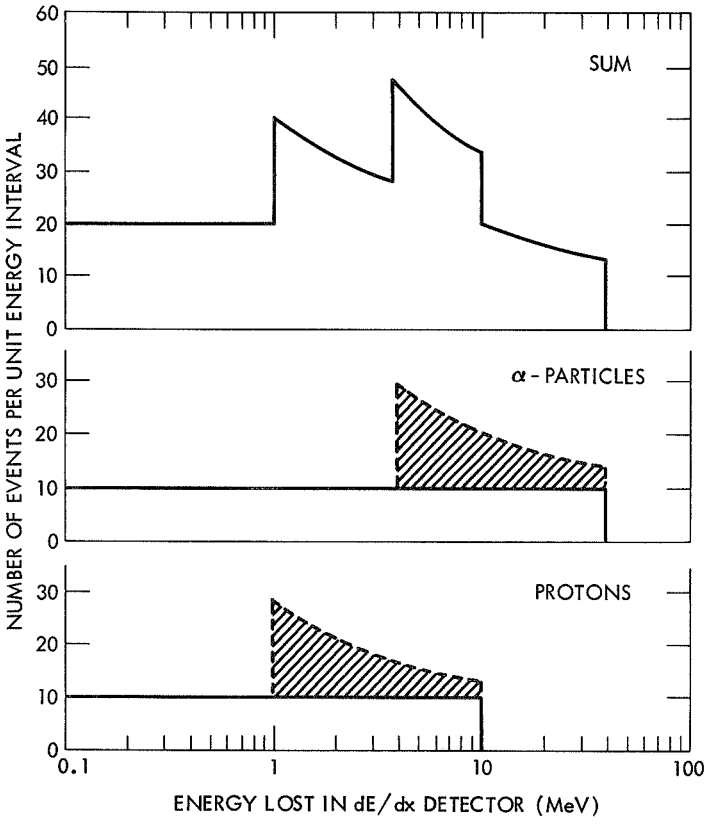

Figure 28–Pulse-height distribution from dE/dx detector with back detector not triggered.

incident proton and α-particles are independent of energy and that their abundances are equal. Energy losses above 10 MeV/nucleon can result only from α-particles with energies between T_1 and T_2 as indicated in Figure 27. For other energies the charge separation is not straightforward, but is possible under favorable circumstances.

The dE/dx-vs-range instrument is considerably improved by the addition of other detectors and absorbers. A simplified cross section and top view of a four-detector dE/dx-vs-range telescope with an anti-coincidence shield is shown in Figure 29.

Detectors D_1, D_2, D_3, and D_4 are typically circular surface-barrier or lithium-drifted detectors with sensitive areas of ~5- to 10-cm^2 and 500- to 1500-μ depletion depths. (It is easy to imagine the problems

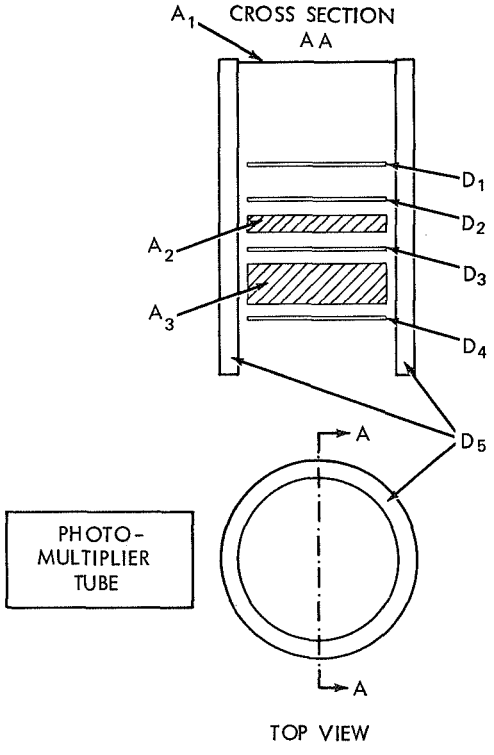

Figure 29–Four-detector dE/dx-vs-range telescope.

that would arise from the use of scintillation crystals and four multiplier tubes instead of the compact semiconductor detectors.) Detector D_5 is a cylindrical plastic scintillator-photo-multiplier-tube assembly. The three absorbers consist of a thin aluminized mylar window A_1 to protect the light-sensitive solid-state detectors and two tungsten absorbers—typically 5 g/cm^2 (A_2) and 15 g/cm^2 (A_3).

The anti-coincidence detector defines the geometrical factor of the telescope and serves to reduce the frequency of background events (as discussed further on in connection with Figures 34 and 35). Typically the outputs of detectors D_1 and D_3 are pulse-height-analyzed; the other detectors are connected to discriminators. Only when a combination of the D_1, D_2, D_3, D_4 detectors is triggered in anticoincidence with D_5 is an event analyzed.

The expected response of this instrument to protons, electrons, and α-particles is shown in Figures 30, 31, and 32. The lowest energy that can be measured, in this illustration ~3 MeV/nucleon, is determined by the thickness of the mylar absorber A_1. Figure 30 shows the energy lost in D_1 as a function of the kinetic energy per nucleon of the incident particles. In the energy range ~3 to 12.5 MeV-nucleon^{-1}, D_1 alone is triggered ($D_1 \bar{D}_2 \bar{D}_3 \bar{D}_4 \bar{D}_5$ mode*), and the total residual energy of the particles is measured. Energy losses in D_1 corresponding to energy region f are primarily due to protons; those in regions g and h are due to α-particles. Above 12.5 MeV/nucleon, D_2 is triggered. In the mode of operation $D_1 D_2 \bar{D}_3 \bar{D}_4 \bar{D}_5$, energy losses in regions b and c are due strictly to protons and those in d and e only to α-particles. Energy losses corresponding to region a are due to 0.9- to 9-MeV electrons. Figure 31 shows the predicted energy losses in detector D_1 as a function of energy losses in detector D_3 for the case when D_1, D_2, and D_3 are triggered but not D_4 and D_5 ($D_1 D_2 D_3 \bar{D}_4 \bar{D}_5$ mode). In this display, electrons, protons, α particles, and heavier elements (not shown) have unique tracks. That is, an event with simultaneous energy losses in D_1 and D_3 falling in region a would be identified as a 50-75 MeV-nucleon^{-1} α-particle. The position of the event on the track gives the energy of the particle. For example, a 75-MeV proton would have D_1, D_3 energy losses located on the proton track between regions c and d. Figure 32 shows the proton and alpha tracks for the $D_1 D_2 D_3 D_4 \bar{D}_5$ mode of operation. Region c corresponds to 265- to 380-MeV-nucleon^{-1} particles, region d to >380-MeV-nucleon^{-1} particles. Again, position along the track determines the energy of a particle.

*A bar over a symbol means anticoincidence. Thus, $D_1 \bar{D}_2$ means that D_1 is triggered but D_2 is not.

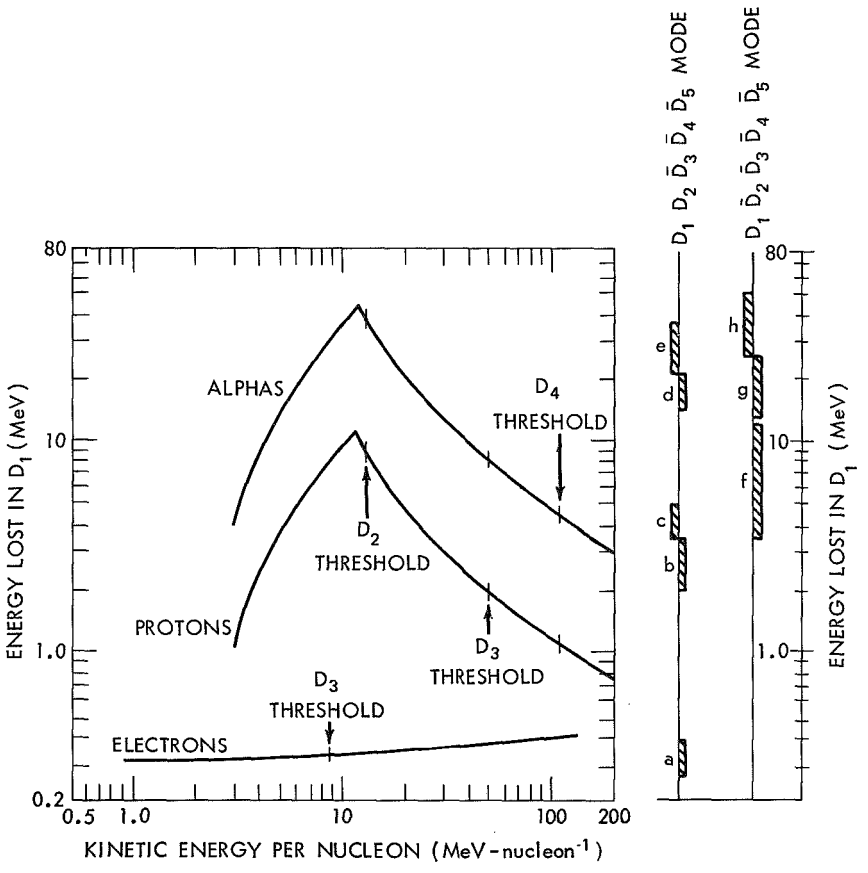

Figure 30–Energy losses for protons and α particles as a function of incident energy in the front D_1 detector of the four-detector dE/dx-vs-range telescope.

The upper energy limit (380-MeV-nucleon^{-1} in this case) is determined by the total absorber thickness in the telescope. Additional detectors and absorbers could be added to increase the energy range covered.

The advantage of a dE/dx-vs-range instrument is that it can be made compact and lightweight, especially if solid-state detectors are used. For example, a four-element telescope and all the associated

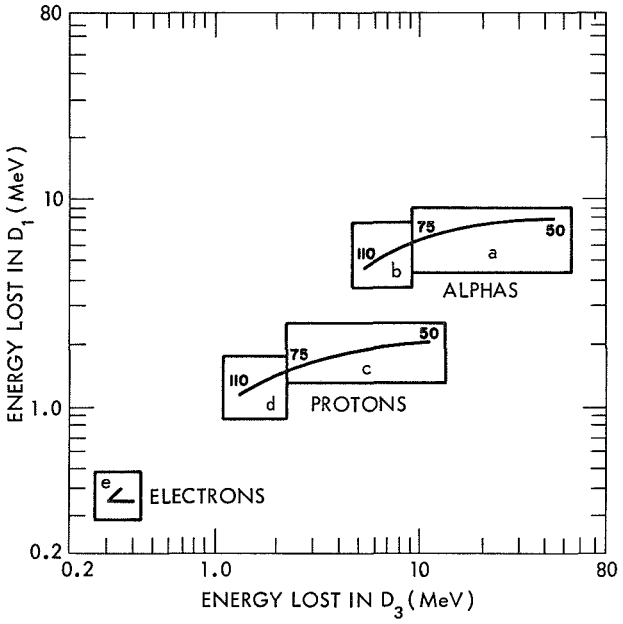

Figure 31–Energy losses in the D_1 detector as a function of energy losses in the D_3 detector of the four-detector dE/dx-vs-range telescope. Detectors D_4 and D_5 are not triggered.

electronics can be constructed to weigh less than 5 lbs; this is desirable and may even be necessary in an instrument for flight on space probes and small satellites.

The dE/dx-vs-Energy Telescope

The dE/dx - E telescope has been providing the most detailed measurements of the isotopic and chemical composition, and energy spectra of cosmic rays in the ~10- to ~300-MeV/nucleon energy range. Such instruments can be designed to be compact, lightweight and rugged—all prerequisites for space flight. To identify particles and determine their energy spectra it is sufficient to telemeter only two pulse heights and one rate.

The principle of operation of the dE/dx-vs-energy telescope is simple. A simultaneous measurement of the energy loss in a thin

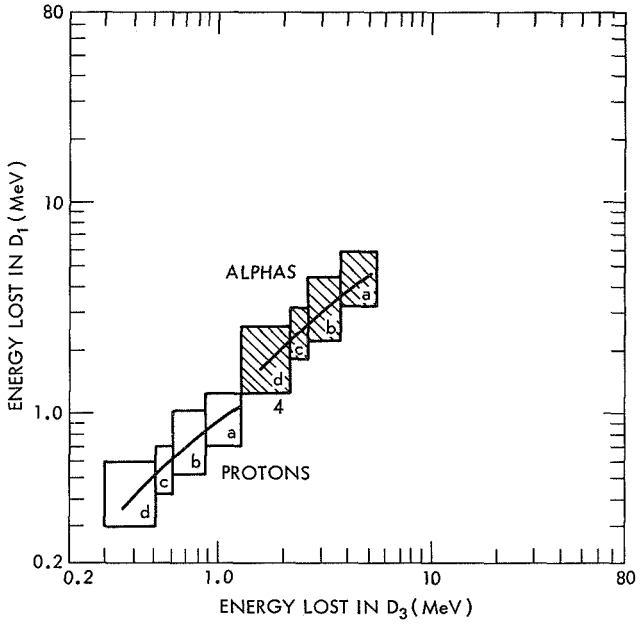

Figure 32–Energy losses in the D_1 detector as a function of energy losses in the D_3 detector of the four-detector dE/dx-vs-range telescope. Detector D_4 is triggered but D_5 is not.

dE/dx detector and the total residual energy E in a thick E detector is sufficient to obtain the mass, charge, and energy of the particle. This follows from the fact that to a good approximation the energy loss is given by

$$\frac{dE}{dx} = \frac{1}{\frac{dR}{dE}} = \left\{\frac{d}{dE}\left[\frac{M}{Z^2}\left(\frac{E}{M}\right)^{\alpha}\right]\right\}^{-1} = \frac{Z^2\, M^{\alpha-1}}{E^{\alpha-1}}\,, \qquad (35)$$

where R, the particle range, is taken to be a power law in kinetic energy per nucleon, E/M, with exponent α. The particle charge is Z. A knowledge of dE/dx and E for a particle stopped in the thick E detector will give the kinetic energy E and the product $Z^2\, M^{\alpha-1}$ for the particle.

The lower energy limit for the instrument depends on the dE/dx-detector thickness, while the upper energy limit depends on the E-detector thickness. To make the energy interval as large as possible, a very thin dE/dx detector ($\sim 300\mu$ silicon solid state) and a very thick E detector ($\sim$10-15 g-cm^{-2} CsI crystal) are used.

We shall now describe a typical dE/dx-vs-E detector system suitable for satellite use. Such instruments have been flown by the University of Chicago and Goddard groups, and detailed descriptions of those experiments may be found in References 6 and 7.

Figure 33 shows a cross-section view, drawn to scale, of the University of Chicago detector system. Detectors D_1 and D_2 are two gold-silicon-surface barrier detectors of 3.5 cm^2 sensitive area and silicon thickness of 300 microns. The depletion depths are 200 microns. An aluminized mylar foil is used to prevent sunlight from striking the photosensitive detector. This window sets a lower energy limit for detection of protons of 0.9 MeV. To produce a D_1 D_2 coincidence requires vertically incident protons or helium nuclei with energy in excess of 6.5 MeV-nucleon^{-1}.

Detector D_3 is a CsI (Tℓ) crystal with a thickness of 11.46 gm/cm^2. The light output from this scintillator is detected by two solid-state photodiodes (P_1 and P_2), each having a photosensitive area of 2.5 cm^2. They are mounted on opposite sides of the CsI crystal. Detection of the D_3 light output by photodiodes eliminates the problem of coupling to photomultiplier tubes, which has been done by Bryant, Ludwig, and McDonald (Reference 7).

Detector D_4 is a plastic scintillator cup which completely surrounds the CsI crystal. This plastic sintillator is coupled to the photomultiplier tube by means of a light-scattering chamber painted with a reflective white paint. The purpose of the D_4 detector is, first, to identify any charged particles that penetrate the D_1 D_2 D_3 detectors; second, to eliminate particles entering from the rear or sides, and finally, eliminate events caused by nuclear interactions within the dense CsI crystal.

For "event" analysis, a charged particle must pass through D_1 and D_2 in coincidence, in which case a measurement of the energy loss dE/dx is obtained in D_1. Note that in this mode the instrument operates as a simple dE/dx-vs-range detector. If the particle penetrates to D_3, an analysis of the pulse height in D_3 is also obtained, thus providing

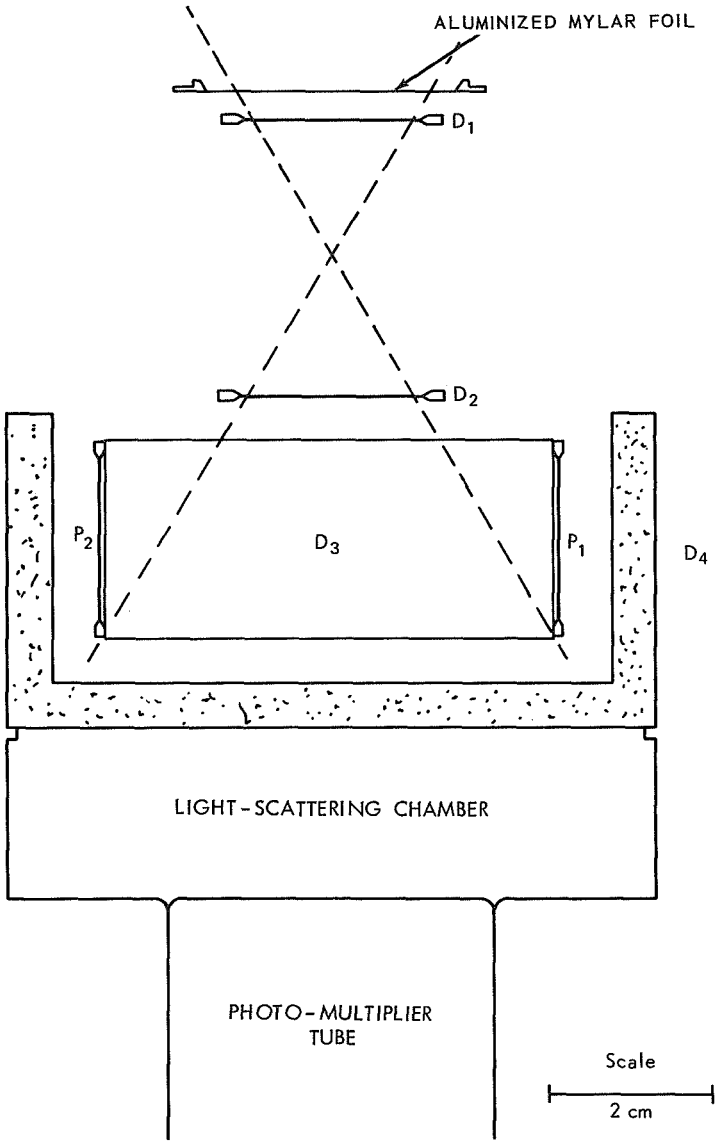

Figure 33–Cross-section view of the dE/dx-vs-energy detector assembly.

the necessary dE/dx and total energy E information. If the particle penetrates far enough to trigger D_4, the event is not analyzed.

The analysis of the data from the dE/dx-vs-E instrument proceeds by raw-data display of the pulse heights in matrix form, as shown in Figure 34. For each event the energy loss, dE/dx, is plotted against the residual energy E. As the incident energy is varied, each isotope of each element traces out a characteristic curve or track. Figure 34 shows only tracks of He, Be, and the B isotopes, while Be^9 and Be^{10} are shown as an unresolved single track. The energy of the incident particle is determined from the position along the track. Because of the finite resolution of the detectors, the individual tracks are smeared out. This makes isotope separation difficult. Furthermore, because of the presence of some residual background, not eliminated by the plastic scintillator anticoincidence counter (D_4 in Figure 33), there is a more or less smooth distribution of events ranging across the dE/dx-vs-E plane which is most intense at low values of dE/dx and E. The main source of

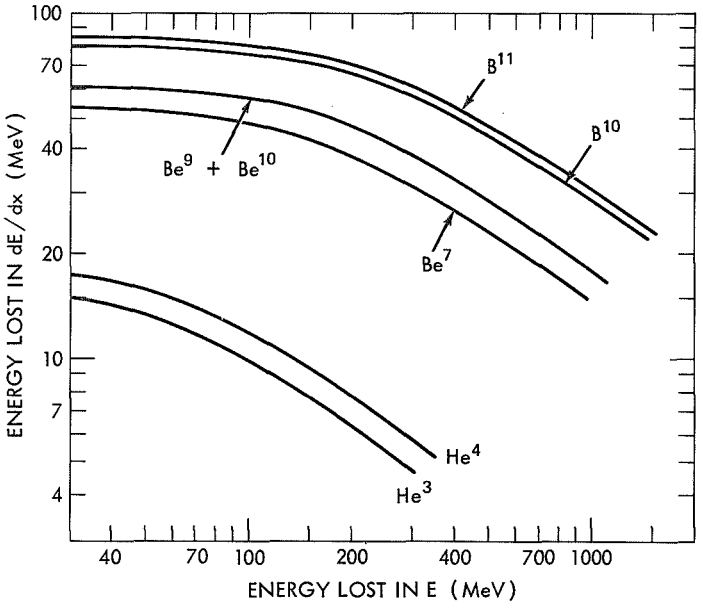

Figure 34–Calculated curves of energy loss vs residual energy for various chemical elements and isotopes for a dE/dx-vs-energy detector system.

this background probably comes from secondary particles produced either by protons interacting in the E crystal or by γ radiation which is locally produced in the spacecraft, penetrates the anticoincidence undetected, and interacts within the E crystal. A fairly detailed account of the causes of background is given by Simnett and McDonald (Reference 8).

Background corrections are generally made empirically. To compute the energy spectrum for a particular particle, the position of its track is first determined by using the raw data to compute the mean dE/dx, or, referring to Figure 33, the mean D_1 channel number position for each residual energy or D_3 channel number. A smooth curve is fitted to these points so as to represent the most likely "center of gravity" of the population for that chemical element as a function of energy. This procedure is illustrated in Figure 35 for the case of carbon and oxygen. By selecting given energy intervals, we obtain for each such interval

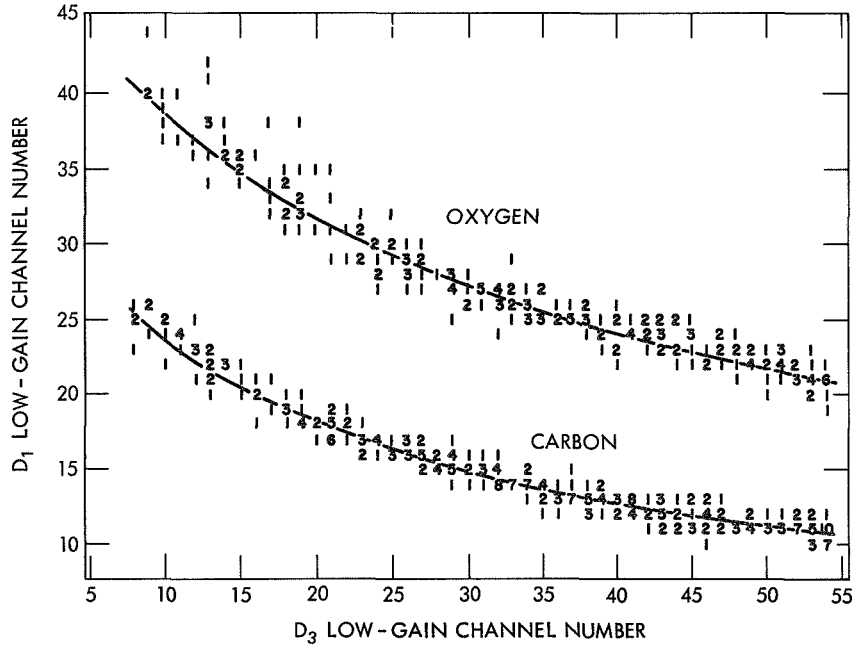

Figure 35–Positions of simultaneous pulse heights from oxygen and carbon stopped in the E detector of a dE/dx-vs-E telescope. Solid curves represent the mean positions deduced from the data.

mass histograms. Assigning the D_1 channel at the track position a zero channel number, we obtain the relative D_1 channel-number distribution. In Figure 36 such distributions are shown for the case of helium. In these mass histograms we note the presence of background as indicated by the dashed curves. Furthermore, the resolution of the two helium isotopes is apparent. (The He^3 contribution is indicated by the shaded area in each histogram.)

One point worth mentioning is that dE/dx-vs-E instruments are self-calibrating. The position of each track is determined by the physical characteristics of the instrument (absorber and detector thicknesses), and the electronic conversion gains from energy lost to pulse height. Over the long time periods of operation of these instruments, these conversion gains are subject to drifts. The tracks shift accordingly, and their new positions (especially of the end points of the tracks) can be used to calibrate the instrument.

Electrostatic Deflection vs. Total-Energy Detection System

It is difficult to extend the low-energy limit below several MeV/nucleon and yet retain two-parameter analysis using the dE/dx-vs-range or dE/dx-vs-energy techniques. This is because the particles must penetrate at least one detector and trigger the second. Thus the thickness of the first detector determines the low-energy limit of the instrument, and with present techniques it is difficult to reduce that thickness to less than several hundred microns. To extend the energy range to ~100 keV, the electrostatic-deflection-vs. total energy technique has been proposed by Gloeckler and Fan (Reference 9).

Measurements of the charge and total energy of a given particle are made by an electrostatic-deflection plate system and windowless solid-state detectors. For illustration, consider a simple system consisting of a collimator followed by two parallel plates maintained at a potential difference of V volts. Then a charged particle which passes through the collimator and thus enters between and parallel to the plates will be deflected from its original direction of motion by the electric field maintained between the parallel plates. The particle will leave the electric field region at a position which is a distance x away from the undeflected trajectory:

$$x = V\left(d^2/4s\right)(Z/E) , \qquad (36)$$

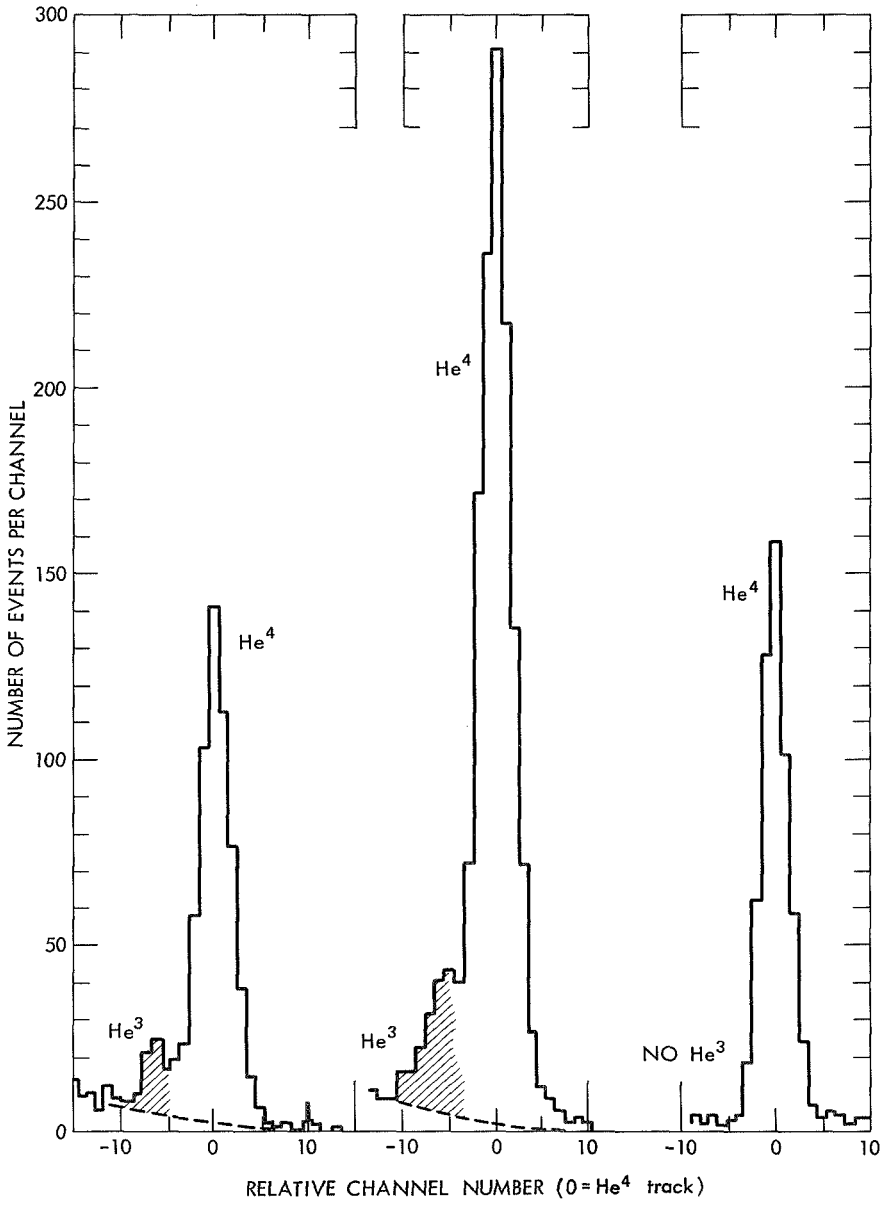

Figure 36–Mass histograms centered on the He^4 track.

where s is the distance in centimeters between the two deflection plates, d (cm) indicates the effective length of the electric-field region, V is the voltage in kilovolts, E is the kinetic energy in keV, and Z is the charge number of the particle. The sign of the charge is determined by whether the particle leaves the electric field region above or below its undeflected trajectory, and the magnitude of the charge can be found from a measurement of x and E by means of Equation 36. For example, if we take s = 1 cm, V = 20 kV, d = 15 cm, and x = 1/2-cm, we find that protons with energies up to 2.25 MeV can be measured by this method.

A simplified cross section of the electrostatic analyzer sensor showing the essential elements is shown in Figure 37. The electrostatic deflection system consists of a collimator assembly, four deflection plates, and the exit slits. The function of the collimator is to select those directions of the incoming particles that are nearly parallel to the deflection plates, and to prevent the direct illumination by sunlight of the photosensitive solid-state detectors. Of the four deflection plates, the two inner plates are maintained at +10 and -10 kV, respectively; the rest of the instrument is at ground potential. The inner plates are supported from their respective ground plates and are thus physically and electrically isolated from one another.

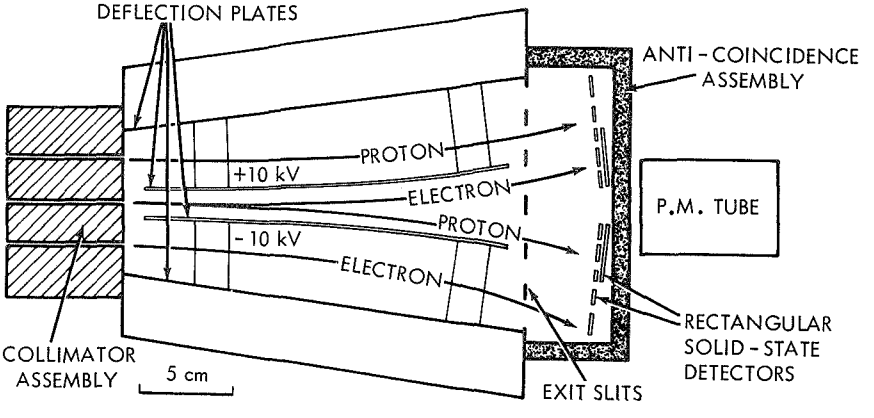

Figure 37--Cross-section view of an electrostatic-analyzer-total-energy detector system.

The detector assembly of the sensor consists of an anticoincidence guard and twelve rectangular solid-state detectors. The width of each detector and its position are selected to give the desired energy intervals and charge resolution. Each of the front ten solid-state detectors measures the energy, deposited by the particles, which enters its sensitive region. For protons and heavier particles the energy deposited is in all cases their total incident energy; while for electrons and positrons the deposited energy in most cases is a known fraction of their total energy. The position of the triggered detector determines the charge/energy of the particle.

The anticoincidence plastic scintillator prevents the analysis of false signals from the solid-state detectors. These are caused either by directly penetrating high-energy cosmic rays or by the secondary radiation they produce in the spacecraft. The small remaining fraction of the false signals still analyzed contributes to a residual background which is expected to have a smooth frequency distribution as a function of the energy measured by the detector.

The lower sensitivity for particle detection of ~100 keV depends primarily on the magnitude of the detector-amplifier noise, while the upper limit of about 2.5 MeV/charge depends primarily on the dimension and strength of the electric-field region.

The instrument detects not only heavy particles—such as protons, α-particles, the carbon-nitrogen-oxygen group, etc.—but also electrons and positrons. Since these light particles have a larger range than the heavy particles at the same energies, electrons and positrons penetrate the front detectors and trigger in coincidence the detector immediately behind it. Positrons are distinguished from protons by the occurrence of coincidences. Electron-positron annihilation results in the emission of two or three γ rays. However, the γ's are unlikely to trigger (and thus veto analysis) either the plastic anticoincidence guard or any of the silicon detectors.

One of the inherent disadvantages of the electrostatic-deflection-total-energy particle detection and identification is the small geometrical factor that results from the required collimation. This difficulty can be overcome to some extent if we increase the number of slits in the collimator, thereby increasing the area through which particles may enter. We cannot increase the acceptance angle without sacrificing the required collimation, but the sensitive area of the solid-state detectors may be enlarged by increasing the length of each detector. This

is possible, since collimation in only one direction (up and down in Figure 37) is required. The geometrical factor that can be achieved with the techniques outlined above is around 0.1 cm^2-ster for an instrument of the size shown in Figure 37. This compares with geometrical factors of ~1 cm^2-ster for dE/dx-vs-energy and dE/dx-vs-range detectors flown on satellites.

REFERENCES

1. Rossi, B., "High Energy Particles," Englewood Cliffs, N. J.: Prentice Hall, 1961.

2. Møeller, C., "Fur Theorie des Durchgauges Schneller Elektronen durch Materie," Ann. Physik 14:531-585, 1932.

3. Berger, M. J., and Seltzer, S. M., "Tables of Energy Losses and Ranges of Electrons and Positrons," NASA Special Publication 3012, 1964.

4. Barkes, W. H., and Berger, M. J., "Tables of Energy Losses and Ranges of Heavy Charged Particles," NASA Special Publication 3013, 1964.

5. Skyrme, D. J., "The Passage of Charged Particles through Silicon," Nuclear Inst. and Methods, 57:61-76, 1967.

6. Fan, C. Y., Gloeckler, G., and Simpson, J. A., "Cosmic Radiation Helium Spectrum Below 90 MeV Per Nucleon Measured on IMP 1 Satellite," J. Geophys. Res. 70(15):3515-3527, 1965.

7. Bryant, D. A., Ludwig, G. H., and McDonald, F. B., "A Scintillator Counter Telescope for Charge and Mass Identification of Primary Cosmic Rays," I.R.E. Trans. Nuclear Sci. 9(3):376-380, 1962.

8. Simnett, G. M., and McDonald, F. B., "Observations of Cosmic Ray Electrons Between 2.7 and 21.5 MeV," Astrophys. J. 157(3):1435-1447, 1969.

9. Gloeckler, G., and Fan, C. Y., "A Proposal for an Experiment to Analyze Ions and Electrons in the Energy Range 100 keV to 15 MeV in the Interplanetary Monitoring Platform (IMP) H, I, and J," Sept. 1966 (unpublished).

BIBLIOGRAPHY

Badwhar, G. D., Deney, C. L., Dennis, B. R., and Kapan, M. F., "The Non-Linear Response of the Plastic Scintillator NE 102," Nuclear Inst. and Methods, 57:116-120, 1967.

Barkes, W. H., and Berger, M. J., "Tables of Energy Losses and Ranges of Heavy Charged Particles," NASA Special Publication 3013, 1964.

Berger, M. J., and Seltzer, S. M., "Tables of Energy Losses and Ranges of Electrons and Positrons," NASA Special Publication 3012, 1964.

Biswas, S., and Fichtel, C. E., "Composition of Solar Cosmic Rays," Space Sci. Revs. 4:709-736, 1965.

Bryant, D. A., Ludwig, G. H., and McDonald, F. B., "A Scintillator Counter Telescope for Charge and Mass Identification of Primary Cosmic Rays," I.R.E. Trans. Nuclear Sci. 9(3):376-380, 1962.

Comstock, G. M., Fan, C. Y., and Simpson, J. A., "Abundances and Energy Spectra of Galactic Cosmic-Ray Nuclei Above 20 MeV per Nucleon in the Nuclear Charge Range $2 \leq Z \leq 26$," Astrophys. J. 146:51-77, 1966.

Dearnaley, G., and Northrop, D. C., "Semiconductor Counters for Nuclear Radiations," New York: John Wiley, 1966.

Fan, C. Y., Gloeckler, G., and Simpson, J. A., "Cosmic Radiation Helium Spectrum Below 90 MeV per Nucleon Measured on IMP 1 Satellite," J. Geophys. Res. 70(15):3515-3527, 1965.

Fan, C. Y., Pick, M., Pyle, R., Simpson, J. A., and Smith, D. R., "Protons Associated with Central Solar Activity and Their Propagation in Interplanetary Magnetic Field Regions Corotating with the Sun," J. Geophys. Res. 73(5):1555-1582, 1968.

Fermi, E., "Nuclear Physics," compiled by J. Orear, A. H. Rosenfeld, and R. A. Schluter, Chicago: The University of Chicago Press, 1960.

Fleischer, R. F., Price, P. B., and Walker, R. M., "Nuclear Tracks in Solids," Sci. American, 220(6):30-39, 1969.

Freier, P. S., and Waddington, C. J., "Electrons, Hydrogen Nuclei, and Helium Nuclei Observed in the Primary Cosmic Radiation During 1963," J. Geophys. Res. 70(23):5753-5768, 1965.

Gloeckler, G., and Fan, C. Y., "A Proposal for an Experiment to Analyze Ions and Electrons in the Energy Range 100 keV to 15 MeV in the Interplanetary Monitoring Platform (IMP) H, I, and J," Sept. 1966 (unpublished).

Meyer, A., and Murray, R. B., "Effect of Energetic Secondary Electrons on the Scintillation Process in Alkali Halide Crystals," Phys. Rev. 128:98-105, 1962.

Meyer, P., "Cosmic Rays in the Galaxy," in Annual Rev. Astron. and Astrophys., 7:1-38, 1969.

Møeller, C., "Für Theorie des Durchganges Schneller Elektronen durch Materie," Ann. Physik 14:531-585, 1932.

Murray, R. B., and Meyer, A., "Scintillation Response of Active Inorganic Crystals to Various Charged Particles," Phys. Rev. 122: 815-826, 1961.

O'Dell, F. W., Shapiro, M. M., Silberberg, R., Stiller, B., Tsao, C. H., Durgaprased, N., Fichtel, C. E., Gress, D. E., and Reames, D. V., "High-Energy Galactic Cosmic-Ray Composition Measured in Gemini XI," Canad. J. Phys. 46(10, Part 3): S569-571, 1968.

Price, P. B., Fleischer, R. L., Peterson, D D., O'Ceallaigh, C., O'Sullivan, D., and Thompson, A., "Identification of Isotopes of Energetic Particles with Dielectric Track Detectors," Phys. Rev. 164:1618-1620, 1967.

Price, W. J., "Nuclear Radiation Detection," New York: McGraw-Hill, 1964.

Rossi, B., "High Energy Particles," Englewood Cliffs, N. J.: Prentice Hall, 1961.

Schardt, A. W., and Opp, A. G., "Particles and Fields: Significant Achievements," Rev. Geophys. 5:411-446, 1967.

Shapiro, M. M., "Adventures of Cosmic Rays in Interstellar Space," Washington Acad. Sci. J. 57(4):93-103, 1967.

Simnett, G. M., and McDonald, F. B., "Observations of Cosmic Ray Electrons Between 2.7 and 21.5 MeV," GSFC Preprint X-611-68-450, 1968. Astrophys. J. 157:1435-1447, 1969.

Skyrme, D. J., "The Passage of Charged Particles through Silicon," Nuclear Inst. and Methods, 57:61-76, 1967.

Taylor, J. M., "Semiconductor Particle Detectors," London: Butterworth, 1963.

II. X-RAY DETECTORS

S. S. Holt
NASA Goddard Space Flight Center
Greenbelt, Maryland

INTRODUCTION

The opacity of the interstellar medium decreases rapidly with energy above ~1 keV, so that X-rays can be observed from distant parts of our galaxy and beyond (see Figure 1). The traditional differentiation between X-rays and gamma-rays (i.e., collisionally-produced versus decay-produced photons) has gradually given way to a rather arbitrary separation of the two regimes in the vicinity of electron-positron annihilation at 511 keV.

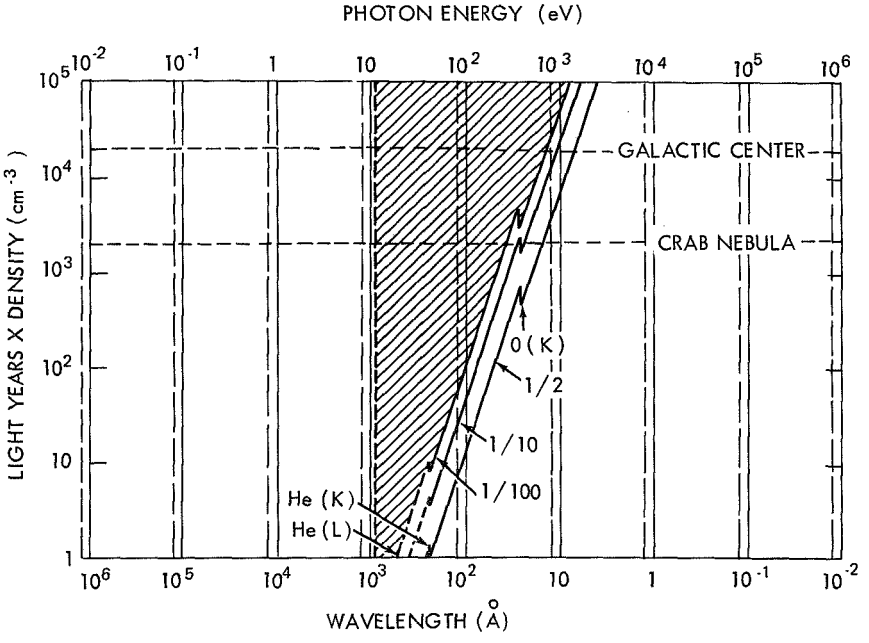

Figure 1–Interstellar absorption. The labelled traces refer to that fraction of the incident beam which is transmitted.

As discussed at length in the literature, these high-energy photons allow us to probe high-energy processes on stellar, nebular, galactic, and metagalactic scales. Present state-of-the-art devices are sensitive enough to give us spectral information from extraterrestrial photons. We shall address ourselves to the optimization of this technology.

First, note that X-ray photons have wavelengths $\lesssim 10\text{Å}$. This means that we cannot easily use antennas for photon detection, but must, instead, utilize the corpuscular properties of electromagnetic radiation. Conventional particle detectors generally measure the energy lost by charged particles in ionizing the detection medium, so that the adaptation of particle detectors for photon counting must, as a prerequisite, involve the conversion of the incident photon energy to the kinetic energy of one or more charged particles.

PHOTON INTERACTIONS IN DETECTION MEDIA

Consider the interaction of photons with an arbitrary neutral medium. As long as we restrict ourselves to photon energies below mc^2, we need not consider pair production or nuclear photodisintegration, so that the effects of interest will be solely in the realm of atomic scattering. We may also disregard coherent photon scattering that entails virtually no loss of photon energy. The mechanisms we need consider are the Compton and photoelectric effects.

Strictly speaking, Compton interactions are photon collisions with free electrons. However, since the binding energies for outer atomic electrons are (typically) much smaller than the photon energies of interest, these electrons can be considered free. We shall also find that in those cases where the binding energy is not small with respect to the photon energy, the photoelectric cross-section usually greatly exceeds the Compton cross-section.

Quite generally (i.e., independent of energy-dependent cross section, polarization, etc.), the conservation of momentum and energy alone yield the following useful formulas for a photon of wavelength λ that scatters off an electron at rest at an angle θ with respect to its incident direction:

$$\lambda' = \lambda + \frac{h}{mc}(1-\cos\theta) = \text{photon wavelength after collision},$$

$$T = \frac{ch^2}{\lambda} \frac{1 - \cos\theta}{\lambda mc + h(1 - \cos\theta)} = \text{kinetic energy of scattered electron,}$$

$$\phi = \text{arc cot} \left[\left(1 + \frac{h}{\lambda mc} \right) \tan \frac{\theta}{2} \right] = \text{angle of scattered electron with respect to incident photon direction.}$$

In a particular detector that utilizes Compton interactions, alone, to measure photon energies, there must obviously be a multiplicity of interactions in order that the incident photon energy shall be sufficiently converted to electron kinetic energy. In a single Compton interaction, the maximum transfer of energy to the electron is

$$T_{max} = \frac{2ch^2}{\lambda^2 mc + 2\lambda h} = \frac{E^2}{(1/2)mc^2 + E}, \qquad E = \frac{hc}{\lambda},$$

so that the maximum fractional energy loss for the photon is

$$f_{max} = \frac{T_{max}\lambda}{hc} = \frac{E}{(1/2)mc^2 + E}.$$

Hence

$$(f_{max})^{-1} = 1 + \frac{\lambda mc}{2h} = 1 + \frac{mc^2}{2E}.$$

It follows that we can transfer a larger fraction of the incident photon energy to the detection medium in a single interaction for higher-energy incident photons. For the upper end of what we have defined as the X-ray band, we have

$$f_{max} = \frac{2}{3} \qquad \text{for} \qquad \frac{hc}{\lambda} = mc^2.$$

On the average, of course, energy transfer will be much less, so that we require either an extremely large number of Compton interactions or a more efficient energy-conversion mechanism at lower

photon energies. We have already mentioned that photoelectric interaction will help in this respect.

The total Compton cross-section may be written:

$$\sigma_{total} = \frac{8\pi}{3}\left(\frac{e^2}{mc^2}\right)^2 \left[1 - 2\,\frac{h}{\lambda mc} + 5.2\left(\frac{h^2}{\lambda^2 m^2 c^2}\right) + \cdots\right]$$

$$\sigma_{total} = \frac{8\pi}{3}\left(\frac{e^2}{mc^2}\right)^2 = \sigma_{Thompson} \text{ as } \frac{hc}{\lambda mc^2} \to 0 .$$

Although the above represents the probability of having <u>any</u> interaction with an electron (i.e., rather than one involving a specific energy deposition), the assumption of many collisions allows us to use a meaningful average cross-section, as follows: If we define the average energy lost per collision as the total energy lost in a large number of collisions divided by the number of collisions, we obtain:

$$\frac{\sigma_{average}}{\sigma_{total}} = \frac{T_{av}}{E} = \frac{E}{mc^2} ,$$

so that for

$$E = \frac{hc}{\lambda} < mc^2$$

the average fractional energy loss per Compton collision is linearly proportional to the photon energy. We then note that for the same atomic density, the number of available electrons for Compton interactions is roughly proportional to Z, so that the cross-section per atom can be approximated:

$$\sigma_{average} \approx \frac{ZE}{mc^2}\,\frac{8\pi}{3}\left(\frac{e^2}{mc^2}\right)^2 ,$$

where we assume that in every collision the photon loses an amount of energy

$$T_{av} = \frac{E^2}{mc^2} .$$

We must remember that this approximation is useful only when the number of Compton interactions in the medium is large.

In photoelectric or inner-shell electron scattering, the atom can take up the momentum necessary for the electron to completely absorb the energy of the incident photon. The emerging electron then has a kinetic energy equal to the photon energy (less the electron binding energy), which will be dissipated in the medium. The atom will usually return promptly to the ground state by emitting a characteristic Lyman line (if the ejected electron is from the k-shell), so that in principle we can detect all the energy if we can convert the characteristic X-ray energy to electron kinetic energy via Auger or Compton interactions.

The cross-section for photoelectric interactions in the energy range of interest varies approximately as

$$\sigma_{photo} \propto \frac{Z^4}{E^3} .$$

It must be remembered that the above expression has discontinuous jumps at the absorption edges, so that the normalizing constant must be updated across each edge. It is important to note the strong dependence on both energy and atomic number, in contrast to the weaker dependences on those parameters in the Compton cross-section. All media have higher photoelectric cross sections at lower energies, and heavier elements have higher cross sections than do lighter elements at the same energy.

We can now discuss the average response of a medium to a beam of monoenergetic photons. The cross sections previously defined are the differential probabilities that the interactions occur in a depth dx of the medium; i.e., if a beam of intensity I cm^{-2} sec^{-1} is incident on a detector of depth dx, the fraction removed from the beam (on the

average) is

$$\frac{dI}{I} = -\mu\, dx ,$$

where μ is the cross section converted to units of, for example, $cm^2\text{-}g^{-1}$ (i.e., the inverse units of dx). The negative sign indicates removal from the incident beam. For a finite thickness x the relation may be integrated directly, yielding

$$I = I_0\, e^{-\mu x} ,$$

so that the probability that a single photon will interact in a depth x is

$$P_\mu = 1 - e^{-\mu x} .$$

If there are competing processes, e.g. Compton and photoelectric, it is clear that

$$\frac{dI}{I} = -\left(\mu_1 + \mu_2\right) dx ,$$

so that

$$I = I_0\, e^{-(\mu_1+\mu_2)x} = I_0\, e^{-\mu_1 x}\, e^{-\mu_2 x} .$$

The probability of having one (but not the other) interaction must then be:

$$P_1 = \frac{\mu_1}{\mu_1 + \mu_2}\left[1 - e^{-(\mu_1+\mu_2)x}\right] .$$

Since those photons which can lose essentially all of their energy in the detection medium are our main concern, it is important

to note that photoelectric interactions will not satisfy this objective unless two non-trivial conditions can be met:

1. The interaction depth must be such that the electron range is well within the medium.

2. The probability of the characteristic line emission escaping the medium is small (all monoelemental media are transparent to their own radiation; i.e., the characteristic line radiation always occurs at the minimum of the discontinuous jump in the photoelectric cross-section).

In addition, Compton interactions may accomplish this objective either approximately (with many Compton interactions) or exactly (with an arbitrary number of Compton interactions ending in a photoelectric interaction). See Figure 2, which gives mass absorption, attenuation, and scattering coefficient for lead.

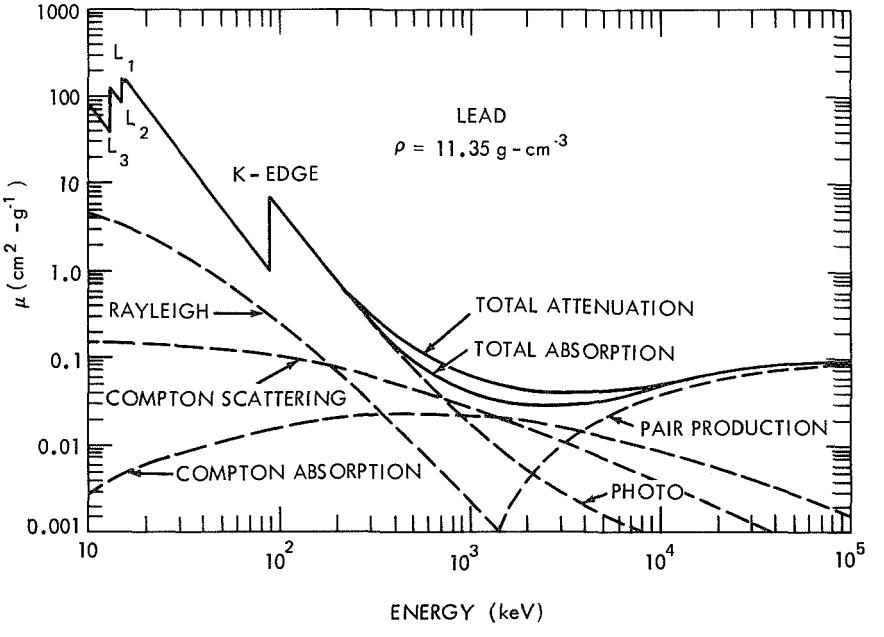

Figure 2–Mass absorption, attenuation, and scattering coefficients for lead.

PROPERTIES OF DETECTION MEDIA

The range of electrons in matter is almost invariably such that the path length is short enough for the detection medium to behave as a calorimeter for the electron kinetic energy. At the highest energy we consider ($\sim mc^2$), the electron range in virtually all media is close to 0.3 g/cm^2, while at lower energies the range is substantially smaller (typically, three orders of magnitude smaller at 10 keV). When we discuss specific media below, we shall see that electron escape from the medium is rarely an important consideration.

The geometry of the medium does play a significant role in the operation of the detector, but this is generally a result of inefficient collection rather than inefficient energy deposition in the X-ray regime. Once the energy is deposited in ionization (i.e., free, cold electrons and ions), we can use the number of ionizations to obtain the total energy deposited. We can do this by collecting the charge directly (e.g., solid-state detectors), internally amplifying the charge (e.g., proportional counters), or converting the ionization energy back to electromagnetic energy in a different frequency band which may then be detected by other means (e.g., scintillator-photomultiplier counters). Regardless of the type of counter we are dealing with, the limiting resolution of the instrument is the statistical uncertainty in the collected charge. Even for a perfect counter (i.e., one for which all the separated charge is collected), there is still finite resolution because of the statistical uncertainty in the amount of charges produced in the ionization process. The specific ionization gives us the amount of energy deposited per unit path length, and we have already mentioned that all of the energy is dissipated in the medium. The truly relevant parameter, then, is the number of ion pairs produced per unit energy interval. The total charge separated is this charge production rate times the total energy of the incident photon (since we are assuming that all of this energy has been converted to electron kinetic energy which, in turn, accomplishes the charge separation). The number of discrete electronic charges separated is, then, linearly proportional to the photon energy, and, since the charge separation is governed by Poisson (random) statistics, we may assume that

$$N(E) = \overline{N(E)} \pm \delta N(E)$$

$$= \frac{dN}{dE} E \pm \sqrt{\frac{dN}{dE} E} ,$$

where N(E) is the number of ion pairs for an energy deposition E in a medium in which, on the average, dN/dE is the number of ion pairs produced by unit energy deposition. The inherent resolution of the device can be represented by a standard deviation, i.e.,

$$\sigma(E) = \delta N(E) = \sqrt{\frac{dN}{dE} E} .$$

We usually express the energy resolution of a device as a fraction, i.e.,

$$\text{Percent FWHM} = 2.36 \times 10^2 \frac{\sigma(E)}{N(E)} \propto \frac{1}{\sqrt{E}} .$$

Evidently the inherent resolution of a counter is finite even for perfect charge collection, and should improve percentage-wise (as $1/\sqrt{E}$) for higher energies, reflecting the fact that percentage fluctuations in a larger sample are smaller.

Detectors are not usually perfect collectors, however, so that inefficient chargé collection will degrade the detector response. In order to optimize charge collection, the detector geometry is the most important consideration. Charge must not only be collected before it recombines, but also must be accomplished within the integration time of the signal. Inefficient collection (or multiplication, in the case of proportional counters) is invariably geometry-dependent, so that a detector wrongly designed may respond differently to photons that convert in different portions of its volume.

Figure 3 shows a generalized detector response to monoenergetic photons, illustrating the operation of such a system. Included are single Compton interactions, as well as photoelectric interactions (the shaded portion) which are either perfectly collected (main peak), imperfectly collected (baseline shift), or those for which characteristic line emission of the medium has escaped the detector (secondary peak; note that the energy difference between the primary and secondary peaks is precisely the energy of the characteristic line E_0).

We can construct the response function in a fairly straightforward manner. If we neglect the Compton interactions (T_{max} is a very small

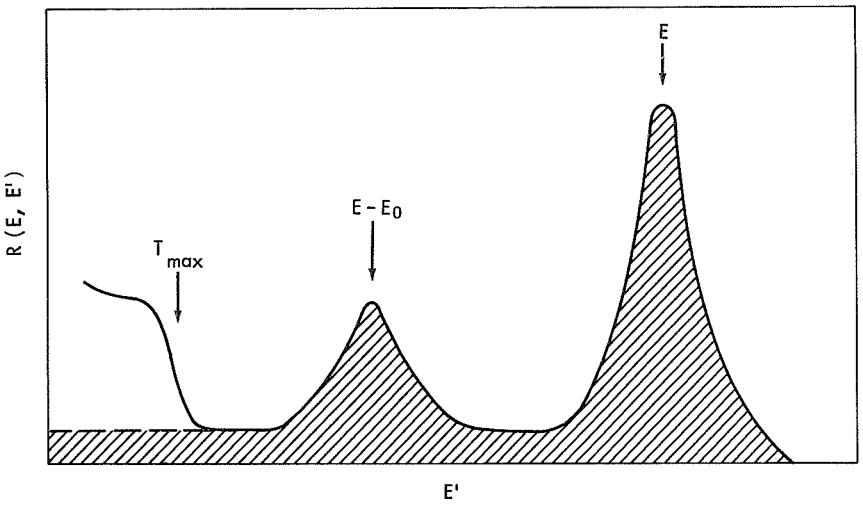

Figure 3–Schematic pulse-height response E′ of a detector to photons of incident energy E.

fraction of E for the lower energy portion of the X-ray range, and is usually below the detector threshold), the total detector efficiency is

$$\phi(E) = e^{-\mu_w(E)t}\left(1 - e^{-\mu_p(E)x}\right),$$

where μ_w and μ_p are the photoelectric attenuation coefficients (as defined previously) for the detector window (dead material) and active volume, respectively, and t and x are their thicknesses. Of the total photoelectric interactions undergone, a fraction χ have characteristic X-ray escape associated with them, while a fraction η are inefficiently collected. We will assume that these inefficiently collected events have equal probabilities for all energy depositions up to the incident energy. The probability, therefore, of observing a photon of energy E

at a pulse height corresponding to an energy E′ is then:

$$R(E, E') = \phi(E)\left[\frac{1-\chi-\eta}{\sqrt{2\pi}\,\sigma(E)}\exp\left\{-\frac{(E-E')^2}{2\left[\sigma(E)\right]^2}\right\}\right.$$

$$\left. + \frac{\chi}{\sqrt{2\pi}\,\sigma\left(E-E_0\right)}\exp\left\{-\frac{\left(E-E_0-E'\right)^2}{2\left[\sigma\left(E-E_0\right)\right]^2}\right\} + \frac{\eta}{E}\right];$$

$$\phi(E) = \int R(E, E')\,dE' \ .$$

For a photon beam with differential energy distribution f(E), the observed pulse height distribution is

$$P(E') = \int f(E)\,R(E, E')\,dE \ .$$

The inversion from pulse-height to input spectrum is obviously not unique. For that reason, the most unambiguous way to treat experimental data is to assume an input f(E) based upon a physical model and propagate it through the known (calibrated) detector response, allowing a meaningful comparison to be made with the data. We can then use χ^2 tests to exclude (but not necessarily verify) trial models.

SPECIFIC DETECTION DEVICES

The oldest and still most commonly used of the present generation of charge-collecting X-ray detectors is the proportional counter. In this device, consisting of a gas volume in which there are large electric-field gradients near the electron-collecting anode, an incoming charged particle (or a photon-produced electron from the gas, itself) will lose its kinetic energy in ionizing the medium, as described in the previous section. In a gas, it generally takes 20-30 eV to produce an ion pair.

The cold electrons then accelerate toward the anode, producing more ionization pairs as they proceed. In present counter designs, the geometry is such that all primarily produced ionization electrons produce the same number of cascade electrons, so that the detector volume itself can be used as a low-noise signal amplifier without degrading the inherent resolution of the counter. The most commonly utilized counters have depths ~5 cm and operate at ~1500 volts. The gas mixtures are mostly noble gases (to minimize spurious counts from free electrons), with ~10 percent of a quench gas to prevent the formation of secondary electrons by the positive ions. Figure 4 illustrates the photoelectric absorption coefficients for these noble gases.

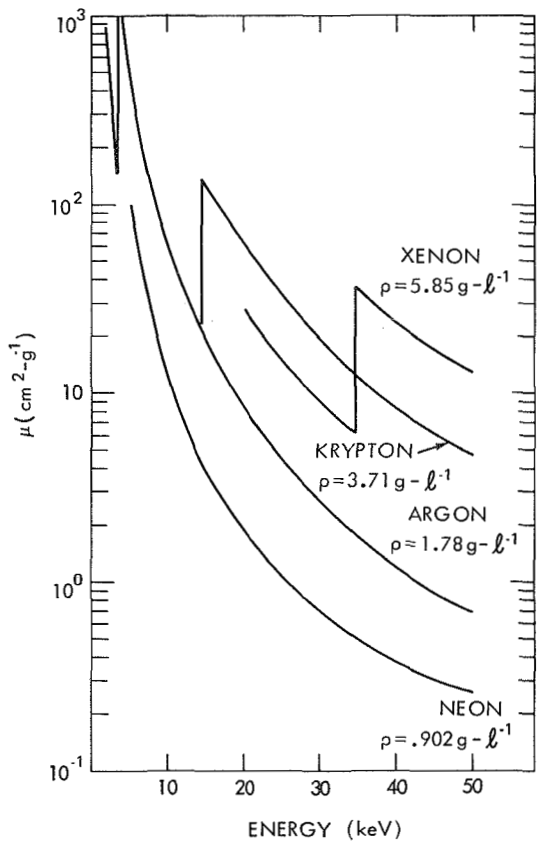

Figure 4—Photoelectric mass absorption coefficients for noble gases.

It is obvious that proportional counters are best utilized in the region 1-30 keV. The low-energy end of this range is determined primarily by the counter window, while the photoelectric efficiency determines the highest energy at which the counter can give useful information. It would seem as though xenon should be used exclusively if photoelectric efficiency were the only consideration, but the heavier gases are more easily poisoned, so that argon is generally the easiest gas to use for long-term stability and reasonable efficiency. The high photoelectric efficiency of heavier gases above the working range of the instrument can be a disadvantage, contaminating the spectrum at lower energies. At a pressure of 1 atmosphere, the density of argon is 1.78×10^{-3} g-cm^{-3}, so that a range of 4×10^{-4} g-cm^{-2} at 10 keV is an electron path length of only 2 mm. This means that an argon counter with dimensions of centimeters is ideally suited for 1- to 10-keV spectroscopy; the electron path lengths are short compared to counter depth, and the photoelectric cross section is not large enough for the preponderance of the photoelectrons to lose all their energy at the boundary of the medium.

Scintillators are materials capable of converting the ionization energy deposited in them to electromagnetic energy promptly, usually in the visible or near the UV range. The scintillation light is then collected (with ~10 percent efficiency) at the photocathode of a photomultiplier tube, and the resulting electron multiplication is used as a low-noise amplifier. Scintillators have inherently poorer resolution than do proportional counters because of the larger amount of energy necessary to produce an electron in the photomultiplier (typically, 1 keV on the average). For this reason, scintillators are used only at energies in excess of those at which proportional counters can be used effectively, i.e., $\gtrsim$10 keV. The high photoelectric cross-section in some inorganic scintillators (see Figure 5) makes them useful up to γ-ray energies.

Crystals of CsI and NaI may now be made with areas >100 cm^2, but severe dead-time considerations limit the usefulness of such large-area devices. The light pulse generally requires ~100 μsec for complete collection, compared with <10 μsec for proportional counters. This means that the size of the crystal must be so constrained that the counting rate does not become large enough to paralyze its operation. Note that anti-coincidence does not help eliminate residual light from events of no interest, so that the crystals must be relatively small (compared to proportional counters of like efficiency) in order that the attainable resolution shall be realized.

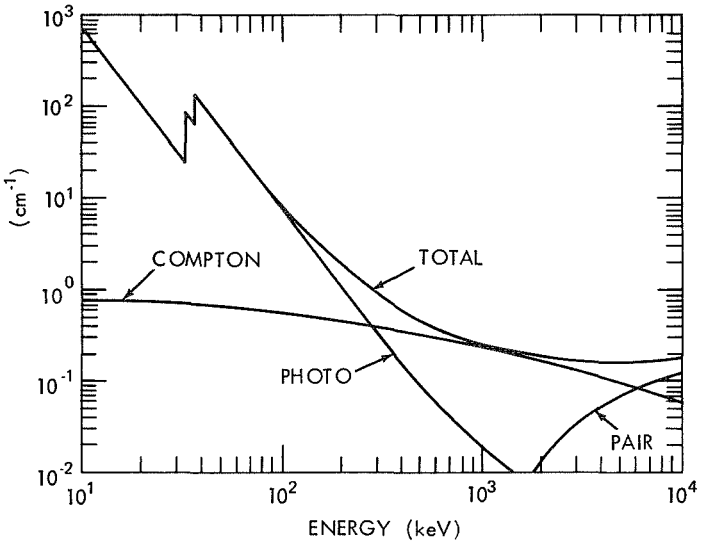

Figure 5–Mass absorption coefficients for CsI.

Of the newer X-ray spectrometers, perhaps the most important will be the application of solid-state detector technology to X-ray astronomy. Lithium-drifted silicon and germanium crystals have (in principle) even better inherent resolution than have proportional counters, as only ~3 eV is required to produce an ion pair. There is no internal multiplication of charge, unfortunately, so that we need cryogenic temperatures and high-power preamplifiers in order to obtain the resolution advantage over proportional counters. These spectrometers have maximum areas ~10 cm^2 at present, and the resolution is still strictly noise-limited (although recent breakthroughs in preamplifier technology have pushed the attainable resolution close to the theoretical limit).

There are many digital detection devices that do not give spectral information directly in a pulse-height mode, but can be used in conjunction with filters, gratings, or crystals to obtain indirect spectral information. Photographic emulsions are the oldest of this class of detector, of course; some others being ionization chambers (for total integrated intensity) and electron multipliers.

X-RAY OPTICS

Before detection, X-rays may be reflected from materials, to assist spectrometry and polarization studies and enable a detection system to increase its sensitivity when placed at the focus of an X-ray collector.

The technique of X-ray crystal spectrometry is well known: by way of Bragg scattering, X-rays undergo selective reflection in narrow energy bands (albeit with poor efficiency), so that much better resolution may be attained than with a charge-collecting counter alone. Such spectrometers have been flown on OSO satellites to enable the study of X-ray line emission from solar flares, but the sensitivity of such a system to celestial X-ray emitters is much too low.

Atomic scattering of X-rays is polarization-dependent, so that, in principle, polarization studies utilizing the scattering off low-Z (low photoelectric attenuation) targets and detection with digital detectors as a function of angle should be capable of yielding information regarding the polarization of incident X-rays. As yet, the sensitivity of polarimeters so constructed has been too low to give definitive information on the nature of the polarization of celestial sources.

X-ray collectors utilize either selective energy and/or polarization-dependent reflection maxima or, more generally, grazing incidence optics. It is possible that such an X-ray collector will make crystal spectrometry and polarization studies in X-ray astronomy feasible in the foreseeable future. As an illustration of this technique, consider a double-reflecting paraboloid-hyperboloid telescope (such a system is capable of imaging), as shown in Figure 6.

Grazing-incidence reflection of X-rays is similar to total internal reflection of optical light, except that there is a short-wavelength (high-energy) cutoff of reflectivity. This cutoff angle depends on the surface material and is roughly proportional to the wavelength of the incident X-ray for any given surface ($\alpha_{cutoff} \approx \beta/E$). Some values of the cutoff angle for several energies and various surfaces are listed in Table 1.

From Figure 4, we can define

$$f = \frac{D}{F} = 2 \tan 4\alpha$$

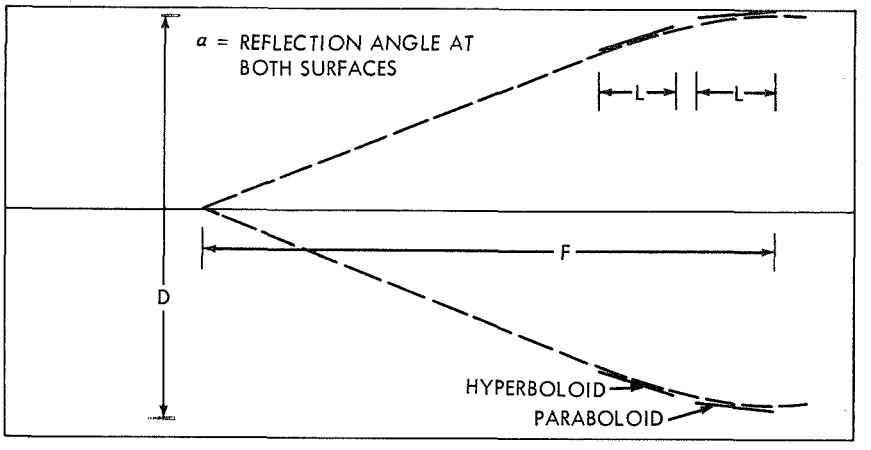

Figure 6–Schematic representation of a paraboloid-hyperboloid grazing incidence X-ray telescope.

Table 1. Cutoff Reflection Angles
(50-percent reflection at one surface)

	Reflection Angle (degrees)			
	Ni	Au	Al	Glass
8 keV	0.4	0.25	0.25	0.25
5.4 keV	0.6	0.55	0.36	0.34
1.5 keV	1.5	1.9	edge	1.2
0.5 keV	3.6	2.5	3	2.2

and, since α is small,

$$f = \frac{D}{F} \rightarrow 8\alpha = \frac{8\beta}{E} .$$

Choosing an energy and a material fixes the focal ratio f. In order that the telescope shall be the most efficient collector, we should

maximize its collecting area. We must therefore trade off between the high-energy limit of the telescope and the maximum attainable area.

If the paraboloid has a depth L, its projected thickness δ seen by an incoming ray is $L\alpha$, i.e.,

$$\delta = L \tan \alpha \approx L\alpha = LD/8F .$$

The frontal geometric area of this pair of surfaces will be

$$A = \pi \left(\frac{D}{2}\right)^2 - \pi \left(\frac{D - \delta}{2}\right)^2$$

$$\approx \pi \left(\frac{D}{2}\right)^2 \left(\frac{L}{4F}\right) ,$$

so that only a fraction L/4F of the total lens area will be useful for the collection of X-rays. We can do better by nesting additional surfaces within, but the problems of keeping all the surfaces confocal, etc., are obvious. At the present time, the feasibility of a telescope with focal length ~20 feet, collecting area $\sim 10^3$ cm^2, and image resolution of a few seconds (a few mils in the focal plane) is under investigation for a satellite-borne X-ray observatory.

STATISTICAL CONSIDERATIONS

In designing any experiment, a prime consideration is the expected statistical significance of the result. If we begin at the level of signal detectability in the form of a number of counts N (which are assumed to be the signature of the effect we seek), an unambiguous measure of the probability that the phenomenon is not merely a statistical fluctuation is the standard deviation $\sigma(N)$ of the counting rate. If we make a large number of independent measurements of N, we can define a reasonable expectation value $\bar{N}$ as the arithmetic mean of the large number of the determinations of N. If there are no systematic effects in our measurements, we expect that the values of N will be distributed

Table 2. Probability That Measurements are Merely Statistical Fluctuations

n	Probable occurrence
0.675	0.50
1.0	0.32
2.0	0.046
3.0	0.0027
4.0	6.3×10^{-5}
5.0	5.7×10^{-7}

about $\bar{N}$ randomly, i.e., that the distribution

$$|N - \bar{N}| > n\sqrt{\bar{N}}$$

will be in accord with Table 2.

In performing an actual experiment, we can make only a single measurement of N. Since we expect our measurement to conform to the above distribution, it is not unreasonable to assign a probable error to the measurement which approximates the standard deviation $\sqrt{\bar{N}}$ of this distribution, i.e.,

$$\sigma(N) \equiv \sqrt{N} \approx \sqrt{\bar{N}} .$$

This constitutes the basis of our statistical analysis.

If we possessed a background-free detector, we could then claim that any measurement N we make is a positive indication of the effect we seek, where the reliability of the result can be measured by

$$n = \frac{N}{\sigma(N)} = \frac{N}{\sqrt{N}} = \sqrt{N} .$$

The "probable occurrences" in the preceding table can then be properly interpreted as the probability that our positive measurement is merely a statistical fluctuation.

As a practical matter, there will always be detector background to contend with. If the number of background counts is B, the number of counts observed in the experiment will be N + B. We can independently determine $\bar{B}$ as precisely as we wish, but the fluctuations in the

background will never be smaller than $\sqrt{\bar{B}}$; therefore

$$\sigma(N+B) = \sqrt{N+B}$$

$$\sigma(B) = \sqrt{B}$$

$$\sigma(N) = \sqrt{\left(\sigma(N+B)\right)^2 + \left(\sigma(B)\right)^2}$$

$$= \sqrt{N+2B} \ .$$

It is obvious from inspection of $\sigma(N+B)$ and $\sigma(N)$ that the experimenter pays a severe statistical penalty for every background count when searching for a small effect. We note that it is unnecessary to evaluate $\sigma(N)$ if mere yes-no detection is the object of the experiment; i.e., all we need consider is

$$n = \frac{(N+B)-\bar{B}}{\sqrt{\bar{B}}}$$

provided that we are certain that $\bar{B}$ is a reliable measure of B. If we want to estimate the error in the magnitude determination (rather than just the presence of the effect as above) then we must consider

$$n = \frac{(N+B)-\bar{B}}{\sqrt{N+B+\bar{B}}} \ .$$

For purposes of testing data against a model, a χ^2 test for goodness (more properly, badness) of fit can be performed. Actually χ^2 is a measure of the degree to which the data are consistent with truly random fluctuations from the "expected" values. The method consists of comparing the variances of the data points with the squares of their statistical errors. For a series of n measurements of quantities N_i

with standard deviations δN_i,

$$\chi^2 = \sum_{i=1}^{n} \frac{\left(N_i - \langle N_i \rangle\right)^2}{\left(\delta N_i\right)^2} .$$

Note that δN_i should, properly, be the expected standard deviation with respect to $\langle N_i \rangle$, not its approximate value $\sqrt{N_i}$. If the measurements are all made on the same quantity, i.e., if $\langle N_i \rangle = \langle N \rangle$, then

$$\chi^2 = \sum_{i=1}^{n} \frac{\left(N_i - \langle N \rangle\right)^2}{\left(\delta N_i\right)^2} = \sum_{i=1}^{n} \frac{\left(N_i - \langle N \rangle\right)^2}{\langle N \rangle} ,$$

since $\delta N_i = \sqrt{\langle N \rangle}$.

$$\langle N \rangle = \frac{\sum_{i=1}^{n} N_i / \left(\delta N_i\right)^2}{\sum_{i=1}^{n} 1 / \left(\delta N_i\right)^2} \rightarrow \frac{\sum_{i=1}^{n} N_i}{n} .$$

since the $(\delta N_i)^2$ are equal weighting factors.

Table 3 gives confidence intervals for values of $n \leq 30$. For $n > 30$, the χ^2 distribution is peaked at approximately n (with standard deviation $\sqrt{2n}$), so that the table of probable occurrences given at the beginning of this section may be used. Strictly speaking, the number of degrees of freedom in the analysis is one less than the number of trials, but this distinction is relatively unimportant for large n.

Table 3. Confidence Intervals for $n \leq 30$

n, number of measurements in series being analyzed	Ranges of χ^2 values		
	High confidence (80% probability)	Standard confidence (90% probability)	Basic confidence (98% probability)
3	0.211 - 4.605	0.103 - 5.991	0.020 - 9.210
4	0.584 - 6.251	0.352 - 7.815	0.115 - 11.345
5	1.064 - 7.779	0.711 - 9.488	0.297 - 13.277
6	1.610 - 9.236	1.145 - 11.070	0.554 - 15.086
7	2.204 - 10.645	1.635 - 12.592	0.872 - 16.812
8	2.833 - 12.017	2.167 - 14.067	1.239 - 18.475
9	3.490 - 13.362	2.733 - 15.507	1.646 - 20.090
10	4.168 - 14.684	3.325 - 16.919	2.088 - 21.666
11	4.865 - 15.987	3.940 - 18.307	2.558 - 23.209
12	5.578 - 17.275	4.575 - 19.675	3.053 - 24.725
13	6.304 - 18.549	5.226 - 21.026	3.571 - 26.217
14	7.042 - 19.812	5.892 - 22.362	4.107 - 27.688
15	7.790 - 21.064	6.571 - 23.685	4.660 - 29.141
16	8.547 - 22.307	7.261 - 24.996	5.229 - 30.578
17	9.312 - 23.542	7.962 - 26.296	5.812 - 32.000
18	10.085 - 24.769	8.672 - 27.587	6.408 - 33.409
19	10.865 - 25.989	9.390 - 28.869	7.015 - 34.805
20	11.651 - 27.204	10.117 - 30.144	7.633 - 36.191
21	12.443 - 28.412	10.851 - 31.410	8.260 - 37.566
22	13.240 - 29.615	11.591 - 32.671	8.897 - 38.932
23	14.041 - 30.813	12.338 - 33.924	9.542 - 40.289
24	14.848 - 32.007	13.091 - 35.172	10.196 - 41.638
25	15.659 - 33.196	13.848 - 36.415	10.856 - 42.980
26	16.473 - 34.382	14.611 - 37.382	11.524 - 44.314
27	17.292 - 35.563	15.379 - 38.885	12.198 - 45.642
28	18.114 - 36.741	16.151 - 40.113	12.879 - 46.963
29	18.939 - 37.916	16.928 - 41.337	13.565 - 48.278
30	19.768 - 39.087	17.708 - 42.557	14.256 - 49.588

As an illustration of the power of this technique, we cite the search for pulsar characteristics in the X-ray emission of the Crab Nebula. Knowing the approximate pulsar period from measurements conducted in 1969, the GSFC group analyzed data from a flight conducted in 1968 (before the pulsar was discovered) for X-ray pulsation. Periods about that expected were assumed, with each trial period being broken into 40 equal segments. The values of χ^2 obtained for these 39 degrees of freedom and each trial period are displayed in Figure 7. The departure from randomness is clearly indicated in the vicinity of the expected period; i.e., the data fails the χ^2 test for consistency with random data at the pulsation period. It is a simple matter then to superpose the data in phase at the proper period, to obtain the temporal shape of the X-ray pulsation.

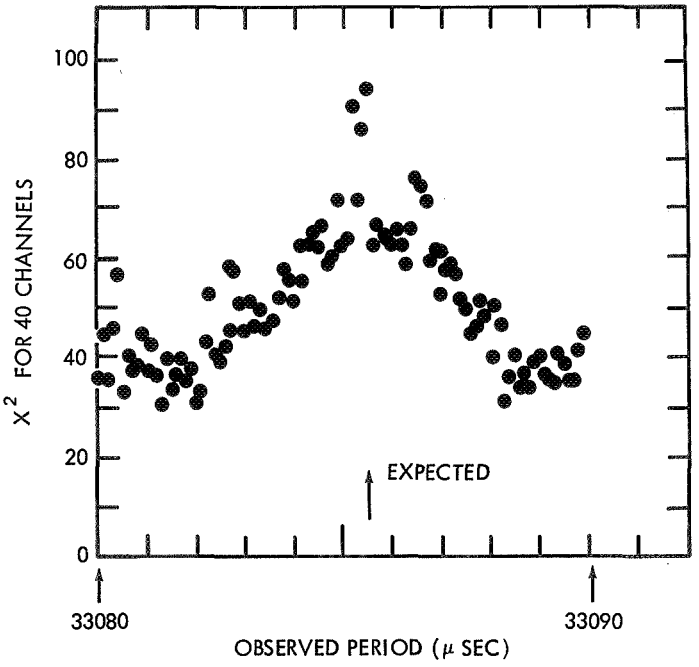

Figure 7–Test for randomness on non-random (pulsed) data.

OBSERVATIONAL CONSIDERATIONS

We can distinguish between two different background regimes, i.e., X-ray photons which enter through the detector aperture but are not part of the desired signal, and "internal background" which may be due to a variety of systematic effects (and which are not correlated with the detector X-ray aperture). As a specific example, we shall choose an argon proportional counter as a basic detection system, and attempt to optimize its response with respect to the following detectabilities:

1. source,
2. spectral-feature,
3. spatial-feature, and
4. temporal-feature.

We start with the photoelectric efficiency of an argon counter,

$$\phi(E) = e^{-\mu_w(E)t}\left[1 - e^{-\mu_p(E)x}\right] .$$

It is advantageous, of course, to make the window as thin (and low-Z) as possible. Beryllium of thickness $\sim 5 \times 10^{-3}$ cm has been used successfully, as have hydrocarbon films of thickness approaching 10^{-3} cm. Windows such as these make the counters useful above ~1 keV and, in the case of the hydrocarbon films, the carbon edge at ~1/4 keV allows for additional low-energy response. One atmosphere is a convenient working pressure, and inspection of Figure 4 quickly leads one to the conclusion that more than ~5 cm is neither necessary nor desirable. This is because we want to take advantage of the exponential in its nonlinear range; once it approaches linearity we have to accept too much background contamination (since it is roughly proportional to the volume). With a depth of 5 cm, the exponent will be ~unity at 10 keV, giving us an effective dynamic range exceeding a decade. This is reasonable, as the resolution we can attain (FWHM) with argon in this range is about an order of magnitude less than the dynamic range.

We will assume that the internal-detector background is $\sim 10^{-2}$ cm^{-2} sec^{-1}, once we have surrounded the detector with $\gtrsim 2\pi$ anti-coincidence to prevent cosmic rays from masquerading as real events. It is essential that some sort of particle anti-coincidence be employed,

as a minimum ionizing particle will deposit ~10 keV in the detector, which is within the acceptable range of our pulse-height spectrum for X-rays.

In addition to internal background, it is now well known that the entire celestial sphere is aglow with a seemingly isotropic X-ray background, of intensity $dI/dE \approx 10\ E^{-1.4}$ cm^{-2} sec^{-1} ster^{-1} keV^{-1}. The actual contribution to the counting rate is

$$\int_{E'_{min}}^{E'_{max}} \int_{0}^{\infty} \frac{dI}{dE} R(E, E')\, dE\, dE' \qquad \text{cm}^{-2}\ \text{sec}^{-1}\ \text{ster}^{-1},$$

which is approximately 20 cm^{-2} sec^{-1} ster^{-1}. If we are interested in making a measurement of a point source, it is advantageous to make the detector solid angle as small as possible. Present rocket platforms can be stabilized to better than 1 degree, so that we shall consider a 2- by 2-degree rectangular collimator, just to be on the safe side. The solid angle corresponding to this collimator is approximately 10^{-3} ster, so that the diffuse-background contribution to the counting rate is $\sim 2 \times 10^{-2}$ cm^{-2} sec^{-1}. It would be unwise to tighten up the collimation much more than this, because the diffuse background contribution is already of the same order as the internal-background contribution. Decreasing the diffuse component will not reduce the total background considerably, but will increase the chance of experiment failure if pointing inaccuracy is more than anticipated.

Figure 8 shows a detector for use in rocket-borne astronomy experiments. The collimator is constructed of rectangular tubing, and is used to support the mylar window against the one-atmosphere pressure differential. The central wire in each cell is an anode, while the boundary wires are cathodes at ground potential. All anodes may be treated as separate signals and are operated in anticoincidence (the bottom layer of anodes and those next to the wall are utilized solely for anticoincidence purposes). Since this anticoincidence is possible only on two of the four sides, the counter is rectangular rather than square so that gamma-produced electrons from the walls will yield a minimum of internal-counter background. In addition, pulse-shape discrimination may be performed on each signal to aid in rejecting electrons with paths parallel to the wires.

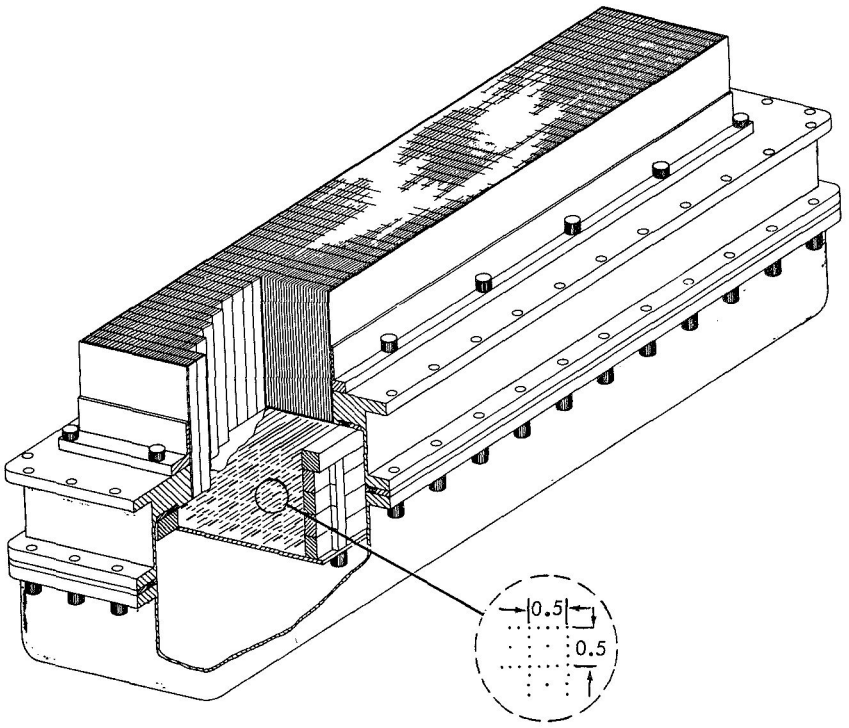

Figure 8–A detector for use in rocket-borne X-ray astronomy experiments.

We are now in a position to consider the minimum detectable source we can resolve with such a system. The total background will be

$$B = 3 \times 10^{-2} \text{ cm}^{-2} \text{ sec}^{-1} ,$$

while the exposure time available in an Aerobee rocket is of the order of 10^2 sec. Therefore we expect

$$B = 3 \text{ cm}^{-2} .$$

Since both components of the background increase linearly with the area, as does the counting rate from the source, it is advantageous for us to have as large an area as possible. The detection of a signal at n from a source of strength J $\text{cm}^{-2} \text{ sec}^{-1}$ (assuming ~80 percent

detection efficiency) can easily be analyzed as a function of detector area A. The total counting rate obtained in an exposure of t seconds is:

$$N + B = (0.8J + 0.03)\,At\ .$$

Unfortunately, the only way to make an unambiguous measurement of $\bar{B}$ in the neighborhood of the source candidate is to spend considerably more time in the determination of $\bar{B}$ than on the source candidate itself (i.e., this is the only way to be sure that the statistical error in $\bar{B}$ is no larger than $\sqrt{\bar{B}}$ during the time of exposure to the source).

We can construct proportional counters with area 10^3 cm^2, so that with exposure times of 10^2 sec we can, in principle, obtain 4σ results for $J \approx 3 \times 10^{-3}$ cm^{-2} sec^{-1}. In practice, however, all of the reported X-ray sources are more than an order of magnitude more intense. This is because rocket flights are too expensive to expose to a single source candidate, so that the sources are usually discovered in scans, where the time devoted to single sources is much smaller (in addition, the collimation is not as tight, nor is the area necessarily as large). If we had a specific source candidate in mind, however, and the wherewithal to devote an entire rocket flight to finding whether it was an X-ray emitter, we could expect to achieve a sensitivity approaching that calculated above.

Spectral measurements require a wholly different point of view, as we must now study the differential response of the counter to the source. As mentioned previously, the finite resolution of the device introduces a non-unique aspect to the determination of the input spectrum, so that the proper treatment of experimental data involves their comparison with hypothetical model spectra folded through the counter response. Early X-ray spectral determinations indicated that all the discrete X-ray sources in the sky could be fitted with rather simple trial spectra: power laws or exponentials. The statistical significance of the early data points was not extremely good, but there was good reason to choose these trial forms. If the origin of the X-ray emission was collisional (thermal), the X-ray distribution from an optically thin Maxwellian gas of ~universal elemental abundance was expected to be, to an approximation much better than the statistical significance of the

early data,

$$E \frac{dN}{dE} \propto \exp\left\{-\frac{E}{kT}\right\},$$

where dN/dE is the incident differential spectrum (cm^{-2} sec^{-1} keV^{-1}) from the source of temperature T. This sort of spectrum has been observed from solar flares with temperatures of several million degrees. The fit to the brightest X-ray source in the sky, Sco X-1, with this spectrum was excellent (with a temperature of ~50 million degrees). More recent studies of Sco X-1 in the radio, visible, and hard X-ray bands indicate that any model for Sco X-1 must be considerably more complicated than a single isothermal hot plasma, but the 1-10 keV emission from the source is still explicable in terms of such a plasma in the source that dominates the emission in this energy range.

Any emission process will have a spectrum that reflects the electron spectrum. It is assumed, therefore, that a power-law X-ray spectrum indicates non-thermal emission, insofar as the generating electron spectrum would appear to be closer to a power law than a Maxwellian. The source in the Crab Nebula, for example, exhibits a single power-law shape from the optical to the highest X-ray energies measured, and has been interpreted as synchrotron emission because of the polarization observed in the optical. The main problem this model has had to overcome is the short (~1 year) lifetime that the high-energy electrons generating the X-ray emission would have; it seems that the pulsar recently discovered in the Crab can provide the key to the mystery.

The problem is not so simple, however. Plausible models have been constructed wherein collisional (thermal) sources yield power-law output spectra, and synchrotron sources yield spectra that may masquerade as thermal. What is needed, clearly, is some sort of definitive signature of the origin, in addition to the overall spectral shape. One possibility is the detectability of discrete spectral features, such as emission lines and/or recombination edges. Fortunately, the counter system we are considering can be used to shed some light on this issue.

If the spectrum is thermal, and the temperature is of the order of 50 million degrees, there will be considerable emission from the two highest ionization states of iron at 6.64 and 6.89 keV. Since there will

be no comparable line emission above ~4 keV from any element save iron for any reasonable choice of elemental abundance, the detection of iron-line emission can be used to identify thermal emission. Note that the attainable resolution of ~1 keV FWHM at these energies should be adequate for purposes of iron-line identification.

As in the case of source detectability, we must maximize the exposure (area × time) to obtain as much spectral information as possible. To a first approximation, we can stipulate that the condition for the detection of iron-line emission is the observation of an $n\sigma$ increase over the simple exponential in a 1-keV window centered at 6.75 keV. However, since the presence of such emission means that the continuum with which it must be compared is not a pure exponential, we had better have $n \gtrsim 10$ for a really unambiguous identification. The GSFC group has observed such a bump at $\sim 3\sigma$ (at about 5 percent above the continuum in this window), which effectively rules out thermal emission from an optically thin supernova remnant for Sco X-1 (there would then be much more iron emission than is observed); this is consistent with universal elemental abundance. It will take a more sensitive experiment to make a case for a thermal-source definitive, but it will not be easy to accomplish from a rocket platform. In the case of Sco X-1, the effective exposure is not determined by area, but by telemetry capability. The intensity of Sco X-1 is $\sim 20\ \mathrm{cm}^{-2}\ \mathrm{sec}^{-1}$, so that 100 cm^2 will give $2 \times 10^3\ \mathrm{sec}^{-1}$, effectively saturating the GSFC telemetry capability of $\sim 3 \times 10^3\ \mathrm{sec}^{-1}$. In order to better the GSFC results, then, we would need a much faster telemetry system before increasing the area could help.

Line emission is not the only spectral structure that can be observed with proportional counters. There is some evidence that the diffuse background has a break in its power-law spectrum (of magnitude unity) somewhere in the range 10-100 keV. If such a break is sharp, it may be observable in the same way as line emission (so far, however, the evidence indicates that the break in the background spectrum is not sharp). We can estimate the sensitivity of our system to spectral features by considering the reliability of the neighboring spectrum, i.e., the featureless portion of the spectrum with which we must compare the candidate feature. The resolution of our counter is the limiting constraint on the minimum size of the window that we can choose. If we demand an $n\sigma$ result for a positive indication of a feature above the extrapolated value of the neighboring bins, it is a straightforward matter to determine the minimum exposure necessary with a bin size

δE. We will assume a number of bins S and a relatively flat spectrum over the range of accepted photons ΔE, so that the number of photons in each pulse-height bin is

$$\frac{N}{S} = N \frac{\delta E}{\Delta E} = \frac{JAt}{S} = \iint f(E)\, R(E, E')\, dE\, dE' \ .$$

The statistical error in the candidate bin is then approximately the same as that in all adjacent bins, so that the expected counting rate in that bin (as defined from the neighboring bins) has the same uncertainty. We can say that the observed counting rate in the bin, N', can be tested for the feature by the usual prescription

$$N' - \frac{N}{S} = n\sqrt{\frac{N}{S}} \ .$$

For the argon counter, with $\delta E \sim 1$ keV, $\Delta E \sim 10$ keV, $A \sim 10^3$ cm^2, $t \sim 10^2$ sec and an overall efficiency of ~ 0.8, we obtain the spectral sensitivity to a source of strength J. We must remember, however, that we are telemetry-limited, so that we can never have $N > 3 \times 10^5$. Note that although this analysis has assumed a flat pulse-height spectrum, the actual analysis will not be very different numerically, since the errors are proportional to the square root, and so will not change very rapidly from bin to bin.

Thus far, the spatial information about celestial X-rays in our library has been obtained with mechanical collimators. These collimators limit the field of view of the detectors in either an integral or differential manner. An integral collimator is one that cuts off the edges of the field of view, so to speak, and allows a response to some central region only; this is the type of collimator we proposed using at the outset of this chapter. Aside from the problems we encounter attempting to properly point the detector (once the field of view becomes small), the disadvantages of large depth and/or considerable obstruction of a large portion of the detector area start to become important. For these reasons, integral collimators have only been used for angles $\gtrsim 2$ degrees and therefore cannot locate discrete sources much more closely than that.

Differential modulation collimators have provided our most accurate source locations. These collimators define not only the periphery of the detector response, but also slice the direct field of view. They are generally constructed of wires or grids with sizes of the order of mils, and either rotate in front of the detector or are fixed (in which case the detectors roll slowly over the source candidates). The counting-rate maxima and minima so observed can then define the source location to the order of arc seconds for strong sources.

Finally, with regard to temporal measurements of discrete X-ray sources, we can propose the rather obvious technique of observing sources at different times. In several instances, marked changes have been observed. Cyg X-1 exhibited a change in intensity of a factor of four during the space of a few months, and Cen X-2 (once almost as intense as Sco X-1) has virtually disappeared. On a smaller scale, pulsar characteristics are being searched for in all X-ray emitters, but have been found only in the Crab. The method of analysis is fairly simple. If the period is not known, but all recorded photons are tagged with their arrival times, we can perform a Fourier analysis of the data record for periodicity. In the case of the Crab, where the period is known, this periodicity can be assumed and the data then superposed in phase. The important consideration, regardless of what technique is used, is to locate the arrival time of each photon as accurately as possible, and to minimize the system dead time.

BIBLIOGRAPHY

Introductory X-Ray Astronomy

Boldt, E., Cosmic Ray Photons, In "Lectures in High Energy Astrophysics," NASA Special Publication 199, 1969.

Gould, R. J., Origin of Cosmic X-Rays, Am. J. Phys. 35(5):376-393, May 1967.

Morrison, P., Extra-Solar X-Ray Sources, Ann. Rev. Astron. and Astrophys. 5:325-350, 1967.

Tucker, W., Cosmic X-Ray Sources, Astrophys. J. 148(3):745-765, June 1967.

Photon Interactions in Detectors

Evans, R. D., "The Atomic Nucleus," New York: McGraw-Hill, 1955.

Korff, S. A., "Electron and Nuclear Counters," New York: D. Van Nostrand, 2nd Ed., 1955.

Sharpe, J., "Nuclear Radiation Detectors," New York: John Wiley, 1955.

Experimental Statistical Analysis

Beers, Y., "Introduction to the Theory of Error," Reading, Mass.: Addison-Wesley Publ. Co., 2nd Ed., 1957.

Orear, J., Notes on Statistics for Physicists, University of California, Berkeley, UCRL-8417, 1958.

New Techniques in Experimental X-Ray Astronomy

Giacconi, R., Reidy, W. P., Vaiana, G. S., Van Speybroeck, L. P., and Zehnpfennig, T. F., "Grazing-Incidence Telescopes for X-Ray Astronomy," Space Science Rev. 9(1):3-57, Feb. 1969.

Gorenstein, P., and Mickiewicz, S., "Reduction of Cosmic Background in an X-Ray Proportional Counter through Risetime Discrimination," Rev. Sci. Instr. 39(6):816-820, June 1968.

III. HIGH-ENERGY PHOTON DETECTORS IN ASTRONOMY

H. Ögelman*†
NASA Goddard Space Flight Center
Greenbelt, Maryland

INTRODUCTION

Compared to the radio, optical, and X-ray region of the electromagnetic spectrum, the astrophysical information obtained through the gamma-ray channel (usually defined as 10^6 eV and higher-energy photons) has been limited. As late as 1968 all the experimental data mostly consisted of upper limits to the flux with few statistically insignificant positive claims. Effectively, the OSO-III Satellite results of Clark et al., constitute the first clear evidence of cosmic gamma rays. This is another analog in astronomy of a child's first steps. The bulk of the work still lies ahead; in the near future more sophisticated instruments will probe the gamma ray channel and reveal hitherto inaccessible information about the universe.

Already, radio and optical data suggest that high-energy particles dominate the energetics of various objects and regions in the universe. Even prior to the precise location of these relativistic particles, cosmic rays had indicated that high-energy processes do constitute a significant fraction of the total energy in our galactic neighborhood. Cosmic rays, being predominantly charged protons and nuclei, are hard to relate to their origin owing to the complicated paths they are forced to take through intervening magnetic fields. Gamma rays are the most promising means of directly measuring high-energy activity and learning its origin.

The primary aim of this paper is to examine the experimental techniques of gamma-ray astronomy. In order to provide some background and motivation, the present theoretical and experimental status of gamma-ray astronomy will be briefly treated.

*National Academy of Sciences, Resident Postdoctoral Research Associate.
†Present address: Faculty of Science, Middle East Technical University, Ankara, Turkey.

THEORETICAL BACKGROUND

Various nuclear and high-energy interactions that lead to gamma-ray production have been extensively studied in the laboratory by means of a wide range of particle accelerators. The task of theoretical calculations in gamma-ray astronomy is to apply this knowledge to the conditions of various regions in the universe and determine the output in gamma rays. This task is a difficult one; every component of matter and radiation in the particular region must be estimated from the limited information available.

The six decades of energy interval for the gamma rays under discussion imply a variety of production mechanisms that may dominate at certain energy bands. Let us organize these processes in their astrophysical context. The region between 10^6 and 10^7 eV (1 - 10 MeV) can throw light on the low-energy nuclear transitions that take place in the universe. A similar case is the optical photons and the valuable information they have yielded about the atomic processes that take place in the stars and gaseous regions of the cosmos. In the case of low-energy gamma rays, we can study nuclear excitations that may take place in stellar atmospheres and envelopes of supernova shells. Although nuclear reactions take place abundantly in hot, dense stellar interiors providing their energy source, the gamma rays produced in such reactions cannot escape from the interior.

The gamma rays produced in nuclear de-excitation processes should have line structure, that is, peaks in energy spectrum corresponding to the energy of transition.

Another source of low-energy gamma-ray line intensity is the radiation at 5×10^5 eV (0.5 MeV) produced by the annihilation of electron-positrons.

Processes that may lead to production of a broad spectrum of gamma rays in all energy regions are:

a. Synchrotron process where high-energy electrons emit photons when they are deflected in magnetic fields,

b. Inverse Compton process where high-energy electrons impart large energies to low-energy photons through elastic scatterings,

c. Bremsstrahlung process where energetic electrons emit gamma rays, since they are in the electric fields of nuclei,

d. Electromagnetic decay of mesons produced in nuclear collisions. The predominant process for this case is the decay of a neutral π° meson into two gamma rays.

Table 1 lists these processes, the typical energy of the produced photons, and, in applicable cases, the lifetimes of the electrons that lose energy through that particular process. Approximate energy loss rates can be obtained from the ratio of electron energy to electron lifetime.

Theoretical estimates for gamma-ray flux fall into two distinct groups: (1) diffuse gamma-ray flux such as that produced in the interstellar medium of our local galaxy or metagalactic space, (2) gamma-ray production in discrete objects such as supernova remnants, radio

Table 1. Dominant Gamma-Ray Production Mechanisms

Process	Typical gamma-ray energy (eV)	Lifetime of electrons (sec)
Synchrotron	$2 \times 10^{-20} H E_e^2$	$2.5 \times 10^{11} / H^2 E_e$
Inverse Compton	$4 \times 10^{-12} \epsilon E_e^2$ for $\epsilon E \ll 2.5 \times 10^{11}$	$10^{25} / \rho E_e$
Bremsstrahlung	E_e	$10^{15} / N_H$
$e^+ - e^-$ Annihilation	5×10^5	$10^{14} / N_e$ (positron lifetime) ($E_e + \lesssim 10^7$ eV)
Nuclear Trans.	$10^6 - 10^7$ (line emission)	—
π° decay	Broad distribution with peak at 7×10^7	—

E_e = electron energy (eV)
ϵ = low-energy photon (eV)
N_h = H atoms-cm^{-3}
H = magnetic field (gauss)
ρ = low-energy photon energy density (eV-cm^{-3})
N_e = electrons-cm^{-3}

galaxies, and quasi-stellar objects. This discrimination is purely for convenience in experimental investigation, since the responsible processes do not differ much.

Table 2 lists the rough estimates of gamma-ray fluxes at various energies for galactic, metagalactic, diffuse components; also two representative samples of discrete objects. As can be inferred from the table, a large range of uncertainty is involved in the theoretical estimates, owing to the lack of sufficient data concerning the conditions of the media.

SUMMARY OF EXPERIMENTAL STATUS

Before going into experimental details, let us briefly examine the state of experimental information. Predominantly the experiments in this energy region have negative upper limits. The first positive measurement in the field is due to Clark et al. With a satellite-borne detector, a definite anisotropic flux of gamma rays above 100 MeV has been detected. The results indicate an intensity as high as 10^{-2} photons-cm^{-2}-sec^{-1}-$ster^{-1}$ toward the galactic center. This surprising result is more than an order of magnitude higher than the predicted intensity. Already the theoretical calculations are being modified to accommodate this unexpected intensity.

The unambiguous detection of discrete sources of gamma rays still lies ahead. Figure 1 shows a graph of experimental sensitivity for discrete sources achieved at various energy levels. This curve also represents the energy-dependent upper limits for a variety of galactic and extragalactic objects examined in wide sky surveys. The discontinuities as a function of energy is purely due to the sensitivities of various instrumental techniques which in turn are dependent on the different interaction properties of gamma rays at different energies.

INTERACTION OF GAMMA RAYS WITH MATTER

General Principles

All of the present detection methods of physics as well as astrophysics depend on some form of macroscopic amplification of electric signals that are produced at quantum levels. This implies that in order

Table 2. Theoretical Estimates of Gamma Rays

Source	Estimated range of integral intensity (or flux)			
	$>10^6$ (eV)	$>5 \times 10^7$ (eV)	$>10^9$ (eV)	
Galactic Center	$5 \times 10^{-4} - 10^{-6}$	3×10^{-4}	2×10^{-5}	Intensity (photons cm^{-2}-sec^{-1}-$ster^{-1}$)
Metagalaxy	$10^{-2} - 10^{-4}$	$10^{-2} - 10^{-7}$	$5 \times 10^{-6} - 10^{-8}$	
Crab Nebula (supernova remnant)	$10^{-2} - 10^{-4}$	$10^{-5} - 10^{-9}$	$10^{-6} - 10^{-11}$	Flux (photons cm^{-2}-sec^{-1})
Virgo A (radio galaxy)	—	$10^{-8} - 10^{-10}$	—	

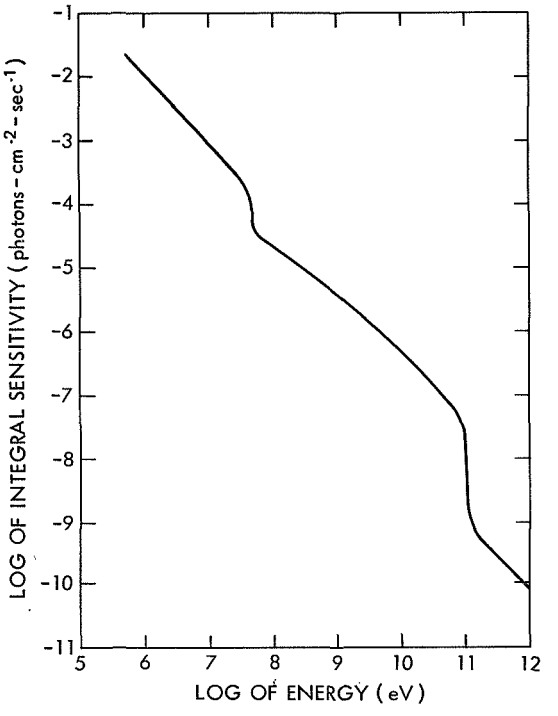

Figure 1—Sensitivity of gamma-ray sky surveys for discrete sources.

for us to detect a gamma ray, it must interact and produce a charged secondary. The importance of understanding the interaction of gamma rays with matter is evident, since a measurement is possible only through the charged secondaries. It is ironic that virtual photon exchanges, through which charged particles are measured and amplified, provide the means of detecting a real photon.

The three major interactions for gamma ray are: photoelectric effect, Compton effect, and pair production process.

Figure 2 shows the relative importance of these interactions as a function of energy of the photon and the nuclear charge Z of the absorbing material. As can be seen from the figure, for the gamma rays

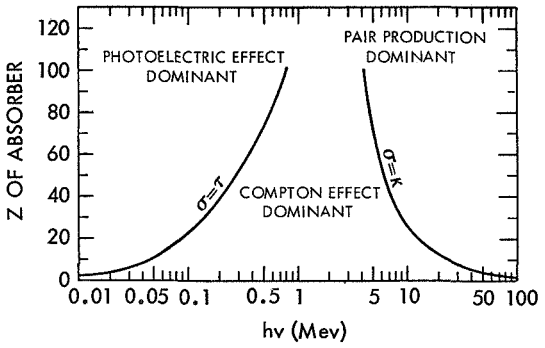

Figure 2–Relative importance of the three major types of γ-ray interaction. The lines show the values of Z and $h\nu$ for which the two neighboring effects are just equal. (Taken from Evans, 1955, p. 712.)

under discussion, the Compton and pair production processes dominate for a reasonable range of Z values. As will be shown later, the Compton process is undesirable in experimental techniques. Consequently the majority of experiments avoid this region by proper choice of interaction material. In the MeV region, high-Z materials are used to enhance the photoelectric effect; in the 10-MeV region, they are used to enhance the pair-production effect. Since the photoelectric effect is covered in the X-ray work, let us examine in more detail the Compton and pair-production processes.

Compton Process

The basic interaction is sketched in Figure 3.

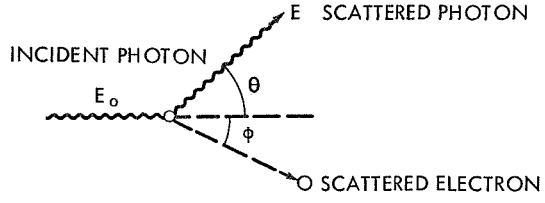

Figure 3–Compton process.

A gamma ray incident on an atomic electron scatters, losing energy by kicking off an electron. The kinematics of the interaction gives

$$\frac{1}{E'} = \frac{1}{m_e c^2}(1 - \cos\theta) + \frac{1}{E_0},$$

where E_0 is the energy of the incident photon, and E' is the energy of the photon after scattering through an angle θ. Photons of 10 MeV may lose 95 percent of their energy in a collision, whereas a photon of 0.5 MeV loses only 25 percent. Two basic difficulties that arise in detecting cosmic photons through the electrons produced in Compton collisions are:

a. The photon may take several collisions to impart all of its energy to the charged secondaries, in which case energy measurements become difficult.

b. The angular distribution of secondary electrons reflects the direction of the primary very loosely, thereby making it difficult to obtain good angular resolution. Figure 4 shows the angular distribution of the electrons for different incident photon energies.

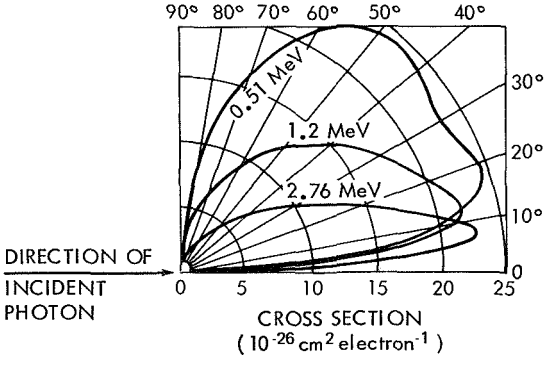

Figure 4—Number-vs-angle distribution of Compton electrons. (Taken from Davisson and Evans, 1952.)

Pair-Production Process

For photons above 10 MeV, pair-production process predominates, especially in high-Z materials such as lead. Figure 5 is a schematic diagram of the interaction.

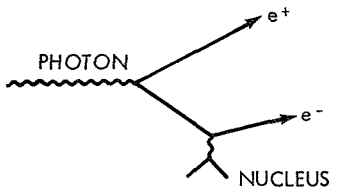

Figure 5–Pair-production process.

A real photon can materialize the virtual photon field surrounding the nucleus by producing an electron positron pair. Although the nucleus takes part of the energy of the interaction, owing to its relatively large mass, most of the energy is in the electron-positron pair, $E_\gamma \simeq E_{e^-} + E_{e^+}$. The pair-production process is, from a quantum electrodynamic point of view, very similar to the Bremsstrahlung process; consequently, the typical interaction length is commensurable with radiation length X_0, which is a function of target material.

$$\frac{1}{X_0} = \frac{4NZ(Z+1)}{137}\left(\frac{e^2}{m_e c^2}\right)^2 \ln 183\, Z^{-1/3}\left[(1+0.12)\left(\frac{Z}{82}\right)^2\right],$$

where N is the number of atoms-gm^{-1}, and $1/X_0$ is in cm^2-gm^{-1}.

The probability $dP(E, E')/dE'$ of producing an electron-positron pair per radiation length, where the energy of the electron is between E' and $E' + dE'$, is approximately given by

$$\frac{dP(E, E')}{dE'} \simeq \frac{7}{9}\frac{1}{E},$$

i.e., the total probability of pair production is 7/9 per radiation length. Deviations of these approximations from the exact solutions are illustrated in Figure 6 (see Ritson, 1961, in Bibliography) for two different materials: air and lead.

In summary, to obtain charged secondaries for photons above approximately 10 MeV we rely on pair production process. We can use

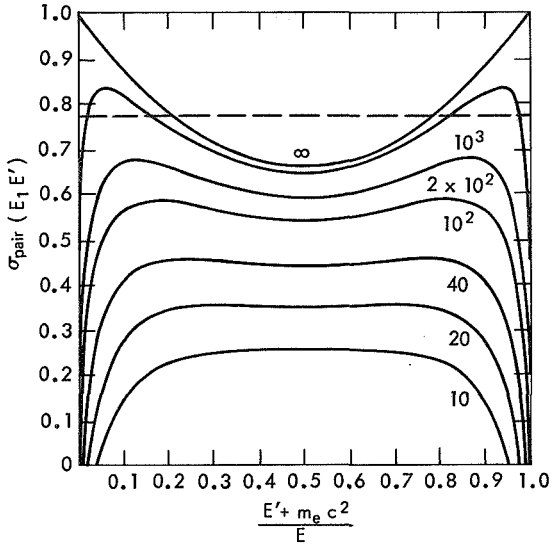

(a) IN AIR

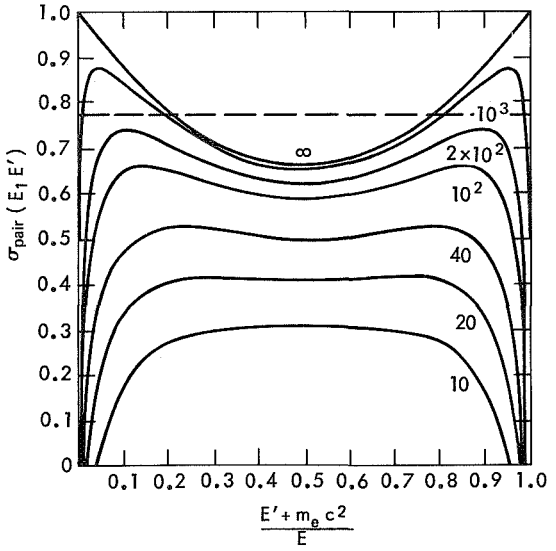

(b) IN LEAD

Figure 6–Differential cross section as a function of energy of the pair electrons for various incident γ-ray energies in natural units.

subsequently charged particle detection methods to achieve our experimental objectives.

Multiple Coulomb Scattering

Although this is a charged-particle effect (being concerned with arrival direction of photons and their energy determination), we should briefly familiarize ourselves with multiple Coulomb scattering of electrons.

From the results of ionization loss of charged particles in matter we know that the average transverse momentum Δp transferred to an electron passing within a distance b of a nucleus of charge Ze is

$$\Delta p = \frac{2Z e^2}{b\beta c} ;$$

therefore, the angle θ of scattering is

$$\theta = \frac{\Delta p}{p} = \frac{2Z e^2}{b\beta c p} .$$

The probability of scattering into an angle θ with $d\theta$ is proportional to $2\pi\, b\, db$, where b and θ are related by the above equation. The probability $P(\theta)$ of scattering into a solid angle $d\Omega$ for a small θ per gram of material can be expressed as

$$P(\theta)\, d\Omega = \frac{N}{A}\left(\frac{2Z e^2}{\beta p c}\right)\frac{d\Omega}{\theta''} ,$$

where N is Avogadro's number, and A is the mass number.

What we are really interested in is the average behavior of final deflection after an electron passes through x gm cm^{-2} material. This final average, called $\langle \theta^2 \rangle$, is composed of a large number of small

deflections added at random:

$$\langle \theta^2 \rangle = \int_{\theta_{min}}^{\theta_{max}} x\,\theta^2\,P(\theta)\,d\theta = 2\pi \frac{N}{A}\left(\frac{2Z\,e^2}{\beta c p}\right)^2 x \int_{\theta_{min}}^{\theta_{max}} \frac{d\theta}{\theta} .$$

With the substitution

$$\frac{\theta_{max}}{\theta_{min}} \quad \frac{b_{max}}{b_{min}} = \frac{5.3 \times 10^{-9} Z^{-1/3}}{A^{1/3}\,1.2 \times 10^{-13}}$$

and

$$r_e = \frac{e^2}{m_e c^2} ,$$

and approximating

$$\ln\left(\frac{r_{max}}{r_{min}}\right)^{1/2} \simeq \ln 183\, Z^{-1/3} ,$$

we can write

$$\langle \theta^2 \rangle \simeq \left(\frac{21}{p\beta}\right)^2 t ,$$

where t is in radiation lengths, p is in MeV/c, and $\langle \theta^2 \rangle$ is in radian^2. In one radiation length, a 100-MeV electron will scatter about 12 degrees while a 1-GeV electron will scatter about 1.2 degree.

EXPERIMENTAL METHODS

For high-energy gamma-ray measurements the earth's atmosphere is a nuisance. Figure 7 shows the mean free path of photons in air as

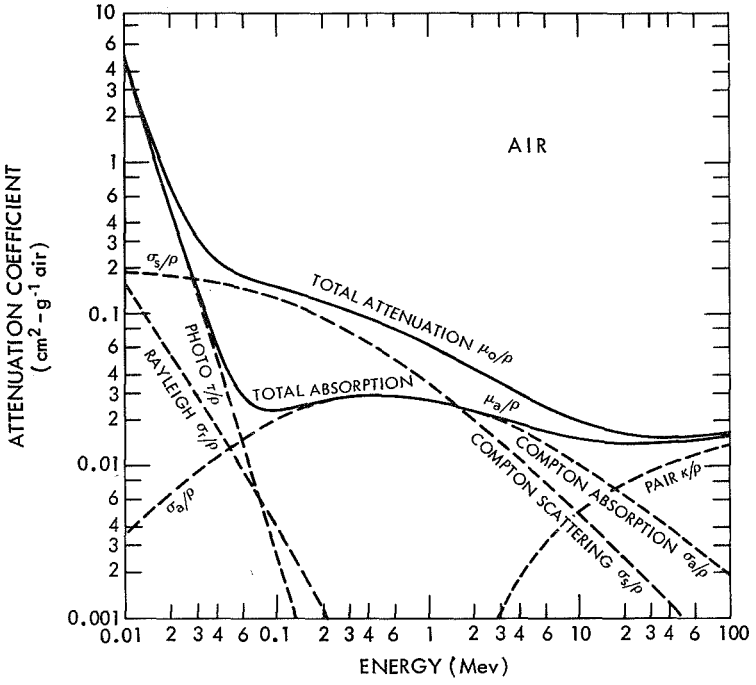

Figure 7–Mass attenuation coefficients for photons in air.
(Taken from Evans, 1955, p. 713.)

a function of energy. Since the atmosphere is about 1000 g-cm^{-2} thick, high-energy photons must traverse 25 mean free paths to reach sea level (probability of success $\sim e^{-25}$). Consequently we must design our instruments to be flown to the top of the atmosphere via balloons, rockets or satellites. This imposes restrictions on the size of the apparatus and on exposure time. It would be correct to say that the advances in gamma-ray astronomy have been restricted primarily by technological and financial restrictions on vehicles that can perform the experiments above the earth's atmosphere. Table 4 summarizes present-day limits of the three systems and typical costs of vehicle and experiments. Rockets, owing to the low area-exposure factor, are mostly useful for a small region of the spectrum at energies of a few MeV, where the expected intensity of gamma rays is higher. Satellites are ideal vehicles in this field, but, owing to their high cost, they have been used in only a few experiments. One of these, the OSO-3

Table 4. Area-Exposure Factor and Cost Comparison for Present-day Gamma-ray Experiments

Vehicle	Present day maximum area-exposure capacity (cm^2-sec)	Cost of vehicle ($)	Cost of experiment ($)
Rockets	10^5	10^4	10^5
Balloons	10^8	10^4	10^5
Satellites	10^{11}	10^6	10^6

experiment, has given the first definite evidence for galactic gamma rays above 100 MeV. The rocket and satellite experiments have the added advantage of being free from the secondary flux of undesirable gamma rays that still exist at balloon altitudes. On the other hand, balloons have been cheap and easy to come by. Historically, the brunt of instrument design and testing—as well as establishing valuable upper limits—has been borne by balloon-borne instruments; satellite models are generally streamlined extensions of these instruments.

GENERAL OUTLINE OF GAMMA-RAY-DETECTION PROBLEMS

The logical sequence of a typical gamma-ray detector is as follows: we start by providing a suitable medium in which the gamma ray produces the detectable charged secondary. Via a scintillator or comparable charged-particle detector, this secondary (or secondaries) is detected. Simultaneously, we require the status of an anticoincidence shield to assure the fact that the incoming primary was neutral. For events with proper signatures we may also measure the direction and energy of the primary more accurately.

Let us examine various parts of such a detection scheme.

Rejection of Charged Particles

Rejection of the incoming charged-particle primary flux is very important, since the charged particle flux is about 1000 times higher than the gamma-ray flux. Figure 8 illustrates various anticoincidence shields

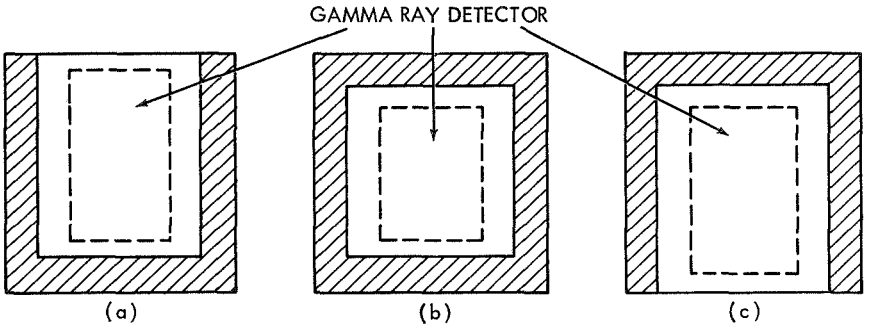

Figure 8–Various anticoincidence shield designs.

that may be used. The material of the anticoincidence shield should be transparent to gamma rays of interest (except when the shield serves also as a collimator) and be sensitive to charged particles. Thin slabs of plastic scintillator are well suited for this purpose. Configurations (a) and (b) (Figure 8) are used for low-energy gamma ray work, where the photon and its secondaries are completely absorbed in the photon detector. Configuration (c) is the sensible choice for high-energy photon detectors, because energetic secondaries of the gamma ray cannot be easily contained in the detector.

Signal-to-Background Considerations

Any gamma-ray detector is liable to detect undesirable events and fail to detect desirable events. In the case of balloon-borne detectors, the secondary flux of gamma rays produced at balloon altitudes constitutes one background impossible to differentiate from the true signal by using instrumental tricks. Consequently, the signals measured by balloon-borne detectors must be statistically above the secondary background. Figure 9 shows the gamma-ray intensity spectrum at balloon altitudes. The usual figure of merit possible to measure as a diffuse primary intensity is comparable to or more than the atmospheric secondaries. In the search for a discrete source of gamma rays, the other relevant parameter is $\Delta\theta$, the angular resolution of the apparatus. Assume that the experiment is exposed to a source of flux F_s with area A for time T and efficiency of detection ϵ. The total number of counts N_s recorded from the source will be

$$N_s = F_s \epsilon A T ,$$

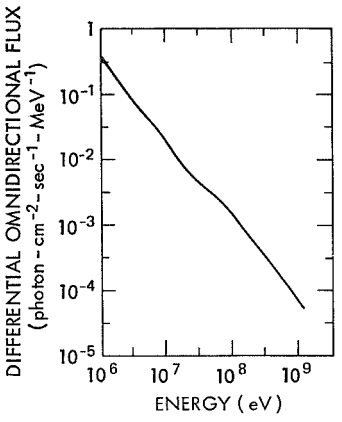

Figure 9—Atmospheric gamma rays at 3.5 g-cm^{-2} depth.

and most of these counts will come from an area of $\pi \Delta\theta^2$ in the sky, centered on the source. The number of background counts N_B in the same solid angle is

$$N_B = \pi \Delta\theta^2 \, I_B \, \epsilon \, AT \, ,$$

where I_B is the atmospheric background intensity (note that flux F_s is in CGS units of photons/cm^2 per sec, whereas intensity I_B is in units of photons-cm^{-2}-sec^{-1}-ster^{-1}).

The sensitivity of the telescope for a point source is given by signal-to-noise ratio S:

$$S = \frac{N_s}{\sqrt{N_B}} = \frac{F_s}{\Delta\theta} \sqrt{\frac{\epsilon \, AT}{\pi \, I_B}} \, .$$

To claim positive detection, S must usually be 3 or more.

The gamma-ray detectors have inherent angular resolution and detection-efficiency capabilities that depend on the process that produces the secondary. For Compton process, the inherent spread in a secondary electron's direction is large: about 20 degrees at an incident photon energy of 3 MeV (see Figure 4). Furthermore, the secondary electron scatters within the region of interaction. As a result, the detectors around this energy region achieve their angular resolution not by measuring the direction of the secondary but rather by using collimators that allow photons to enter only from a particular opening angle. Typically, these detectors have an opening angle and resolution of about 30 degrees.

Detectors that work in the pair-production region have distinct advantages: (a) the photon completely transfers practically all its energy to the electron-positron pair; (b) the electron-positron pair preserves the direction of the incident photon fairly well. The typical

separation between the pair is $\sim M_e c^2/E_{photon}$ which is about 0.3 degrees at 100 MeV. The actual angular resolution is limited by the multiple scattering of the electron-positron.

The electron-positron pair lends itself elegantly to track delineating detectors such as spark chambers or nuclear emulsions, where it is possible to detect the direction and energy of the gamma ray. The angular measurements with such instruments have achieved 1-degree resolution.

Aperture vs. Angular Resolution

Another important design factor in the design of gamma-ray telescopes is the angle of acceptance, called the aperture. In exploratory stages of the experiments it is desirable to scan wide regions of the sky and also avoid precise steering problems, while observing a likely source. In the case of low-energy photon detectors where a telescope system determines the angular resolution, the objectives of good angular resolution and wide aperture conflict with each other; this results in a compromise. The two objectives can be achieved simultaneously in the case of high-energy photon detectors with spark chambers or similar track-measuring devices.

Energy Measurements

The energy-measurement capability of the photon telescopes is an important design factor. The theoretical models can be differentiated also on the basis of spectral shapes. Low-energy detectors can absorb the total radiation of the incident photon and thereby achieve good energy resolution, typically $\Delta E/E \sim 10$ percent. At higher energies it becomes increasingly hard to contain the total secondaries initiated by the primary photon, owing to usual weight restrictions. Consequently, we must measure the energy by sampling the secondaries at various stages of development or by using multiple scattering methods on the electron-positron pair. These measurements are considered satisfactory if they achieve 40- to 50-percent resolution.

Dead-Time vs. Counting-Rate Considerations

A well designed gamma-ray detector should not "bite off more than it can chew." Biting, here, means accepting or triggering on gamma-ray-type events; chewing means storing away the data. If the average dead-time due to recording is τ and the rate of gamma ray events that

trigger the detector is R_γ, then the percentage of time that the detector can record the incoming events is given by

$$\text{Recording efficiency} = \frac{1}{1 + R_\gamma \tau} .$$

A detector with a dead time $\tau > 1/R_\gamma$ is operating inefficiently and not making use of its counting capacity or, effectively, its area. The same sensitivity in such case could be achieved by a smaller chamber at reduced cost and effort. Usually dead-time considerations are more important for large-area spark-chamber-type telescopes, where it takes about 1/10 second to obtain track-direction information.

Having indicated general points of concern in the design of gamma-ray detectors, we shall next investigate in detail a few representative detectors in the low- and high-energy regions.

Low-Energy Gamma-Ray Detectors

The representative gamma-ray detector we shall discuss for low-energy photons is one designed and constructed at Goddard Space Flight Center by Frost and Rothe. A schematic diagram is shown in Figure 10 Basically the detector is composed of a CsI (T_ℓ) crystal 1 inch in

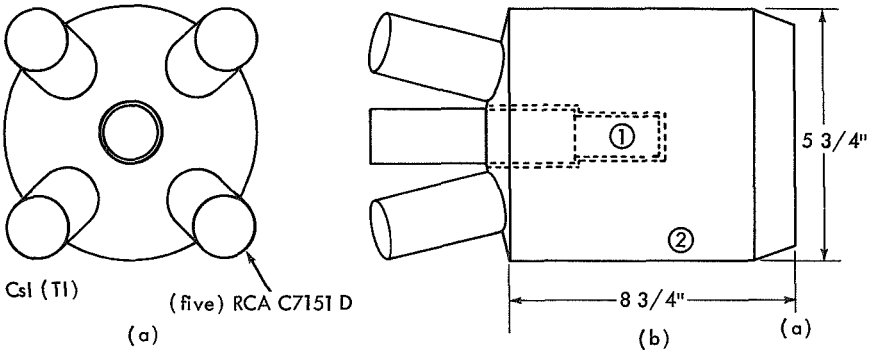

Figure 10–Collimated gamma-ray scintillation spectrometer for energy range 0.1 to 3 MeV. (a) Central CsI (T_ℓ) crystal, 1 inch in diameter by 2 inches long; (b) anti-coincidence CsI (T_ℓ) shield crystal for discrimination against gamma rays and charged particles and suppression of Compton continuum. (Taken from Frost and Rothe, 1962.)

diameter and 2 inches long, inserted into a hole drilled in a large CsI (T_ℓ) crystal operated in anticoincidence mode. The angular response of the detector to a Cs^{137} 0.662-MeV gamma-ray test source is shown in Figure 11.

Full width at half maximum is about 60 degrees. This detector is basically geared to detecting the gamma ray through the photoelectric effect, since this provides better energy resolution and more suitable detection geometry.

The efficiency of the detector was about 18 percent at 0.662 MeV and 13 percent at 1.28 MeV.

The rejection of charged particles is accomplished with the anti-coincidence crystal and by pulse-height analysis with the central detector. Most of the charged particles that come through the hole and stop in the central crystal give a pulse height above 3 MeV. Other ones that graze the central crystal are bound to give a pulse height in the anticoincidence shield.

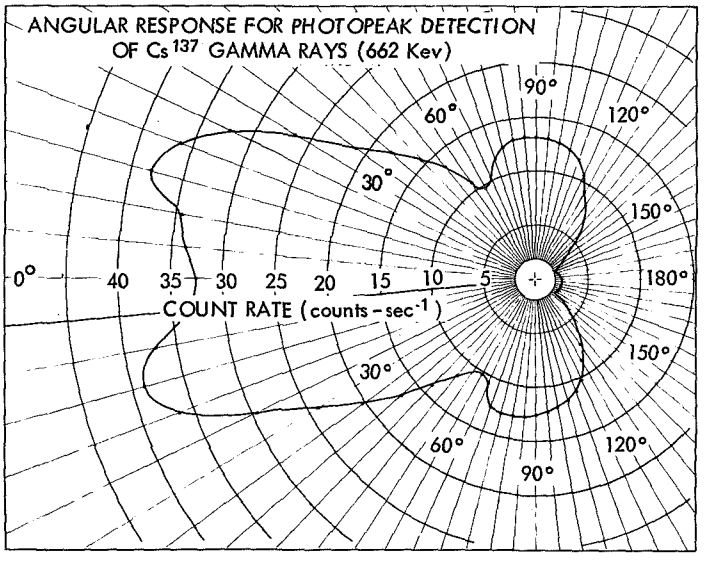

Figure 11–Angular response for photopeak detection of Cs^{137} gamma-rays (662 keV). (Taken from Frost and Rothe, 1962.)

The energy resolution for gamma rays was 19, 16, and 11 percent at 0.511, 0.662, and 1.28 MeV, respectively.

High-Energy Gamma-Ray Detectors

As we previously mentioned, gamma rays in the energy region above 10^7 eV interact mostly by pair production. Subsequently all the information about the photon resides in the pair. By actually tracing the pair's direction we can obtain good angular resolution. However, we shall start the examination of the detector systems with a counter telescope which, as we realize, does not use all the information available. On the other hand, as we also pointed out, the most significant data on gamma-ray photons to date has been obtained via a counter telescope flown on board the OSO-III satellite launched into orbit in March 1967. Since the satellite programs take a considerable time between design and launch, there is about a three-year phase lag between the state of experimental sophistication and actual data-yielding experiments; hence the simplicity of most significant gamma-ray experiments today.

OSO-III Gamma-Ray Detector

As was mentioned earlier, one of the most likely sources of high-energy photons is the decay product of inelastic proton-proton collisions:

$$p + p \rightarrow \pi^\circ + p + p$$
$$\pi^\circ \rightarrow \gamma + \gamma \ .$$

At higher energies, multiple pions and K-mesons could be produced. The π° mesons quickly decay into two photons

$$\pi^\circ \rightarrow 2\gamma \ .$$

The peak of the energy distribution of the photons is at $M_\pi C^2/2$,—namely, 70 MeV. Consequently, experiments have concentrated on this energy region. The OSO-3 experiment is one of these; Figure 12 is a schematic diagram of the detector used therein. The whole detector is surrounded by a three-piece plastic anticoincidence scintillator that vetoes charged-particle events. The trigger requirement for the detector is a pulse in the plastic counter under the CsI crystals, a pulse in the lucite

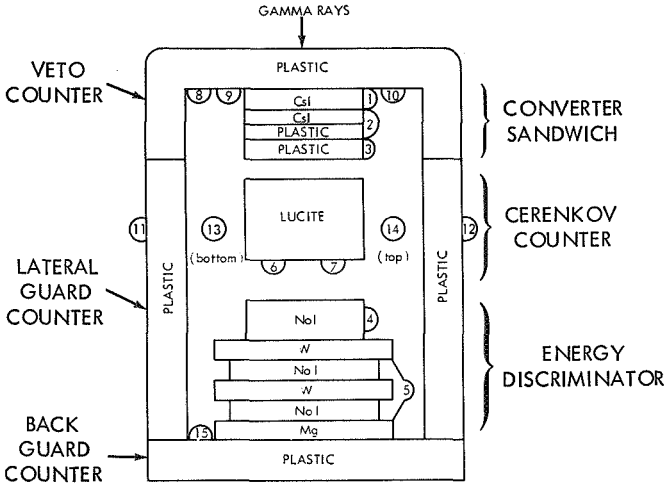

Figure 12–Schematic diagram of the OSO-III gamma-ray detector. (Taken from Kraushaar et al., 1968.)

Čerenkov counter, a pulse in the energy detector, and no pulses in the side and top portions of the anticoincidence shield. The converter sandwich at the top comprises CsI crystals, high-Z materials that provide sufficient radiation length to cause the high-energy photon to pair-production. The energy discriminator at the bottom comprises portions of NaI and tungsten that provide a small calorimeter to measure the energy of the incident photon. The trigger logic is designed for minimum signature of a downcoming gamma ray. Absence of a pulse in the top and side walls of the anticoincidence scintillator signifies neutrality of the particle; a signal below the CsI crystal signifies that the neutral produced a charged secondary; the directional lucite Čerenkov counter signifies that the incident particle was coming from above; an energy-calorimeter signal signifies that the photon is above the threshold of interest.

In portions of various counters of the telescope there is additional valuable information about the event. This information is recorded and used later during the analysis. There is an important experimental

philosophy here that should be made clear. In an exploratory experiment such as this—where the experimenter does not really know what to expect and is not there to modify the experiment while it is in progress—it is wise to lower one's standards of selecting events for recording to a point where one gets rid of most of the undesirable background but not necessarily all. The rest of the more stringent selection can then be done on the ground via computers where we can establish criteria by examining the results of various counter responses. Effectively this provides the choice of modifying the experiment after the experiment is over.

The rest of the information recorded is as follows:

a. Response of the top and bottom CsI crystal. This information gives, in a statistical sense, the mean free paths of interaction of the triggering particles. Thus we can determine what fraction of the triggers are caused by neutral primaries, such as neutrons, that have nuclear mean free paths.

b. Response of the different NaI crystals in the energy calorimeter. This sample of shower development at different depths helps to determine the photon energy.

c. Response of the bottom anticoincidence scintillator. This determines whether the gamma-ray secondaries have been contained in the energy calorimeter.

d. Response of the various parts of the anticoincidence guard counters of 1 to 3.5 microseconds and 3.5 to 10 microseconds, prior to the trigger. This information is useful in determining what fraction of the events may be due to freak events, such as a μ meson coming to rest in the converters and then decaying a few microseconds later after the veto pulse is over, or the electron produced in the $\mu^{\pm} \rightarrow e^{\pm} + \nu$ process simulating a gamma ray.

The compromise between angular resolution and a large geometrical factor has led to the following parameters: the geometrical factor is 5.6 cm^2-ster; the angular response falls to 1/e at 15 degrees.

The thickness of the CsI counters is 8.5 g/cm^2, which is 0.55 radiation lengths thick. The efficiency of triggering as a function of energy is shown in Figure 13. The falloff at higher energies is due to

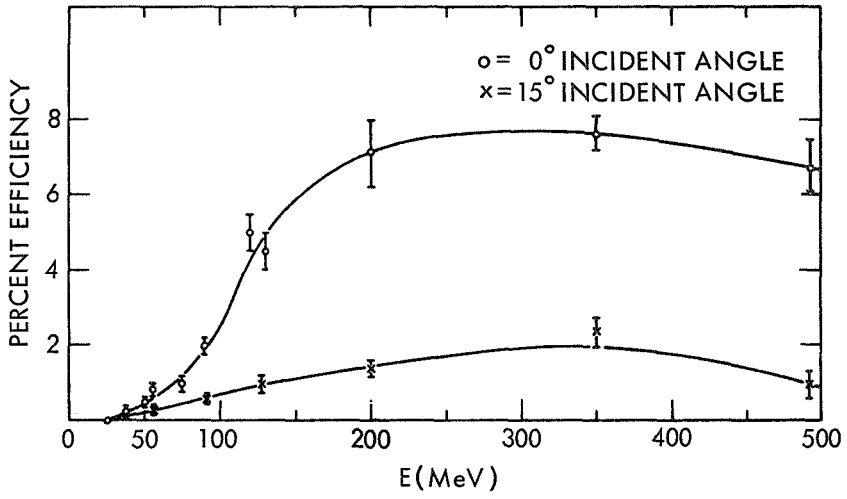

Figure 13–Detector response as a function of incident angle and energy. (Taken from Kraushaar et al., 1968.)

the secondaries produced by the apparatus spilling over to the side walls of the anticoincidence detector. The energy resolution of the instrument is about 100 percent at 100 MeV.

To obtain the direction of the gamma ray, we must also find the celestial-pointing direction of the telescope. This is done via magnetometers that measure the direction of the earth's magnetic field with respect to the apparatus. With the additional knowledge of the actual position of the satellite from the orbit data, the direction of pointing was determined to ±2-degree accuracy which is more than adequate for the 15-degree 1/e response of the detector.

Cornell University Photographic Spark-Chamber Telescope

This detector has been designed to be flown via balloon and search for discrete sources of gamma rays. Figure 14 shows a schematic drawing of the telescope. The detector consists of a 14- by 14-inch (1260 cm^2) spark chamber with twelve gaps 1 cm wide. The top and two adjacent sides of the spark chamber are surrounded by anticoincidence scintillators. The other two sides must be left open to take stereo pictures of the pair trajectories in the spark chamber. (See Appendix A for a general description of spark chambers.) The top two gaps of the chamber are below the top anticoincidence scintillator A but above the

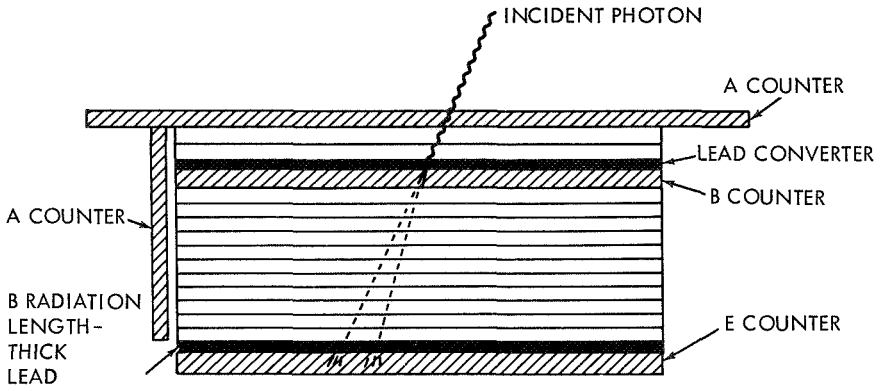

Figure 14–Cornell spark-chamber gamma-ray telescope.

one-radiation-length-thick lead converter. Absence of sparks in these gaps provides extra assurance that the incoming primary is a neutral. The trigger scintillator B, right under the lead converter, detects the signal due to the pair produced in the converter. The 3-radiation-length lead multiplier and a plastic scintillator beneath, at the bottom of the chamber, constitute an energy detector to select photons above 1 GeV. The coincidence signals between the B and E counters in anti-coincidence with A are used to fire a 10-kV high-voltage pulse to the spark chamber. Two right-angle views of the chamber are photographed on 2-mile-long film which continuously moves at 1-3/4 inch per second. The geometric factor for the detector is 1360 cm^2-ster. The aperture of the telescope allows the simultaneous viewing of the sky within 55 degrees from the zenith. Within this aperture the angular resolution of each gamma ray is 1 degree at 1 GeV. This resolving angle $\Delta\theta$ is inherently limited by the detection techniques of high-energy gamma rays. There are two conflicting objectives: (1) high efficiency of conversion, which requires material close to one radiation length thick; (2) to keep the electron and positrons from scattering too much (so as to preserve good angular resolution), which requires minimal radiation length in the path of electron and positron. As far as signal-to-noise ratio S is concerned,

$$S \propto \frac{\sqrt{\epsilon}}{\Delta\theta} ,$$

where ϵ is efficiency, and $\Delta\theta$ is angular resolution. Since $\Delta\theta \propto \sqrt{t}$, where t is radiation length, and $\epsilon \propto t$, S is independent of t as long as some

events are recorded. Consequently it is best to have about one radiation length of converter, so as to maximize the number of events. (The next detector to be studied will ullustrate how to resolve this conflict somewhat.)

The actual efficiency of detection was about 50 percent, which included the dead time as well as pair-production efficiencies.

The orientation of the chamber with respect to earth was determined by a camera taking pictures of the terrain below every 20 seconds.

A rough energy measurement was obtained from a measurement of E-detector pulse height.

This telescope achieved a sensitivity of about 10^{-6} photons/cm^2-sec for point sources.

To summarize, the advantages of a trajectory-measuring device such as the one discussed are as follows:

Good angular resolution,

Wide aperture, and

Possible visual discrimination against undesirable events.

The next spark-chamber gamma-ray telescope we shall discuss will be somewhat different.

Goddard Digitized Spark-Chamber Gamma-Ray Telescope

We have indicated the desirability of photon detectors around 100 MeV that are sensitive to π° gamma-ray production. As compared with the previously discussed Cornell telescope that was designed for 1 GeV, this lower-energy experiment must be designed with greater care in order to prevent the smearing of angular resolution due to multiple Coulomb scattering, since the scattering angle $\langle\theta\rangle$ is proportional to 1/E. The challenge is to preserve good angular resolution and still retain good conversion probability. This is accomplished by the use of fairly numerous thin conversion materials distributed over many gaps of the spark chamber. The directional information can be obtained before the pair has scattered too much. If the pair detection scintillator that verifies the conversion of the photon is placed below the multilayered conversion plates, a fairly high detection probability can still

be retained. This philosophy is further refined by a new generation of experiments where the conversion material consists of nuclear-emulsion stacks interspersed with the spark-chamber plates. The function of the spark chamber is to locate the position of the pair in the emulsion and give time resolution to the events. The emulsion then effectively provides a very large number of very thin conversion materials where the direction of the photons can be measured to closer than 1 degree.

The lower spark-chamber deck of the telescope is mostly used to measure the energy of the pair by a multiple-scattering technique developed extensively for nuclear emulsion work.

The schematic of the detector is shown in Figure 15. The heart of the detector, the spark chamber, is composed of 32 independent spark modules, each constructed from two orthogonal sets of 400 wires. The active area is 50 × 50 cm and the spacing between the grids is 4.0 mm. In contrast with the optical spark chamber previously discussed, this

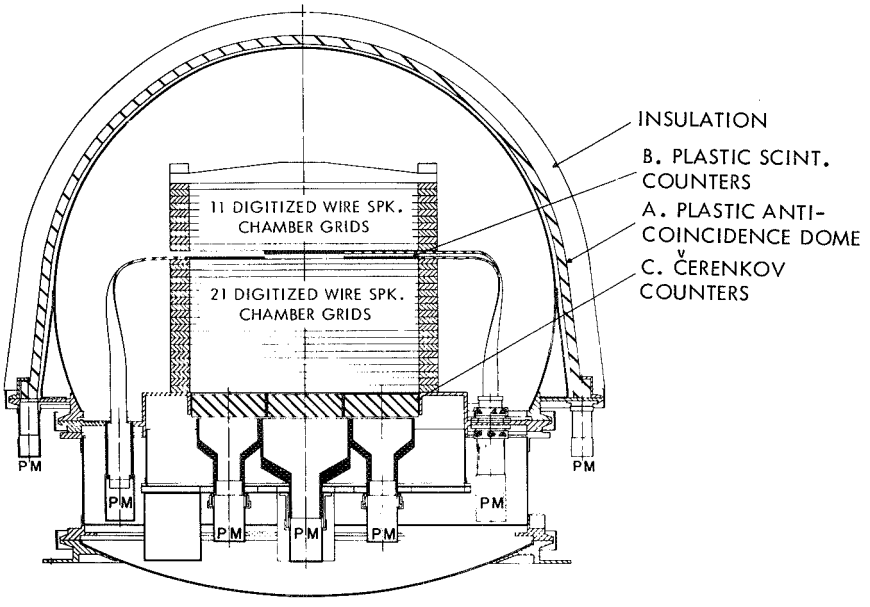

Figure 15–Schematic of 1/2 × 1/2-M digitized spark-chamber gamma-ray telescope. (Taken from Ross, et al., 1969.)

chamber records the data in a digital fashion. The initiation of a spark causes current to flow through the correct wires, "setting," i.e., changing the magnetic state of a little ferrite core threaded at the end of each wire, thus recording the coordinate of the spark. The advantages of such a spark chamber are:

a. The data is already in digital form, which greatly aids the reduction of the data that may amount to over 10^4 events in one single balloon flight.

b. It makes it possible to telemeter the information and dispenses with the necessity of recovering the payload, which makes it ideal for satellite work.

c. The amount of energy that must be dissipated into the spark to set these magnetic cores is less than that required to produce sufficient visible photons to record on film. Consequently the applied high voltage is reduced, which greatly helps the electronic noise-pickup problems.

d. The elimination of mirror systems around the spark chambers makes it possible to have a more compact detector with complete anticoincidence shield protection.

Stainless-steel conversion plates 0.03 radiation-length thick are included between each of the top eleven modules, comprising a total of 0.2 radiation length prior to the middle scintillator. The lower gaps have 0.02-radiation-length stainless-steel plates, used mostly to determine the energy of the electrons and positrons and hence the gamma rays.

The triggering telescope system for the spark chamber consists of plastic scintillator counters B that verify the conversion of the photon in the upper deck, and the Čerenkov counters C that define the geometry of the system and ensure that the propagation direction is downward. As usual, the anticoincidence dome covers the detector to prevent any charged particle triggering. Each counter layer plane is composed of nine equal area tiles used as a telescope with their vertical counterpart. This assures the rejection of the majority of events coming in from the sides of the spark chambers.

This detector has an angular resolution of about 2 degrees ~50 MeV (proportionally better at higher energies) and an energy resolution of

30 percent at the same energy (proportionally worse at higher energies). It is expected to have sensitivity close to 10^{-6} photons cm^{-2}-sec^{-1} for point sources at around 50 MeV and higher energies.

Bizarre Gamma-Ray Detectors

As has been indicated earlier, advances in the field of gamma-ray astronomy have been restricted by the existence of the absorbing atmosphere. However, scientific ingenuity has been able to perform experiments at sea level looking for cosmic photons by actually using the atmosphere as a part of the detector system.

Two distinct types of atmospheric detector will be briefly discussed.

Atmospheric Čerenkov Detectors for Gamma-rays

As a primary gamma-ray photon traverses the atmosphere it interacts with air molecules and produces charged secondaries which in turn emit Čerenkov light in the atmosphere. Owing to the collimation of secondary particles along the primary direction, and to the collimation of Čerenkov light along the direction of secondary particles, a light pulse of short time duration (several nanoseconds) striking the ground is incident along the direction of the primary photon with a spread of a few degrees. A typical detector for such photons would consist of a large-area mirror with a photomultiplier at the focus. As such detectors can only operate at night and even then are subject to the general night-sky background of starlight (about 5×10^{7} photons-cm^{-2}-sec^{-1}-$ster^{-1}$), depending on the size of the mirror used, there is a minimum detectable shower size. For example, a 5-foot-diameter searchlight with a 5-inch photomultiplier on the focus would be able to record showers above 7×10^{12} eV in energy, whereas a 2-foot mirror with the same 5-inch tube would be able to detect 5×10^{13} eV showers. In such a system the usual mode of operation is to point the telescope to a particular region of interest in the sky and look for excess of events. The dominant background for such a detector is the showers caused by the proton component of primary cosmic rays, and there is no clear-cut way of discrimating against these. However, it is possible to see a directional anisotropy if there is a sufficient number of photons coming from a source, as the proton background only constitutes an isotropic background.

The most advanced detector of this type is operated by the Smithsonian Astrophysical Observatory at Mt. Hopkins, Arizona. The detector shown in Figure 16 is a 10-meter mosaic of 248 hexagonal mirrors constituting a big dish. Typical energy threshold of this detector is around 10^{12} eV, and its background counting rate due to proton showers is about 300 per minute. Several nights of operation could detect fluxes as low as 10^{-10} photons cm^{-2}-sec^{-1}.

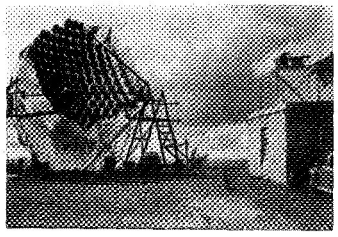

Figure 16—Smithsonian Astrophysical Observatory 10-meter gamma-ray telescope at Mt. Hopkins, Ariz.

Atmospheric Fluorescence Detector

As gamma-rays interact in the atmosphere, produce secondaries, and so on, energy is used up in ionizing and exciting the molecules of air. Similar to plastic scintillators, the atmosphere will fluoresce under the influence of ionizing radiation and emit visible photons. However, unlike Čerenkov light, the fluorescence process is isotropic and does not retain the direction of the primary. Owing to this fact, and its inefficient production the fluorescence radiation in an air shower is not as useful as the Čerenkov light in the detection of energetic photons. However, if it were possible to have a shower of photons that have been produced in a pulsed mode at the source itself through some astrophysical process, then the atmospheric fluorescence radiation would be ideally suited for studying it. There is indeed reason to expect short-time-scale (sub-millisecond) photon pulses of astrophysical origin. With the discovery of cosmic synchrotron radiation and its interpretation in terms of high-energy electrons trapped in the magnetic fields of exceptional objects like the supernovae remnants, the main problems of cosmic ray production has been shifted from slow statistical mechanisms to violent coherent acceleration processes that might take place in discrete sources such as supernova explosions or pulsars. While detailed calculations of acceleration processes in supernova explosions and pulsars are lacking because of insufficient data, both phenomena must be regarded as plausible cosmic-ray sources on the basis of available energy. Supernovae, with energy outputs of 10^{49} to 10^{52} ergs, constitute the most energetic discrete events in our galaxy. Pulsars, which now appear to be neutron stars formed in the core of supernovae, evidently have an energy content comparable to that of a supernova explosion. According to recent calculations of shock hydrodynamics,

a burst of energetic photons should accompany the cosmic-ray acceleration in supernova explosions. Regardless of the details of mechanism, it seems evident that relativistically exploding stellar plasma shells would emit short-time-scale electromagnetic radiation.

In the case of pulsars, the energy released in a single pulse is many orders of magnitude smaller than that from a supernova explosion. Besides the regular pulses, pulsars might undergo exceptional changes, such as the abrupt increase in the frequency of the Vela pulsar around the end of February 1969.

Work done on the phenomenon of atmospheric fluorescence, shows that the emission consists almost entirely of the N_2 second positive and the N_2^+ first negative band system of molecular nitrogen and that the bulk of the light that reaches sea level is in the wavelength band from 3200Å to 4500Å.

Atmospheric fluorescence will be induced by wide-band incident photon energies, ranging from high-energy photons produced in cascade showers down to soft X-rays and ultraviolet photons. The primary photons deposit their energy at different altitudes, depending on their energy. In addition, fluorescence efficiency is a function of pressure; consequently photons of different energy will have different fluorescence yields.

Figure 17 shows fluorescence efficiency and the absorption coefficient in air as a function of incident photon energy. For photons above 100 keV, the Compton and pair production processes dominate, depositing most of the energy around 20 to 30 km in altitude where the fluorescence efficiency is around 5×10^{-4}. For photons below 10 keV the photoelectric process dominates, causing the photons to deposit their energy at altitudes where the fluorescence efficiency is close to its limiting zero pressure value of 5×10^{-3}.

A wide-angle photomultiplier system, aimed toward the zenith, would collect fluorescence photons coming from a large region of the atmosphere. Consequently, the pulse shape observed by such a system would be broadened by the propagation time difference between various parts of the source region.

The maximum sensible energy range to search for such a pulse is between keV X-rays and gamma rays of a few GeV. Below this range,

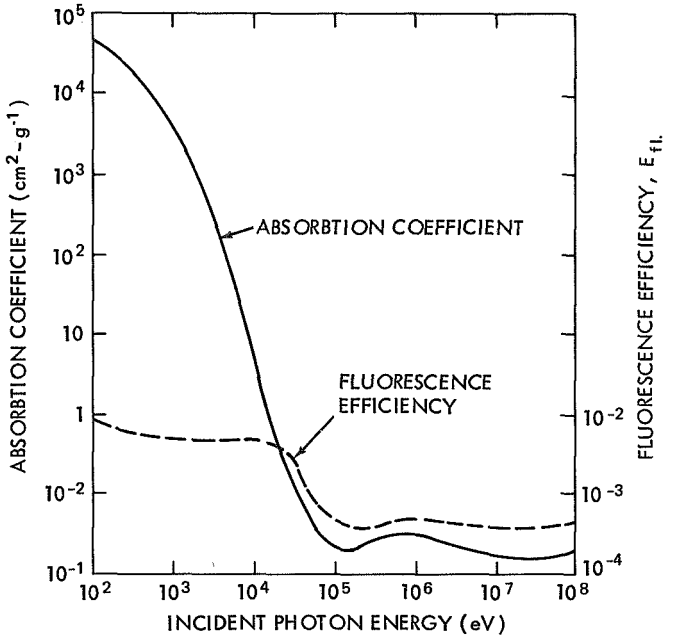

Figure 17–Absorption coefficient and fluorescence efficiency in the atmosphere as a function of incident photon energy.

the interstellar absorption limits the observable flux; above this range, Čerenkov light detectors or actual particle counters would be more efficient. Consequently, the interesting region of altitudes for fluorescence emission lies between 100 and 30 km, implying time scales of 300 to 100 microseconds, even for very short incident primary pulses.

To detect a pulse just described against the night-sky background, the threshold for detection should be such that the signal is greater than background noise fluctuations during the integration time τ_i of the detector electronics. Assuming that $\tau_i \geq \tau$, where τ is the length of the incident primary pulse, the total number of photoelectrons, S, produced in the photomultiplier is approximately

$$S \simeq \frac{AW\epsilon_{fl}\,\epsilon_{pm}\,\epsilon_t}{8\pi R^2 E_\nu}$$

where

A = area of photomultiplier,

W = energy in the primary pulse,

ϵ_{fl} = fluorescence efficiency of air,

ϵ_{pm} = photoelectron efficiency of the photocathode,

ϵ_t = total transmission efficiency,

R = distance to the source of primary pulse,

E_ν = average energy of the fluorescence photons.

The total noise N due to the omnidirectional night-sky background flux B during the integration time τ_i is

$$N \simeq BA\tau_i \epsilon_{pm} ,$$

and the signal-to-noise ratio is:

$$\frac{S}{\sqrt{N}} \simeq \left(\frac{A\epsilon_{pm}}{B\tau_i}\right)^{1/2} \frac{W\epsilon_{fl}\epsilon_t}{8\pi R^2 E_\nu} .$$

An estimate of the rate n of supernova events can be made by requiring that the signal-to-noise ratio exceed at least 5 for good confidence, and by assuming that galaxies are uniformly distributed with a density ρ_g, each with f supernova per unit time of energy W in energetic photons. The rate is then

$$n \simeq 10^{-3} \rho_g f \left(\frac{A\epsilon_{pm}}{B\tau_i}\right)^{3/4} \left(\frac{W\epsilon_{fl}\epsilon_t}{E_\nu}\right)^{3/2} .$$

Using the following estimated values:

$\rho_g = 5 \times 10^{-75}$ galaxies $(\text{cm})^{-3}$,

f = 1 supernova $(\text{galaxy})^{-1}$ $(100 \text{ years})^{-1}$
$(3.2 \times 10^{-10} \text{ sec}^{-1} \text{ galaxy}^{-1})$,

$$A = 500\ \text{cm}^2,$$
$$\epsilon_{pm} = 0.1,$$
$$B = 5 \times 10^7\ \text{photons/cm}^2\text{-sec},$$
$$\tau_i = 10^{-4}\ \text{sec},$$
$$W = 5 \times 10^{47}\ \text{ergs},$$
$$\epsilon_{fl} = 10^{-3},$$
$$\epsilon_t = 0.3,$$
$$E_\nu = 5 \times 10^{-12}\ \text{ergs},$$

gives a rate of one event per 18 hours, which should be easily observed.

Besides the night sky background fluctuations, there are other sources of real light pulses in the atmosphere such as lightning, meteors, aurora, Čerenkov light from air showers, as well as man-made signals including airplanes, airport beacons, etc. While there are ways of discriminating against such pulses locally, one of the most effective ways of eliminating this noise is to have an array of detectors separated by a few hundred kilometers and have accurate timing information. By our demanding a coincidence between widely separated events, local noise is eliminated. Furthermore, accurate timing of the relative arrival time of signals at separated stations can be used to determine the direction of the source.

At present, a pilot program is being carried out by the Goddard Space Flight Center's cosmic ray group, where two independent stations separated by 175 km are being maintained. One is located near Greenbelt, Maryland at the Goddard Space Flight Center's Optical Site, and the other is at the Fan Mountain Observatory of the University of Virginia in Charlottesville, Virginia.

Each station consists of the following equipment, as illustrated in the block diagram of Figure 18. Three photomultiplier tubes are housed in a weatherproof container with an automatic dome system to protect the tubes during the day. The tubes are all pointed toward the zenith. Two of them have transmission filters covering the useful fluorescence region between wavelengths of 3200 and 4300Å and are denoted by V_1 and V_2 (violet) in the subsequent discussions. The third tube has a filter with a lower wavelength cutoff of about 4300Å, which is effectively above the fluorescence emission bands. This tube is denoted by Y_3

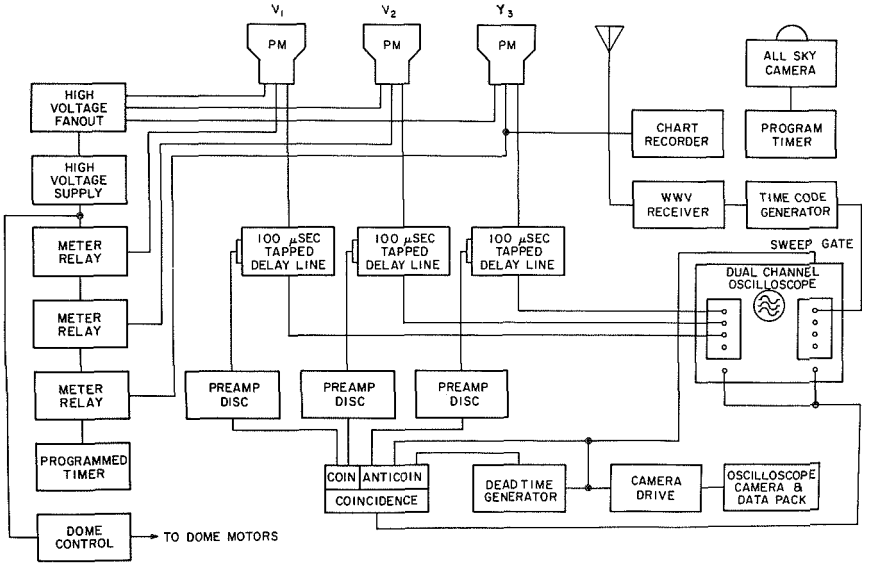

Figure 18–Block diagram of the experimental arrangement for a single station of fluorescence detector.

(yellow). This two-level spectroscopic information provides an extremely useful means of distinguishing various noise pulses from the type of pulses of interest.

Where there is sufficient signal in the photomultipliers, both beams of a dual beam oscilloscope are triggered. One beam, operated at a sweep rate of 100 μsec/cm is chopped between three inputs displaying the light-pulse shape from the 100-microsecond delayed output of each photomultiplier. The second beam of the oscilloscope is operated at a sweep of 0.1 sec/cm and contains a 36-bit NASA time code that gives the days, hours, minutes, and seconds in a serial code frame of one second. Using this time code, the time of the event can be read to a 10 millisecond absolute accuracy. A 35mm camera with an open shutter records the oscilloscope traces as they are swept. The preliminary results have encouraged further development of these ideas.

CONCLUSION

The diverse methods of gamma-ray astronomy discussed in these chapters reflect the large range of energies lumped under the term

"gamma rays." This grouping together is justified by the fact that all gamma rays are directional, that they are all connected with nuclear and high-energy processes, and that they should be prominent in exceptional objects. This causes the involved scientists to be familiar with the whole range and makes gamma rays a cohesive topic.

BIBLIOGRAPHY

Gamma-Ray Astronomy

Fazio, G. G., "Gamma Radiation from Celestial Objects," Annual Rev. Astron. and Astrophys., 5:481-524, 1967.

Garmire, G. and Kraushaar, W., "High Energy Cosmic Gamma Rays," Space Science Rev. 4:123-146, 1965.

Greisen, K., "Experimental Gamma Ray Astronomy" in Perspectives in Modern Physics, ed. by R. E. Marshak, New York: Interscience, 1966, p. 355.

Interaction of Gamma Rays

Davisson, C. M., and Evans, R. D., Revs. Modern Phys., 24:79-107, 1952.

Evans, R. D., "The Atomic Nucleus," New York: McGraw-Hill, 1955.

Ritson, D. M., "Techniques of High Energy Physics," New York: Interscience, 1961, pp. 1-53.

Rossi, B., "High-Energy Particles," New York: Prentice-Hall, 1952.

OSO-3 Gamma Ray Results

Clark, G. W., Garmire, G. P., and Kraushaar, W. L., "Observation of High-Energy Cosmic Gamma Rays," Astrophys. J. Lett, 153(3) Pt. 2:L203-L207, 1968.

Detectors Discussed in Text

Delraille, J. P., Albats, P., Greisen, K. I., and Ögelman, H. B., "Search for Point Sources of High-Energy Gamma Rays—The Photographic Spark Chamber," Canad. J. Phys., 46(10), Part 3:425-426, May 15, 1968.

Frost, K. J., and Rothe, E. D., "A Detector for Low Energy Gamma Ray Astronomy Experiments" in Proceedings of Eight Scintillation Counter Symposium IRE Trans. on Nuclear Science NS-9(3), 381-385, 1962.

Jelley, J. V., "Čerenkov Radiation and its Applications" (Pergamon Press, 1958).

Kraushaar, W. L., Clark, C. W., and Garmire, G., "Preliminary Results of Gamma Ray Observations from OSO-3," Canad. J. Phys. 46(10), Pt. 3:414-418, May 15, 1968.

Ögelman, H. and Bertsch, D., "Search for Short Pulses of Energetic Photons from Supernovae Using the Atmospheric Fluorescence," NASA Goddard Space Flight Center Document X-611-69-397, September 1969. (To be published in Acta Physica Hungarica.)

Ross, R. W., Ehrmann, C. H., Fichtel, C. E., Kniffen, D. A., and Ögelman, H. B., "A Gamma Ray Telescope Utilizing Large Area Wire Spark Chambers," IEEE Trans. Nuclear Sci. NS-16(1): 304-308, 1969.

Spark Chambers

Wenzel, W. A., "Spark Chambers" Annual Review of Nucl. Science, 14, 205, (1969).

Appendix A

SPARK CHAMBERS

Historically speaking, the spark chambers are a new addition to the other track-measuring devices such as emulsions and cloud chambers. Although the idea has existed since 1949, the useful form of the spark chamber emerged during the past decade. The rapid development in this technology is mostly due to the demands of high-energy accelerator experiments, although cosmic-ray experiments exploit the full advantages of the device. Figure A-1 illustrates the operation principle of a spark chamber. A counter telescope composed of two scintillators detects the passage of a particle via the coincidence circuit. Subsequently a spark gap (or some other type of fast, high-voltage switching device) is triggered; this grounds one side of the capacitor C which is already charged up to 10 kilovolts through resistor R_1. This causes the high voltage to appear on alternate plates of the spark chamber. The chamber is usually filled with some noble gas such as neon. The gas breakdown preferentially occurs at the points where the charged particle has left an ionized trail of electron-ion pairs. This avalanche

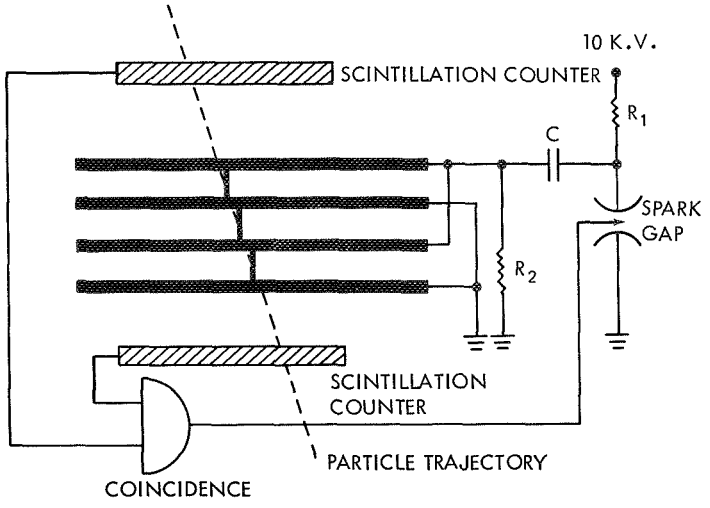

Figure A-1–Schematic diagram of spark chamber.

can be made to have enough light output for it to be photographed, enough sonic energy for it to be easily detected by microphones, enough charge flowing through it to "set" magnetic cores—provided that the plates are composed of fine-wire grid systems.

The time of discharge is of the order of 100 nanoseconds. The spatial resolution of the trajectory can be better than 0.5 mm.

Detection efficiency for a single particle is mostly limited by the number of ion pairs in the path. However, considering that in a typical noble gas such as neon there are 25 ion pairs per cm, it is easy to see that efficiency over 99 percent per gap is no problem. On the other hand, multiple-spark efficiency (i.e., probability that several simultaneous trajectories will all have sparks associated with them) is lower. This is primarily because some tracks will rob the discharge from the others.

The ion pairs produced in the chamber take about 10^{-5} to 10^{-4} seconds to recombine after the passage of the particle. In case high voltage is applied and there is a spark, the recombination time becomes tens of milliseconds. These times can be decreased by the application of a DC clearing field of about 100 volts. The clearing time of unsparked tracks (10^{-4} - 10^{-6} sec) determines the window of sensitive time of the chamber. By applying high voltage at the opportune moment one will pick up only events of interest. This sensitive time can be compared to the tens of milliseconds in cloud chambers. The recovery time (time to sweep away the spark discharge ions) can be as short as 10 milliseconds in accelerator experiments, although space applications do not need such fast recovery. The recovery time could be compared to the several seconds for cloud chambers.

IV. HIGH-ENERGY COSMIC-RAY DETECTORS

J. F. Ormes
NASA Goddard Space Flight Center
Greenbelt, Maryland

INTRODUCTION

As is well known, primary cosmic radiation consists of energetic corpuscular radiation containing electrons and nuclei from protons up to at least the lead-uranium region of the periodic table. The elements are completely ionized nuclei with energies extending up to 10^{20} eV, or 10^9 times as much energy as can be put into a single nucleus using man-made machines. Cosmic rays carry important astrophysical information which will supplement that carried by the electromagnetic spectrum.

In order to tap the cosmic rays for astrophysical information, we must first understand the particles themselves; so one of the primary aims of research of this type is to understand the origin and acceleration of the particles and their storage and propagation in galactic magnetic fields. In trying to answer these questions, we are dealing with some of the most energetic phenomena that take place in the universe.

When we turn more directly to astrophysics, the cosmic rays bring us the only sample of matter we are ever likely to obtain from outside the solar system, and as such they contain information about the composition of their source and about the thermonuclear reactions that take place there.

In addition, cosmic rays can provide energetic particles for use in high-energy nuclear physics. With the present levels of technology, only the simplest nuclear physics experiments can be performed using cosmic rays, owing to their low flux and the problems of high background. The earth-based colliding-beam experiment now being built at Cern will provide the equivalent laboratory frame energy of a 1600-GeV proton; beyond this energy, cosmic rays are the only available beam.

Direct measurements of cosmic rays have been made until recently in the energy range 100-2000 MeV using ionization loss counters (dE/dx: employing scintillators, ion chambers, proportional counters, solid state

counters, nuclear emulsions, etc.), Čerenkov counters, and range or total-energy devices.

In Chapter I, the devices used at energies below 200 MeV/nucleon have been discussed. We shall now consider applications at higher energy. In fact, since the earth's magnetic field has been successfully used as a spectrometer in the range 2-10 GeV, we are primarily interested in the energy range 10 GeV to $\approx 10^5$ GeV. The energy range 200-2000 MeV has spawned many of the techniques to be used at higher energies. Since this range is not specifically covered elsewhere in this course, we shall briefly consider some applications from lower energies.

The upper limit of 10^5 GeV is not set by techniques but by statistics. In principle, at least, most of the techniques to be described for use in this range would work regardless of particle energy. This statistical limit serves to emphasize the major experimental constraint that must be satisfied. Large geometrical factors and long collection times are prerequisites for obtaining statistically meaningful results.

Before considering specific techniques let us remind ourselves of the principal characteristics of what we wish to measure. All components of the radiation have energy spectra in this range that can be written in the form $dN/dE = k/E^{+\gamma}$, with $\gamma \approx 2.6$. The integral spectra are then given by $N(>E) = k/(\gamma - 1)\ (E^{\gamma-1})$. Table 1 lists the principle cosmic-ray components and gives the relative intensity for each. The first column gives the differential intensities of various cosmic-ray components at 1 GeV. The exponent at this energy is typically 1.5, steepening to 2.5 at 10 GeV. The integral spectra are presented in the second and third columns. The estimates of $\gamma - 1$ are very crude at this time and should be used as rough estimates. The data on charge composition comes from geomagnetic cutoff measurements and from a measurement using a gas Čerenkov detector. The proton fluxes shown in parentheses are from the Russian Proton series of satellites. The differences in $\gamma - 1$ shown in the last column are probably not outside experimental error, although the possible significance of the trend with increasing Z should not be overlooked. The first column shows the individual ratios of the nuclei that comprise a given group.

The early data available on the electron spectrum are shown in Figure 1. Of crucial interest in this spectrum is the question: is there a bend or change of slope above a few GeV where one is sure to be free of

Table 1. Cosmic-Ray Intensities

	Differential intensities dN/dE (1 GeV) (particles-m^{-2} $ster^{-1}$ sec^{-1} GeV^{-1})	Integral spectrum N (>10 GeV) (particles-m^{-2} $ster^{-1}$ sec^{-1})	$\gamma - 1$
Electrons	30	2.5	$\approx$1.65
Protons	1000	180 (9×10^2)	1.6 (1.85)
Helium	100	10	1.54
L nuclei Li, Be, B	1.8 0.3:0.2:0.5	0.12	1.56
M nuclei C, N, O, F	6.5 0.45:0.13:0.41:0.009	0.5	1.51
LH nuclei $10 \leq Z \leq 19$	1.8	0.15	1.47
VH nuclei $20 \leq Z \leq 29$	0.6 F/VH = 0.4	5×10^{-2}	1.40
te group			
All $Z > 30$		(rough estimate) 2.5×10^{-5}	

solar modulation effects? The change in slope is related to the lifetime of cosmic rays against synchrotron and inverse Compton-energy losses. Existing data do not yet provide an answer. (More recent data have confused, rather than clarified, the situation.)

At present, practically the only results on the high-energy proton spectrum are due to the Russian satellite work (see Grigorov et. al., 1967, 1969). These results and those at higher energy from air shower work are shown in Figure 2. There is little charge composition information in this range. The direct measurements available show the same charge composition as has been determined at lower energies and discussed in Chapter I by Dr. Gloeckler. Some air-shower measurements on multiple-core showers indicate that above 10^{15} eV the composition is the same as that at 1 BeV. However, the Russian work suggests that the heavy nuclei (all nuclei heavier than protons are lumped) increase in proportion to protons between 10^{12} and 10^{14} eV. The only other work (an

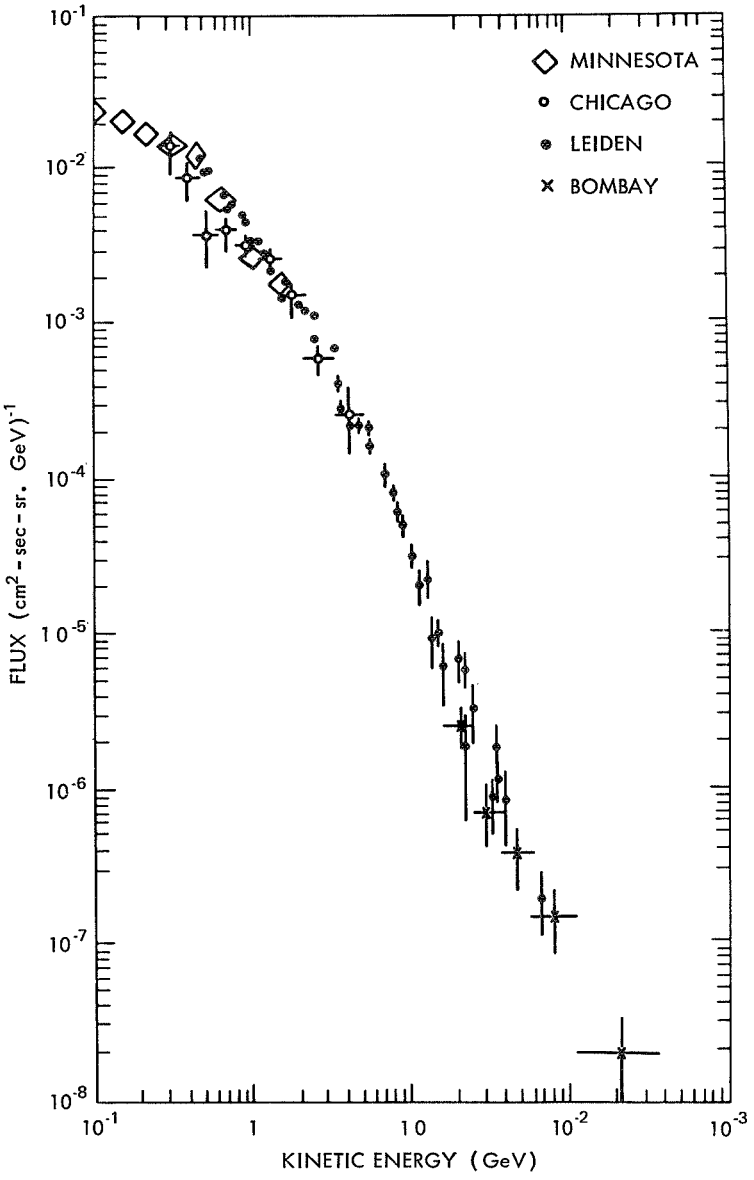

Figure 1–The differential energy spectrum of primary electrons as of 1968. (Taken from Ögelman and Wayland, 1969.)

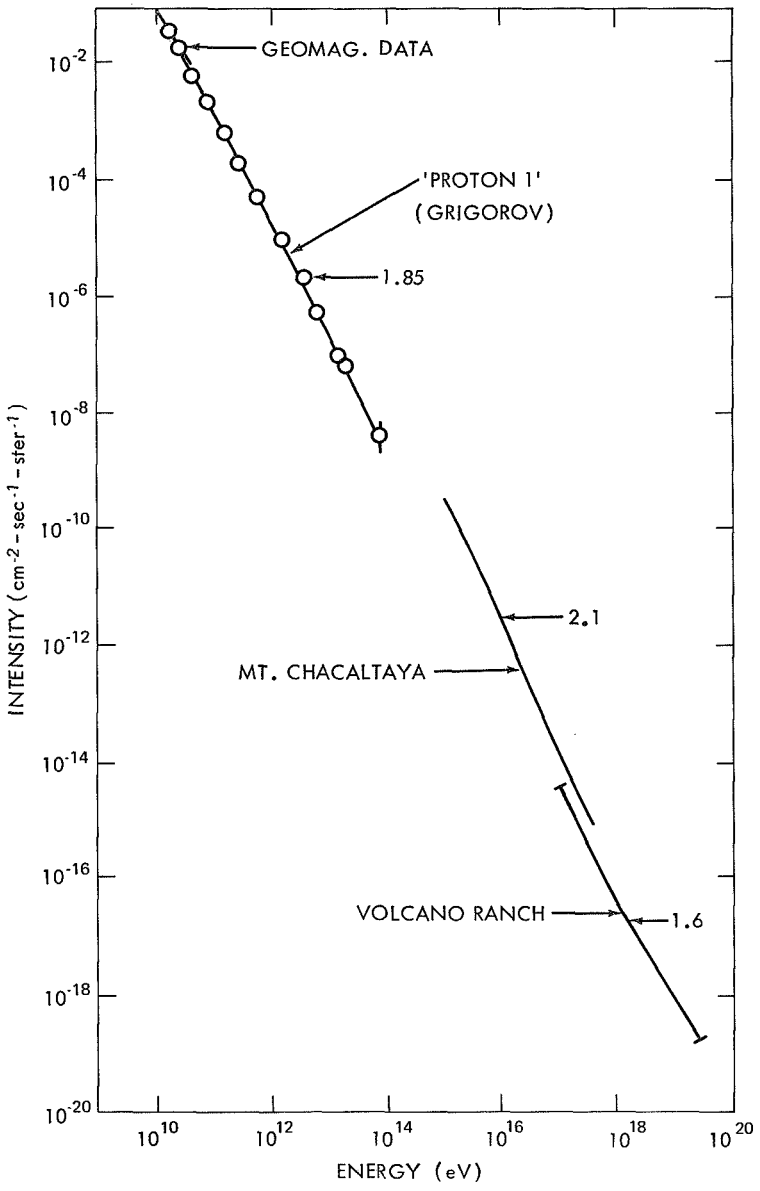

Figure 2–Integral energy spectrum of primary cosmic-ray protons over 10 orders of magnitude.

international collaboration called the "Brawley Stack" in which high energy nuclear interactions called jets are looked at in emulsions) suggests the opposite, i.e., that heavies are decreasing in proportion to protons in 10^{12}-eV range.

We can now consider an example of how we are limited by statistics. Suppose we wish to collect 100 iron nuclei at 10^{13} eV. There are 0.4 iron nuclei for every very heavy nucleus and there are 5×10^{-2} VH/m^2 ster sec (from Table 1). Thus,

$$0.4 \frac{\text{Fe}}{\text{VH}} \left(5 \times 10^{-2} \text{ VH/m}^2 \text{ ster sec}\right)_{10\,\text{GeV}} \left(\frac{10^{10} \text{ eV}}{10^{13} \text{ eV}}\right)^{1.5} \times 3 \times 10^7 \text{ sec/yr}$$

$$\times\ 2\ \text{Fe/m}^2 \text{ ster yr} = 50\ \text{m}^2 \text{ ster yr}$$

to collect 100 Fe nuclei.

Typical low-energy detectors that have been flown on satellites in the past have had collection factors of a few cm^2 ster years.

In order to determine the properties of the cosmic radiation above 10 GeV we must determine each particle's charge, energy, and mass. We will consider the determination of each of these observables in turn and shall end with a description of some of the devices now being used.

CHARGE MEASUREMENTS

Ionization Losses

Charged particles lose energy by ionization. The ionization loss is given by the familiar Bethe-Bloch formula recently derived by Dr. Gloeckler. We write it in the following form:

$$\frac{dE}{dX_{ave}} = \frac{-kZ^2}{\beta^2} \left[\ln \frac{4 m_e^2 c^4 \beta^4}{\left(1-\beta^2\right)^2 I^2(Z)} - 2\beta^2 - \delta \right], \qquad (1)$$

where $k = 2C m_e c^2$ is a constant including the density of electrons in the medium, while $C = 0.15$ Å/Z, and $I(Z)$, the ionization potential, are properties of the target material, and δ is the density-effect correction which will be considered later.

The range of a particle of energy E is given by

$$R = \int_E^0 \frac{1}{\left(\frac{dE}{dx}\right)_{ave}} dE . \qquad (2)$$

In a thin counter this energy loss is subject to statistical fluctuations known as Landau fluctuations. A whole distribution of possible energy losses is available to a particle as it collides with individual electrons. These fluctuations determine the ultimate resolution of any counter. The "worst case" distribution for a singly charged particle through a thin detector is known as a Landau distribution and is shown in Figure 3.

The long tail on this distribution is caused when a large amount of energy is transferred to a single electron. Typical energy losses in a

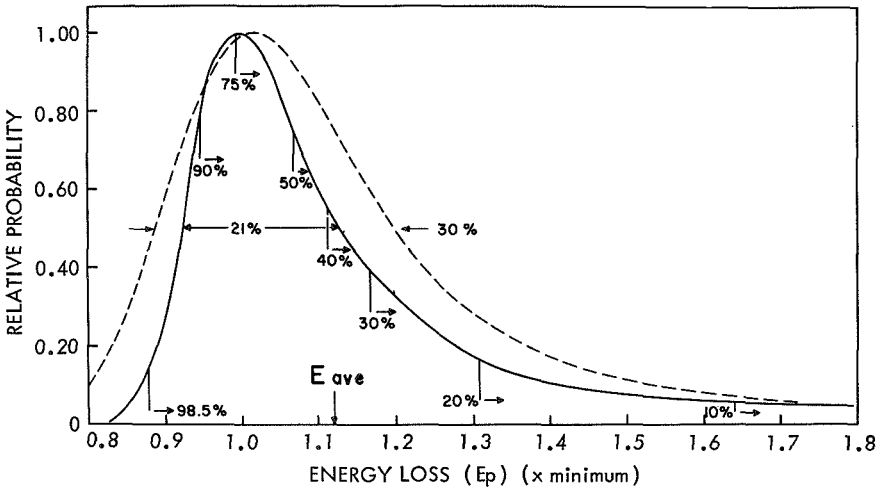

Figure 3–Solid line represents a Landau distribution in energy loss for relativistic singly charged particles in a thin detector. Dashed line is this Landau distribution convoluted with a Gaussian distribution with 20-percent full width at half maximum. E_{ave} comes at the point indicated on the scale for both curves. Note that the most probable energy has moved relative to E_{ave} in the convoluted distribution.

1 g-cm^{-2} thick layer are 1-2 MeV for minimum ionizing singly charged particles. The maximum transferable energy can be formed from the following derivation:

Particle Mass	Particle Momentum	
	before	after
m	p	p''
m_e	0	p'

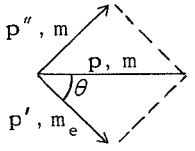

$$\vec{p} = \vec{p}' + \vec{p}''$$

Conservation of energy gives

$$\sqrt{p^2 c^2 + m^2 c^4} + m_e c^2 = \sqrt{p''^2 c^2 + m^2 c^4} + E' + m_e c^2 .$$

Conservation of momentum gives

$$p''^2 = p^2 + p'^2 - 2p p' \cos\theta .$$

Eliminate p''; set $\cos\theta = 0$ for E'_{max}:

$$E_m' = 2 m_e c^2 \frac{p^2 c^2}{m_e^2 c^4 + m^2 c^4 + 2 m_e c^2 \left(p^2 c^2 + m^2 c^4\right)^{1/2}}$$

for protons, etc. with $m >> m_e$ and large momenta $p/mc >> m/m_e$,

$$E_m' = pc .$$

For $m >> m_e$, with small momenta $p << m^2 c/m_e$,

$$E_m' \approx 2 m_e c^2 \left(\frac{pc}{mc^2}\right)^2 = 2 m_e c^2 \frac{\beta^2}{1-\beta^2} . \qquad (3)$$

For minimum ionizing particles, $\beta \approx 1$, $\gamma \approx 3$, and so $E'_{max} \approx 9$ MeV. Thus the transfer of a large amount of energy to a single electron can cause a large fluctuation in energy loss. These high-energy electrons are called knock-on electrons.

As the energy loss in a given detector increases, the distribution becomes less asymmetrical. This is simply because a single collision can no longer dominate to the same extent.

The curve for any given case may be determined by the method outlined in Rossi (1952). The peak of these distribution functions, called the most probable energy losses, are given by

$$E_p = \frac{AZ^2}{\beta^2}\left[\ln\frac{AZ^2}{\beta^2} + \ln\frac{2m_e c^2\beta^2}{I^2(Z)\left(1-\beta^2\right)} - \beta^2 + j(\beta, Z) - \delta\right]. \quad (4)$$

Here $j(p, Z)$ is a small correction term, which ensures that as the fraction of energy lost to ionization approaches 1, Ep becomes

$$\int \left(\frac{dE}{dx}\right)_{ave} dx .$$

Note especially the term containing the $\ln Z^2$. This makes the most probable ionization loss increase faster than Z^2.

Note that Equation 1 contains the term $\ln\gamma$, where $\gamma = 1/\sqrt{1-\beta^2}$. This could be used as a measure of energy except for the so-called density effect. Equations 1 and 4 are derived on the basis of isolated atoms. At large energies the more and more distant collisions become important, and a particle interacts with more than one atom at a time. The net result of this correction is to reduce the energy loss at high energies, preventing the ionization loss from increasing as fast as $\ln\gamma$. However, in gases where the density is low the $\ln\gamma$ dependence does hold up to $\gamma \approx 100$. Nevertheless, in practice it is difficult to obtain sufficient energy deposit using gases to overcome the problem of the Landau fluctuations in a measurement of this type.

Since $\beta \approx 1$ for all particle energies under consideration here, dE/dx in principle can be used to determine particle charge uniquely. Turning now to specific ionization detectors, we must bear in mind that we need a large sensitive area, 2500 cm^2 at least.

Organic scintillators would be ideal but for their nonlinear response. The light output from a given scintillator can be written as

$$\frac{dL}{dE} = \frac{k \frac{dE}{dx}}{1 + A \frac{dE}{dx} + B \left(\frac{dE}{dx}\right)^2 + \cdots} . \tag{5}$$

An example is shown in Figure 4. This nonlinearity varies from one batch of scintillators to the next and from type to type and so must be determined for any sample. The net effect is that above $Z \approx 10$ the light increases as Z rather than Z^2, making resolution of adjacent charges much more difficult. Plastic has the enormous advantage that it can be easily constructed in any shape, and large areas present no

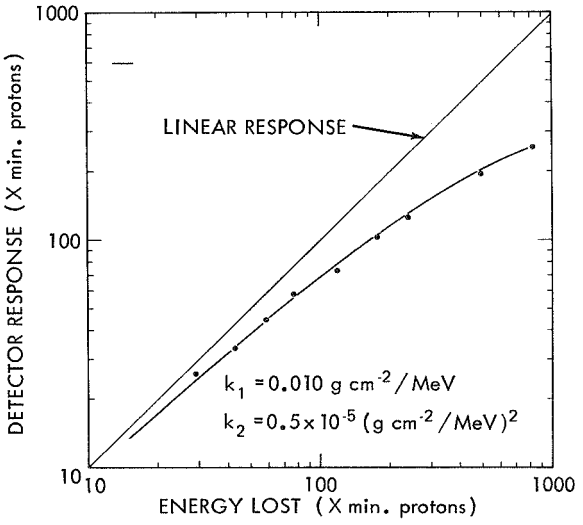

Figure 4–Nonlinear response of plastic scintillator. The light response of the detector does not increase as fast as the energy loss.

construction problems. Plastic light guides can easily be utilized with them; so ample light is available for most purposes from a 1-cm-thick piece.

Inorganic scintillators such as CsI are much slower, but have linear response over a much larger dynamic range. This makes them desirable for studies in the range Z = 10, 30. The larger light yield of inorganic over organic scintillators is difficult to take advantage of because we cannot permanently bond plastic light guides to inorganic crystals. A great disadvantage is that crystals larger than 25 cm in diameter are difficult to grow; so large areas must be achieved by mosaic techniques.

Proportional counters of very large area are difficult to build because of the uniformity in electric-field configuration that must be maintained. However, for extremely heavy nuclei, e.g., $Z \geq 30$, sufficient ionization is available, so that gas-filled counters can be operated in the ion-chamber mode where the resolution problem is much simpler. All that is required is good ion-pair collection efficiency throughout the volume of the counter. For these high-Z particles, enough ion pairs are produced to ensure that statistical fluctuations do not affect charge determination. Because of the very low mass content of gas-filled counters, multiple samplings can easily be taken with a very thin detector. Multiple samplings can greatly improve the resolution by effectively tracing the Landau fluctuation curve. With multiple samplings from gas-filled counters, it may eventually be possible to determine particle energy through the $\ln\gamma$ term.

Emulsions in which ionization tracks can be permanently recorded have been used for charge composition studies. They have the great advantage of providing accurate positional information. Large areas can be constructed and were used for the first positive identification of super heavy nuclei in cosmic rays. However, fine resolution is difficult and large statistics are difficult to achieve because of the tedious scanning process involved.

This completes the discussion of ionization devices for making charge measurements.

Čerenkov Radiation

Another valuable tool in charge measurements is Čerenkov radiation. This phenomenon was discovered by P. A. Čerenkov in 1937 and has found wide experimental use at high energies.

A charged particle in rectilinear motion in free space not being accelerated does not radiate. However, if the particle enters a dielectric medium in which the particle velocity exceeds the phase velocity of light, Čerenkov radiation is emitted. It involves a co-operative phenomenon in which large numbers of the atoms of the medium are involved. The radiation itself is caused by the acceleration of the particles of the medium in the electric field of the passing particle. The relativistically distorted field tends to polarize the atoms of the medium in an asymmetrical way such that they emit dipole radiation as the particle passes. A simple Huyghens construction will give us the condition for emission. This is shown in Figure 5.

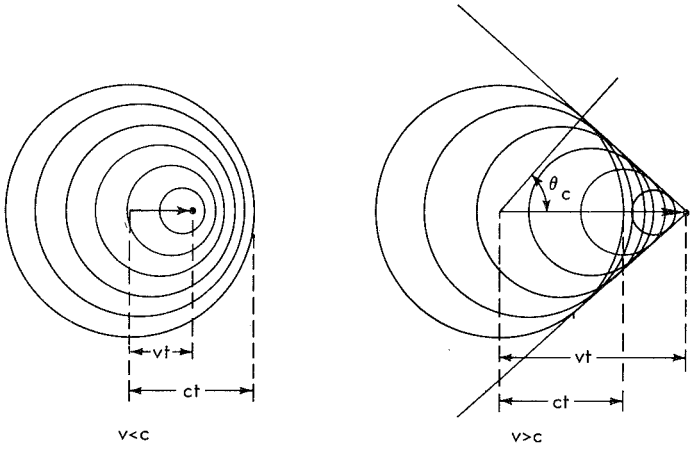

Figure 5–Čerenkov radiation. Spherical wavelets of fields of a particle traveling at less than, and greater than, the velocity of light in the medium. For v > c an electromagnetic shock wave appears, moving in the direction given by the Čerenkov angle θ_c. (Taken from Jackson, 1952, page 494.)

$$vt \cos\theta = \frac{ct}{n}, \qquad \cos\theta = \frac{c}{nv} = \frac{1}{\beta n}, \tag{6}$$

where n is the index of refraction of the material.

This immediately implies that the condition for emission is $1/\beta n \leq 1$ and that cos > 1 corresponds to the situation in which there

is no constructive interference. Table 2 gives values of n for various substances.

Table 2. Refractive Indices of Various Materials

Material	Index of refraction
Lucite or Plexiglass	1.5
Sapphire	1.8
Glasses	1.4 1.95
Water	1.33
Titanium dioxide	2.7
Diamond	2.42
Air	1.00029 at STP

The energy radiated per unit frequency per unit path length is given by

$$\frac{d^2 E(\omega)}{d\omega\, dx} = \frac{Z^2 e^2 \omega}{c^2} \left(\sin^2 \theta\right) . \qquad (7)$$

At $\theta = 0$, emission becomes 0. As $\beta \to 1, \cos\theta \to 1/n$ and θ_{max} is reached.

The high directionality of the radiation is very useful. It can be used to discriminate against backward-moving particles in some cosmic-ray detector schemes. In well-defined particle beams it can be used as a velocity selector.

The threshold can be used to separate particles of different mass at the same momentum. For example, gas Čerenkov detectors with indices of refraction $n = 1 + k$ (where $k = 3 \times 10^{-4}$) can separate high-energy protons from high-energy electrons.

$$n = 1 + k$$

$$\beta_{t_{threshold}} = \beta_t = \frac{1}{1+k} \approx 1 - k$$

$$\gamma_t = \frac{1}{\sqrt{1-\beta_t^2}} = \frac{1}{\left[1-\left(1-2k+k^2\right)\right]^{1/2}} \approx \frac{1}{\sqrt{2k}} \approx 40 ;$$

$$E_{electron} = 20\,MeV, \qquad \text{while} \qquad E_{proton} \approx 40\,BeV .$$

Note that k is a function of density, so the threshold can be varied by varying the pressure of the gas. The threshold is also a function of temperature too, which can be a problem in some applications.

The light levels involved in Čerenkov radiation tend to be quite low. The number of photons N is obtained from Equation 7 by dividing by the energy of a photon. Thus,

$$\frac{d^2N}{d\lambda\,dx} = \frac{1}{137}\frac{Z^2}{\lambda^2}\left(1-\frac{1}{(\beta n)^2}\right) . \tag{8}$$

Integrating over the useful range for photo-multiplier tubes (typically 3500-5500Å) and taking the maximum emission ($\beta = 1$) for $n = 1.5$ yields

$$N = 300\,Z^2 \text{ photons } gm^{-1}\ cm^2 . \tag{9}$$

These low light levels require the use of long paths and good collection geometries. They also mean that any small contamination of latent scintillation light can be a serious problem.

At high energies, the Z^2 dependence of the radiation can be used for charge-composition studies ($\beta \approx 1$ for all particles). Until recently most solid Čerenkov detectors have been restricted in size to photo-multiplier cathode areas. Coupling radiators directly to the photo-multiplier windows (in some cases the windows themselves have been used as radiators) has achieved the essential good photon collection efficiency.

The advent of adiabatic light guides has partially freed one from this restriction. These are strip light guides which map a detector

area to be viewed onto the face of a photo-multiplier tube (see Figure 6). They are adiabatic in the sense that there are no sharp bends, so that total internal reflection is preserved. (The condition for adiabaticity is that the radii of curvatures be much greater than the dimensions of the strip. One can convince oneself that this is so by considering some simple ray diagrams.) These represent a definite improvement over the old tapered light guides. In these, light has to fight its way "upstream" in one of the dimensions even though the flow is downstream in the other (see Figure 7). Using adiabatic light guides, Čerenkov detectors much larger than photomultiplier tubes can be used. However, because the highly directional light is collected by total internal reflection, there are large variations in the fraction of light collected. These are variations with incident angle and with particle velocity (if one wishes to go below $\beta \approx 0.95$).

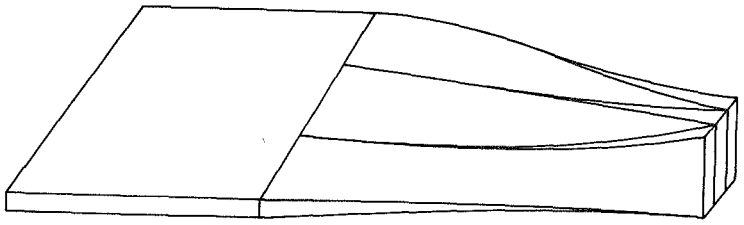

Figure 6–Adiabatic light guide. Area of edge of detector is mapped onto face of a photomultiplier tube. It is adiabatic in the sense that all radii of curvature are large compared with the thickness of the strip.

Another interesting phenomenon closely resembling Čerenkov radiation may prove useful in the future. It is called transition radiation because it is radiation emitted as a particle passes from one medium to another with a different dielectric constant. The radiation is exceedingly weak, but it has been detected in the visible range by Dr. Yuan at Brookhaven. In the X-ray range it can be detected by anyone with some IBM cards and some film. Place a film under a stack of IBM cards. The layers of air and paper provide the transition layers which should produce the transition radiation from sea-level muons necessary to blacken the film. A control film with the equivalent matter but without air gaps and another with nothing above it should be unblackened. The electromagnetic nature of this radiation makes it proportional to Z^2. However, there are still problems to overcome, because the probability of obtaining an optical photon from a single interface from a singly charged particle is about 10^{-3}. The visible radiation is proportional to $\ln \gamma$.

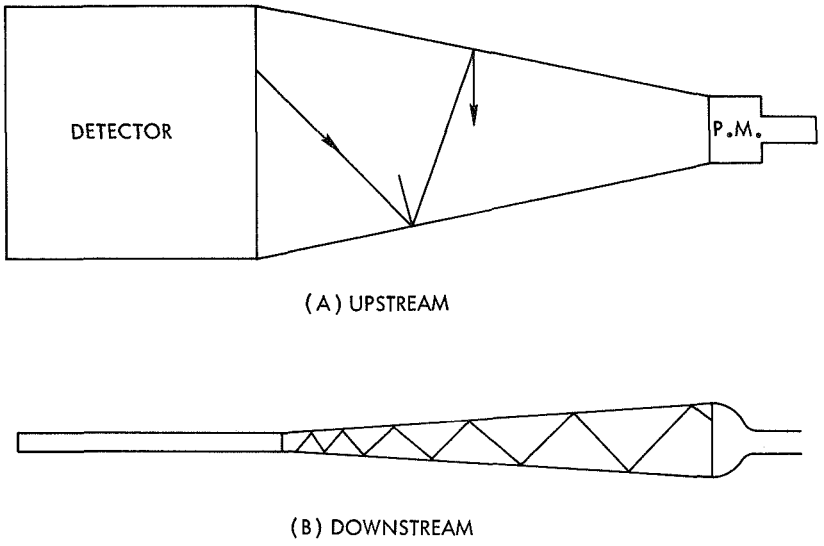

Figure 7–Transmission by total internal reflection frustrated by converging and aided by diverging geometry.

RESOLUTION AND BACKGROUND

The ultimate success of any cosmic-ray charge-composition experiment depends upon its charge resolution and ability to discriminate against background events. The intrinsic resolution of a detector is determined by the Landau fluctuations. Other factors that contribute to the resolution are affected by experimental design. The efficiency with which photons are collected, for example, affects any variations due to statistical fluctuations in the production of photoelectrons. Variations in path length and in collection efficiency as a function of position over the detector area will contribute to the resolution.

Figure 8 shows the differential geometric factor as a function of path-length in a detector. Most path lengths are near the minimum because $\cos\theta$ varies slowly near 0 degrees, but there is a significant tail at large path lengths. This problem does not exist for detectors used in accelerator beams but does exist for isotropic cosmic radiation. This tail strongly affects the ability to separate adjacent charges. For

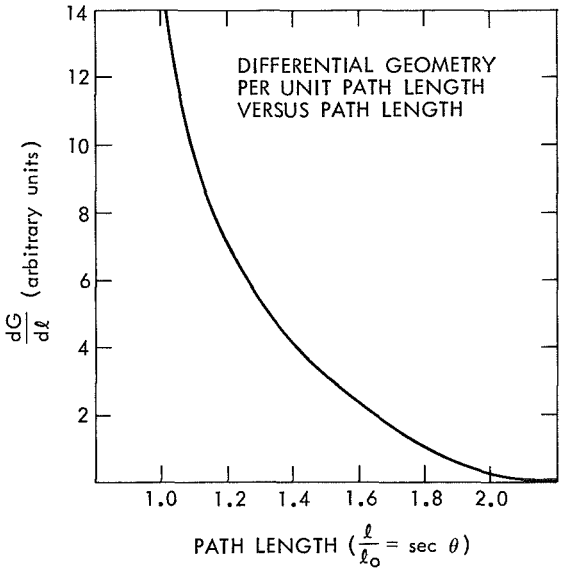

Figure 8–Differential geometry as a function of path length in a detector. Pulse out is proportional to path length. This detector has a very large opening angle, but the shape is typical.

example, a carbon with a 30-percent increase in path length will look like a nitrogen nucleus.

The detector response function is a convolution of the Landau distribution $L(x)$, the path-length distribution $dG(x)/d\ell$, the efficiency $A(x)$ of collection-vs-position variation, the Gaussian distribution $G(x)$ due to photoelectron statistics, etc.

$$\text{Gaussian distribution} = \frac{1}{\sqrt{2\pi\sigma}} e^{-(x-x_0)^2/2\sigma} .$$

These convolutions are defined in the following manner with the aid of Figure 9. Let x be some coordinate representing detector output. Suppose we wish to find the response function for Landau fluctuations plus some photoelectron fluctuations. In this case $R(x)$ can be written as the sum (integral) of all the Gaussian distributions normalized

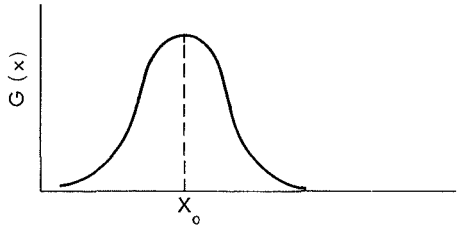

(a) GAUSSIAN DISTRIBUTION

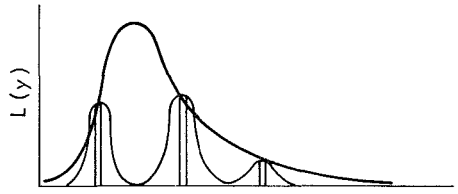

(b) LANDAU DISTRIBUTION

Figure 9–The symmetrical Gaussian distribution convoluted with an asymmetrical Landau distribution.

by the Landau distribution (the inverse integral is equivalent):

$$R(x) = \int_{-\infty}^{\infty} G(x-y)\,L(y)\,dy\ . \tag{10}$$

In general,

$$R(x) = \int_{-\infty}^{\infty} du\,\frac{dG}{d\ell}(x-u) \int_{-\infty}^{\infty} dz\,A(u-z) \int_{-\infty}^{\infty} dy\,G(z-y)\,L(y)\,, \tag{11}$$

which represents the detector response. The standard measurement of resolution is given as full width at half maximum (FWHM) = 2.36σ for Gaussian distributions, but this parameter can be misleading in

the case of distributions like $dG/d\ell$. We have

$$\sigma_{tot} \approx \sqrt{\sigma_G^2 + \sigma_L^2 + \sigma_A^2 + \sigma_{dG/d\ell}^2 + \cdots} \quad . \tag{12}$$

FWHM due to Landau distribution is ≈20 percent for a typical detector on singly charged particles; so resolutions of 30 percent are considered quite good when measured with muons at sea level. In Figure 3 a response function is shown which is the convolution of a Landau distribution and a Gaussian of FWHM = 20 percent. Note that the most probable energy is shifted to almost halfway between E_p and E_{ave}.

Any device that enables us to determine particle trajectories, such as a spark chamber or a hodoscope, allows us to correct for variations with path length and position. In principle, then, we can eliminate A and $dG/d\ell$ by reducing the distributions to delta functions. By starting with enough photons and collecting them efficiently we can reduce σ_G to a negligible contribution and approach the intrinsic resolution of the counter.

Background is somewhat more difficult to discuss. It consists of those events that simulate real particles. We reduce it by making the identification requirements as strict as possible. The most direct way to do this is to increase the number of measurements made of a given parameter in a given event. The probability that a background event can simulate a real event is the product of the probabilities in the individual detectors.

Each time another measurement is made, however, the particle being measured suffers another perturbation, thus increasing the fraction of the particles destroyed by the measurement. This process is additive. In most cases a trade-off is made, which depends upon the experimental details.

Particle charge Z is usually measured with some combination of these detectors and techniques. We shall look at some specific examples later.

ENERGY DETERMINATION

Some of the previously mentioned devices, such as the relativistic increase in gases and transition radiation, can in principle be used to

measure particle energy through the term proportional to $\ln \gamma$. Let us now turn our attention to devices that actually measure the energy of a particle by bringing it to rest, containing all of its energy. At high energies this is the natural extension of the low-energy technique of bringing a particle to rest by ionization loss.

At these high energies the particle is brought to rest by a series of interactions which produce secondary particles. These multiple interactions subdivide the single high-energy particle into very many low-energy particles which stop by ionization loss. A device sensitive to the total energy deposited by a particle through multiple interactions in a detector has been called an ionization calorimeter by the Russian scientists who first investigated its properties in depth. It is more properly a total-ionization spectrometer or an absorption spectrometer.

Let us consider this process in detail: electromagnetic and nucleonic cascade showers and their measurement, and the problems of relating these measurements to the particle parameters.

Electromagnetic Cascade Showers

Showers are formed by radiation and pair production in nuclear electric fields. The electrons emit photons by Bremsstrahlung; the γ rays produce pairs which emit more γ's, and so on until an electromagnetic shower is developed.

An electron can lose energy by radiation or collision losses. The relative importance of these two effects is a strong function of energy and depends upon the atomic number and atomic weight of the material in which the shower is to develop. This can be seen in Figure 10, where the fractional energy loss per radiation length is compared for lead and for air. Collision losses become important at much higher energy in air than in lead. This is chiefly because a radiation length in air (in $g\text{-}cm^{-2}$) is some 7 times that in lead. From this figure we can obtain an approximate definition for a radiation length as being that distance in which an electron will lose all its energy by radiative collisions (Bremsstrahlung). Because this definition is exact only at a unique energy and because radiative losses are probabilistic in nature, this definition is only valid as an aid to understanding. The exact

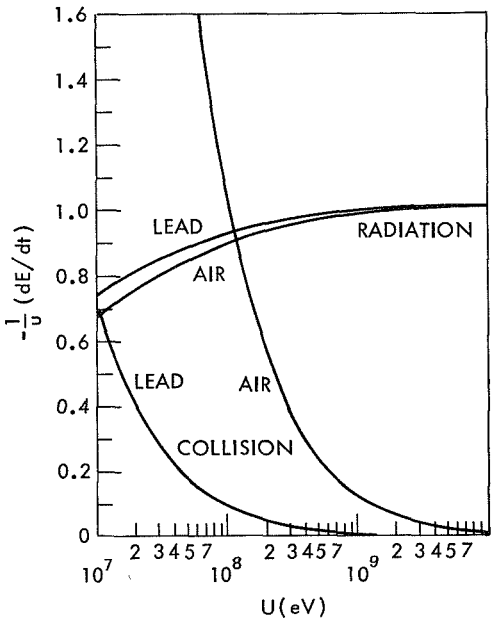

Figure 10–Fractional energy loss by collision and by radiation, per radiation length, for air and lead. (Taken from Rossi, 1952, page 52.)

definition is

$$\frac{1}{X_0} = 4\alpha \frac{N}{A} Z(Z+1)\, r_e^2 \ln\left(183\, Z^{-1/3}\right) \times \left[1 + 0.12\left(\frac{Z}{82}\right)^2\right] . \qquad (13)$$

The form of this equation can be derived by considering the particle trajectory in the field of the nucleus and using the classical energy loss formula

$$\frac{dE}{dt} = \frac{2}{3}\frac{e^2 a^2}{c^3} .$$

The term $(Z^2 + Z)$ replaces Z^2 and allows for collisions of the particle with the Z atomic electrons. This is important only for the lighter elements. The term $\ln (183\ Z^{-1/3})$ comes from the screening effect of the electrons. Since the most important collisions for total energy losses are distant collisions (they are the most numerous) this effect must be taken into account. Screening becomes more important at higher energies. At the same time, its importance is inversely related to the energy of the radiated photon, primarily because closer collisions produce more energetic photons. The Born approximation used to obtain the above expression is most reliable for low atomic numbers, being valid when $Z/137 \ll 1$. The experimentally determined term $\left[1 + 0.12\ (Z/82)^2\right]$ corrects for this fact.

After Rossi, we define $\Phi_{rad}\ (E, E')\, dE'\, dx$ as the probability for an electron of energy E to radiate a photon of energy within dE′ of E′ in a thickness dx g/cm^2. Figure 11 presents curves of Φ_{rad} from Rossi

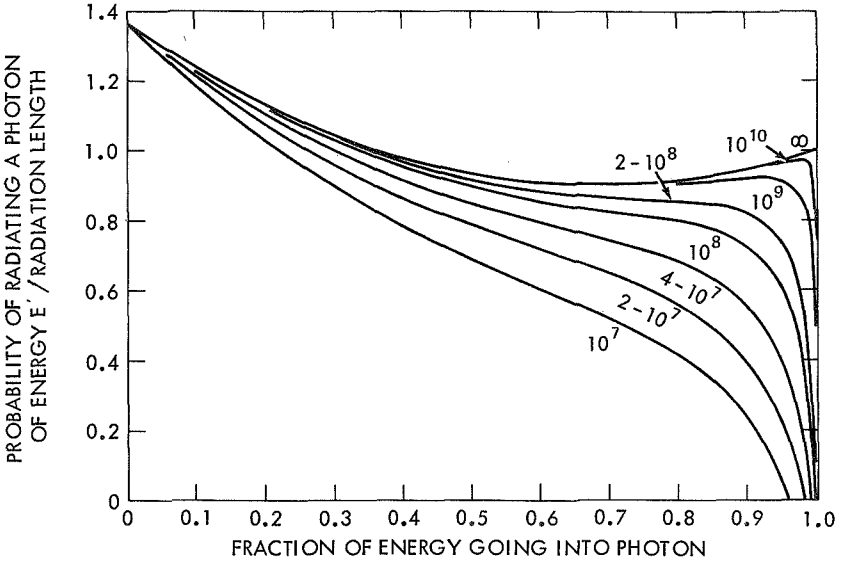

Figure 11–Differential radiation probability per radiation length of lead for electrons of various energies. The numbers on the curves indicate the total energy, U, of the primary electron. (Taken from Rossi, 1952, page 51.)

calculated from the Born approximation for lead. By probabilistically utilizing these curves we can determine the radiative history of any particle. Note: $t = x/X_0$ = distance in units of radiation length; $U = E + mec^2$ = total energy. The average fractional energy loss per radiation length is given by

$$-\frac{1}{U}\frac{dE}{dt} = \frac{X_0}{U}\int_0^E E' \Phi_{rad}(E, E')\, dE' .$$

There are two processes by which the energy carried by photons can be transferred to electrons: pair production and Compton collisions. The relative importance of these two effects is seen in Figure 12 for air and lead. Photons above 10^8 eV will almost all pair-produce in 1.25 radiation lengths, but below this energy some will produce Compton electrons. In lead (or other high Z materials), γ rays of a few MeV can go up to 5 radiation lengths on the average before converting.

The pair-production process is similar to Bremsstrahlung in which a photon is emitted by a particle in making a transition between two positive-energy states. In pair production, a photon is absorbed causing an electron of negative energy to make a transition to a state of positive energy. In this case also Rossi presents curves, Figure 13, representing the differential probability ϕ pair that a γ ray of energy E will produce a positron of kinetic energy E' and an electron of energy $E'' = E - 2m_e c^2 - E'$. The curves are, of course, symmetrical about $E' = E/2 - m_e c^2$. As the energy of the photon increases it becomes more and more likely that the energy in the two electrons will be asymmetrically divided. The probability of producing a pair in one radiation length is given by

$$\mu = \int_0^{E-2mec^2} \phi_{pair}(E, E')\, dE' .$$

Electromagnetic showers occur when electrons (or γ rays) incident upon material lose energy by Bremsstrahlung to γ rays, which convert into pairs which, in turn, undergo Bremsstrahlung and produce more pairs. The showers continue to develop in this manner until the energy of the electrons is low enough to them to come to rest by collision loss

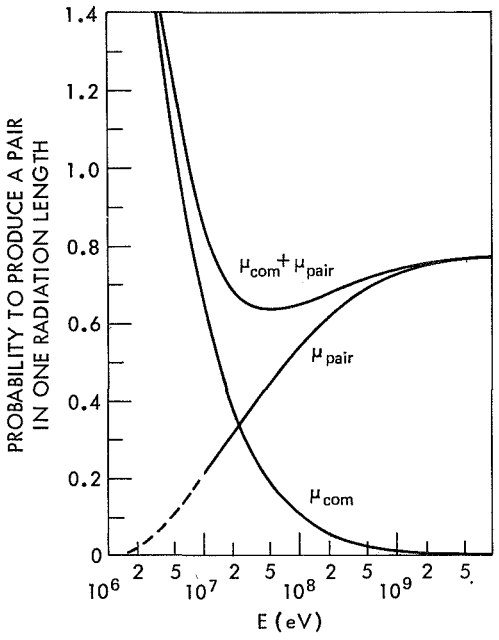

(a) FOR AIR

(b) FOR LEAD

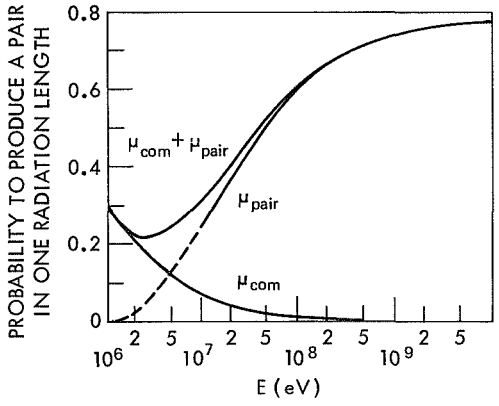

Figure 12–Total probability per radiation length of air and lead for Compton Scattering (μ_{com}), for pair production (μ_{pair}), and for either effect ($\mu_{com} + \mu_{pair}$). (Taken from Rossi, 1952, page 84).

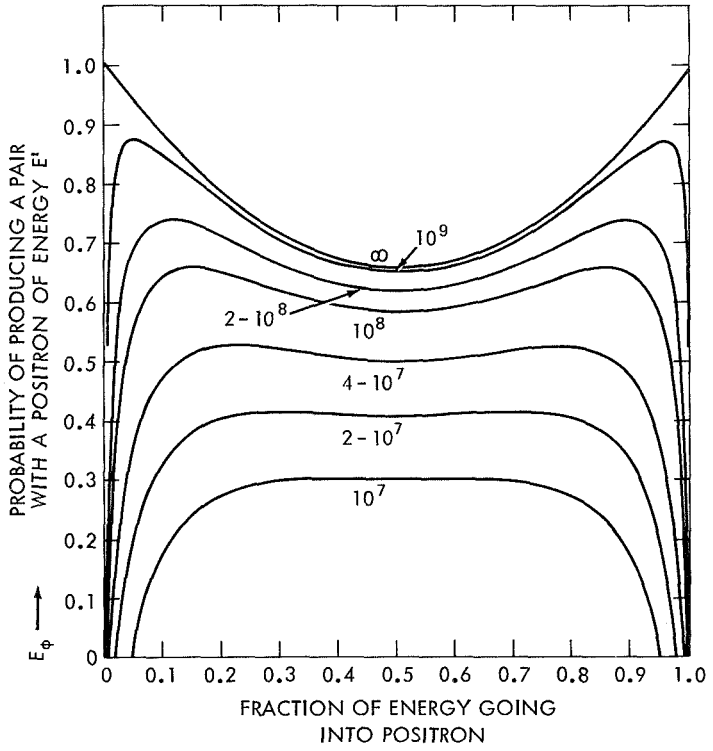

Figure 13–Differential probability of pair production for pair production per radiation length of lead for photons of various energies. The numbers on the curves indicate the energy E of the primary photon. (Taken from Rossi, 1952, page 83.)

rather than by radiating additional energy. It will be recalled that collision loss varies with $1/\beta^2$ at low energies and so increases very rapidly compared to the radiation-loss change with energy (see Figure 10). This defines a critical energy at which radiative losses become unimportant and an electron comes to rest without further multiplication.

Table 3 lists the radiation length and critical energy of a number of common substances. Also included is the interaction mean free path for protons which will be of use later.

Figure 14 shows some sample shower curves as presented in Rossi (1952). The logarithm of the mean number of particles is presented as a function of distance along the shower axis in units of radiation length.

Table 3. Radiation Lengths and Critical Energies

	Z	A	X_0 (g/cm^2)	X_0 (cm)	ϵc MeV	λ (g/cm^2)	λ (cm)	ρ (g/cm^3)	λ/X_0
Carbon	6	12	44.6	12.6	7.1	92.2	26.2	3.52	2.1
Aluminum	13	27	24.5	10.6	51.0	115.1	41.5	2.7	3.9
Iron	26	55.84	13.98	1.8	27.4	138.1	17.0	7.86	9.6
Copper	29	63.57	13.1	1.45	24.8	137.9	15.5	8.9	10.6
Tungsten	74	183.85	6.91	0.36	10.2	185.96	9.2	19.3	25.6
Lead	82	207.2	6.53	0.58	9.5	191.6	16.2	11.35	28.15
Air (NTP)	7.37	14.78	37.7	2.9×10^4	102	95	7.2×10^4	13×10^{-3}	2.5
Water	7.23	14.3	37.1	37.1	92	92	920	1	2.5

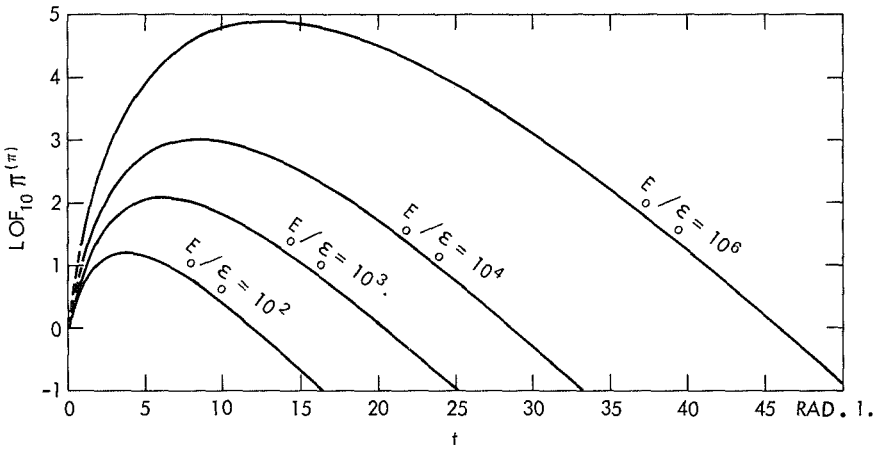

Figure 14—Total number of electrons in a shower $\pi_{(E_0,0,t)}$ initiated by an electron of energy E_0 as a function of depth in units of radiation length. It has been computed under Rossi's approximation B in which Compton collisions have been neglected. E_0/ϵ_0 is the energy in units of critical energy. (Taken from Rossi, 1952, page 258.)

The number of particles at a given depth in the shower can be determined by means of thin (0.01 rad-length) scintillators placed in the shower medium; for example, tungsten sheets 1 or 2 radiation-lengths thick can be made into a sandwich with scintillators. The number of particles at any depth is equal to the ratio of recorded pulse height to one average pulse height measured from minimum ionizing particles. (Electrons are minimum-ionizing until their range becomes $\approx 2 g\text{-}cm^{-2}$.) In this way the differential properties of the shower can be measured, e.g., the number of particles as a function of depth, the location of the shower maximum, etc. Calibrations are then required to relate given shower curves to primary particle energy.

This technique is an extension of that used at lower energies, where the complete shower is developed in a translucent medium and the integral pulse height is measured. These detectors have been made of such substances as lead glass and sodium iodide. However, it is not possible to build this type of detector with the necessary area to study cosmic rays at very high energies. In the first place, in order to study high-energy showers we need enormous depths to completely contain the shower. In the second place, we need large-area detectors and these quickly become prohibitively expensive.

Nucleonic Cascade Showers

This cascade-shower technique can be extended to nuclear active particles. Strongly interacting particles, called hadrons, interact with the nucleons of the spectrometer in a characteristic distance called the interaction mean free path.

$$\lambda = \frac{1}{\frac{N_0}{A}\sigma_0} A^{3/4} = \frac{10^4}{6\sigma_0\,(\mathrm{mb})} A^{1/4} ,$$

$$\sigma_0 = 33\,\mathrm{mb} \qquad \text{for} \qquad \text{p, p reactions.} \tag{15}$$

Typical values are given in Table 3. This empirical formula differs slightly from the geometrical cross section which varies as $A^{2/3}$.

These interactions are called stars in emulsions; they show very thick, short tracks, due to low-energy fragments from the interaction. They are knock on nucleons produced as the primary particle strikes the nucleus. They can be either protons or neutrons. The neutrons will carry away from the interaction some energy that cannot be detected. On the other hand, the low-energy protons lose energy at a high rate and if they happen to be detected they will indicate disproportionately the amount of energy they carry away from the interaction.

Most of the energy lost by the interacting particle is carried away by mesons.

We now determine the energy required to produce a π meson ($m_\pi c^2 \sim 140$ MeV) in the interaction:

$$p + p \rightarrow p + n + \pi^+$$

or

$$p + p \rightarrow p + p + \pi^\circ , \qquad m_\pi c^2 = 2E^* , \tag{16}$$

where E^* is the kinetic energy of the two nucleons in the center-of-mass system (c.m.) before the interaction. This is the threshold energy and leaves all particles at rest in the c.m. after the collision. In the laboratory frame the three particles will move with equal velocity (the c.m. velocity) after the collision. Let E be the kinetic energy of the moving proton in the laboratory, and let the momentum be p.

Recall that rest energy is an invariant under Lorentz transformation. Then

$$\left(E + 2M_p c^2\right)^2 - c^2 p^2 = \left(2E^4 + 2M_p c^2\right)^2 - 0 ,$$

$$(\text{Rest Energy})^2 = (\text{Total Energy})^2 - (\text{Momentum})^2 . \qquad (17)$$

And, for the proton in the lab frame,

$$\left(E + M_p c^2\right)^2 - c^2 p^2 = M_p^2 c^4 ,$$

$$c^2 p^2 = E^2 + 2E M_p c^2 .$$

Eliminating $c^2 p^2$ gives

$$\left(E^2 + 4E M_p c^2 + 4M_p^2 c^4 - E^2 - 2E M_p c^2\right)$$

$$= 4E^{*2} + 8E^* M_p c^2 + 4M_p^2 c^4 ,$$

$$2E M_p c^2 = 4E^{*2} + 8E^* M_p c^2 ,$$

$$E = 4E^* \left(1 + \frac{E^*}{2M_p c^2}\right) . \qquad (18)$$

This gives the proton the kinetic energy required to produce any particle of mass m where $2E^* = mc^2$. In the case of π's,

$$E = 2m_\pi c^2 \left(1 + \frac{1}{4}\frac{m_\pi}{M_P}\right) = 290 \text{ MeV} . \tag{19}$$

We are dealing with primary protons with sufficient energy to produce numerous mesons in a single collision. In fact, it is known that the multiplicity for meson production will increase slowly with energy at high energies, perhaps as $E^{1/4}$, with a nominal value of about 10 at 100 GeV. Of course this meson production is a probabilistic phenomenon. The multiplicity in any given interaction may have a wide range of possible values open to it. The theories of nuclear interaction are not well enough understood to make it worth-while going into further detail.

The mesons produced will be roughly equally divided between three types: π^+, π^-, and π°. The charged π's are hadrons and most of them will strongly interact with other nuclei in a spectrometer. A small percentage may decay before they interact. Let us see how many this will be for iron. In iron, λ_i is 138 gm-cm^{-2}, and the density is 7.9 gm-cm$^{-3} \rightarrow \lambda_i \approx 17.5$ cm. But a meson can travel 750 cm in its lifetime of 25 nanosec. Thus 17.5/750 or 2 percent will decay into mesons in that time. On the other hand, the neutral π's will all decay before they interact because they only go about 100 atomic radii in their lifetime. It is the energy that goes into π°'s that is most readily measured, because

$$\pi^\circ \rightarrow 2\gamma \rightarrow 2 \text{ pairs of electrons} . \tag{20}$$

The subsequent electromagnetic showers are described as above. The fraction of the energy of the primary contained in this first electromagnetic shower depends upon the inelasticity of the collision.

The inelasticity of the interaction varies with the atomic weight of the target nucleus. It is about 0.3-0.6 for substances such as carbon, while for more tightly bound, higher-A substances such as iron it may approach 1. This can be qualitatively understood by considering the tunnel model of the nucleus. See Figure 15. The radius of the iron nucleus should be about 1.65 times that of the carbon nucleus.

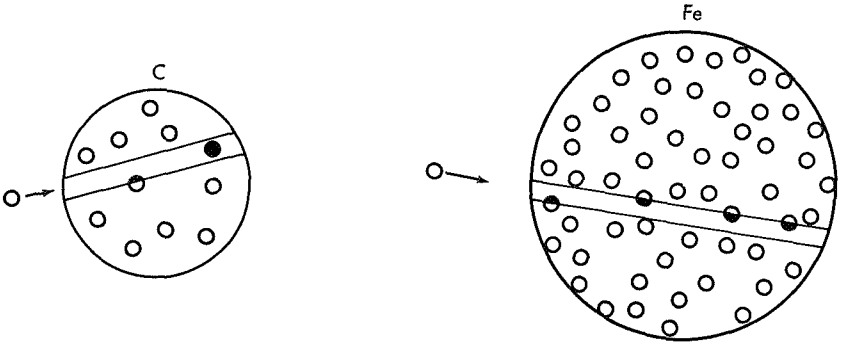

Figure 15–Qualitative illustration showing why inelasticity increases with increasing A for a (p, A) collision.

In the lighter elements the projectile nucleus tends to interact with only a single nucleon, which in the heavier elements the path through the nucleus is quite likely to intersect more than 1 nucleon. However, in any given collision there tends to be a wide range of inelasticities open to the particle.

Through multiple interactions a high-energy cosmic ray deposits its energy in any sufficiently thick block of material. Assuming that the dissipation of energy of the hadrons in the shower takes place solely through the transfer of energy to the π° mesons, we can calculate the thickness required to contain the energy. We follow the calculation of Grigorov et. al., (1964).

The energy in nuclear active particles E_{na} decreases exponentially with depth x:

$$E_{na}(x) = E_0 \exp\left(-\frac{kx}{3\lambda}\right), \qquad (21)$$

where E_0 is the energy of the primary particle, λ is the interaction mean free path (all hadrons interact with about the same λ), k is the inelasticity, and the factor 1/3 is the ratio of the number of π°'s produced to the total number of mesons produced. The energy in π_0's

becomes

$$E_{\pi^\circ}(x) = E_0 - E_{na}(x) = E_0 \left[1 - \exp\left(\frac{-kx}{3\lambda}\right)\right] . \tag{22}$$

If we wish to contain 90 percent of the energy of the primary, then

$$\frac{E_{\pi^\circ}(x_0)}{E_0} = 1 - \exp\left(\frac{-kx}{3\lambda}\right) = 0.9 , \tag{23}$$

$$x_0 = 7\,\frac{\lambda}{k} .$$

The shower produced will be the superposition of several electromagnetic showers. Since the elasticity, k, is nearly 1 in an iron spectrometer, the first interaction is likely to produce higher energy π_0's than subsequent ones, so the shower curve might resemble that shown in Figure 16.

By taking samples of the ionization loss at various depths in the material, we can find the area under the type of curve shown in Figure 16. It is clear that the energy of the primary particle will be directly related to this area.

Above, we have calculated the depth required to contain 90 percent of this area. From Table 3 we can compute that 7 mean free paths (mpf) of iron implies a thickness of about 1.2 m of material. Clearly the weight of such a thickness can become prohibitive in large areas. Reducing the thickness of a counter will not destroy the proportionality between area and energy, because if the whole area is related to energy, so is some fraction of the area. The problem becomes one of fluctuations in the fraction actually measured. Recently a calorimeter has been calibrated in the beam at Brookhaven AGS (30 GeV protons). It is found that the rms fluctuations are optimized for particles which suffer their first interaction near the top of the spectrometer. Unfortunately the spectrometer used was only 3 mfp thick, but, even so, the mean area of the shower curve was found to go linearly with beam energy. Fluctuations tended to produce oversized rather than undersized showers and were quite severe. Standard deviations were typically +50 and -30 percent.

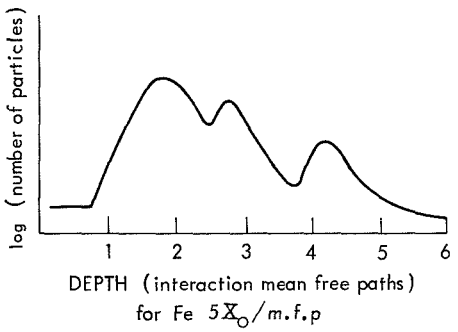

Figure 16–Qualitative illustration showing the fluctuations expected in the development of nuclear cascade showers.

Experimental Considerations

One of the first problems that must be solved is how to separate electrons from protons. As we have seen, this can be done up to several 10's of GeV using gas Čerenkov separation, but at higher energies this technique becomes much less easy to employ.

Even though the initial portion of a proton-interaction shower can appear to be exactly like that for electrons, subsequent interactions will make it seem quite different. If the "early" part of the spectrometer is made of material with a very large number of radiation lengths per mean free path, then this effect is enhanced. Table 3 gives this ratio. Tungsten and lead satisfy the condition; but tungsten is difficult to mill because of its hardness, and lead is difficult to use because of its softness. In either of these materials, though, electron showers will develop quickly while the nucleons interact with relatively low probability.

Why not make the whole spectrometer of this material? Suppose we fix the area of our detector elements at some value, say 2500 cm^2. Then, according to Table 3, we can minimize the weight of the spectrometer by utilizing the lowest-A material. However, it is not quite so simple. Firstly, below iron in the Periodic Table the inelasticity will decrease, requiring the spectrometer to contain more interaction mean free paths. Secondly, the collection area is inversely proportional to the square of the height; so added thickness implies a decrease in geometry. The column in Table 3 showing λ in cm suggests a best compromise of iron or copper.

The spectrometer then consists of a tungsten (or lead) section on top, perhaps 6-12 radiation lengths thick, and an iron (or copper) section following which is at least 3 or 4 interaction mean free paths thick. The various aspects of how often ionization measuring devices should be placed in the spectrometer are left as one of the problems at the end of this paper.

Such a spectrometer with 2500 cm area would weigh in the neighborhood of 1.6×10^3 kgms ≈ 2 tons—something ill-suited to balloon technology. It is possible to launch this payload weight on balloons made of mylar and laminated with a scrim of nylon threads which carry the weight. The scrim is glued onto the mylar and, at present, is being laid on in patterns that can vary from location to location on the balloon and be controlled by computer. These balloons are being built in volumes of 35×10^6 ft^3, and the present limit appears to be the length of the plant in which they are constructed.

Balloons called tandem balloons consist of large main balloons with a launch balloon attached to the top. These top balloons can carry the helium required at launch. The load includes payload weight, ballast (20 percent of payload), balloon, and free lift. The gross inflation for these large balloons is in the neighborhood of 8000-10,000 lbs.

Since these balloons are vastly expensive compared with standard stratofilm balloons, hybrid systems with a mylar scrim launch balloon and a stratofilm main balloon are now being tested.

Magnetic Analyzers

Another technique for determining energies in this range is the magnetic analyzer. Recall that the bending radius ρ of a particle in a magnetic field B is given by

$$\rho(\text{cm}) = \frac{R(\text{volts})}{300\, B(\text{gauss})} , \tag{24}$$

where R is the magnetic rigidity or momentum per unit charge given by

$$R = \frac{pc}{Ze} \tag{25}$$

and is measured in volts.

If path length in the magnetic field is given by ℓ, the angular displacement by θ, and lateral displacement by Δx, then

$$\tan\theta \approx \frac{\ell}{\rho} \approx \frac{\Delta x}{\rho}$$

$$\frac{\ell}{\rho} \approx \frac{300\, Ze\, \ell B(\text{gauss})}{pc} . \tag{26}$$

The highest rigidity to which one is sensitive is given by

$$\frac{pc}{Ze} = \frac{300 \int \vec{B} \cdot d\vec{\ell}}{\Delta\theta} . \tag{27}$$

Then $\Delta\theta$ is the smallest angle that can be measured.

This defines the upper limit in rigidity that can be determined. In order to deal with rigidities in the neighborhood of 10^{12} eV, emulsion techniques are required for measuring $\Delta\theta$ in the range of 10^{-4} radians and

$$\int \vec{B} \cdot d\vec{\ell} \approx 10^5 \text{ gauss cm} .$$

Combination detectors including spark chambers and emulsions have been proposed for finding the trajectories of particles in magnetic fields. The spark chamber would give one the region of the emulsion in which to find the track and determine the details of its trajectory. This requires some method of returning the emulsions to earth and so is applicable only to some sort of manned space station in which resupply missions occur every three months or so. If the emulsions remain longer in space, the background of tracks will become so large that tracks of interest cannot be found.

EXAMPLE INSTRUMENTS

We will follow the development of detectors built around scintillator Čerenkov combinations for measuring charge, because they provide a good set of examples to illustrate what we have been discussing.

We will begin with an example using low energies. In the range from about 100 to 2000 MeV/nucleon, counter telescopes have been utilized containing typically two scintillators and a Čerenkov detector in some combination. These detectors have had geometric factors in the neighborhood of 50 ster cm^2. An example is shown in Figure 17.

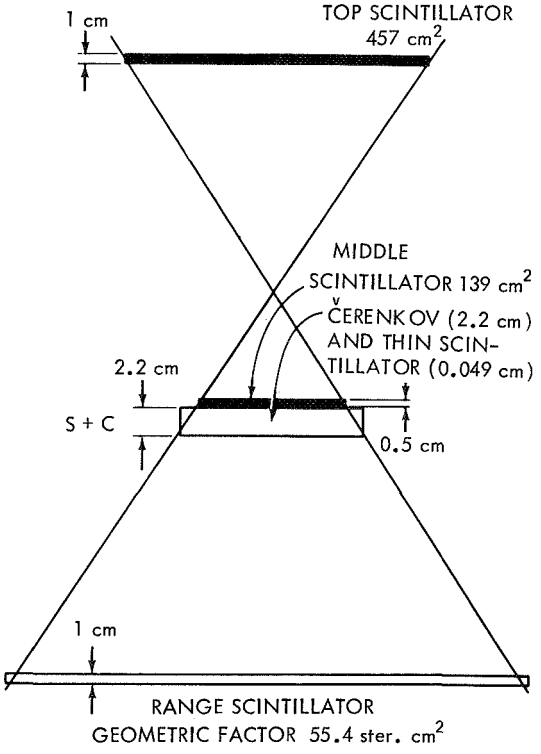

Figure 17–Schematic diagram of a Čerenkov scintillator for studying charge composition and energy spectra between 30 MeV and 2 GeV. (Used by the author while at the University of Minnesota.)

The two scintillators respond as Z^2/β^2 and the Čerenkov-plus-scintillator detector as

$$Z^2\left(1 - \frac{1}{\beta^2\eta^2}\right) + \frac{Z^2}{\beta^2} ,$$

so that both Z and β can be determined from the measurement. Figure 18 shows a plot of the expected response. In the region of confusion where the response is the same for two particles—say protons of low velocity and helium of high velocity—helium nuclei are above the Čerenkov threshold (320 MeV/nucleon) and have sufficient energy to pass through the penetration counter. However, the protons have low energy and do not trigger the penetration counter. This separation works also for all the higher charges.

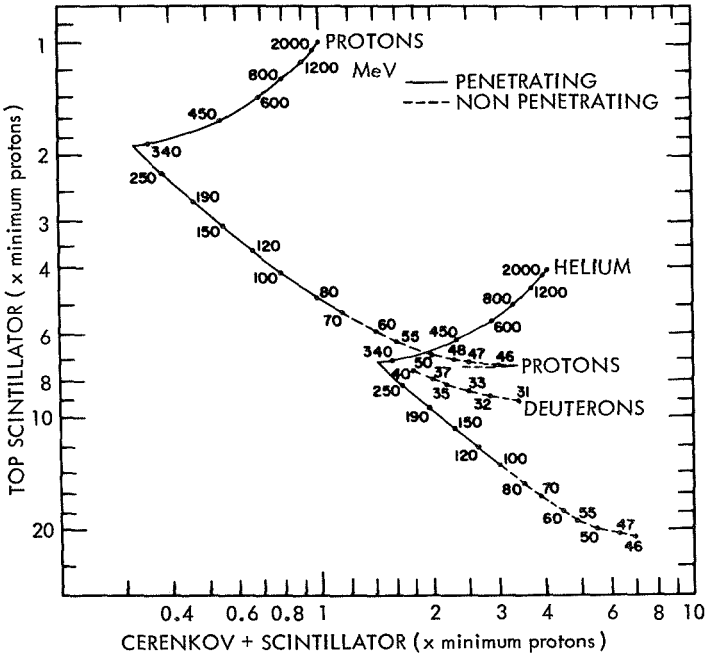

Figure 18—Two-dimensional response of the detector shown in Figure 17. Particles on the solid line penetrate the range detector; those on the dashed lines do not penetrate the range detector.

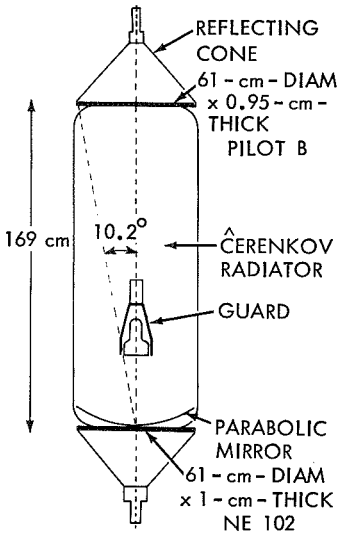

Figure 19–Gas Čerenkov detector for studying charge composition above the range where geomagnetic cutoff is useful. This was designed and built by T. T. Von Rosenvinge while at the University of Minnesota.

Figure 19 shows the detector from which the highest-energy charge composition data yet available have come. It consists of a 1.7-m gas Čerenkov detector used as a threshold counter. It is used in conjunction with two plastic scintillators, which form the coincidence geometry. They are viewed by photomultiplier tubes at the apexes of conical air light guides. The variation of light collected with position on the scintillator was optically compensated for by black circles drawn on the surface of the scintillator, thus partially absorbing the light from regions of higher collection efficiency. The charge resolution obtained from one of these scintillators is shown in Figure 20.

Figure 21 is a schematic diagram of a system used to measure low-energy electrons. The gas Čerenkov on top is used to separate protons from

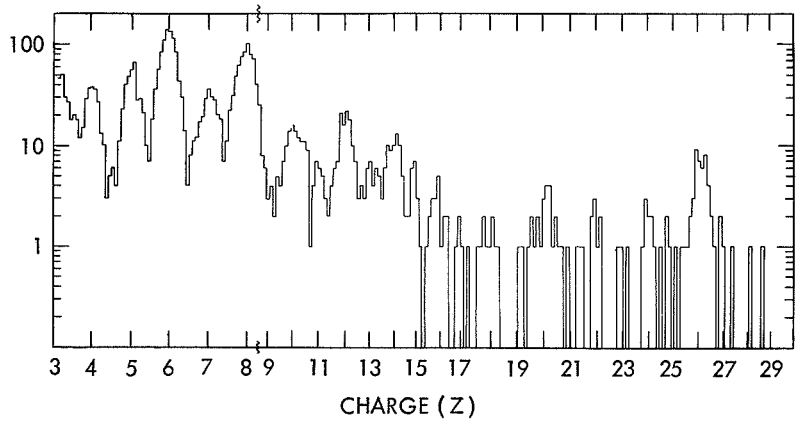

Figure 20–Charge histogram obtained using the detector shown in Figure 18.

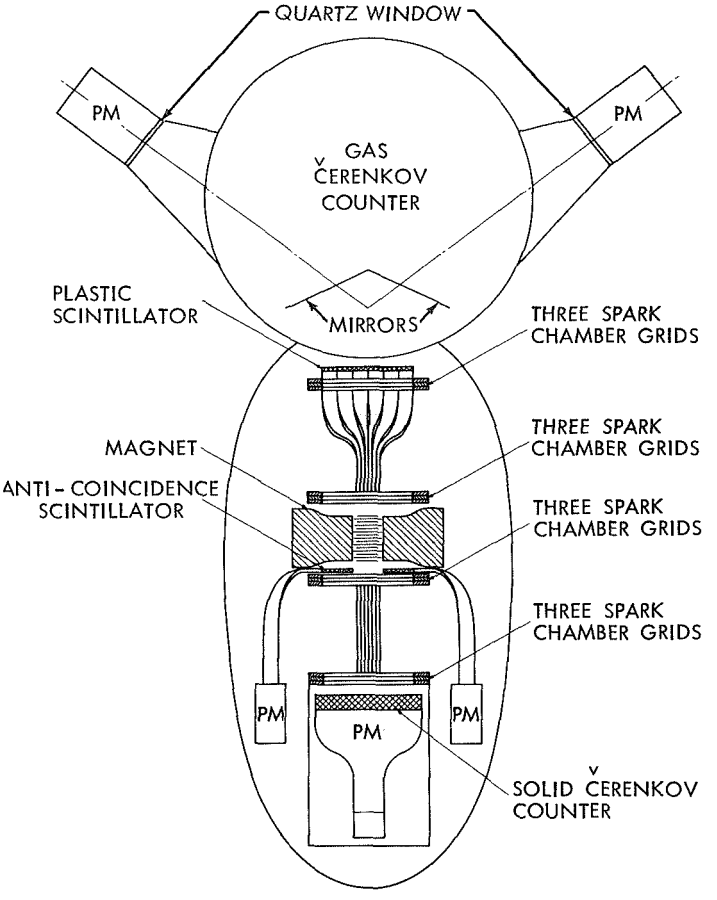

Figure 21–Gas Čerenkov detector used in conjunction with a permanent magnet in order to study the e^+/e^- composition in the cosmic radiation. (This experiment was flown on balloons by Fichtel and collaborators at NASA.)

electrons. The energy is determined from the electron deflection in the magnetic field, measured with wire-grid spark chambers. The plastic scintillator and the solid Čerenkov counter form the coincidence geometry. The anticoincidence scintillator is used for particles that pass through the magnet pole faces.

Another electron detector is shown in Figure 22. This also has a gas counter, for separating electrons from protons. Scintillators T_1 and T_3 define the aperture and determine the charge of the particle. The shower is developed in the tungsten scintillator sandwich shown.

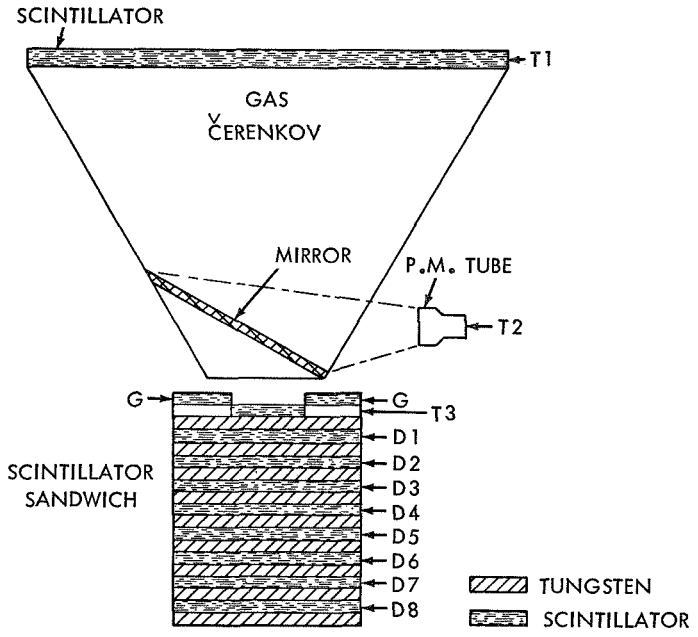

Figure 22–An experiment to study the energy spectrum of high-energy electrons. The electron energy is determined from the cascade shower in the tungsten scintillator sandwich. This experiment has been proposed by Dr. P. Meyer of the University of Chicago.

The last example is shown in Figures 23 and 24. This detector is designed to measure the cosmic-ray charge and energy spectra and to separate electrons and protons. Charge is determined first by the module shown in Figure 23. Geometry is defined by plastic scintillators at the top and bottom viewed through adiabatic light guides by photomultipliers. Charge is determined using the fourfold measurement including the two plastic scintillators, a Čerenkov detector, and a CsI mosaic. The particle trajectory is determined by the three spark chambers shown. This allows the response of the large scintillators to be compensated for spatial and angular variations of response. This section sits on top of the ionization calorimeter shown in Figure 24. The top section is a sandwich of tungsten and scintillator, to rapidly develop the electromagnetic cascades. The second part consists of iron modules each half a mean free path thick. There are seven shown, each viewed by a separate photomultiplier tube. The scintillator samples are taken 3 every half mean free path or about every 1.5 radiation lengths.

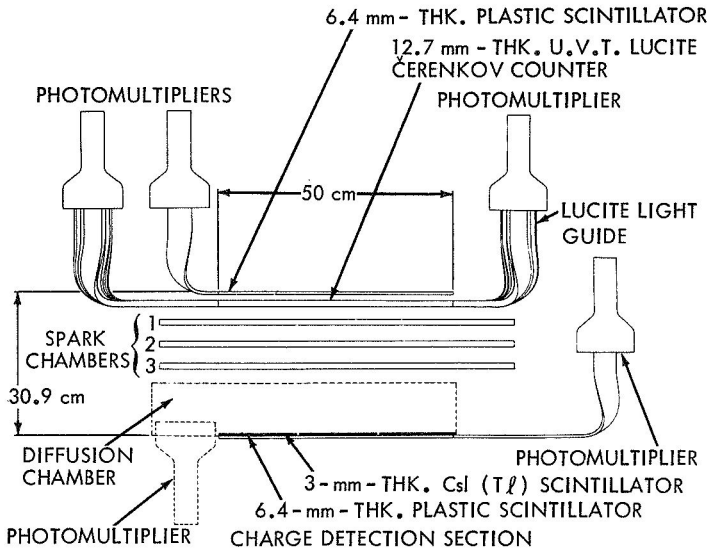

Figure 23–Charge detection section of a high-energy cosmic-ray experiment being built at NASA.

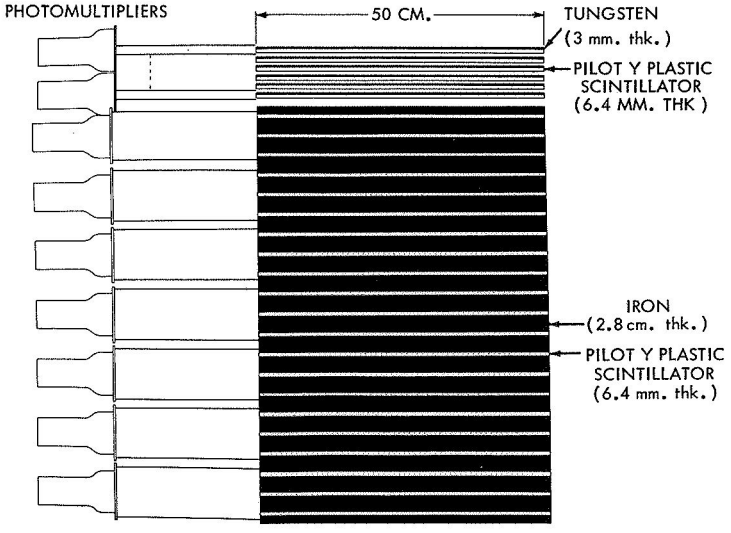

Figure 24–Energy-detection section of the NASA high-energy cosmic-ray experiment.

REFERENCES

Grigorov, N. L., Rapoport, I. D., Savenko, I. A., and Skuridin, G., "The Study of Energy Spectrum of Primary Cosmic-Ray Particles of High and Ultrahigh Energies from the Proton Series of Satellites," Proc. Internat. Conf. on Cosmic-Ray Physics, Budapest, Hungary, 1969.

Jackson, J. D., "Classical Electrodynamics," New York: John Wiley, 1962.

Ögelman, H., "Current Problems of High-Energy Astrophysics," in "Lectures in High-Energy Astrophysics" by H. Ogelman and J. R. Wayland, NASA Special Publication 199, 1969.

Rossi, R., "High Energy Particles," Englewood Cliffs, N. J.: Prentice Hall, 1952.

Grigorov, N. L., Nesterov, V. E., Rapoport, I. D., Savenko, I. A., and Skuridin, G., "The Study of the High-Energy Cosmic-Ray Particles with the Proton Satellites," Part A, Proc. Tenth Internat. Cosmic-Ray Conf., Calgary, Canada, 1967.

BIBLIOGRAPHY

Cosmic Rays: General

Ginzberg, V. L., and Syrovatski, S. I., "The Origin of Cosmic-Rays," New York: Pergamon Press, 1964.

Grigorov, N. L., Nesterov, V. E., Rapoport, I. D., Savenko, I. A., and Skuridin, G., "The Study of the High-Energy Cosmic-Ray Particles with the Proton Satellites," Part A, Proc. Tenth Internat. Cosmic-Ray Conf., Calgary, Canada, 1967.

Ögelman, H., and Wayland, J. R., "Lectures in High-Energy Astrophysics," NASA Special Report 199, 1969.

Webber, W. R., "The Spectrum and Charge Composition of the Primary Cosmic Radiation," in "Handbuch der Physik," 46/2, Berlin: Springer Verlag.

General References on Electrodynamics and Techniques

Allen, C. W., "Astrophysical Quantities," London: Athlone Press, University of London, 1963.

Barkas, W. H., and Berger, M. J., "Tables of Energy Losses and Ranges of Heavy Charged Particles," NASA SP-3013.

Jackson, J. D., "Classical Electrodynamics," New York: John Wiley and Sons, 1952.

Jelley, J. V., "Čerenkov Radiation and its Applications," New York: Pergamon Press, 1958.

Ritson, D. M., "Monographs and Texts in Physics and Astronomy. Techniques of High-Energy Physics," Interscience, 1961.

Rossi, B., "High-Energy Particles," Englewood Cliffs, N. J.: Prentice Hall, 1952.

Calorimeters

Grigorov, N. L., Rapoport, I. D., Savenko, I. A., and Skuridin, G. A., "Problems and Perspectives in Cosmic-Ray Research," Cosmic Physics, 2:636, 1964.

Jones, W. V., Pinkau, K., Pollvogt, U., Schmidt, W. K. H., and Huggett, R. W., "A Study of the Properties of an Ionization Spectrometer with 10, 20.5, and 28 GeV/c Incident Protons," to be published in the Physical Review.

Nuclear Interactions

Camerini, U., Lode, W. O., and Perkins, D. H., "The Analysis of Energetic Nuclear Encounters Occurring in Photographic Emulsions," in "Progress in Cosmic-Ray Physics, Vol. 1," Amsterdam: North Holland, 1957.

Hopper, V. D., "Cosmic Radiation and High-Energy Interactions," Englewood Cliffs, N. J.: Prentice-Hall, 1964.

V. EXTENSIVE AIR SHOWERS

M. LaPointe
*University of Maryland**
College Park, Maryland

INTRODUCTION

The existence of cosmic radiation had been known for some 25 years before time-coincident particles were first observed in the atmosphere in 1938 (Greisen, 1956; Galbraith, 1958). The initial observations were first made with trays of Geiger counters spaced several tens of centimeters, but soon time coincidences with separations of up to 100 meters were noted. Such events were named extensive air showers (EAS).

Prior to this discovery it had been noted that cosmic-ray particles often multiplied on passing through material. The electronic nature of secondary particles had been recognized in Wilson cloud chambers immersed in a magnetic field and the phenomena of the electron-photon (EP) cascade seemed to explain the multiplication. (The details of quantum electrodynamics had been recently developed.)

Cloud chambers were soon used in coincidence with trays of Geiger counters to confirm that the particles observed in the atmosphere were electrons and positrons of energy 10^7—10^8 eV. From the local density of particles observed in the cloud chamber it was estimated that the largest events observed arose from primaries of the order of 10^{16} eV. Thus an EAS represented the secondary effects of the most energetic particles in cosmic radiation.

The cloud-chamber photographs also recorded an occasional slow-proton track. A shielded counter tray operated in coincidence with unshielded sets of trays also indicated a component of air showers able to pass without interaction through 15—20 cm of lead. Thus the presence of a nucleonic component and a small penetrating component were inferred. For almost a decade, however, it was thought that EAS represented a pure electromagnetic cascade arising from an ultra-high-energy primary electron or photon. The other components were thought to be somehow secondary to the electron-photon cascade.

*Department of Physics and Astronomy.

Both theory and experiment eventually indicated that there would be practically no electrons or photons of such energies in the primary cosmic radiation. High-energy experiments were just then revealing that multiple meson production takes place in relativistic nuclear interactions. The key to the understanding of EAS development was the discovery of the neutral pion and its rapid decay into two gamma rays which initiate the EP cascade. The primaries are protons and heavier nuclei; EAS originate in nuclear interactions with air molecules high in the atmosphere. Nucleons and charged pions originating in the first interaction are capable of producing additional interactions, which enhance and sustain the electron-photon component. At sea level, the electron-photon component, though numerically predominant, is secondary to the nucleonic cascade which generically is more closely related to the initial interaction. The penetrating component was identified with mu-mesons secondary to charged pions which decay in the atmosphere.

An EAS as observed at ground level is thus the result of a series of complex interactions whose properties are not well understood. Each shower can only be sampled in a minimal way and it is only by studying large samples of showers that we can determine average characteristics. There are large fluctuations in shower development which tend to blur the details that are sought. Present studies are concerned with the nature of nuclear interactions at high energies and the composition of primary radiation above 10^{14} eV.

Unfortunately there is not now—nor likely to be in the near future—a more direct way to study the interactions and the nature of the primaries at these high energies. The highest accelerator energies available will be from the CERN colliding beam system, where 30 GeV protons will provide 1.6×10^{12} eV in the laboratory frame.

A satellite platform could in a reasonable time collect data on interactions up to 10^{14} eV; someday a detector may be placed on the moon. The steepness of the energy spectrum is such that the upper limit of the energies will not be extended much beyond this.

Figure 1 has been reproduced from Ögelman (1969, p. 6). It gives the integral spectrum of cosmic-ray nuclei, and from it one can derive the time involved in accumulating events above a given energy in a detector of reasonable size.

The atmosphere acts as an amplifier by producing thousands to millions of secondary particles each time a primary cosmic ray of sufficient energy impinges on it. The secondary particles are spread over many acres and it is fairly simple to detect these events and estimate the primary energy involved. Inferences as to the nature of the primaries and the details of the nuclear interactions involved are much more difficult, requiring large and complex detectors which, because of their size, usually lack the refinements possible in smaller instruments.

The detection methods used have for the most part been described in lectures during this course. Here, our concern will be to describe the form the detectors take for EAS studies and to give some insight into the analysis used on the data.

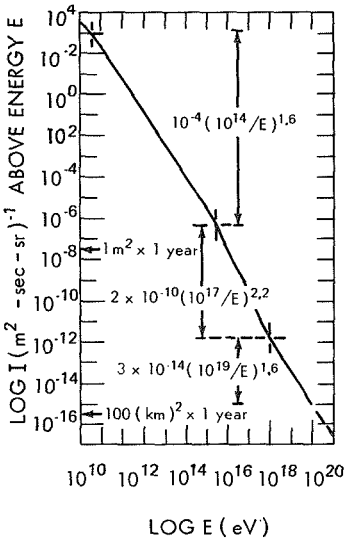

Figure 1—Integral flow of primary cosmic rays above a given energy.

A QUALITATIVE DESCRIPTION OF EAS DEVELOPMENT

(See Cocconi, 1961)

Suppose that a 10^{15}-eV proton impinges on the atmosphere. Typically it suffers a nuclear collision at a depth equal to the mean free path (MFP) in air (~70—80 g-cm^{-2}) or roughly at about 16-km altitude. The details of the interaction are as yet uncertain but the most abundant particles produced are certainly pi-mesons. Nucleons (protons and neutrons), and a variety of strange particles, are also present. Yet in emulsion studies at lower energies, pion production dominates the process and the pions carry off the main portion of the energy lost. These studies also indicate that the collision is only partially inelastic—that is, the primary particle may retain a considerable fraction (about half) of its initial energy after the collision. There is also indication that in the center-of-mass system the created secondary particles are not distributed isotropically but are collimated in the forward-backward direction. In the laboratory frame all the particles are extremely collimated in the forward direction but only half of them carry appreciable energy.

About 20-30 percent of the secondary particles are neutral pions. If we assume that 40 particles are produced in the interaction, 20 of them will carry most of the energy (mean energy $\sim 2.5 \times 10^{13}$ eV/particle). If five of these are neutral pions, there are produced almost immediately 10 photons of mean energy 1.25×10^{13} eV. These photons pair-produce with a mean free path of about 45 g-cm^{-2} to start the electromagnetic cascade.

The charged pions have a mean life at rest of about 2×10^{-8} sec. Those moving in the forward direction would have a mean life of about 4×10^{-3} seconds. Charged pions are nuclearactive particles which also interact with air nuclei with a MFP of about 80 g-cm^{-2}. These interactions are thought to be completely inelastic, e.g., no individual secondary can be identified by its exceptional energy to be the incoming particle. Again, of course, a fraction of the secondaries are neutral pions which add to the development of the EP cascade.

The primary nucleon, degraded in energy by about 50 percent, suffers additional interactions down through the atmosphere, in each case giving rise to more secondaries, a fraction of which are neutral pions. This is the prime source of sustenance for the electromagnetic cascade.

Such a shower develops to a maximum at about 7—8 km, where it contains about 5×10^5 relativistic particles. About 90 percent of these are electrons. Roughly, 10 percent are muons and about one percent are nuclearactive particles (energetic protons and charged pions). One nucleon (the degraded primary proton) may carry as much as 1-5 percent of the primary energy.

At sea level the shower may still contain about 2×10^5 particles. The muon component will be enhanced to perhaps 15 percent. While the nuclearactive component is also numerically enhanced, the mean energy is considerably lower. The most energetic nucleon will typically have on the order of 0.1 percent of the energy estimated as that of the primary.

Figure 2 gives a rough idea of the development of the electron component down through the atmosphere. It was generated on a computer using Monte-Carlo methods. Each of the individual cascades was produced by successive interactions of a primary proton ($E_0 = 10^{15}$) allowed to vary about interaction mean free path (I.M.F.P.) of 80 g-cm^{-2}. The amount of energy retained by the nucleon in each collision was also allowed to vary about a mean of 0.5 and a fixed fraction of the

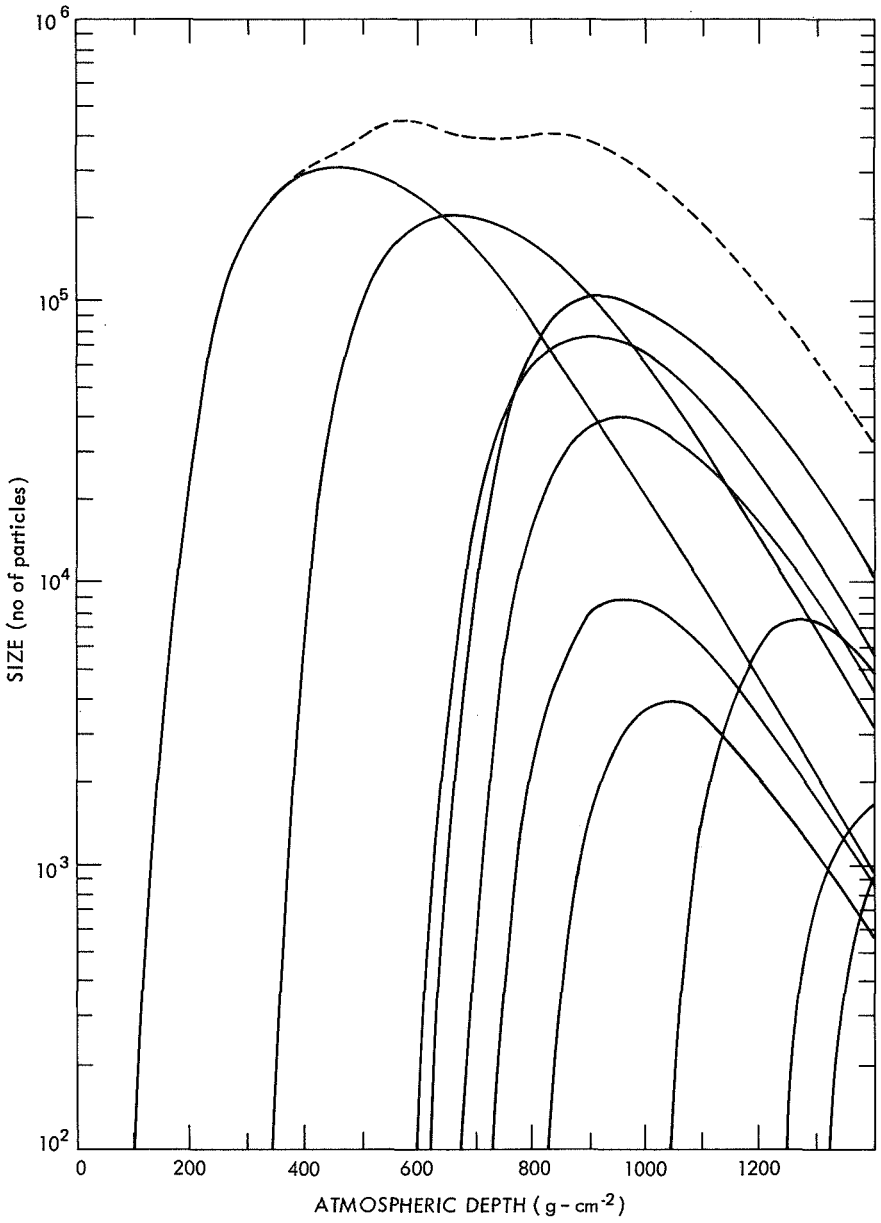

Figure 2–An example of a generated air shower showing the contribution of each nuclear interaction.

energy lost was assumed to go into the subsequent development of an electronic cascade (including those developed by secondary nuclear interactions of charged pions). The resulting composite shower is shown by the dashed line.

The lateral spread of the EP cascade arises principally from multiple Coulomb scattering. The highest density of particles is to be found near the projected axis of the primary particle (the core of the EAS). The mean energy of particles is also highest in this region, since the energetic nucleons that replenish the EP cascade are localized in the core. The density of particles tails off from the core roughly as R^{-1}, and about half the particles at sea level are to be found within 80 meters of the core.

The lateral spread of the muons that arise from charged pion decay is much broader than for electrons. Here the divergence arises principally from the transverse momenta imparted to the parent pions. The mean radius of the muons is several hundred meters at sea level. The lateral spread of the nucleons, on the other hand, is much less although the exact relationship critically depends on the energy threshold considered. However, essentially no energetic nucleons are found at distances greater than about 30 meters from the core.

The time spread of the EP cascade is several nanoseconds. Thus the shower front is only a few meters thick. The shower front has only a slight curvature (the radius is several kilometers). Heavier particles are delayed relative to this front by a factor which depends on their energy. Slow neutrons are not depleted by collision loss and may have delays of several microseconds. Muons are intermediate, with delays of up to 100 nanoseconds relative to the shower front.

THEORY AND EXPERIMENT

(See Nishimura, 1967; Rossi, 1952; Rossi and Greisen, 1941)

The Electromagnetic Cascade

Of all the processes involved in the development of an EAS, those governing the development of the EP cascade are best understood. The processes that contribute to cascade development and attenuation are the following:

1. For photons:
   a. Pair production,
   b. Compton scattering losses,

c. Photoelectric effect,
d. Photonuclear interactions.

2. For electrons:

a. Radiation (Bremsstrahlung),
b. Ionization losses,
c. Čerenkov radiation,
d. Direct pair production.

With the possible exceptions of 1.d and 2.d, the theoretical expressions for the above processes have been confirmed by experiments, and the basis for the theory has been shown to be sound.

Pair production and radiation are the main processes by which the electron-photon cascade develops. 1.b and 1.c have cross-sections that drop drastically at high energies. Ionization loss by electrons is the main attenuating factor in cascade development. Čerenkov losses are negligible by comparison.

In light (low Z) materials such as air, it is possible to separate the longitudinal and lateral developments of a cascade. The longitudinal development extends over several km down through the atmosphere, while the lateral displacement extends only over a few hundred meters. Thus deviations from a line source are insignificant.

A set of diffusion equations can be used to describe the number of electrons and photons of a particular energy at a given depth interval. All the above mentioned processes can be incorporated to describe the incrementation and depletion of particles in that differential interval. An analytic solution to the set of equations is possible only if certain simplifications are made. Only radiation, pair production, and ionization-loss processes are considered. Asymptotic expressions are used, valid for extremely high energies where complete screening by orbital electrons takes place. Ionization loss is considered a continuous process, and it is assumed to be constant instead of slightly energy-dependent.

A natural unit in which to measure thickness of material evolves from the asymptotic expressions for radiation and pair production. The radiation length, t_r, is physically the distance in which an electron of a certain energy ($E > 10^9$ eV) loses 1/e of this energy by radiation. For pair-production, the characteristic length (or mean free path) is

$$t_{pair} = 9/7\, t_r .$$

For air (with a correction to take into account the probability of the processes occurring in the electric field of the orbital electrons in addition to the field of the nucleus) the radiation length is 37.7 g/cm^2.

Another quantity of interest is the critical energy, e_c: the energy at which an electron loses equal amounts of energy by ionization and by radiation. For air, its value is 84.2 meV. This is also the value assumed in the cascade-theory approximation for the constant ionization loss per radiation length.

The semi-analytic solutions to the diffusion equations with the above simplifications have been labelled Approximation B. The solutions yield numbers and energy distributions of photons and electrons at various depths.

Figure 3 gives the most practical result of one of these calculations. It shows the number of electrons of all energies that arise from a photon of energy W_0, plotted against depth or thickness of air. The abscissa is shown in gms-cm^{-2}. More commonly the depth would be in radiation units.

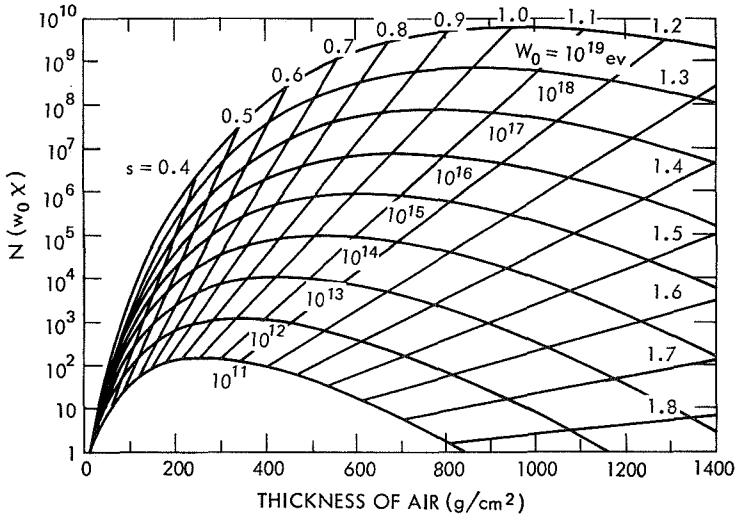

Figure 3–The total number of electrons as a function of the thickness g/cm^2 of air crossed, produced by photons of various energies, W_0, in eV.

The diagonal lines delineate age parameter, s. At shower maxima, s = 1. The depth at maximum development increases with increasing primary energy W_0.

The development curves may be approximated by an equation.

$$N(W_0, t) = \frac{0.31}{\beta_0^{1/2}} \exp\left[t(1 - 3/2 \log s)\right] ,$$

where t is measured in radiation units,

$$\beta_0 = \log \frac{W_0}{e_c} ,$$

and

$$s = \frac{3t}{t + 2\beta_0} .$$

The above figure is for a photon-initiated shower. An electron-initiated cascade would yield almost the same development curve. The development is shown starting from the point of the first interaction. The radiation length in air is only about 38 g-cm^{-2} and it is obvious that variations in the depth of the first interaction will contribute most to subsequent fluctuations in the cascade development.

The Lateral Development

(See Nishimura, 1967)

Energetic secondary electrons and photons are produced at very small angles to the direction of the parent particle. The predominant contribution to the displacement of the particles is multiple Coulomb scattering, in which the electrons undergo repeated small-angle scattering in the presence of the air nuclei. An occasional close encounter will result in a large scattering, but the probability of this is quite low.

Essentially, only the effect of multiple Coulomb scattering is taken into account in calculations of the lateral displacement. The characteristic

expression that gives the mean angle of scattering for an electron of energy E ($E \gg mc^2$) in crossing a thickness $\delta x = t/t_r$ is

$$\langle \delta\theta \rangle = \left(\frac{E_s}{E}\right) \delta x \ ,$$

where E_s is the scattering energy: 21.2 meV for air.

Usually, we want to know the lateral spread of electrons of all energies. For such a calculation, a natural unit is the spread of electrons of critical energy, e_c, since electrons below this energy are quickly absorbed. The scattering unit or Moliere Length, $R_1 = \left(E_{s/e_c}\right) t_r$, is the lateral distance an electron of energy e_c is scattered in traversing a thickness of one radiation length. For air, the value is 9.5 g-cm^{-2} or about 80 meters at sea level.

An implicit assumption in the calculations is that the shape of the lateral distribution depends only slightly on the energy of the initiating particle, provided that the cascades from different energy primaries are considered at the same stage of their development. Thus the local density at a distance r meters from the axis can be expressed as

$$\Delta(r) = \frac{N}{R_1^2} f\left(r/R_1, s\right) .$$

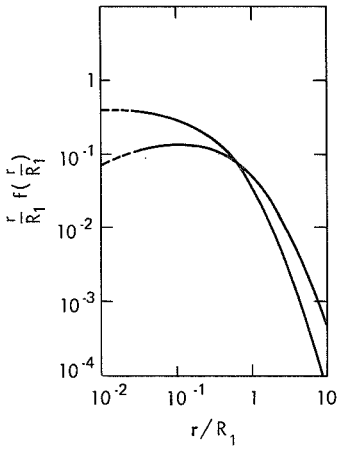

Figure 4–Lateral distribution of all electrons in showers at their maxima (s = 1) and in showers of age s = 1.4. The curves represent the calculations of Nishimura and Kamata (1951), made under Approximation B (see Greisen, 1956).

The calculations of Nishimura and Kamata are probably the most extended and accurate so far. They presented a distribution of electrons of all energies at shower maxima (s = 1) and for rather old showers (s = 1.4). Their distributions are shown by the solid lines in Figure 4, where $f\left(r/R_1, s\right)$ has been multiplied by r/R_1, since the function diverges at r = 0. (See Greisen, 1956.) The solid curves represent the calculations of Nishimura and Kamata (1951).

Greisen (Reference 1) has derived an empirical expression for the NK

distribution:

$$f\left(r/R_1,\ s\right) \;=\; C(s)\left(r/R_1\right)^{s-2}\left(1+r/R_1\right)^{s-4.5},$$

where $C(s)$ is chosen so that the expression is properly normalized, i.e.:

$$\int_0^\infty f\left(r/R_1,\ s\right) 2\pi\, r\, dr \;=\; 1\ .$$

The analytic expression probably describes the Nishimura-Kamata distribution fairly accurately for $0.6 < s < 1.6$. Over this range the normalization constant can be expressed by:

$$C(s) \;=\; 0.443s^2\,(1.9-s)\ .$$

Comparison With Experiment

Since EAS do not arise from electron or photon primaries, the above lateral distribution is of only passing interest except that it has been found to give a fairly good agreement with measurements on the lateral distribution. For showers ranging in size from about 10^4 particles to about 5×10^7 and from lower mountain altitudes (800 g-cm^{-2}) to 1800 g-cm^{-2} (EAS inclined at 55° at sea level), the N.K.G. distribution with the age parameter $s \cong 1.3$ fits the data within the limits of experimental accuracy.

There are some qualifications to this statement. Showers around 10^4 particles arrive frequently enough to intercept a core detector but have only a few particles-m^{-2} at a distance 10m from the core. Showers of 10^7 particles, on the other hand can only be detected at distances far from the core. The composite result can have only limited validity. However, it may be shown that a line source of photons with energy varying as $e^{-t/\lambda}$, where λ is the nuclear absorption MFP, leads to a lateral distribution with $s = 1.3$ at sea level if $\lambda \cong 150$ g-cm^{-2}, provided that we consider distances not less than several meters from the core.

Near the core, showers do show significant fluctuations that reveal nucleonic origin. Events have been recorded in which the distributions (up to 10m or so from the core) vary from $s = 0.6$ (very steep) to $s = 1.5$ (very flat). The obvious interpretation is that this detailed structure reveals the height above the observation level at which the last interaction took place. The variations do not greatly affect the overall-size estimate of the EAS.

A few percent of the showers studied in detail at this core also reveal a lumpy distribution that indicates transverse momenta imparted to the nucleons and pions in the nuclear interactions. If the lateral distribution of the subsidiary cores can be determined, an estimate of the transverse momenta can be made. Only events in which the imparted momenta are unusually large can be observed, so that it is the tail of the momentum distribution that is studied. The frequency of events with transverse momenta greater than 1 GeV-c^{-1} seems to be higher than that predicted from accelerator studies.

The Penetrating Component

(See Greisen, 1960)

The mu-meson component of EAS is due to the decay of charged pions and kaons arising from the many nuclear interactions in the atmosphere. The mean lifetime for decay of pions is only 2×10^{-8} seconds at rest, but for a 10^{12}-eV pion this is dilated by 10^4, which means that the pion can travel 60 km before decaying. Thus there is competition between decay and nuclear interaction, which depends on the energy and the density of the atmosphere through which the pions travel.

One consequence of this is that an EAS arising from a primary impinging at a large zenith angle will contain more muons than the EAS produced by the same primary arriving in the direction of the zenith.

Muons, of course, have lifetimes 100 times greater than the parent pions and essentially lose energy only by ionization. Thus the muon content in an EAS builds up to a maximum at a certain depth, below which the number is essentially constant.

Muons are considerably less abundant than electrons in the EAS. Near the core their number is about 1 to 2 percent of the total particle density, but the lateral distribution is much flatter, and beyond several hundred meters radial distance they are the dominant particles. The muons compose from 10 to 20 percent of the particles observed,

depending, of course, on the degree to which the shower has been attenuated.

Because the muon content is so much lower in the region usually observed in air showers (0—150m), their detection, though not difficult, is subject to large statistical uncertainties. What is quoted is usually an average obtained from samples of several thousand showers, grouped according to radius and size. It has been found that at sea level the larger showers are poorer in muons than are smaller showers. With a threshold of 1 GeV the muon content of EAS at sea level has been found to be proportional to $N^{0.75}$ from size 10^5 to 10^8 particles. This reflects the fact that smaller showers are more attenuated at the observation level than larger ones. It also probably reflects the altering nature of the conflict between charged-pion interaction-decay and increasing energy.

The lateral distribution of muons in the EAS is similar to the electron lateral distribution tailing off approximately as $r^{-0.75}$ near the core region. However the distribution becomes progressively flatter at larger distances from the core. The distribution is thought not to depend on shower size. On this assumption, a lateral distribution may be obtained from accumulated EAS data (Greisen, 1960). At sea level,

$$P(N, r) \cong 18\left(N/10^6\right)^{0.75} r^{-0.75} (1 + r/320)^{-2.5} .$$

Integration of this distribution shows that half the muons land at distances more than 320 meters from the core. The mean radius seems to be at 1600 meters, but this depends on the shape of the distribution in a region where it has not been measured.

Once a lateral distribution is obtained, it may be integrated to give the total number of particles. For the above distribution for muons above about 1 GeV,

$$N_\mu (>1 \text{ GeV}) = 95{,}000\left(N/10^6\right)^{0.75} .$$

The principal mechanism causing the lateral spread of the muons is the transverse momentum imparted to the parent pions in the nuclear interactions. Coulomb scattering plays a lesser (but not insignificant)

role. The observed lateral distribution is consistent with a transverse momenta distribution of from 0.2 to 0.7 GeV/c.

The energy spectrum of muons in the EAS is much flatter than unassociated muons in the cosmic radiation. A sea-level energy spectrum valid for shower size from perhaps 10^5 to 10^8 has been given as

$$N_\mu (>E, N) = 1.7 \times 10^5 \left[2/(E+2)\right]^{1.37} \left(N/10^6\right)^{0.75} .$$

The mean energy of the muons obtained from the above equation is about 5.5 GeV, and their total energy (of a shower of size 10^6) is 9×10^{14} eV. This is several times the energy carried by the EP component. It should be mentioned that the lateral distribution for muons is energy-dependent. The higher-energy muons are to be found progressively closer to the axis of the EAS and their lateral distribution steeper than that given above.

The Nucleonic Component

There is considerable nuclear debris in an air shower. Neutrons (even down to thermal energies) are particularly abundant since they are not removed by ionization. Low-energy protons are present, of course, as are heavier nuclei.

There have been some measurements in the MeV regions but most of the effort has been directed to measurements of particles, with energy over 1 GeV, that can contribute substantially to further shower development. These nuclearactive particles (NAP) consisting of nucleons, charged pions, and perhaps kaons, are found mainly in the core region of EAS. Their absolute number is everywhere low but the lateral distribution is critically dependent on the energy of the particles. Above 10^{12} eV the particles are usually within 2m of the core and are never found at radii greater than 5m. Particles of 10^{11} eV are usually within 10 meters of the core and are seldom found at distances greater than 30m.

There is therefore a basic difficulty in determination of the NA component. It is only found in the core region. At shower sizes much above 10^6 particles, the frequency of showers becomes too low for such measurements. At the lower sizes ($\sim 10^4$) the NAP component softens appreciably, and there are few if any particles with energies greater than 10^{11} eV.

Finally, there is a complication: large-area detectors having good spatial resolution and giving energy determinations at these energies are difficult to achieve.

For these reasons, the results cannot be as concisely stated as can results on the penetrating component. A few features can be summarized that apply to shower sizes between 10^4 and 10^6.

The number of NAP above one GeV can be given by $N_N \propto N^{\alpha}$, where N is the shower size. The index α is energy-dependent, varying from about 0.6 below 10 GeV to 1.7 at 10^{13} eV. Above one or two GeV, the relationship is

$$N_N \cong 0.35 N^{-0.6} .$$

The energy carried by the NA component at sea level is about equal to that of the EP cascade. For a shower of size 3×10^5 particles, each carries about 5×10^{13} eV. This energy balance seems to be maintained over the lower 30 percent of the atmosphere.

Gradually, more detailed information on the nucleonic component is being obtained. Figure 5 (Chatterjee et al. 1965) shows some fairly complete results obtained at lower mountain altitude (800 g-cm^{-2}) for nucleons above a few GeV. The lateral distribution of the nucleons is shown to become steeper with increasing size up to about 10^6, where it seems to flatten out. The solid lines drawn in the plots represent the distribution $r^{-\alpha_m}$ where the exponent is attached to each line. The investigators have further subdivided this data according to whether the electron lateral distribution is flat or peaked and have found a positive correlation between the shapes of the electronic and nucleonic distribution.

DETECTION METHODS FOR EAS

Most of the detectors used in EAS studies are common to other fields of nuclear physics. The majority of these detectors have been described in connection with topics other than those discussed in these notes. The detectors used in EAS studies differ mainly in that they are measured in square meters rather than square centimeters.

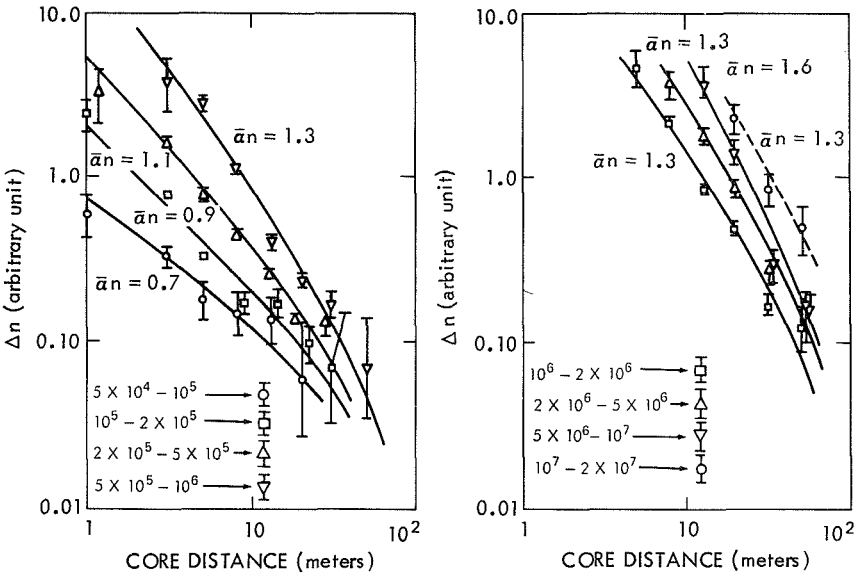

Figure 5–Average lateral distribution of N particles in showers of various size (Chatterjee et al., 1965).

Usually an EAS array consists of a combination of detectors of different type and is assembled in stages. Typically, one would first build up an array of unshielded particle detectors to allow detection of the EP component. Additional detectors are then added to make detailed core studies or to study the muon component. The detector array thus evolves gradually, and parts of it may be in use for ten years or more. It is not surprising that the techniques used are often rather dated.

Geiger Counters

The first detectors used for EAS studies were Geiger counters and they still find application in some installations. Counters constructed for air-shower use are typically thin cylinders of brass or glass with lengths ranging from 25 cm to 2m in length and with diameters from 2 to 10 cm. The detectors are usually the self-quenching type, in which an organic gas or a halogen is added to the primary gas to prevent positive ions from knocking electrons from the walls of the tube that would sustain the discharge. A Geiger counter gives only a yes or no answer as to whether at least one ionizing particle has passed through.

To determine the density of particles falling on a certain area, trays containing several Geiger counters must be used. The number of counters forming such a detector might range from several to as many as 50.

In determining a local density of particles with such a detector it is necessary to assume that the density, Δ, does not vary over the area of the detector and that the particles are spatially uncorrelated.

If Δparticles-m^{-2} is the mean density of particles falling on the detector, and each counter has an area S, then the average number of particles passing through a counter is ΔS. The probability of exactly m particles striking the detector is

$$P(m) = \frac{(\Delta S)^m e^{-\Delta s}}{m!} ,$$

and the probability that at least one particle strikes is

$$P(\geq 1) = \sum_{m=0}^{m=\infty} P(m) - P(0) = 1 - e^{-\Delta s} .$$

If there are ℓ similar counters in the tray, the probability that exactly k counters discharge while the remaining $\ell - k$ counters do not is:

$$P_1(k) = \frac{\ell!}{k!\,(\ell - k)!} \left(1 - e^{-\Delta s}\right)^k \left(e^{-\Delta s}\right)^{\ell - k} .$$

if ℓ is large (>7) and $\ell - k > 2$, then

$$P_1(k) \cong k/\ell \cong 1 - e^{-\Delta s}$$

so that

$$\Delta \cong \frac{1}{S} \ln \frac{\ell}{\ell - k}$$

gives a reasonable estimate of the local density.

More sophisticated approaches may be used to calculate the local density of particles. Detector trays are sometimes made up of large and small Geiger tubes, which, with proper analysis, give a satisfactory estimate of a very wide range of particle densities.

A discharging Geiger tube can produce a 10-volt output pulse. An EAS array may contain a few thousand tubes, in all. A simple readout system has been devised around 3-element neon glow lamps; the pulse from the tube is applied to a trigger element, turning on the lamp. A logically arranged panel of these lamps can be photographed to provide a record of the event. Alternatively, a system can be devised to read out directly to a form (e.g., paper tape) suitable for input to a computer.

The Wilson Cloud Chamber

The Wilson Cloud Chamber is a rather old-fashioned instrument that still finds applications in EAS studies. Basically it is simply an enclosure that includes a piston or diaphragm that can be suddenly released, allowing an adiabatic expansion of the gas (which includes a saturable vapor) inside the chamber. If the expansion is properly controlled, the gas inside is left in a supersaturated condition. Condensation takes place preferentially on any disturbance center, including dust particles or ionized molecules. Droplets are formed which grow in size with time, and the rate of growth is slow enough for the droplets to be a few tenths of millimeters in diameter after 20 or 30 milliseconds. Thus the slow mechanical expansion can be activated by counters through which the ionizing radiation has passed before entering the chamber (post-triggering). In fact, the long sensitive time of the chamber means that tracks left by unassociated cosmic rays passing through up to a second or so before the event complicate analysis. This can be alleviated by an electric field, which continuously sweeps ions from the chamber.

The chamber has glass or lucite side plates and the area is illuminated by a light pulse of short duration. Steroscopic cameras

record the droplet trails at this instant. An automatic cycling system then clears and recompresses the chamber, advances the film, and otherwise prepares the system for the next event. The recycling takes at least a minute for large chambers.

Cloud chambers are limited to areas of one or two square meters. They can never be made fully automatic for long periods of time. The analysis of the film records can be very slow for complicated events. Nevertheless the fine spatial resolution is second only to emulsions, and the visual record prevents ambiguities that would be present with any counter arrangement.

Cloud chambers, used to measure the local densities very near the core region of EAS, have revealed something about lateral distribution. They have also been used to determine the energy of the EP component at greater distances from the core. In this application, the cloud chamber is sectioned by inserted horizontal plates of steel or lead. Provided that the local density of particles is not too high, the cascade development of each electron or photon can be followed through the material, and the energy of the incoming particle measured.

Another application also involves a multiplate design. A cloud chamber may be used to estimate the energy of an NA particle. A nucleon or pion that interacts in one of the upper plates produces an EP cascade which develops in the lower plates; we can follow the development down through the plates by counting the number of charged particles at each level. Usually, only the electromagnetic cascade arising in the first interaction is observed, since it is difficult to incorporate more than two interaction lengths of the material in the chamber. The energy estimates thus depend on the fraction of the energy going into pion production. The fluctuations are known to be quite large.

At energies above 10^{11} eV another limitation is encountered. The particle density that develops is so concentrated that the chamber saturates. The individual tracks can no longer be distinguished. Alternate means of energy estimates can then be applied but these become more uncertain with increasing energy. The upper limit of usefulness is below 10^{12} eV.

Cloud chambers have been used with magnets to form spectrometers for measurement of the muon spectrum. Two cloud chambers, one placed above and the other below a piece of highly magnetized iron, can

resolve energies up to about 100 GeV. In general, spark chambers are now being used for such spatial-resolution studies.

Scintillation Detectors

Scintillation detectors are the most widely used device for EAS studies. The large areas required have limited the scintillation material to organic-liquid scintillators in which an organic scintillation material (fluor) is dissolved in an organic liquid solvent such as polyvinyltoluene, or in a plastic solvent such as styrene prior to polymerization. The organic solvents used initially were highly toxic and flammable, and performance of the solutions had a tendency to deteriorate with time. These drawbacks prompted the development of plastic scintillators that could be cast in large slabs a square meter or more in area. These detectors are by far the most convenient to use, although stable, non-toxic liquid scintillators have since been developed with solvents such as highly refined mineral oil.

The solute is present to only a fraction of a percent, so that it is the solvent that receives the excitation and ionization energy when a charged particle passes through. The available light output would be in the far ultraviolet and unusable. This excitation energy, however, is quickly transferred to the solute before quenching can occur. The energy is thus trapped in the solute and subsequently released as fluorescent radiation typical of the solute. A second solute called a wavelength shifter is often added in trace amounts. This fluorescent material shifts the spectrum produced by the primary solute to longer wavelengths, so as to more closely match the spectral response of the phototube.

A measure of the effectiveness of a scintillator is the energy of the light output in proportion to the energy lost in the scintillator. For an inorganic crystal (NATl) the value may be as high as 10 percent. For an organic liquid the value is closer to 1-2 percent. Various factors, such as the difference in the spectral distribution of light emitted to the spectral response of the photomultiplier tube, the transparency of the scintillator, and the efficiency of the light collection, reduce the actual light collected by at least another factor of 10 in any detector used in EAS studies.

Unlike inorganic crystal scintillators, organic scintillators exhibit no phosphorescence that prolongs the light pulse. The organic-liquid

scintillators have the shortest light output of all—about 5×10^{-9} seconds. Thus light pile-up is not a problem—at least in cosmic-ray studies.

The scintillator counts directly the number of particles passing through. In measuring a local particle density in the EAS, the response of the detector is the same, regardless of shower inclination, because the decrease in the projected target area for inclined showers is exactly compensated for by the increased track length for each incident particle.

An electron is minimum-ionizing at about 1 MeV, whereas the mean energy of shower electrons is ~100 MeV. Thus the majority of the electrons pass through with an ionization loss of about 2 MeV-g^{-1}-cm^{-2}. Landau fluctuations in the energy lost by a particle passing through the material mask any effect due to the slight energy-dependence of the ionization loss. Indeed, the only way to calibrate a scintillation detector above 100 MeV is to use the flux of cosmic rays in the atmosphere, and these are mostly muons. Figure 6 (Clark et al. 1961) shows a pulse-height distribution for a plastic scintillation detector. The geometry of the particular detector is shown in the inset. This geometry is particularly convenient and is in use in at least three installations. However the linearity from center to edge varies by almost a factor of two.

There is a basic difficulty in choosing from the pulse-height distributions the best pulse-height definition for a single particle. The mean of the near vertical spectrum (A + B) is undoubtedly the best level to use. However the median is much easier to obtain and differs but slightly from the mean.

For the particular geometry shower in the figure, it is noted that the median value for near vertical particles coincides with the peak of the omnidirectional spectrum. In operation, this spectrum is the only one that can be easily obtained on routine checks, and it is customary to use the peak value of this plot as the single particle definition.

Organic scintillators are low-Z materials that are thought not to disturb the shower flux appreciably. There is, however (Shibata et al., 1965), an anomalous effect that occurs in scintillators in measurements taken very close to the core region (0-5 meters). Cloud chambers, Geiger-tube trays and spark chambers give consistent density measurements in this region. Scintillators, though, give higher responses when compared to one of these other detectors. Figure 7 shows the

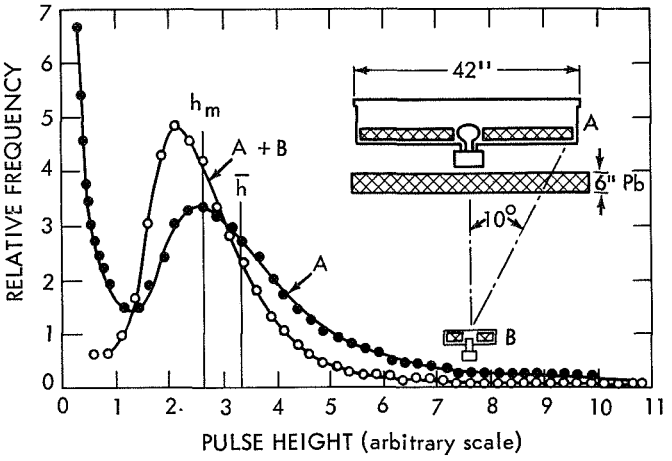

Figure 6–Differential distributions in size for pulses from a 42-in detector, with (curve A + B) and without (curve A) coincident pulses from another small detector under 6 in of lead. The inset is a schematic diagram of the 42-in detector, and the coincidence arrangement whereby pulses due to single penetrating particles were selected to obtain curve A + B. The vertical line labeled "h" marks the standard calibration pulse height defined so that the rate for pulses of height greater than h produced by uncollimated particles is 70 sec^{-1}. The vertical line labeled "h_m" marks the median height of pulses due to single penetrating nearly vertical particles. (Clark, 1961.)

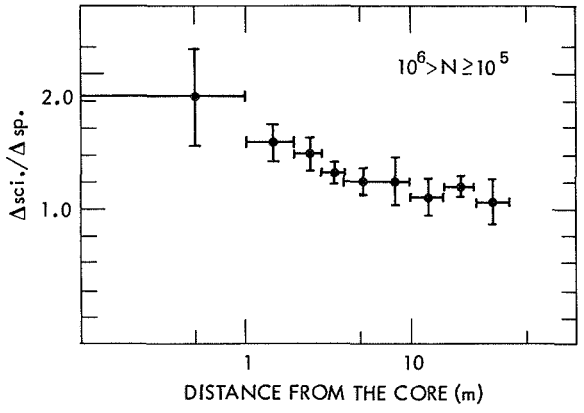

Figure 7–Variation of the average ratio of the densities counted by the scintillation counter and the spark chamber, as a function of distance from the shower axis. (Shibata, 1965.)

average ratio $\Delta sc/\Delta sp$ of a scintillator placed directly under a spark chamber. The effect is significant only at radii < 5 meters. The fluctuations in this ratio as shown in Figure 8 are quite pronounced; note, especially, some high values.

The phenomenon is not fully understood. The average energy of particles near the core is very high (>4.0 BeV) and the core contains a large number of high-energy photons. Thus the response is thought to represent EP cascading. An occasional nuclear interaction in the scintillator or in material above can account for the exceptionally high

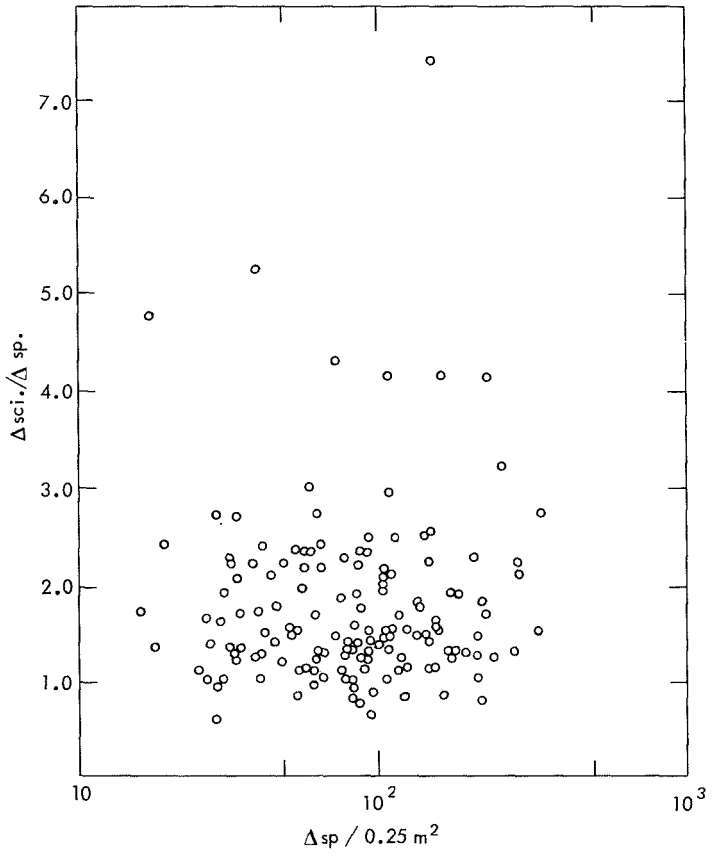

Figure 8–Ratio of densities counted by a scintillation counter and a spark chamber at radii ≤ 2 m. (Shibata, 1965.)

response obtained in a few cases. The spark chamber could not resolve the dense bundle of tracks.

The net affect of the scintillators' response is to cause an overestimate of the number of particles in the core. This could seriously affect results only for measurements of shower sizes less than 10^4, where only detectors within a few meters of the core can be used in size estimations.

Spark Chambers

(See Shibata et al., 1965)

Spark chambers have found wide application in cosmic-ray and high-energy accelerator studies. We mention one type that is unique to EAS studies: this concerns the detailed density measurements in the core of EAS. If the top plate of a narrow gap chamber is made of glass instead of metal (with a wire screen placed outside the glass serving as the electrode), the sparks can be photographed from above. This provides spatial resolution without the need for stereo views. The glass plate provides a high resistance and prevents the charge from dumping into a few spark tracks. Thus high track densities (up to $10^4/m^2$) can be achieved. Tracks separated by only a few mm can be resolved.

In this application, many units are laid out on the floor of a light-tight enclosure to form a detector of 10-20 m^2. The enclosure is high enough to contain one or two wide-angle cameras. Generally it must also be an electrically shielded room to prevent the intense RF noise of the pulses from disturbing the electronics of nearby scintillation detectors. Track efficiency is 100 percent, provided that the spark chambers are pulsed within a half microsecond after the passage of the shower particles.

Čerenkov Detectors

Energy-Flow Measurements

A large casting of optical-grade glass, with an unusually high concentration of a lead compound, can measure the energy flow of an EP cascade by causing each high-energy electron or photon to produce a local cascade in the glass. The lead additive reduces radiation length and lowers the critical energy to a few MeV. The casting is deep

(10-15 radiation lengths) and the local cascades essentially die out in the material. Since the threshold for Čerenkov radiation is only a few MeV, every electron produced by pair-production contributes to the light output which is thus proportional to the energy entering the detector.

In application, the number of electrons entering the detector is estimated by the response of adjacent scintillators. An energy per electron is determined in this way. The energy flow as a function of size or of distance from the core can then be determined from large samples of showers. Alternatively, the energy flow at a given size or radius can be compared for groups of showers in which some other parameter (such as muon content) indicates differences in primary composition.

Lateral Density-Distribution Measurements
(See Tenent, 1968)

Čerenkov detectors provide an attractive means of measuring local particle densities, especially in regions where there is a low flux of particles and the area of the detectors must be large. Large Čerenkov water detectors are being used in a sea-level installation to measure the flux of particles in large EAS ($>10^7$) at distances of several hundred meters from the core. At such distances the majority of the particles are muons, most of which have energies considerably in excess of the Čerenkov threshold in water ($\sim$60 MeV). An energetic muon (>1 BeV) loses about 220 MeV by ionization in passing through the one-meter depth of the tank.

A complication in interpreting the response of these detectors is that low-energy photons ($\sim$50 MeV) are also quite numerous at these large distances. In effect, the detectors measure the energy flow more directly than they count particles. A wavelength shifter may be added to convert some of the Čerenkov light to frequencies that better match the photomultiplier's response. The increase in response may be as high as four.

Ionization Spectrometers
(See Murzin, 1967)

Ionization spectrometers or calorimeters have been described elsewhere in this paper in considerable detail. The emphasis there is for compact devices that could be used on balloon or satellite platforms to measure directly the flux and nature of the primary cosmic radiation

above 10^{11} eV. Ground-based calorimeters are being used with and without EAS arrays to measure the flux of NA particles in the core region of air showers or, more directly, to use this flux of energetic hadrons to measure parameters (such as the cross section) involved in extremely high-energy interactions.

The devices are called calorimeters, since most of the energy of an incoming hadron is lost in the material though ionization. The absorbing material is most frequently iron, with detectors interspersed down through the layers to sample the ionization at various depths. As was mentioned, to absorb 90 percent of the energy of an "average" incoming proton requires about 7 interaction depths of absorber. The weight of the absorber will thus be about 1 kg/cm^2. Useful areas for ground-based calorimeters range from about 4 to 10 square meters; so the calorimeter weighs from 50 to 125 tons.

The detection layers may consist of trays of ionization chambers or proportional counters, or may be a large slab of scintillator. The first two instruments have the advantage of spacial resolution, especially if alternate layers have cross axes or if one detector consists of two crossed trays. If scintillators are used, a few spark chambers placed in the stack will provide some spacial resolution. It is important to know whether part of the energy leaks out of the sides of the chamber or whether, especially in the core of an EAS, other energetic particles are entering from the side.

No matter how good the ability to trace the local burst of particles through the stack, the results of a calorimeter event are truly unambiguous only when a single energetic hadron enters the chamber. The core region of an EAS is difficult to treat since there may be several energetic nucleons or pions intercepting the chamber. There is also a dense flux of the energetic EP cascade that must be eliminated by shielding, part of which is the upper layers of the chamber itself.

In attempts to measure parameters involved in elementary processes, an accurate energy determination is needed, and the identity of the incoming particle is important. Events are selected by means of a scintillator telescope placed above the calorimeter; those are selected in which not more than one particle is recorded as entering the chamber. This mode preferentially selects nucleons from air showers that have died out in the atmosphere above. By using the air shower array in anticoincidence, we can select events in which there are no accompanying particles. At mountain altitudes and over a narrow energy region,

such triggering selects, with a high probability, residual primary protons that have not interacted in the atmosphere. If the interaction mean free path is 80 g-cm^{-2}, then at 560 gm-cm^{-2}, e^{-7} or about 0.1 percent of the primary proton component will remain. The usefulness of this method extends from about 5×10^{11} to 5×10^{13} eV. It could be extended to lower energies, provided that some way were devised to distinguish nucleons from charged pions.

AIR-SHOWER INSTALLATIONS

For Small-to-Moderately-Large Showers ($10^4 - 5 \times 10^7$)

As an example of an air shower installation, designed to record a wide range of shower sizes, the array of detectors on Mt. Chacaltaya in Bolivia is described. (See Suga, 1962.)

The altitude of the station is 17,600 ft. At this altitude the atmospheric cover (530 g-cm^{-2}) is only half that at sea level. Attenuation of showers by the atmosphere is much less, and showers from primaries above 10^{16} eV are observed near maximum development. Showers arising from primary protons as low as 5×10^{13} eV can be sensibly recorded at this altitude.

In arranging detectors to form an array there are conflicting requirements. For large showers, low intensity is the problem; detectors must enclose a large area but may be placed fairly far apart. For smaller showers, counters must be placed more closely but the sensitive area need not be as great.

Figure 9 shows the layout of the array. There are 20 density detectors. Five are at the center and five each in rings at 15, 40, and 150 meters radius. Each of these detectors consists of a disk of plastic scintillator of 0.85-meters area and 10-cm thickness viewed by one 5-inch photomultiplier tube. At the center of the array there are additional detectors designed to measure the muon and nucleonic component. Figure 10 shows the central installation. Characteristic of the array is a 60-m^2 shielded muon detector with 4-m^2 resolution. The shielding is 320 g-cm^{-2} of concrete and lead ore (galena), which means that muons above 600 MeV can be detected. Each 4-m^2 unit is viewed by a 15-inch photomultiplier tube.

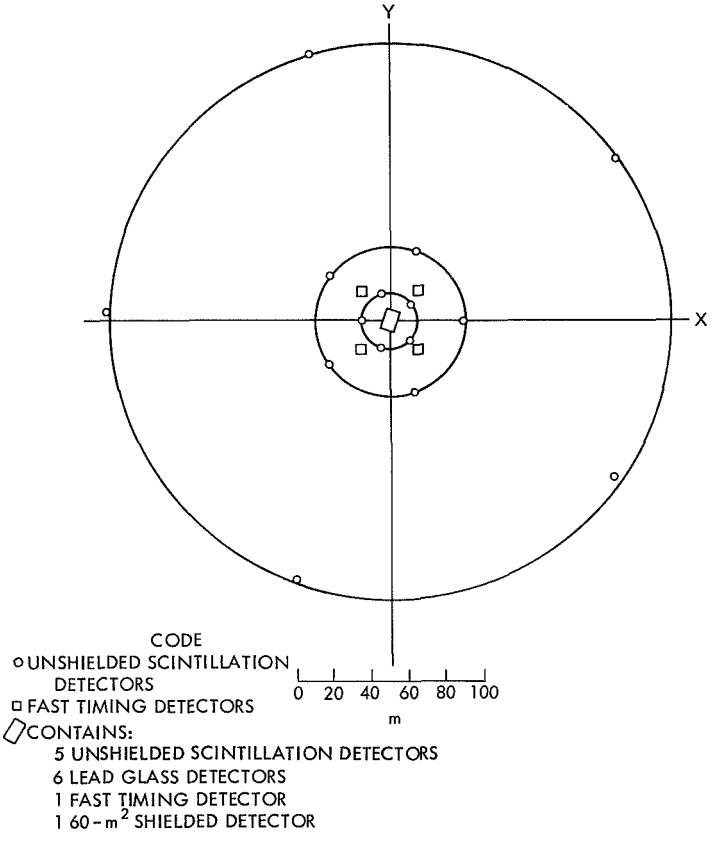

Figure 9–Example of an air shower array.

Additional detectors include several lead-glass Čerenkov detectors which are 12 radiation units deep. They provide the means of sampling the energy content of the EP cascade.

The tower supports one of five timing scintillators. The others are 10 meters lower on a square of 30 meters/side. The time differences (measured to a few nanoseconds) provide the means of deriving the arrival direction of the shower front which, to a good degree of accuracy, may be considered a plane. Typically both the zenith and azimuthal angles may be determined to ±5 degrees.

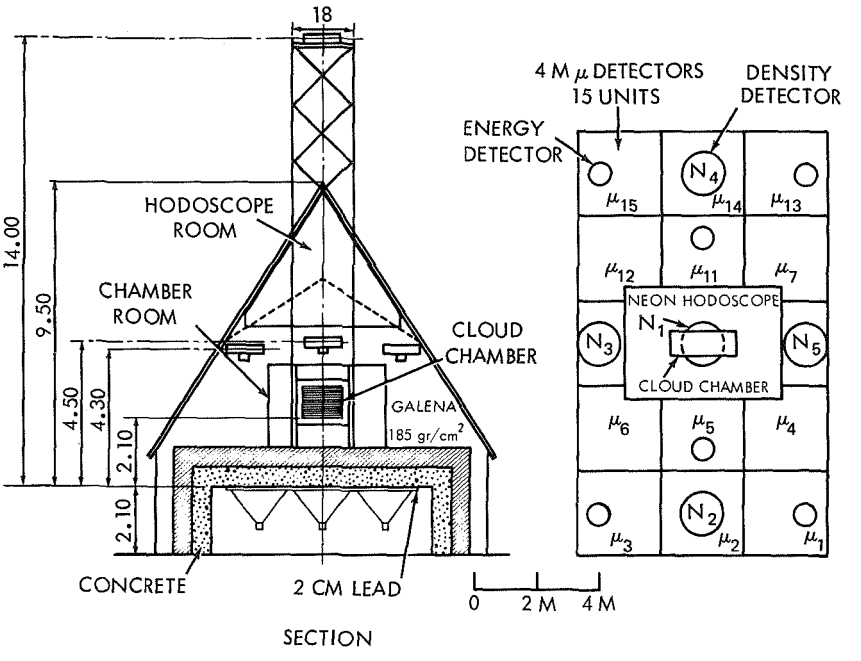

Figure 10–Central array.

Additional detectors include a multiplate cloud chamber that samples the nuclearactive component in the shower core, and a grid of narrow-gap spark chambers for detailed core studies.

The electronics for amplifying and recording air showers need not be very fast but must have a wide dynamic range to register equally well the passage of one or several thousand particles passing through a detector.

A single ionizing particle produces about one mV signal at the anode of the photomultiplier. A preamplifier at the site amplifies by 10 and provides a low-impedance output to drive the long signal cables. Main amplifiers at a central location amplify the signal by an additional 300. A decay time constant (~10 microsec) established by the RC load at the anode of the photomultiplier is carefully preserved throughout the system. The exponentially decaying pulse activates a Schmidt discriminator which remains on for a length of time proportional to the logarithm of the pulse amplitude. This height-to-time conversion remains accurate, even though the signal driving the Schmidt saturates at

a few particles. The rectangular pulses from the various detectors gate open digital scalers to a 1-Mc clock-pulse. The scalers hold the counts until they are read out sequentially by stepping switches which drive a paper-tape punch and an output typewriter.

Ionizing particles pass through the individual detectors at the rate of ~1,000-second^{-1}. These are uncorrelated cosmic rays and must be held off from the scalers. It is possible to select, for recording, showers whose local density exceeds a certain level by demanding a coincidence of amplitude signals from these detectors taken from an appropriate point in the amplifier chain. The logarithmic output pulses are delayed by a few microseconds to allow this coincidence enough time to enable the scalers to signal the arrival of a suitable air shower. This gate pulse cannot be too short, since particles in the shower front arriving at the distant detectors may have time differences of several hundred nanoseconds. Even for vertical showers, differing cable delays introduce appreciable time differences.

Readout time with this particular system requires 20 seconds. This dead time is not an inconvenience provided it is held constant and is precisely known. Showers of about 10^4 particles arrive at the rate of several/min (over a radius of 10 meters) and knowledge of the dead time is essential in deriving the true rate.

Arrays for Very Large Showers (>10^8)

An installation designed to study events of size 10^8 and above is necessarily simpler in concept and objectives than one for smaller sizes. A shower of size 10^8 at maximum development represents a primary energy of about 2×10^{17} eV. A glance at the primary energy spectrum (Figure 1) shows that the rate of such showers is too low to make any core-region measurements. Only the EP and muon components can be sampled, and these at large distances from the core.

For the size of a detected shower to be reasonably estimated, its core must land within the perimeter delineated by the outer detectors of an array. The rate of events of size 10^9 and above is so low that the arrays used to detect them have dimensions measured in kilometers rather than meters.

We briefly describe the array that was used to determine the primary energy spectrum above 10^{18} eV (Linsley and Scarsi, 1962).

This array was in operation in New Mexico from about 1960 to 1963. The altitude of the station was approximately 2,000 meters above sea level (820 g/cm^2). Showers arising from 10^{18} eV primaries are near maximum development at this altitude.

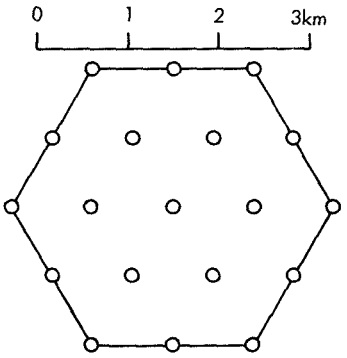

Figure 11–Geometry of the Volcano Ranch air shower array. (Each detector area = 3.5m^2.)

Figure 11 shows the layout of the array, which encompasses about 3.5 square miles. Each detector is a plastic scintillator of 3.3 m^2 area. The arrangement was designed to give a well-defined boundary and give similar status to all areas within the boundary.

The relative arrival times of the signals, and the pulse height information from each detector, are recorded. In this way the arrival direction of each shower may be determined without the errors that would arise from shower-front curvature.

For showers as large as this, most density measurements are made at several hundred meters from the core. The lateral distribution used to determine the size of the showers must be determined from the showers themselves. Enough showers were collected, between 10^8 and 10^9, to construct a semi-empirical distribution and to note the dependence of the distribution on shower size. The results were then extrapolated to sizes of 10^{10} particles and above. The distribution at distances less than 70-80 meters from the core could not be determined but were assumed to vary as R^{-1}, as predicted by cascade theory.

The results of this survey with this array will be reported later. They are of sufficient significance in the light of certain astrophysical predictions (which continuing efforts are being made to verify) and to extend the measurements to even higher energies. One such array being constructed in Australia (Brownlee et al., 1968), has an area of about 40 km^2 and contains about 40 stations with two scintillation detectors at each station. A novel but necessary step in the design was one which freed each station from being tied into a central location by transmission lines. Each station is entirely independent and records on magnetic tape the particle densities recorded in the detectors each time a threshold level is exceeded. Calibration information is

also recorded, as is a time signal constantly supplied by a radio link. The time correlation is made by computer and is so precise that arrival directions of the showers may be determined.

ANALYSES OF AIR-SHOWER DATA

Derivation of the Primary-Energy Spectrum

From 10^{15} to 10^{18} With Data From the Chacaltaya Array
(Bradt et al., 1965)

Showers at maximum development are expected to show much smaller fluctuations than when observed at lower altitudes where the EP is attenuated. Thus certain size showers recorded at maximum development supposedly represent more uniquely a definite primary energy. Figure 12 represents the results of

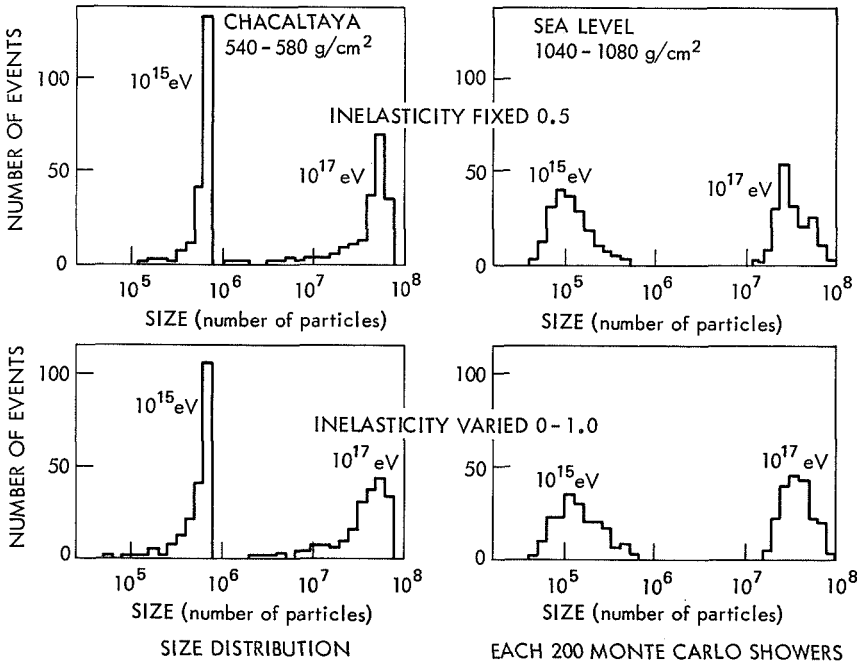

Figure 12–Size distribution of generated showers at two energies. Distribution at the depth of Chacaltaya and at sea level.

a Monte-Carlo calculation which illustrates this. The distribution of shower sizes resulting from a 10^{15}-eV proton primary observed at a depth of 540 g-cm^{-2} is much narrower than the same showers observed at sea level (1030 g-cm^{-2}).

To determine the primary energy spectrum, showers were collected in several periods of operation ranging from several days to about two years. Each run was obtained with a different triggering threshold level since characteristically only a small range of shower sizes will be efficiently collected with a particular setting.

Each shower was processed by an iterative least-squares fitting process to the NKG distribution, yielding a size and core location. The age parameter used for each size range was that determined to provide the best fitting for a sample of showers in that size range.

The processed showers were grouped by size; a distribution of frequency-versus-radius is plotted from each grouping to determine the area over which the triggering efficiency was 100 percent for that interval. Showers falling within this area were the only ones used for subsequent analysis.

From the effective areas and running times, size spectra or frequency-versus-size plots were then derived for showers grouped according to zenith angle- or slant-depth-intervals. The depth intervals were so chosen that each encompassed the same solid angle. Figure 13 shows the integral spectrum for near-vertical showers at Chacaltaya, and Figure 14 shows a comparison of inclined showers, recorded at Chacaltaya ($1.2 < \sec\theta < 1.3$), with vertical showers recorded at a lower altitude in a preliminary experiment (4300 m). This favorable comparison was reassuring since the array at lower altitude was quite different in design and size.

Figure 15 shows the combined size spectra at different depths. The idea behind the analysis is that the integral intensities at various depths in the atmosphere delineate threshold showers arising from primaries of the same energies. By making intensity cuts on the size spectra, longitudinal development curves of a sort are delineated as shown in Figure 16. From these curves it may be inferred that only at sizes above 10^6 are showers at maximum development at 5,200 m.a.s.l.

Figure 17 shows the size at maximum development.

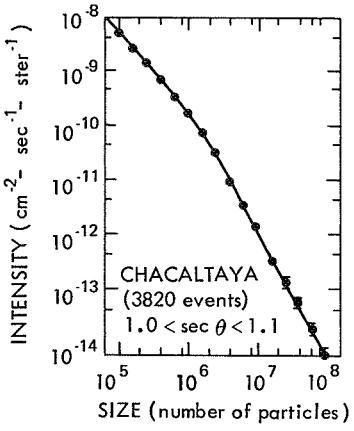

Figure 13–Air shower integral size spectrum at 5,200m altitude.

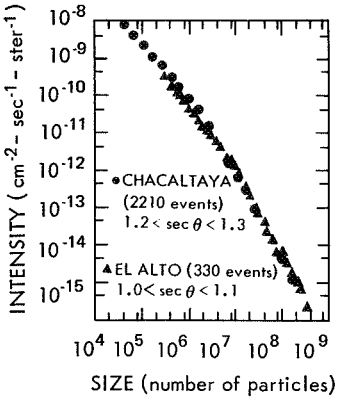

Figure 14–Air shower integral size spectrum at 4,300m altitude.

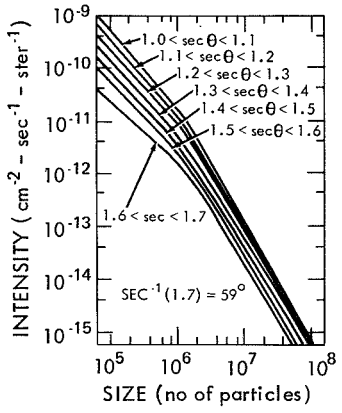

Figure 15–Air shower integral size spectra at various atmospheric depths.

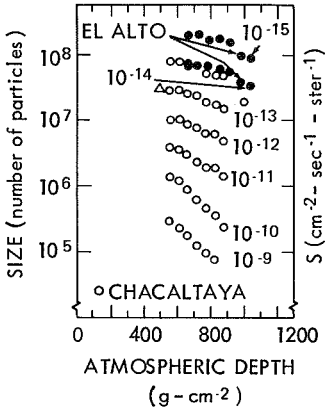

Figure 16–Longitudinal development curves obtained from constant-intensity cuts of size spectra at different atmospheric levels.

The last step in obtaining a primary energy spectrum is merely to convert from maximum size to primary energy. Most models predict an almost linear relationship of close to $E_0 = 2 \times 10^9 N$ (max). A slight

energy dependence does steepen the spectra slightly. For this reason the exponent of -2.15 in the size spectrum becomes -2.2 in the energy spectrum. This spectrum is shown in Figure 18.

The Energy Spectrum Above 10^{18} eV

The energy spectrum above 10^{18} eV is derived mainly from the results of the Volcano Ranch experiment in New Mexico (Figure 11). Showers above 10^{18} eV are at or near maximum development at the atmospheric depth of this site (820 g-cm^{-2}), and at these energies the maximum should extend over a large range of depths. By assuming that all showers recorded are at maximum development, a lower limit is set on the energy spectra. On this basis alone, the upward bend in the spectra (returning to an exponent of -1.6) seems convincing.

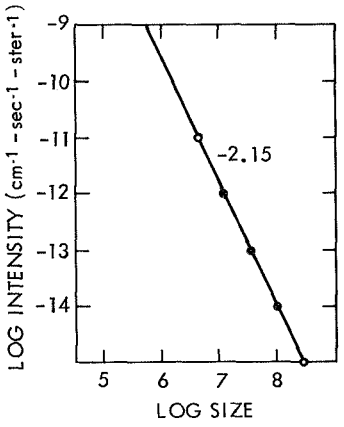

Figure 17—Integral intensity vs size at maximum.

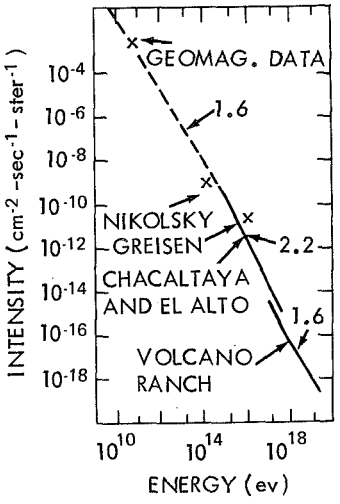

Figure 18—Integral energy spectra of primary cosmic rays obtained from EAS studies. Crosses indicate estimates of the flux based on the total measured energy carried by the various components of air showers of a given size plus estimates of the total energy dissipated in the atmosphere above the observation level.

There were few showers recorded with energy greater than 10^{19} eV (only 7 events were recorded estimated with size greater than N = 10^{10} in about three years of observations). A difficult task is making an accurate size estimation for each shower. This was done conservatively, in that the shower size was more likely underestimated than overestimated. A possible source of the flattening spectra might be that at these energies the production mechanisms in nuclear

interactions might be changing in such a way that shower production becomes more efficient.

It is usually assumed that if the flattening spectrum does indeed represent the primary energy spectrum, then this represents the spectrum of extragalactic cosmic rays. The muon content of these showers was also recorded; by studying the fluctuations in the muon densities for a given shower size, it may be inferred (from the narrowness of the fluctuations) that the composition of the primaries is fairly pure. The primary cosmic rays in this energy region are either nuclei in the iron group or mainly protons. Another test favors the second alternative, which is consistent with extragalactic origin.

Other Detection Methods and Analyses

General Survey

We have covered what might be called the classical detection methods used in air shower studies and touched upon the approaches one uses in analyzing the data. In this second category, the most serious omission has probably been not mentioning the attempts to determine the primary composition in the EAS region. The results seem to indicate that the composition remains similar to that around 10^{12} eV, at least up to 10^{15}–10^{16} eV. However, the analyses are somewhat model-dependent and are subject to large uncertainties and should not be considered conclusive.

A shower formed by a primary nucleus of mass number A and total energy E_0 is essentially a composite of A showers each of energy E_0/A. Iron nuclei will certainly first interact closer to the top of the atmosphere then will protons; we could probably distinguish between these two if the primary radiation did not include particles with all intermediate mass numbers. If complete breakup of the primary nucleus occurs in the first interaction, the composite picture is most valid. The resulting shower would probably have a shorter attenuation length in the atmosphere, in spite of fluctuations. However, individual showers can not be measured at two depths to determine the attenuation length.

The lateral destributions of the EP cascade may differ for a proton and an iron shower, but this is hard to determine since even pure-proton showers should exhibit large fluctuations in this parameter.

An approach that has yielded results has been to examine the distributions in either the muon or the nucleonic component. A high-Z primary should be richer in muons than a proton primary. The muon component from any shower is expected to build up to a maximum flux which is thereafter essentially flat over large depths. It is therefore less subject to depth fluctuations than the EP cascade. With the limitation that one is everywhere dealing with low densities, the muon flux probably does sensitively reflect the nature of the primary. One must, however, compare the muon densities for showers in a region of given size. A few percent of the showers certainly arise from much more energetic primaries than the median energy for this size range. They, of course, will be richer in muons and will appear as events arising from high-Z primaries.

The study of the nucleonic component relies on other parameters for the composition estimates. Again, however, the fluctuations in shower development make predictions extremely difficult.

Regarding other methods of EAS detection, at least four possibilities are being explored.

Čerenkov Light From EAS
(See Jelley, J. V., 1967)

The cascade of electrons in the atmosphere produces a considerable column of Čerenkov light which, because of the low index of refraction, is strongly collimated in the direction of the shower path. The techniques of examining this light have been highly developed. Since we are collecting light from a large depth interval we feel that the light flux more closely reflects shower development than any particle measurement at a certain depth. Some estimates of composition have been made from the study of the Čerenkov light, but the chief application of this phenomenon has been to look for point sources of primary gamma rays. Since the light observed originates high in the atmosphere, the detection threshold is lower ($\sim 10^{12}$ eV) than EAS arrays. The high rate at these low energies means that likely sources can be examined in a few scans.

Scintillation Light From EAS
(See Bunner, 1968)

Another mechanism which produces radiation in the visible region is the process of ionization and ion-recombination in the atmosphere.

The intensity is only about 10^{-2} of Čerenkov radiation and the light is isotropic rather than collimated. Nevertheless, the process can yield detectable amounts of light from giant air showers ($>10^{19}$ eV) at great distances from the shower axis. The method offers an attractive possibility for examining the upper limits of the spectrum with considerably less complexity than using a conventional EAS array would entail.

Radio Pulses From EAS

Bursts of radio noise have been detected in coincidence with EAS at frequencies ranging from 20 to 100 MHz. The recorded showers were of sizes corresponding to primary energies of 10^{15}—10^{16} eV; in the various measurements that have been made, typically only a few percent of the showers recorded were accompanied by radio pulses much above the rms noise background.

Several mechanisms have been proposed to explain the phenomenon and possibly each contributes to the radio pulses (Reference 9). One mechanism is coherent Čerenkov radiation by the negative-charge excess that occurs in the shower front as positrons are annihilated in flight. Another theory predicts that charge separation due to the earth's magnetic field produces a dipole which radiates coherently. This theory also predicts an additional component which arises from a transverse polarization current that flows between the ends of the dipole to maintain this current against losses by electron capture.

Again, our interest in the radio technique lies in the possibility of developing it into an independent method of detecting giant air showers. This method is particularly attractive since it would not demand dark, clear skies, as do the Čerenkov and scintillation techniques.

Radio Echo Technique

(See Matano, et al., 1968)

Another method which is being explored for the detection of giant air showers is the radio echo technique. An air shower leaves behind a trail of ionized atoms. The recombination time for the ions is several minutes, and the ionization column reflects radio waves as does the earth's ionosphere. The present experiment makes use of a LORAN radio beacon which transmits pulses isotropically.

REFERENCES

General Articles and Monographs

Bradt, H., Clark, G., LaPointe, M., Domingo V., Escoban, I., Kamata, K., Murakami, K., Suge, K., and Toyoda, Y., "The Primary Energy Spectrum from 8×10^{14} eV—4×10^{17} eV," Proc. Ninth Internat. Conf. on Cosmic Rays 2:715-717, 1965.

Brownlee, R. G., Fisher, A. J., Goorerich, L., Kohn, P. C., McCusker, C. B. A., Ogelman, H. B., Parkinson, A. F., Peak, L. S., Rathgeber, M. H., Ryan, M. J., and Winn, M. M., "Design of an Array to Record Air Showers of Energy up to 10^{21} eV^1," Canad. J. Phys. 46(10), Pt. 2:259-262, May 15, 1968.

Bunner, A. N., Greisen, K., and Landecker, P. B., "An Imaging System for EAS Optical Emission," Canad. J. Phys. 46(10), Pt. 2:266-269, May 15, 1968.

Chatterjee, B. K., Murthy, G. T., Naranan, S., Sreekantan, B. V., Srinivasa Rao, M. V., Tonwar, S. C., and Vatcha, R. H., "Correlations Between the Electron, Muon and N Components in Extensive Air Showers," Proc. Ninth Internat. Conf. on Cosmic Rays 2:734-737, 1965.

Clark, G. W., Earl. J., Kraushaar, W. L., Linsley, J., Rossi, B. B., Scherb, F., and Scott, D. W., "Cosmic-Ray Air Showers at Sea Level," Phys. Rev. 122(2):637-654, April 15, 1961.

Cocconi, G., in "Handbuch der Physik," vol. 46/1, ed. by S. Flügge, Berlin: Springer-Verlag, 1961.

Galbraith, W., "Extensive Air Showers," London: Academic Press, 1958.

Greisen, K., "The Extensive Air Showers," in "Progress in Cosmic Ray Physics," vol. III, ed. by J. G. Wilson, Amsterdam: North-Holland, 1956, pp. 1-141.

Greisen, K., "Cosmic Ray Showers," in "Annual Review of Nuclear Science," vol. 10, ed. by Emilio Sergrè, Palo Alto, Calif.: Annual Reviews, Inc., 1960, pp. 63-108.

Suga, K., J. Phys. Soc. Japan 17:128- X, Suppl. A-III, 1962.

Ögelman, H. B., NASA Special Publication 199, 1969.

Linsley, J., and Scarsi, L., "Arrival Times of Air Shower Particles at Large Distances from the Axis," Phys. Rev. 128(5):2384-2392, December 1, 1962.

Matano, T., Nagano, M., Suga, K., and Tanahashi, G., "Tokyo Large Air Shower Project," Canad. J. Phys. 46(10), Pt. 2:255-258, May 15, 1968.

Nishimura and Kamata, 1951.

Shibata, S., Nagano, M., Matano, T., Suga, K., and Hasegawá, H., "Fine Structure of Air Shower Cores Observed with 20 m^2 Spark Chamber," Proc. Ninth Internat. Conf. on Cosmic Rays 2:672-675, 1965.

Tennent, R. M., "Experimental Facilities at the Haverah Park 500-m EAS Array," Canad. J. Phys. 46(10), Pt. 2:1-4, May 15, 1968.

Cascade Theory

Nishimura, J., in "Handbuch der Physik," vol. 46/2, ed. by S. Flügge, Berlin: Springer-Verlag, 1967.

Rossi, B., "High-Energy Particles," New York: Prentice-Hall, 1952.

Rossi, B., and Greisen, K., "Cosmic-Ray Theory," Rev. Mod. Phys. 13(4):240-309, October 1941.

Ionization Calorimeters

Murzin, V. S., in "Progress in Elementary Particle and Cosmic Ray Physics," vol. IX, ed. by J. G. Wilson, New York: John Wiley, 1967, pp. 247-311.

Air-Shower Čerenkov Radiation

Jelley, J. V., in "Progress in Elementary Particle and Cosmic Ray Physics," vol. IX, ed. by J. G. Wilson, New York: John Wiley, 1967, pp. 39-156.

VI. RADIO-ASTRONOMICAL OBSERVATIONS OF HIGH-ENERGY PARTICLES

Thomas A. Clark
Radio Astronomy Branch
Goddard Space Flight Center
Greenbelt, Maryland

INTRODUCTION

In this paper we shall briefly explore the contributions to high-energy astrophysics at the lowest end of the energy scale: the radio photons. As this is only a brief survey, we shall restrict our comments to a few specific areas:

The general concepts of radio astronomy

- Basic definitions - flux density, brightness, noise, temperatures, etc.
- Simple radio telescopes - dishes and arrays
- Interferometers

Non-thermal radio emission and absorption processes

- Thermal processes, H II absorption
- Synchrotron radiation
- Synchrotron self-absorption
- Particle energy losses

Radio observations of galactic cosmic ray electrons

Radio observations of extra-galactic objects

- The normal galaxies
- The "abnormal" objects - QSOs and radio galaxies

In this brief survey we cannot discuss other items of current interest, most notably pulsars, line emission and absorption (Neutral Hydrogen, OH, H_2O, NH_3, CH_2O), and cosmology, etc.

THE GENERAL CONCEPT OF RADIO ASTRONOMY

Astronomers and archaeologists have a handicap in common: they act only as observers, while their counterparts in the other sciences act as experimenters. This is true even today, after the advent of Radar Astronomy and space probes. The (radio) astronomer must observe the electromagnetic (E-M) waves originating in an object of interest, as modified by the intervening medium (including the terrestrial atmosphere); and as further modified by his instrument. In general, there are a total of eight observable parameters that completely specify the nature of the E-M signal:

1. I	The four Stokes' parameters, which specify the intensity and state of polarization of a signal.
2. Q	
3. U	
4. V	
5. α	Two position (angle) coordinates, which specify a location on the celestial sphere.
6. δ	
7. f (or ν)	Frequency (or its reciprocal λ = wavelength).
8. t	Time.

Once the complete specification of a signal in terms of these parameters is achieved, the task of the observational astronomer is finished and only the theoretician can perform. Fortunately this state of completeness is unobtainable.

Intensity Parameters, Temperature, Noise

In the ensuing discussion we shall assume that the state of polarization is random. This assumption eliminates three of the required parameters from consideration. This is not to imply that polarization observations are unimportant; many crucial observations can only be made ignoring this restriction. In general, a more complete specification of the state of polarization is important in a description of any radiation

process involving magnetic fields, as is the case for most celestial objects. Let us now define some basic parameters.

In Figure 1 we show the basic geometry used in defining the intensity parameters. The energy flow dE(f) per unit interval of time in the frequency band from f to f + df through an elemental area dA from a region on the celestial sphere dΩ in the direction P is

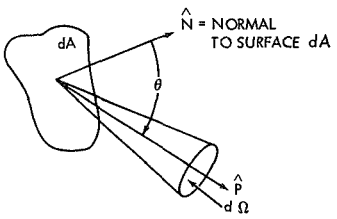

Figure 1–Defining the flow of radiation from a region of angular size dΩ in a direction P through a surface dA.

$$dE(f) = I(f)\,(dA\cos\theta)\,df\,d\Omega\,dt\,df\ ,$$

where θ is the angle between the surface normal N and the direction P. In radio astronomy we typically use power flow rather then energy flow and refer to our collecting apertures in terms of projected area $dA' = dA\cos\theta$, so that

$$dP(f) = \frac{1}{2}\,I(f)\,dA'\,d\Omega\,df\ ,$$

where P(f) is the power dE(f)/dt, and factor of 1/2 is included because a typical collecting aperture (antenna) receives only one of two possible polarizations. Since we have assumed that the signal is unpolarized, the power flow is equally divided between these two degrees of freedom. The quantity I(f) is usually called specific intensity or brightness. Units of I(f) are usually given in watts meter^{-2} steradian^{-1} (cycle/second)$^{-1}$ (= w m^{-2} ster^{-1} Hz^{-1}). In the case of discrete radio sources where the integral

$$\int_{\text{source}} I(f)\,d\Omega$$

can be well defined, the quantity

$$S(f) = \int_{\text{source}} I(f)\,d\Omega = \frac{2dP(f)}{dA'\,df} \qquad (1)$$

is called the flux density with units $w\,m^{-2}\,Hz^{-1}$. Another very common unit of convenient size for radio astronomical use is

$$1 \text{ flux unit} = 10^{-26}\, w m^{-2}\, Hz^{-1} . \tag{2}$$

In this discussion we shall restrict our discussion to wide-band (continuum) sources for which we may regard the power flow $P(f)$ as a constant over the band of frequencies received. In this case,

$$\int I(f)\, df \rightarrow I(f)\, \Delta f ,$$

where Δf is the receiver bandwidth. This restriction is not valid for sources that emit over narrow bandwidths, as in most spectral line observations of neutral hydrogen, OH, etc. We also express

$$\int dA'$$

as an equivalent effective collecting area which we denote A_{eff}. Thus the total power intercepted will be

$$P(f) = \frac{1}{2}\, \Delta f\, A_{eff} \int I(f)\, d\Omega \text{ for large sources} ,$$

or

$$P(f) = \frac{1}{2}\, S(f)\, \Delta f\, A_{eff} \text{ for small sources} . \tag{3}$$

If we place the area A_{eff} inside a blackbody of temperature T, as in Figure 2a, the laws of thermodynamics require that the specific intensity (brightness) in the above equations be given by the Planck

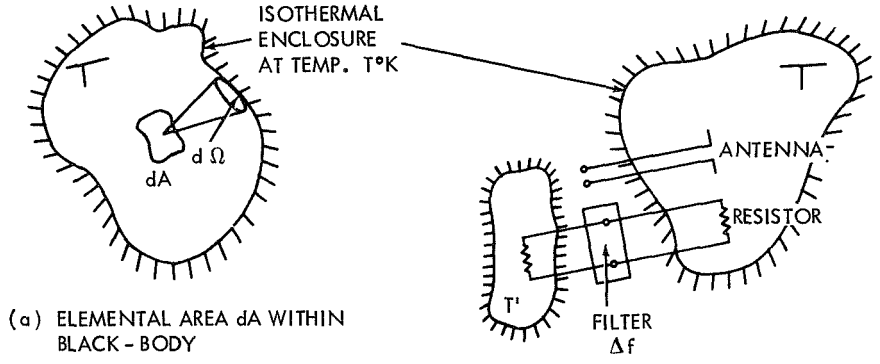

Figure 2–Temperature concepts used in radio astronomy.

function

$$I(f) = \frac{2hf^3}{c^2}\left(e^{hf/kT} - 1\right)^{-1},$$

where h = Planck's constant (6.62×10^{-34} mks), and k = Boltzmann's Constant (1.38×10^{-23} wHz^{-1}°K^{-1}). In the radio case f $\lesssim 10^{10}$ Hz (λ = 3 cm) to 10^{11} Hz (λ = 3 mm) so, if T $\gtrsim$10°K, hf/kT << 1 and we are under the regime of the Rayleigh-Jeans law, where

$$I(f) = \frac{2kT}{c^2} f^2 = \frac{2kT}{\lambda^2}. \qquad (4)$$

In radio astronomy it is conventional to refer to brightness temperature defined as above, even if the spectrum of the source in question is nonthermal. In such a case, the brightness temperature T_B is frequency-dependent. Since our receivers measure the power P(f) and we know Δf and A_{eff}, we usually write the above equations as

$$S(f) = 2P(f)/(\Delta f\, A_{eff}),$$

$$I(f) = 2P(f)/\Delta f\, A_{eff}\, \Omega_s,$$

$$T_B(f) = P(f)\left(\lambda^2/k\,\Delta f\, A_{eff}\,\Omega_s\right), \tag{5}$$

where Ω_s is the equivalent solid angle subtended by the source. We also frequently use the concepts of temperature in our measurement of $P(f)$.

Consider the case analogous to that shown previously, wherein we replace the elemental area dA with a resistor; we can extract power from the system and transfer it to another enclosure at some lower temperature T′. If we wait sufficiently long, T′ will increase and T decrease until they become equal. The power that flows from the higher temperature enclosure is $=2\ kT\,\Delta f$, where Δf is the width of the frequency band that can be transferred via the wires interconnecting the two systems. We may also regard Δf as the number of independent samples of T which are made in a unit interval of time (i.e., the number of degrees of freedom for the system). An ultraviolet catastrophe is avoided since the thermal radiation field has little energy (under the Planck-law regime) at frequencies $f \gtrsim kT/h$. In a similar fashion, the resistor in the second enclosure returns an amount of power equal to $2\ kT'\,\Delta F$, and the net power transfer is $2k(T - T')\,\Delta f$ with the direction of the flow from the higher temperature, T, to the lower, T′. If we had used an antenna instead of a resistor, the same considerations would be applicable, except that the antenna then transfers energy from the electromagnetic field at radio frequencies rather than from the thermal heating of the resistor. If the second enclosure were a radio receiver, then the thermal resistor and antenna case would be indistinguishable (assuming that the resistance of the resistor, the feed impedance of the antenna and the characteristic impedance of the interconnecting transmission line were matched). This is how radio-astronomy receivers are calibrated; the input to the receiver is switched between the antenna and a resistor at a known (usually cryogenic) temperature. The power delivered by the antenna to the receiver is frequently referred to as an antenna temperature T_{ant}, where

$$P(f) = K \cdot T_{ant} \cdot \Delta f\,,$$

where we again include the factor of 1/2 to account for the antenna being sensitive to only one of two orthogonal components. In general, T_{ant} is a function of frequency. Therefore our equations given earlier

can also be expressed in the form

$$S(f) = 2K\,T_{ant}/A_{eff}\,,$$

$$I(f) = 2K\,T_{ant}/A_{eff}\,\Omega_s\,,$$

$$T_B(f) = T_{ant}\,\lambda^2/A_{eff}\,\Omega_s\,. \qquad (6)$$

As we shall discuss later, the solid angle of the antenna beam will be

$$\Omega_{ant} = \frac{\lambda^2}{A_{eff}}\,,$$

so the above could also be written

$$I(f) = \frac{2K \cdot T_{ant}}{\lambda^2} \cdot \frac{\Omega_{ant}}{\Omega_s}$$

and

$$T_B(f) = T_{ant} \cdot \frac{\Omega_{ant}}{\Omega_s}\,. \qquad (7)$$

In radio astronomy we deal with noise signals. This is to say that the characteristics of the signal have all of the properties of a stationary random variable: zero mean value, non-zero variance (the square of which is a measure of power flow), and Gaussian amplitude distribution. It is convenient to consider that our noise arises from an ensemble of independent oscillators which have uncorrelated amplitude and phase characteristics. Such a model is physically realistic, since the observed radiation properties usually reflect the aggregate properties of a number of independent radiating particles. Such a model for a noise signal indicates that if the signal (i.e., the voltage at the terminals of an antenna) were Fourier-analyzed, it would be of the form

$$V(t) = \sum_{n=n}^{n_2} A_n \cos\left(2n\,\Delta f_0\,t + \phi_n\right)\,,$$

where Δf_0 is a small unit-frequency interval utilized in the analysis, A_n is a normally distributed random variable with a mean square value $\langle A^2 \rangle$, and ϕ_n is random and equally likely to be anywhere in the range $\{0, 2\pi\}$. Since the mean value of $\cos^2 x = 1/2$, the mean square value of this ensemble is

$$\langle V^2 \rangle = \sum_{n=n_1}^{n_2} \langle A_n^2 \rangle \frac{1}{2} = \frac{n_2 - n_1}{2} \langle A_n^2 \rangle = \frac{\langle A^2 \rangle}{2} .$$

Thus this model does have a power $V^2 \propto (n_2 - n_1)\, \Delta f_0 \propto$ (bandwidth). The power contained in each frequency interval Δf_0 is $\langle A_n^2 \rangle / 2$. By invoking the Weiner-Khinchine theorem,* we can show that a signal of this form will have an auto-correlation function of the form

$$\rho(\tau) = \langle V(t)\, V(t-\tau) \rangle = 2 \int_{f-\Delta f/2}^{f+\Delta f/2} P(f) \cos(2\pi f \tau)\, df ,$$

where

$$f = \frac{n_2 + n_1}{2} \Delta f_0 = \text{the mid-frequency of the passband} ,$$

$P(f) = \langle A_n^2 \rangle / 2$, and

$$\Delta f = (n_2 - n_1)\, \Delta f_0 \text{ is the bandwidth of the system} .$$

It can be shown that if $P(f)$ is constant over Δf and zero elsewhere, this integral is of the form

$$\rho(t) \propto \langle A_n^2 \rangle \Delta f \frac{\sin(2\pi \Delta f t)}{2\pi \Delta f t} \sin 2\pi f t ,$$

*The Weiner-Khinchine theorem may be stated: "The auto-correlation function of a stationary variable and its power spectrum are (cosine) Fourier-transform pairs."

which oscillates with a period $1/2\pi f$ and decays in a time $\sim 1/\Delta f$. Thus we may say that the signal remembers its character for a time interval $1/\Delta f$, and hence there are Δf independent samples of the noise signal each second. If we observe for t seconds, we have $N = \Delta f t$ samples of the signal. For a random variable, the variance of a measurement (in this case of power) is $\Delta P/P = 1$ for a single observation and

$$\frac{\Delta P}{P} \sim \frac{1}{\sqrt{N}} \sim \frac{1}{\sqrt{\Delta f t}} \tag{8a}$$

for a series of measurements. We should like to define a typical detection as a deflection larger than ~3-5 standard deviations, so the minimum detectable signal is

$$P_{min} \sim \frac{5P}{\sqrt{\Delta f t}} . \tag{8b}$$

In radio astronomy, the largest contribution to P often comes from noise added by the receiver rather than from the object under observation or from the sky. Let us denote the noise added by the system as an equivalent temperature = T system. Then

$$T_{min} \sim \frac{5T_{system}}{\sqrt{\Delta f t}}$$

is the minimum detectable antenna temperature. Thus we have the detection criteria

$$S_{min} \sim \frac{10\,kT_{system}}{A_{eff}\sqrt{\Delta f t}} ,$$

$$I(f)_{min} \sim \frac{10\,kT_{system}}{\Omega_s A_{eff}\sqrt{\Delta f t}} ,$$

$$T_B(f)_{min} \sim \frac{5T_{system}}{\sqrt{\Delta f t}} \frac{\Omega_{ant}}{\Omega_s} . \tag{9}$$

Simple Radio Telescopes, Dishes, and Arrays

Without going into great detail, let us briefly discuss some of the types of radio telescopes in use. The simplest to visualize is the dish or parabolic mirror. For a physically filled aperture, uniformly illuminated over its extent, a beam of size

$$\theta = \frac{k\lambda}{d} , \tag{10}$$

where $k \sim 1$, and θ is the FWBN (full-width to first nulls) in radians, will be formed. For a two-dimensional, circular, symmetric aperture, the beam has a circular cross-section and $k = 1.22$. The solid angle subtended by this beam is approximately

$$\Omega_A \lesssim \pi \left(\frac{\theta^2}{2}\right) = \pi k^2 \frac{\lambda^2}{d^2}$$

$$= \left(\frac{\pi}{4}\right)^2 k^2 \frac{\lambda^2}{d^2} \simeq 0.9 \frac{\lambda^2}{A_p} ,$$

where A_p is the physical area of the dish. This relation is usually written in the form

$$\Omega_A = \frac{\lambda^2}{A_{eff}} , \tag{11}$$

where A_{eff} is the effective collecting area and takes into account the effects of surface roughness, uniformity of illumination of the aperture, etc. Besides dishes we often use arrays of individual dipole radiators of lower frequency. These phased array antennas serve the same function as a dish.

In strict detail, it can be shown that the voltage-sensitivity (= $\sqrt{\text{power sensitivity}}$) pattern of an array is given by the two-dimensional Fourier transform of the aperture illumination. We here invoke the concept of spatial frequencies (see next section) by noting

that antennas of scale size n-wavelengths respond to structure in the sky which has a component in its angular spectrum at $1/n$ cycles per radian.

Interferometers

General Review

An interferometer consists of two or more elements (frequently, though not necessarily identical) separated by a large distance. Figure 3 shows some typical systems. We observe at a frequency f with a bandwidth Δf_0, which are defined by the use of band-pass filters in the receiving equipment. We observe a source which makes an angle θ with the plane perpendicular to the baseline. First consider the adding interferometer, as shown in Figure 3 (a) and (b). The extra path-length $d \sin\theta$ is examined to compare the phase of the signals at points 1 and 2 of the receiver. Maxima are observed if $d \sin\theta = n\lambda$, and minima if $d \sin\theta = n\lambda + 1/2$, where $n = 0, \pm1, \pm2, \pm3 \ldots$. Therefore, the angular interval between maxima is given by

$$\sin\theta_n - \sin\theta_{n-1} = \frac{\lambda}{d},$$

or, if θ is small,

$$\Delta\theta = \frac{\lambda}{d} \text{ radians}. \tag{12}$$

The pattern can be analytically expressed in the form

$$P(\theta) = 1 + \cos\left(\frac{2\pi d}{\lambda} \sin\theta + \phi\right), \tag{13}$$

where ϕ is an instrumental phase term. The sinusoidal fringes of this interferometer are added to the deflection that would obtain if we used only one antenna. Deflections are always positive. If the source were large compared with the interval between fringes, the fringes would wash out; this condition is known as resolving the source. The ratio of fringe amplitude to the amplitude obtained when $\lambda/d \ll$ the angular

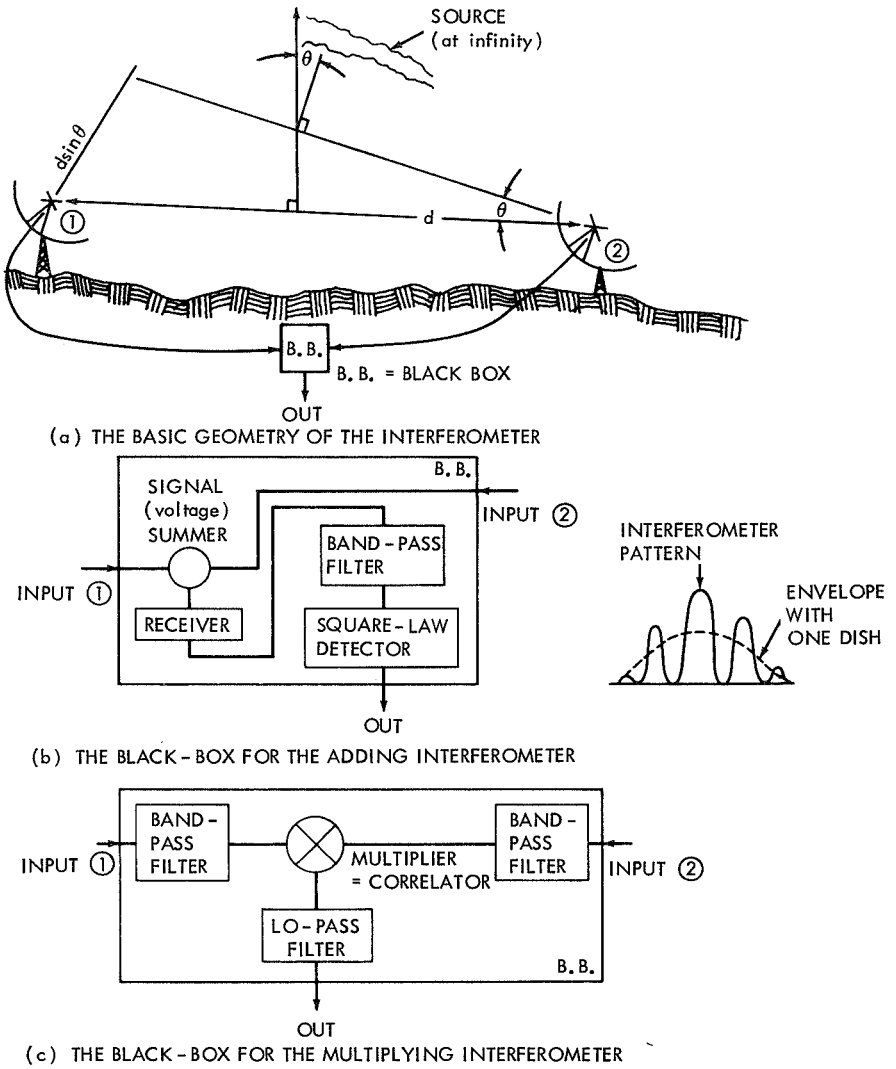

Figure 3–Interferometry.

size of the source is a measure of the size of the source; this ratio is particularly sensitive to sources with sizes $\sim\lambda/d$.

The offset due to the background, i.e., the total power received by the antennas, can be a confusing factor. We often work on sources whose antenna temperatures $\sim 10^{-4}$ of the (system + sky) temperature contributions. To avoid this hang-up, we use the multiplying or correlating interferometer (a familiar term in the literature is switched interferometer = phase switching; this is one of several types of correlating interferometers). Here the signals are brought together and multiplied. It can be demonstrated that this operation cancels background terms due to receiver noise and the structure of the sky that $>\lambda/d$. For this device, the pattern is of the form

$$P(\theta) = \cos\left[\frac{2\pi d}{\lambda}\sin\theta + \phi\right]. \qquad (14)$$

Aperture Synthesis

The notion that the fringes of an interferometer as projected on the sky are periodic with a period of d/λ cycles per radian now introduces us to one of the most powerful techniques the radio astronomer has at his disposal. Consider the situation shown in Figure 4. In A we show five sources denoted a - e. The sizes are chosen such that $a < b < c < d < e$. The size of source c equals one period of the interferometer fringes in B. In C we show the typical outputs that would be obtained with the interferometer for the various sources. Now suppose that instead of five sources we had changed the baseline d/λ and that the five sources in A are all the same. Case c would correspond to that spacing of the elements at which the lobe spacing equals the size of the source, in d we have moved the elements to 1-1/2 times the spacing in c, in e to ~ 2 times that in c, etc. In D we plot the variation in fringe amplitude (and phase) observed as the elements were moved. The curve in D is called a (complex) fringe visibility function. It can be shown that the Fourier transform of this function is precisely the (one-dimensional) brightness distribution of the source (in this case, a uniform line source which is the Fourier transform of the $\sin x/x$ curve in D). These concepts can be extended to two-dimensional maps of the source (or sky) utilizing the projection effects that occur as the earth rotates.

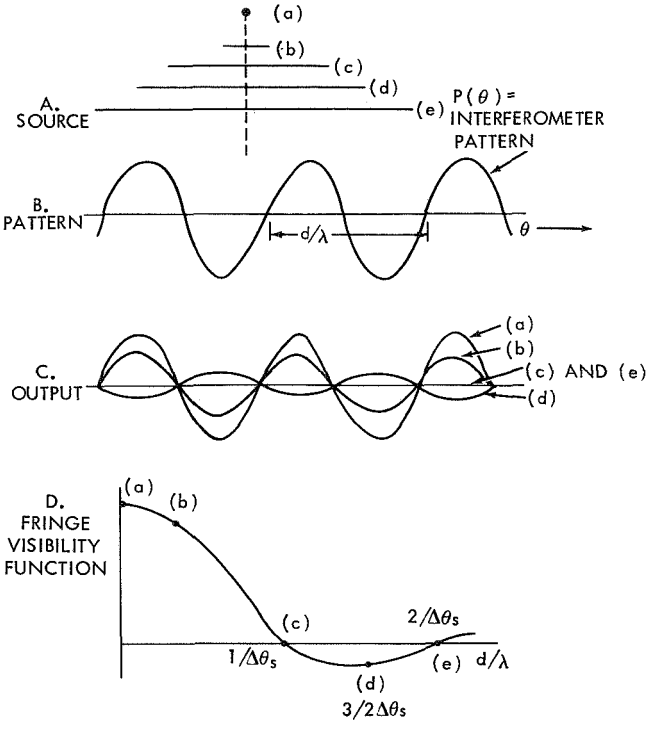

Figure 4–Aperture synthesis.

VLB (Very Long Baseline) Interferometry

A related technique is the VLB interferometry observation (some results are discussed further on). Here we use baselines of many thousands of km. Obviously the scheme shown in Figure 3 (which shows wires connecting the antennas) is ill-adapted to these long baselines. The technique employed is to use very stable oscillators (usually rubidium-vapor or hydrogen maser standards) at each station. These oscillators heterodyne the incoming signals to a much lower frequency, i.e., 20-350 kHz in the system developed by the National Radio Astronomy Observatory (NRAO). The noise signals (which would then be fed to a correlator in the close-spaced case) are fed into digital magnetic-tape recorders along with timing information derived from the same standard oscillators.

The magnetic tapes are brought together weeks or months later and correlated at one location. The NRAO system uses a high-speed digital computer for correlation. With this system we obtain baselines $\sim 10^8\ \lambda$ which yield fringes spaced at ~0.001 seconds of arc (the angle subtended by a football 40,000 miles away). This technique is used in the study of very small-diameter radio sources—QSO's (quasi-stellar objects) and similar sources.

NON-THERMAL RADIO EMISSION AND ABSORPTION PROCESSES

Before discussing the interpretation of radio astronomical data in terms of the properties of the relativistic particles responsible for the emission, we shall briefly discuss how they radiate and how the radiation field interacts with the medium between the emitting particles and the earth. For additional details see the excellent review article by Ginzberg and Syrovatskii (1965).

Thermal Radio Emission and Absorption Processes; the Equation of Radiative Transfer

Thermal radiation arises from the kinetic motion of particles. If the body (ensemble of particles) is opaque, the radiation (to the radio astronomer, the brightness temperature) from such a blackbody will be given by the Planck function (or at $f << kT/h$, the Rayleigh-Jeans formula)

$$I(f) = \frac{2hf^3}{c^2}\left(e^{hf/kT}-1\right)^{-1} \simeq \frac{2kT}{\lambda^2}\,.$$

with units $w\,m^{-2}\,Hz^{-1}\,ster^{-1}$.

Let us now consider the equation of radiative transfer. We first define the following numbers:

K = linear absorption coefficient with units m^{-1} ($= \kappa\rho$ where κ is the atomic absorption coefficient and ρ is the number density of particles),

ϵ = volume emissivity with units $w\,m^{-3}\,ster^{-1}\,Hz^{-1}$ (= brightness increment added in each unit length of path),

S = source function ϵ/K,

z = the distance parameter used,

τ = optical depth = $\int K\,dz$,

Ω_r = solid angle subtended by a receiver as seen by the emitting region (= A_{eff}/Z^2),

Ω_{ant} = solid angle on sky subtended at the receiver.

We first consider the brightness which would be observed in the absence of absorption (K = 0). See Figure 5. The volume of the shaded region containing the emitters in question is

$$dV = (\text{area of end of cone}) \cdot dz' = Z^2\,\Omega_{ant}\,dz' .$$

The region dV therefore emits a power

$$dP_{emitted} = \epsilon\,dV = \epsilon\,Z^2\,\Omega_{ant}\,dz'$$

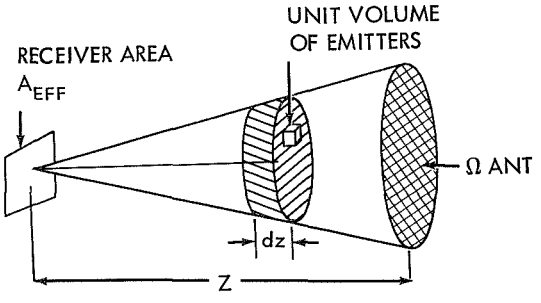

Figure 5–Emission with no absorption.

into one steradian. Of this power, a fraction $\Omega_r = A_{eff}/Z^2$ is received in the unit area of the receiver; so the received power is

$$dP_{received} = \frac{A_{eff}}{Z^2} dP_{emitted} = \epsilon \Omega_{ant} A_{eff} dz$$

and the observed brightness

$$I_0(f) = \int_0^Z \epsilon \, dz = \epsilon Z; \text{ if } \epsilon \neq \epsilon(z) . \tag{15}$$

Now let us include absorption. Our definition of absorption coefficients is such that if an absorbing slab of thickness z were inserted (see Figure 6) in the path between a background source with an intensity I_B, the observed intensity would become

$$I_B' = I_B \exp\left(-\int_z K \, dz\right)$$

$$= I_B e^{-KZ} = I_B e^{-\tau}.$$

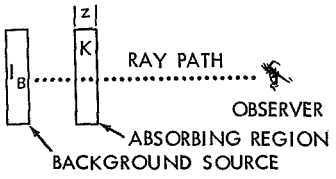

Figure 6—Absorption in a slab.

Now consider a more general condition, wherein we allow the emitting and absorbing regions to be mixed, and include a background (see Figure 7) with brightness I_B. For each slab of thickness dz, the unabsorbed brightness would be $\epsilon \, dz$, and it would be reduced by a factor e^{-KZ} to account for the absorption. The background I_B is attenuated by the full e^{-KZ}. Hence the observed brightness will be

$$I(f) = I_B(f) e^{-KZ} + \int_{z=0}^{Z} \epsilon \, e^{-KZ} \, dz$$

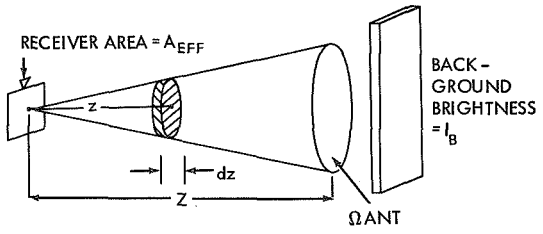

Figure 7–The general case of radiative transfer–emitting and absorbing regions mixed.

or

$$I(f) = I_B e^{-KZ} + \int_0^Z \frac{\epsilon}{K} e^{-KZ} K\, dz$$

$$= I_B e^{-\tau_0} + \int_0^{\tau_0} \frac{\epsilon}{K} e^{-t}\, dt ,$$

(where t is a dummy variable of incremental optical depth). It is customary to define the source function $S = \epsilon/K$ as the ratio of the linear increment of brightness in the absence of absorption to the linear decrement of brightness due to absorption.

$$\therefore I(f) = I_B e^{-\tau_0} + \int_0^{\tau_0} S(t)\, e^{-t}\, dt \qquad (1$$

is the usual form of the equation of radiative transfer. If $S \neq S(z)$, that is, if the emitting and absorbing particle are mixed with a const

ratio, then

$$I(f) = I_B e^{-\tau_0} + \frac{\epsilon}{K}\left(1 - e^{-\tau_0}\right) = I_B e^{-\tau_0} + S\left(1 - e^{-\tau_0}\right) . \quad (17)$$

The term ϵ/K could also be written

$$\frac{\epsilon}{K} = \frac{\epsilon Z}{KZ} = \frac{I_0(f)}{\tau} ,$$

where $I_0(f)$ was derived in Equation 15 as the unabsorbed intensity from the same region. Thus we could write

$$I(f) = I_B(f) e^{-\tau_0} + I_0(f)\left(\frac{1 - e^{-\tau_0}}{\tau_0}\right) , \quad (18a)$$

which for $\tau_0 \gtrsim 5$ ($e^{-\tau_0} \lesssim 7 \times 10^{-3}$), called the optically thick case,

$$I(f) = \frac{I_0(f)}{\tau} . \quad (18b)$$

Also note that if we were to consider as a scale distance $z_1 = 1/K$ corresponding to $\tau = 1$,

$$\frac{\epsilon}{K} = \frac{\epsilon z_1}{K z_1} = \epsilon z_1 .$$

Thus, for large τ_0 and neglecting I_B,

$$I(f) = \epsilon z_1 \left(1 - e^{-\tau_0}\right) \simeq \epsilon z_1 . \quad (18c)$$

That is, with an optically thick region the observed brightness will equal the brightness that would be observed in the absence of absorption

with a limited emitting region of thickness $z_1 = 1/K$ corresponding to $\tau = 1$. Even if the region is not optically thick, but has $\tau > 1$, only a small error (in the astrophysical sense) is made with this assumption; for example, the following correction factors are applicable.

Table 1. Correction Factor vs Optical Depth

τ_0	$(1 - e^{-\tau_0})$
0.1	0.095
0.25	0.221
0.5	0.393
0.75	0.528
1	0.632
1.25	0.713
1.5	0.777
1.75	0.826
2	0.865
2.5	0.918
3	0.950
5	0.993
10	0.99995

Let us now discuss the nature of the absorption coefficient K due to the action of free-free transitions in a thermal, ionized Hydrogen (HII) medium. For an electron density N_e (cm^{-3}), an observing frequency f (MHz) and a kinetic temperature T_e,

$$K \simeq \frac{10^{-19}}{f^2}\left(T_e^{-3/2}\right)\left(3.9 + \ln\frac{T_e^{3/2}}{f}\right)N_e^2 .$$

It is customary to express the distance parameter in parsecs (1 pc = 3.1×10^{18} cm) and to call the parameter $\langle N_e^2 Z\rangle$ the emission measure (after the optical properties of HII emission nebulae). We further approximate the log term for usual temperatures (100-10^4°K) and low frequencies ($\lesssim$100 MHz) and rewrite the above equation.

$$\tau(f) \simeq \frac{4 \cdot 10^5}{f^2}\left(T_e^{-3/2}\right)\langle N_e^2 Z\rangle . \quad (19)$$

This type of absorption is particularly important at low frequencies. We shall return to these concepts later as we derive information on the cosmic noise background from the low-frequency spectrum of galactic background radiation.

Synchrotron Radiation

If an electron is placed in a magnetic field of B microgauss (μG), it will gyrate with a frequency

$$f_H = 2.8\,B \times 10^6\ \text{MHz} .$$

Such an electron will radiate as a dipole at this frequency. This radiation is independent of any velocity component $V \| B$ provided that $\beta = V/C$ is small and the radiation pattern $P(\theta) = 1 + \cos^2 \theta$, where θ is the angle between B (the axis of gyration) and the line of the sight to the observer. If the particle were relativistic, the radiation pattern would shrink to a half-angle $\theta_{1/2} = mc^2/E = (1 - \beta^2)^{1/2} << 1$. The velocity of the particle also doppler-shifts the observing frequency from f_H (in the particle frame) to $f = f_H (1 - \beta^2)^{1/2}/(1 - \beta \cos \phi)$, where ϕ is the angle between the line of sight to the observer and the particle's instantaneous velocity vector. It can be demonstrated that the observer will see this narrow cone "searchlight" every $t = 1/f$ seconds and that the width of the observed pulse $\Delta t \propto (BE^2)^{-1}$. The Fourier transform of this pulse train describes the spectrum of the radiation; it consists of a series of harmonics of f with a peak at a frequency $\sim 1/3 \Delta t$. Numerically, for B in μG and E in GeV,

$$f_{max} = 4.6\, BE^2\ \text{MHz} . \tag{20}$$

The radiated power is $\propto (hf_{max})$ times number of pulses per second $\propto hf_{max}\ f \propto B^2 E^2$. If an ensemble of electrons has a differential power-law distribution of the form

$$dN(E) = K_{CR} E^{-\gamma}\, dE , \tag{21a}$$

and this distribution is convolved with the radiation properties of an individual electron, the emitted signal has the form

$$I = (\text{constant})\, f^{-\alpha} , \qquad \alpha = \frac{\gamma - 1}{2} , \tag{21b}$$

where α is called the spectral index. The volume emissivity is given by

$$\epsilon(f) = (\text{constant}) \cdot K_{CR} \cdot B^{\alpha+1} f^{-\alpha} . \tag{21c}$$

Synchrotron Self-Absorption

The laws of thermodynamics require every radiation process to have an inverse absorption process. This must be the case with synchrotron radiation when the radio photons speed up the relativistic electrons. For an appreciable degree of absorption, the radiation field must be large. Williams (1963) has established the suitable criterion that the monochromatic brightness temperature $T_B(f)$ of a source is comparable to the equivalent kinetic temperature T_k of the relativistic particles.

From Equation 5 we can show that for a source of observed angular size ϕ' minutes of arc (or ϕ'' seconds of arc), the brightness temperature in degrees K is

$$T_B(f) = \frac{S(f)}{f^2 \cdot (\phi')^2} (6.45 \times 10^8) = \frac{S(f)}{f^2 (\phi'')^2} (2.32 \times 10^{12}),$$

where $S(f)$ is the observed flux density in flux units, and f is the observing frequency in MHz. From Equation 20, we saw that a particle with energy E (GeV) radiates at a frequency f MHz

$$f \simeq 4.6 BE^2,$$

where B is the magnetic field in μG. The equivalent kinetic temperature (°K) corresponding to E is

$$T_k = \frac{E}{k} = 1.16 \times 10^{13} E,$$

i.e.,

$$T_k = (1.16 \times 10^{13}) \left(\frac{f}{4.6 B}\right)^{1/2}.$$

Therefore, since this process will be important if $T_B \gtrsim T_k$, we write

$$\frac{S(f)}{f^2 (\phi')^2} (6.45 \times 10^8) \gtrsim (1.16 \times 10^{13}) \left(\frac{f}{4.6 B^2}\right)^{1/2} ;$$

hence the process will be important for small sources:

$$(\phi')^2 \lesssim \frac{3.8 \times 10^{-3} S(f)}{f^{5/2} B^{1/2}}$$

or

$$(\phi'')^2 \lesssim \frac{12.5 S(f)}{f^{5/2} B^{1/2}} . \qquad (22a)$$

From Equation 21b we could have written

$$S(f) = S_0 \left(\frac{f_0}{f}\right)^{\alpha} ,$$

where S_0 is the flux density at frequency $f = f_0$; hence

$$(\phi')^2 \lesssim \frac{3.8 \times 10^{-3} \cdot \left(S_0 f_0^{\alpha}\right)}{B^{1/2}} (f)^{-(5/2+\alpha)} ,$$

or

$$(\phi'')^2 \lesssim \frac{12.5 \cdot \left(S_0 f_0^{\alpha}\right)}{B^{1/2}} (f)^{-(5/2+\alpha)} . \qquad (22b)$$

Thus, the linear size of a source in which synchrotron self-absorption can take place is

$$\phi' \lesssim 0.06\left(S_0^{1/2}\ f_0^{\alpha/2}\right) B^{-1/4}\ f^{-(5/4+\alpha/2)}$$

or

$$\phi' \lesssim 3.6\left(S_0^{1/2}\ f_0^{\alpha/2}\right) B^{-1/4}\ f^{-(5/4+\alpha/2)}\ . \tag{22c}$$

We shall return to this mechansim in our discussion of the results of VLB interferometry under "Extragalactic Objects."

Energy Loss Mechanisms

We have seen that electrons with a characteristic energy E are radiating at frequency $f = 4.6\ BE^2$. Suppose that a large number of electrons with energy E_0 are released at some time t_0; these electrons will lose energy at a rate proportional to $B^2\ E^2$, that is

$$\frac{dE}{dt} = -\ RB^2\ E^2\ \text{GeV/time}\ ,$$

where $R = 3.8 \times 10^{-18}$ if B is in μG, E in GeV and time is in seconds, or $R = 1.2 \times 10^{-10}$ if time is in years. Hence, after a time interval $\Delta t = t - t_0$ has elapsed, the energy will be of the form (assuming $B \neq B(t)$)

$$E(t) = \frac{E_0}{1 + RB^2\ E_0\ \Delta t}\ ; \tag{23}$$

hence the characteristic frequency will decrease with time according to

$$f(t) = \frac{f_0}{\left(1 + RB^2\ E_0\ \Delta t\right)^2}\ .$$

More correctly, we should consider that the field B is trapped in a distribution which expands with time. If the radius varies linearly with time, then $B^2 \propto t^{-3}$, or

$$B^2(t) = B_0^2 (\Delta t)^{-3} .$$

Under these conditions, the "bump" in the emission spectrum will occur at frequency f MHz after time t given by

$$t \sim 2.6 \times 10^{10} \left(B^3 f\right)^{-1/2} \text{years} . \qquad (24)$$

This problem receives a more detailed treatment in Kellermann (1966) and Van der Laan (1963).

Another energy-loss mechanism is inverse-Compton loss. Here a radio photon collides with an electron and becomes a visible, UV, or X-ray photon. Losses from this mechanism also vary with E^2 and act as a "refrigerator" on the radio emission. Kellermann and Pauliny-Toth (1969) have shown that this mechanism limits the maximum-brightness temperature in typical extra-galactic radio sources to $\sim 10^{10}$ °K.

RADIO OBSERVATIONS OF GALACTIC COSMIC-RAY ELECTRONS

Cosmic-ray electrons emit synchrotron radiation which is the dominant noise source below 100 MHz. Their radiation properties should help reveal the nature of relativistic electrons in the galaxy. The region above about 10 MHz has been probed from the ground in great detail, but below this frequency the earth's ionosphere prevents ground-based observations. Several groups in the U.S., Canada, USSR, England, and France have flown space experiments to observe the low-frequency radio spectrum. Most of these efforts have suffered from spacecraft-generated noise (RFI = Radio Frequency Interference), local noise made in the topside of the ionosphere (magnetosphere), and a lack of angular resolution. On July 4, 1968, the GSFC Radio Astronomy group launched the first RAE (Radio Astronomy Explorer) satellite into a high-inclination (59-degree retrograde), high-altitude (5850 km) circular orbit. The RAE was designed with very low RFI levels and includes both a low-resolution (dipole) antenna and high-resolution

(750-foot-long terminated Vee) antennas. The latter are gravity-gradient-stabilized so that one Vee points outward from the earth along the line joining the satellite and the center of the earth, and the other points downward toward the earth. Here we discuss some dipole observations summarized in Alexander et. al., 1969) and their interpretation (for other properties of galactic radio emission, see Mills, 1964). The Vee data were used to help select quiet regions of the sky and thus avoid terrestrial contamination. These results are from the early analysis; more detailed results should soon be available.

In Figure 8 we show the RAE observed spectrum in the vicinity of the north galactic pole ($\alpha \sim 10^h$, $\delta \sim 60°$; $l^{II} \sim 150°$, $b^{II} \sim 50°$). Also shown are the results of reliable ground-based surveys in a similar direction. As we attempt to fit this spectrum as a synchrotron radiation

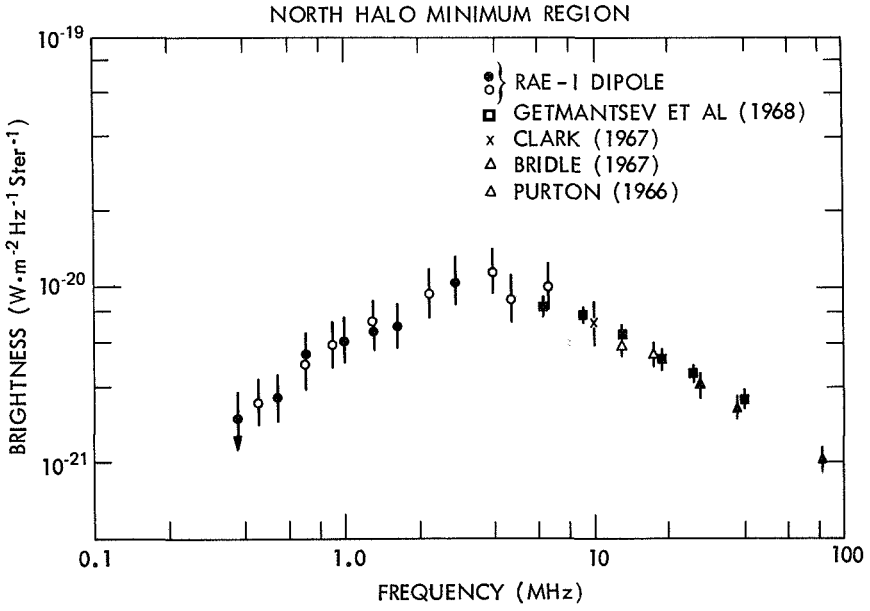

Figure 8–Integrated spectrum of the cosmic-noise background radiation from 0.4 to 100 MHz for a broad region centered on the region of minimum brightness near the north galactic pole. The two symbols used for the RAE data refer to measurements with two independent receiving systems on the same antenna. (Taken from Alexander et. al., 1969.)

spectrum modified by HII Absorption (i.e., using Equations 18, 19, and 21), we find that at $f \gtrsim 8$ MHz a curve $I(f) \propto f^{-0.6}$ results, implying that a galactic cosmic-ray distribution index $\gamma = 2.2$ applies. This is somewhat steeper than the $\gamma = 1.85 - 1.9$ indicated for the direct measurement of the differential spectrum shown in Figure 9. So we

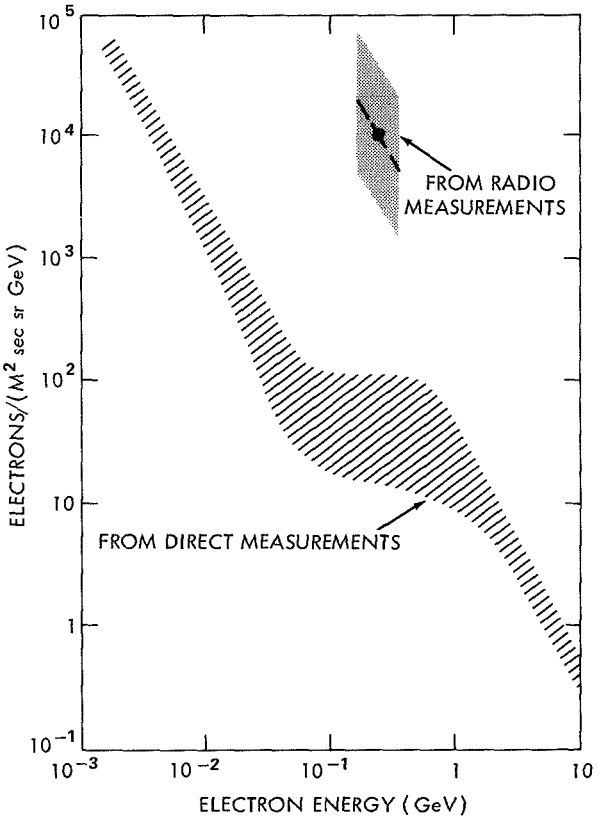

Figure 9—Comparison of cosmic ray fluxes deduced from low-frequency radio measurements with those obtained by direct measurement. (Taken from Alexander et. al., 1970.)

now examine the region $f \lesssim 1$ MHz. In this region, any galactic halo or extragalactic component should be absorbed and, if we assume that the emitting and absorbing regions are mixed uniformly (with a constant source function), the spectrum takes the form

$$I(f) = I_0(f)\left(\frac{1 - e^{-\tau}}{\tau}\right),$$

where

$$I_0(f) = \text{constant} \times f^{-\alpha};$$

thus, since $\tau \propto f^{-2}$,

$$I(f) = \text{constant} \times \frac{f^{-\alpha}}{f^{-2}}\left(1 - e^{-\tau}\right),$$

or, for $\tau \gtrsim 1$-2,

$$I(f) \propto f^{2-\alpha}.$$

With the present data, $2 - \alpha \simeq 1.57$, yielding $\alpha = 0.43 \pm 0.05$; hence $\gamma = 1.86 \pm 0.1$, in good agreement with the observed γ for $E \gtrsim 1$ GeV. Which electrons are we observing? Recalling Equation 20,

$$f \simeq 4.6\, BE^2.$$

The mean magnetic fields in the interstellar medium as derived from Faraday rotation and Zeeman splitting are $\sim 5\ \mu$G; thus

$$E \sim \frac{f^{1/2}}{5}\ \text{GeV},$$

where f is in Mhz. Thus in the region from 0.4 to 1 MHz we are probing the electrons in the 0.1- to 0.3-GeV range. The terrestrial observations shown in Figure 8 show the spectrum "flattening out" at E $\sim$ 0.6 GeV. We suggest, from the consistency of the higher-energy data with our 0.1- to 0.2-GeV number, that the low-energy decrease is an artifact, probably due to the exclusion of low-energy cosmic-ray electrons by solar and interplanetary magnetic field cavity. When the uniform-mixture curve is extrapolated to higher frequencies, we must include an additional component coming from outside of the plane with a spectral index $\alpha \sim 0.7$, to account for the observed spectrum including the $\alpha = 0.6$ spectral index above 8 MHz. Some workers have identified this extra-planar component as a galactic halo, others as something due to the aggregate effect of the extragalactic radio sources. We also have some reason to believe that it is partly due to the breakdown of the constant source-function law assumed in the analysis; there is no a-priori reason to suppose that the relativistic electrons responsible for emission and the thermal electrons responsible for HII absorption have the same distribution function—as we move out of the plane. Work is being done on refining these numbers and will help us decide whether a galactic halo is present.

We pointed out in Equation 18c that if we observed at a very low frequency, the volume emissivity would be $\epsilon(f) = I(f)/z_1$, where z_1 is the distance to $\tau = 1$. In terms of the relativistic electrons and ionized hydrogen in the galaxy, the semi-thickness of the galactic disc is probably 150 pc ($\sim 4.6 \times 10^{18}$ m). For the observations in Figure 3, the center of the antenna beam is at a galactic latitude 60°, implying a path length, when averaged over the beam, of 300 pc. From spectral fitting exercises, we infer that $\tau \sim 2$ at 700 kHz, so the $\tau \approx 1$ distance $\sim$150 pc and the $(1 - e^{-\tau})$ correction factor as given under "Thermal Emission and Absorption Processes" will be 0.8. Thus the volume emissivity will be

$$\epsilon(f) = \frac{5 \times 10^{-21}}{4.6 \times 10^{18} \times 0.8} = 1.3 \times 10^{-39} \text{ wm}^{-3} \text{ Hz}^{-1} \text{ ster}^{-1}$$

for f = 700 kHz. For the synchrotron process, Equation 21c would give $\epsilon(f_1) = 1.2 \times 10^{-39}$ w m^{-3} Hz^{-1} ster^{-1}, for $f_1 = 1$ MHz taken as a reference frequency and $\alpha \sim 0.4$.

An independent derivation for a 2-kpc path length in the disc (Roger, 1969) yields a value at 22.2 MHz of $9.1 \times 10^{-41}\,\mathrm{w\,m^{-3}\,Hz^{-1}\,ster^{-1}}$, or, if we use the spectral dependence $\alpha \sim 0.4$,

$$\epsilon'(f_1) = 3.1 \times 10^{-40}\,\mathrm{w\,m^{-3}\,Hz^{-1}\,ster^{-1}},$$

which is a factor $\sim$4 less than the present value. We suggest that this apparent discrepancy arises because the path length appropriate to $\epsilon'(f)$ traverses 2 kpc, a large portion of which lies between the Orion and Perseus spiral arms. If we assume that the path length in the spiral arms $\sim$1/4 of the total, and that the 700-kHz value measures only the local spiral arm, then the ϵ (interarm) $\lesssim 0.1\,\epsilon$ (arm). The lower emissivity between spiral arms could arise because of lower relativistic particle densities or because of weaker magnetic fields in the inter-arm region. However, for cosmic-ray electrons with energies $\lesssim$a few GeV, the particles can be contained by very small fields, and therefore it is likely that the lower emissivity is due to lower magnetic fields rather than a deficiency of particles. From the dependence of the emissivity on the magnetic field given by Equation 21c, the interarm fields will then be $\lesssim$0.1-0.2 of the few μG fields within the arm, i.e., $\lesssim 1\,\mu$ Gauss.

When the numerical constants are included in Equation 21c, we may evaluate the cosmic-ray distribution constant K_{CR}. The results of such an evaluation are shown in the shaded box of Figure 9, where the size of the box is indicative of all experimental uncertainties and the range of model-dependent parameters for reasonable assumptions on size, magnetic fields, etc. We find the electrons observed to radiate at $\sim$1 MHz have energies of a few hundred MeV, and that the relativistic particle densities in the interstellar medium are a factor $\sim$50 greater than the values observed directly. A part of this difference can be attributed to "solar modulation," wherein only a fraction of the particles leak through the walls of the cavity formed by the solar magnetic field. A modulation as great as a factor of 50 is larger than would be inferred on theoretical and observational grounds. The discrepancy may be due to the solar system being located in a relative "void" of cosmic-ray particles.

EXTRAGALACTIC OBJECTS

Normal Galaxies

The properties we just discussed pertaining to our own galaxy also pertain to the apparent properties of normal external galaxies. Our galaxy, if it were observed from a large distance (several Mpc) would be a small object of relatively low luminosity. Only for our nearest neighbors - like the Magellanic Clouds and the Andromeda Nebula - are the radio emission from classical "normal" galaxies detectable.

"Abnormal Objects"

The radio astronomer first detected extragalactic radiation from objects that are now called radio galaxies. A typical example is the Cygnus-A radio source. The emission spectrum for this object (and the galactic supernova remnant Cassiopeia A - the pair of which are the brightest discrete objects in the northern hemisphere in the range from ~30 MHz to ~1000 MHz) is shown in Figure 10. We note that in

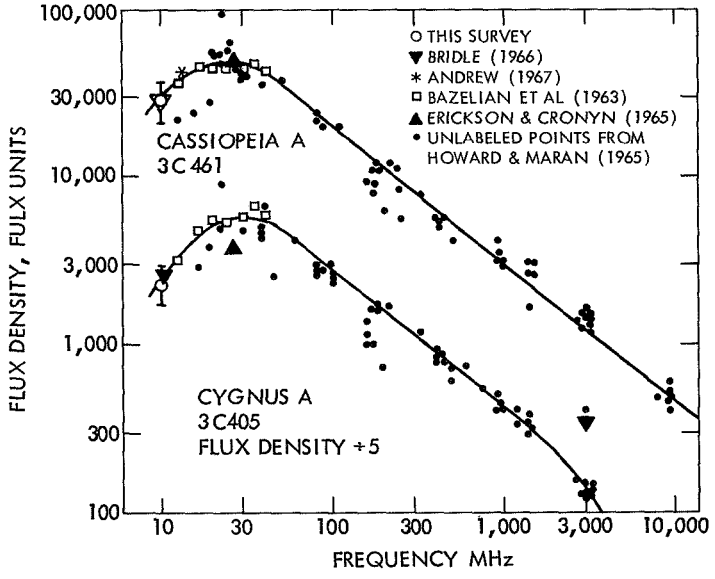

Figure 10–The spectra of the Cygnus-A and Cassiopeia-A radio sources (from Clark, 1967).

the frequency range from ~50 to ~1000 MHz, the spectrum is characterized by $\alpha = 0.7$ or $\gamma = 2.4$, which is somewhat steeper than the "normal" galaxy, but is typical of radio galaxies.

When the location of this source was measured with sufficient precision to permit optical identification, it was found that a galaxy was at that position. The original identification from 200-inch Mt. Palomar telescope plates showed two fuzzy regions close to each other; the first interpretation was two galaxies in collision. Optical spectral observations indicate radial velocity $\sim 17 \times 10^3$ km/sec (receding); if we use the Hubble constant H = 100 km-sec^{-1} Mpc^{-1}, this object is located ~170 Mpc (~5×10^{24} meters) away. Radio observations indicate that the radio object is much larger than the optical, consisting of two regions, ~30 × 50 seconds of arc (~40 kpc × 60 kpc size) separated by 1-1/2 minutes of arc (~100 kpc), with the optical object in the middle. High resolution radio observations showed that the 30 × 50 seconds "bags" are broken up and clumpy. We also note from the spectrum a kink at f ~ 2000 MHz. If we interpret this by invoking Equation 24, with a magnetic field 20 μG, then the age of this feature is $\sim 7 \times 10^6$ years. One pc ~ 3 light years; thus, if ~100 kpc = 3×10^5 light years reflects the epoch of a violent galactic explosion, the expansion velocity has been ~c/20. The total power radiated by such an object is many orders of magnitude greater than normal galaxies (~10^{38} ergs-sec^{-1} vs 10^{45} ergs-sec^{-1}). A number of enlightening reviews of the properties of radio galaxies have been published; see Heeschen (1962), Shklovsky (1960), Steinberg and Lequeux (1963, Chapter 11), and Preister and Rosenberg (1968). Since radio galaxies are indicators of violent activity in galaxies, they must by their very nature be fairly recent (on a cosmic time scale ~10^9 years). At low frequencies we have another probe of old radio sources. Note the spectral behavior of 3C66 and 3C84 in Figure 11. These objects show the behavior observed in ~20 percent of all sources seen below ~20 MHz. The low-frequency emission spectrum shows a marked upturn. We feel that this is due to the sequence discussed under "Energy-Loss Mechanisms." High-energy electrons lose energy through radiation losses and become low-energy (although still relativistic) electrons, and magnetic fields become weaker through expansion; both factors make such sources radiate at low frequencies from extended halos. Ground-based observations are somewhat hampered by the ionosphere and the huge equivalent collecting areas with the angular resolution needed to see such objects. Space observations to date lack the sensitivity and angular resolution to see them

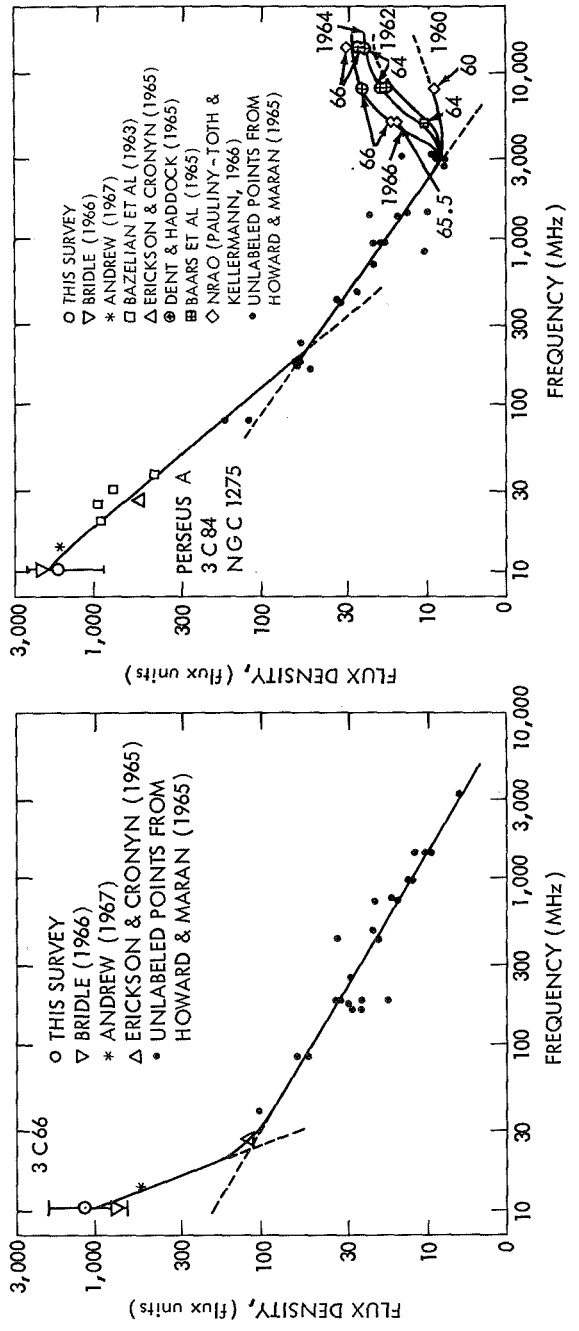

Figure 11–Spectra of the extra-galactic radio sources 3C66 and 3C84 showing anomalous low-frequency enhancement.

below 10 MHz, so we have insufficient knowledge to discuss in detail the evolution of old radio sources.

The source 3C84 is also a young radio source in that its evolution is still proceeding. At frequencies $\gtrsim$5 GHz, the radio emission is variable over time scales of a few years. This object is identified as the Seyfert galaxy NGC1275, the most prominent member of the Perseus cluster of galaxies. Seyfert galaxies have nuclei that are very compact - the size is limited only by optical-telescope resolution for short exposures. These nuclei have properties quite similar to those of quasi-stellar objects (QSO's or quasars). The phenomenon of time variability on time scales $\sim$a year indicates that the size of the objects in question can be no more than a few light years. If these objects are at distances of a few hundred Mpc, the angular size must be $\lesssim 10^{-3}$ seconds of arc. This in turn means that the variable components must exhibit synchrotron self-absorption, as given in Equations 22, at frequencies $\lesssim$ few GHz. This accounts for the spectral jump in 3C84 at $\sim$2 GHz.

A number of these sources show several "lumps" in their spectra in the 1-20 GHz range. This is presumably due to a number of outbursts at earlier epochs. Examples are shown in Figure 12. Each outburst in turn expands and radiates at lower frequencies. It has actually been possible to follow these variations in the spectrum for a few sources (see Kellermann and Pauliny-Toth, 1968, for a survey of the properties of these objects). The small angular size of these objects predicted by both synchrotron self-absorption and the time-scale of variability arguments is verified by VLB interferometry observations. Our hope now is to use VLB techniques to observe the expansion of such an object with time and to map its brightness distribution. We are remarkably close to a coherent solution on these objects—theory and observation are in remarkable agreement, although we still have no fundamental understanding as to why the outbursts occur or what is their fundamental source of energy.

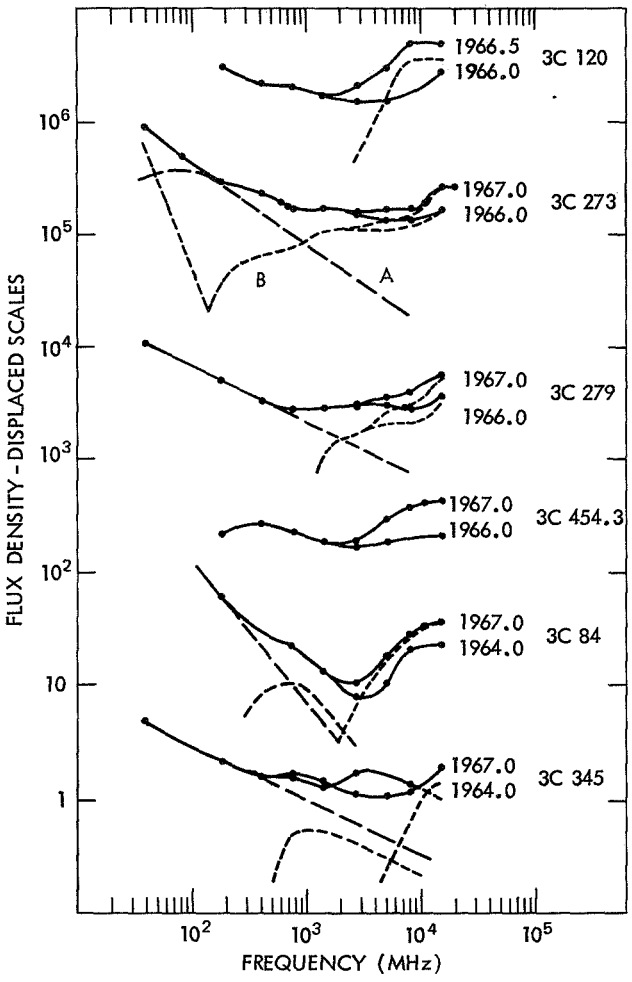

Figure 12—The radio spectra of six variable sources. The spectra are shown at two epochs. In some cases, a possible separation into components is shown, based on interferometer data or on the variations themselves. Errors are not shown, but are usually 2-3 percent in the measurement of a change of flux density and 5-10 percent in the scale of flux density. (From Kellermann and Pauliny-Toth, 1968.)

Alexander, J. K., Brown, L. W., Clark, T. A., Stone, R. G., and Weber, R. R., "The Spectrum of the Cosmic Radio Background Between 0.4 and 6.5 MHz," Astrophys. J. Letters, 157:L163-L165, Sept. 1969.

Alexander, J. K., Brown, L. W., Clark, T. A., and Stone, R. G., "Low Frequency Cosmic Noise Observations of the Constitution of the Local System," NASA-GSFC Preprint X-615-70-22, 1970.

Clark, T. A., "Astronomical Observations at Low Radio Frequencies," Thesis, Unov. of Colorado, 1967.

Ginzberg, V. L., and Syrovatskii, S. I., "Cosmic Magnetobremsstrahlung (Synchrotron Radiation)," Ann. Rev. Astron. Astrophys. 3:297-350, 1965.

Heeschen, D. S., "Radio Galaxies," Sci. Amer. 206(3):41-49, March 1962.

Kellermann, K. I., "On the Interpretation of Radio-Source Spectra and the Evolution of Radio Galaxies and Quasi-Stellar Objects," Astrophys. J. 146:621-633, 1966.

Kellermann, K. I., and Pauliny-Toth, I. I. K., "Variable Radio Sources," Ann. Rev. Astron. Astrophys. 6:417-488, 1968.

Kellermann, K. I., and Pauliny-Toth, I. I. K., "Spectra of Opaque Radio Sources," Astrophys. J. Letters, 155:L71-L78, 1969.

Mills, R. B., "Nonthermal Radio Frequency Radiation from the Galaxy," Ann. Rev. Astron. Astrophys. 2:185-212, 1964.

Ögelman, H., "Current Problems of High-Energy Astrophysics," in Lectures in High-Energy Astrophysics by H. Ögelman and J. R. Wayland, NASA Special Publication 199, 1969.

Preister, W., and Rosenberg, J., "Extragalactic Radio Sources," in Introduction to Space Science by W. N. Hess and G. D. Mead, London: Gordon and Breach, 1968, ch. 22.

Roger, R. S., "Low-Frequency Absorption due IC 1805 and IC 1848," Astrophys. J. 155:831-840, 1969.

Shklovsky, I. S., Cosmic Radio Waves, Cambridge, Mass.: Harvard University Press, 1960.

Steinberg, J. L., and Lequeux, I., Radio Astronomy, New York: McGraw-Hill, 1963, Ch. 11.

Van der Laan, H., "Radio Galaxies," Monthly Notices of the Royal Astronomical Society, 126:519-533 and 535-552, 1963.

Williams, P. J. S., "Absorption in Radio Sources of High Brightness Temperature," Nature, 200:56-57, 1963.

NASA-Langley, 1970 —— 30

"The aeronautical and space activities of the United States shall be conducted so as to contribute . . . to the expansion of human knowledge of phenomena in the atmosphere and space. The Administration shall provide for the widest practicable and appropriate dissemination of information concerning its activities and the results thereof."

— NATIONAL AERONAUTICS AND SPACE ACT OF 1958

NASA SCIENTIFIC AND TECHNICAL PUBLICATIONS

TECHNICAL REPORTS: Scientific and technical information considered important, complete, and a lasting contribution to existing knowledge.

TECHNICAL NOTES: Information less broad in scope but nevertheless of importance as a contribution to existing knowledge.

TECHNICAL MEMORANDUMS: Information receiving limited distribution because of preliminary data, security classification, or other reasons.

CONTRACTOR REPORTS: Scientific and technical information generated under a NASA contract or grant and considered an important contribution to existing knowledge.

TECHNICAL TRANSLATIONS: Information published in a foreign language considered to merit NASA distribution in English.

SPECIAL PUBLICATIONS: Information derived from or of value to NASA activities. Publications include conference proceedings, monographs, data compilations, handbooks, sourcebooks, and special bibliographies.

TECHNOLOGY UTILIZATION PUBLICATIONS: Information on technology used by NASA that may be of particular interest in commercial and other non-aerospace applications. Publications include Tech Briefs, Technology Utilization Reports and Technology Surveys.

Details on the availability of these publications may be obtained from:

SCIENTIFIC AND TECHNICAL INFORMATION DIVISION

NATIONAL AERONAUTICS AND SPACE ADMINISTRATION

Washington, D.C. 20546